DISS. ETH NO. 23188

Advanced Modeling and Algorithms for High-Precision GNSS Analysis

A thesis submitted to attain the degree of

DOCTOR OF SCIENCES of ETH ZURICH

(Dr. sc. ETH Zurich)

presented by

KAN WANG

Dipl.-Ing., University of Stuttgart

born on 03.05.1985

citizen of the People's Republic of China

accepted on the recommendation of

Prof. Dr. M. Rothacher, examiner
Prof. Dr.-Ing. M. Becker, co-examiner

2016

Abstract

In the recent ten years, the Global Navigation Satellite System (GNSS) processing has experienced a fast development in many areas including the increasing number of frequencies, the higher quality of positioning instruments, e.g. the receiver clocks and the satellite clocks, and more integrated modeling and calculation strategies. This thesis includes investigations of different modeling and parameterization methods in modern GNSS positioning with the focus on three important positioning error sources: the receiver clock errors, the phase ambiguities and the ionospheric delays.

The thesis shows that making use of the high-quality receiver clocks and applying appropriate receiver clock modeling can help to improve the kinematic height estimates, which are highly correlated with the receiver clock parameters. An efficient pre-elimination and back-substitution strategy of epoch parameters with relative clock constraints between subsequent and near-subsequent epochs has been developed to enable processing of, e.g., high-rate data. A detailed analysis of the relationship between the clock quality and the improvement of kinematic heights has been performed. Studies were also conducted to decorrelate the receiver clock parameters, the kinematic heights and the troposphere parameters. Experiments with real data have shown that appropriate deterministic and stochastic clock models can also be helpful to increase the resolution of the estimated Zenith Path Delay (ZPD) parameters without obvious degradation of the stability of the kinematic heights.

The second aspect of the thesis focuses on the resolution of triple-frequency phase ambiguities with different linear combinations. A complete analytical investigation of Geometry-Free (GF) and Ionosphere-Free (IF) triple-frequency phase ambiguity resolution with minimized noise level has been performed for different frequency triplets. The analysis was done separately for the best two linear combinations and the third one. Experiments have shown that the fractional parts and the formal errors of the combined ambiguities of the best two linear combinations are relatively small for Galileo E1, E5b and E5a and GPS L1, L2 and L5 triplets, while the third linear combination remains a challenge. Further analysis with the geostationary satellites of the Beidou Navigation Satellite System (BDS) elaborated in the framework of this thesis has also confirmed that the combined ambiguities from the best two GF and IF linear combinations can be fixed by rounding, while the estimated ambiguities on L1 have relatively large deviations from the values obtained from the traditional dual-frequency double-difference ambiguity resolution. Apart from the triple-frequency ambiguity resolution on the double-difference

level, the so-called track-to-track ambiguities between different tracks of the same receiver and the same satellite have also been investigated for the best two triple-frequency linear combinations using GPS L1, L2 and L5 as well as Galileo E1, E5b and E5a observations. The outcome demonstrates that elevation-dependent influences on the observations like Phase Center Variations (PCVs), Phase Center Offsets (PCOs) and multipath are important for the fixing of the track-to-track ambiguities. The combined track-to-track ambiguities using the best two linear combinations are also effective in detecting problems in the observation data.

The third aspect of the thesis includes the investigation of the differential ionospheric delays and gradients in the region of Switzerland from 1999 to 2013. In differential Global Positioning System (GPS) positioning, the ionospheric delays for short baselines are in most cases small enough to be ignored, except under extreme conditions, e.g., during ionospheric stormy days, and for applications with high integrity requirements, e.g., during approach and landing of aircrafts. This thesis introduces an algorithm using double-difference phase measurements with resolved phase ambiguities and global ionosphere maps provided by the Center for Orbit Determination in Europe (CODE) to extract the single-difference ionospheric delays, and enabling an automatic and robust processing of the data over 15 years. The results show that the daily maximum slant ionospheric gradients calculated from the differential slant ionopheric delays and the baseline lengths from 1999 to 2013 are below the slant ionosphere gradient boundary of the Conterminous United States (CONUS) ionospheric anomaly threat model.

Zusammenfassung

In den letzten zehn Jahren hat sich die Prozessierung der Daten der globalen Navigationssatellitensysteme (GNSS) in vielen Bereichen sehr schnell entwickelt. Dazu gehören auch die zunehmende Anzahl der Frequenzen, die erhöhte Qualität der Positionierungsinstrumente, z.B. der Empfängeruhren und der Satellitenuhren, und stärker integrierte Modellierungs- und Berechnungsstrategien. Diese Arbeit enthält Untersuchungen zu verschiedenen Methoden der Modellierung und Parametrisierung in der modernen GNSS-Positionierung mit dem Schwerpunkt auf drei wichtigen Fehlerquellen: die Empfängeruhrfehler, die Phasenmehrdeutigkeiten und die Ionosphärenverzögerungen.

Die Arbeit zeigt, dass die Nutzung von hochwertigen Empfängeruhren und die Anwendung geeigneter Modelle für diese Empfängeruhren die Schätzung von kinematischen Höhen, die stark mit den Empfängeruhrenparametern korreliert werden, verbessern können. Eine effiziente Strategie für die Pre-Elimination und Rück-Substitution von Epochen-Parametern mit relativen Zwängen für die Uhrenparameter zwischen aufeinanderfolgenden oder mehreren aufeinanderfolgenden Epochen ist entwickelt worden, um die Verarbeitung von Daten mit, z.B. hoher Aufzeichnungsrate zu ermöglichen. Eine detaillierte Analyse für den Zusammenhang zwischen der Qualität der Empfängeruhren und der Verbesserung der kinematischen Höhen wurde ausgeführt. Es wurde auch untersucht, wie die Empfängeruhrenparameter, die kinematischen Höhen und die Troposphärenparameter dekorreliert werden können. Experimente mit realen Daten haben gezeigt, dass geeignete deterministische und stochastische Uhrenmodelle auch hilfreich sein können, die Auflösung der geschätzten Zenith Path Delay (ZPD) Parameter zu versteigern, ohne die Stabilität der kinematischen Höhen offensichtlich zu verschlechtern.

Der zweite Aspekt der Arbeit konzentriert sich auf die Auflösung der Tripel-Frequenz-Phasenmehrdeutigkeiten mit verschiedenen Linearkombinationen. Eine vollständige analytische Untersuchung für die Auflösung der geometriefreien (GF) und ionosphärenfreien (IF) Tripel-Frequenz-Phasenmehrdeutigkeiten mit minimiertem Rauschen ist für verschiedene Frequenz-Tripletts durchgeführt worden. Die Analyse wurde getrennt für die besten zwei Linearkombinationen und die dritte Linearkombination durchgeführt. Die Experimente haben gezeigt, dass die Bruchteile und die formalen Fehler der kombinierten Phasenmehrdeutigkeiten der besten zwei Linearkombinationen für Galileo E1, E5b und E5a und GPS L1, L2 und L5 Tripletts relativ klein sind, während die dritte Linearkombination eine Herausforderung bleibt. Eine weitere Analyse der geostationären Satelliten des Beidou-Navigationssatellitensystems (BDS), die im Rahmen dieser Arbeit ausgear-

beitet wurde, hat bestätigt, dass die kombinierten Mehrdeutigkeiten von den besten zwei GF und IF Linearkombinationen mit Runden auf die nächste ganze Zahl fixiert werden können, während die geschätzten Mehrdeutigkeiten auf L1 relativ große Abweichungen zu den Werten haben, die mit der traditionellen Zweifrequenz-Doppeldifferenz-Phasenmehrdeutigkeitslösung berechnet wurden. Neben der Auflösung der Tripel-Frequenz -Phasenmehrdeutigkeiten auf der Doppeldifferenz-Ebene sind auch die sogenannten "track-to-track" Mehrdeutigkeiten zwischen verschiedenen Bahnbögen des gleichen Empfängers und des gleichen Satelliten für die besten zwei Tripel-Frequenz-Linearkombinationen mit Hilfe von GPS L1, L2 und L5 sowie Galileo E1, E5b und E5a Beobachtungen untersucht worden. Das Ergebnis zeigt, dass elevationsabhängige Einflüsse wie Phasenzentrumsvariationen (PZV), Phasenzentrumsoffsets (PZO) und Mehrwegeffekte wichtig für die Fixierung der track-to-track Mehrdeutigkeiten sind. Die kombinierten track-to-track Mehrdeutigkeiten der besten zwei Linearkombinationen sind ebenfalls geeignet, um Probleme in den Beobachtungsdaten zu detektieren.

Der dritte Aspekt der Arbeit beinhaltet die Untersuchung der differentiellen Ionosphärenverzögerungen und -gradienten in der Region der Schweiz von 1999 bis 2013. In der differentiellen Positionierung mit dem Globalen Positionsbestimmungssystem (GPS) sind die Ionosphärenverzögerungen für kurze Basislinien in meisten Fällen so klein, dass man sie ignorieren kann. Ausnahmen gibe es jedoch unter extremen Bedingungen, z.B., während ionosphärischer Stürme für Anwendungen mit hohen Integritätsanforderungen, z.B. beim Anflug und der Landung von Flugzeugen. Diese Arbeit stellt einen Algorithmus vor, der die Doppeldifferenz-Phasenmessungen mit gelösten Phasenmehrdeutigkeiten und die globalen Ionosphärenkarten, die vom Center for Orbit Determination in Europe (CODE) bereitgestellt werden, benutzt, um die Einfachdifferenz-Ionosphärenverzögerungen zu extrahieren, und eine automatische und robuste Prozessierung der Daten über 15 Jahren zu ermöglichen. Die Ergebnisse zeigen, dass sich die täglichen maximalen Ionosphärengradienten in Satellitenrichtung von 1999 bis 2013, die aus den differenziellen Ionosphärenverzögerungen in Satellitenrichtung und den Basislinienlängen berechnet wurden, unterhalb der Grenze für die Ionosphärengradienten vom Conterminous United States (CONUS) Bedrohungsmodell für ionosphärische Anomalien befinden.

Acknowledgement

Firstly, I would like to thank Prof. Dr. Markus Rothacher who has accompanied me throughout the whole dissertation and has given me important guidance on my investigations. I would also like to thank my co-superviser Prof. Dr.-Ing. Matthias Becker for the helpful comments and corrections of the dissertation. In addition to that, I would like to thank the following people for their support in different projects:

PD Dr. Rolf Dach, Astronomical Institute, University of Bern (AIUB)
Dr. Etienne Orliac, AIUB
Univ.-Prof. Dr.phil.nat. Urs Hugentobler, Institute for Astronomical and Physical Geodesy (IAPG), Technical University of Munich (TUM)
Prof. Dr. Alain Geiger, Institute of Geodesy and Photogrammetry, ETH Zurich
Dr. Michael Meindl, Institute of Geodesy and Photogrammetry, ETH Zurich
Dr. Maurizio Scaramuzza, Skyguide – Swiss Air Navigation Services Ltd.
Dr. Pascal Truffer, Skyguide – Swiss Air Navigation Services Ltd.
Dr. Marc Troller, Skyguide – Swiss Air Navigation Services Ltd.
Dr. Michael Müller, Institute of Geodesy and Photogrammetry, ETH Zurich (at the time when the project was running)
Dipl.-Ing. Dominik Voithenleitner, IAPG, TUM (at the time when the project was running)
Dr.-Ing. Mathias Fritsche, Institute of Planetary Geodesy, Technical University of Dresden (now at Helmholtz-Zentrum Potsdam – Deutsches GeoForschungsZentrum (GFZ))
Dr. Krzysztof Sośnica, AIUB (now at Institute of Geodesy and Geoinformatics, WUELS, Wroclaw, Poland)
Dr.-Ing. Carlos Javier Rodríguez Solano, IAPG, TUM (at the time when the project was running)
Dr.-Ing. Peter Steigenberger, IAPG, TUM (now at German Aerospace Center (DLR)/ German Space Operations Center (GSOC))
Dr. Baoqi Sun, Institute of Geodesy and Photogrammetry, ETH Zurich (at the time when the project was running); National Time Service Center, Chinese Academy of Sciences, Xian, China
Prof. Dr.-Ing. Reinhard Dietrich, Institute of Planetary Geodesy, Technical University of Dresden
Drazen Svehla, European Space Agency (ESA)/ European Space Operations Centre (ESOC), Darmstadt, Germany (at the time when the project was running)
Prof. Dr.-Ing. Werner Enderle, ESA/ESOC, Darmstadt, Germany

Dr. Thomas Sean Kelso, Center for Space Standards and Innovation (CSSI), Colorado Springs, Colorado

Apart from that, I would like to acknowledge that part of this work (Papers A, B and C) was financed by ESA as part of the project "Satellite and Station Clock Modelling for GNSS", Reference: AO/1-6231/09/D/SR, and part of this work (Paper D) has been financed by Flughafen Zürich AG as part of the Skyguide (Swiss Air Navigation Services Ltd.) project "Impact of Ionospheric Activities onto GNSS Signal during Approach and Landing" within the frame of the Swiss-wide program to implement new technologies (CHIPS). I would also like to thank swisstopo for providing the data of the Automated GNSS Network for Switzerland (AGNES) for the processing described in Paper D, and CODE and International GNSS Service (IGS) for providing data on their archives for the processing described in Papers A to D.

Additionally, I would like to thank for the financial support of the Swiss National Science Foundation (SNSF) and the German Research Foundation (DFG) within the project "Geodätische und geodynamische Nutzung reprozessierter GPS-, GLONASS- und SLR-Daten" (DFG Projects DI 473/39-1 and HU 1558/1-1, SNF Projects 200021E-131228 and 200021E-129032).

Furthermore, I would also like to acknowledge that Paper A (see Appendix A) was originally published as

Wang K., Rothacher M. (2013): Stochastic modeling of high-stability ground clocks in GPS analysis, Journal of Geodesy 87(5): 427-437. doi:10.1007/s00190-013-0616-5.
The final publication is available at `http://link.springer.com`.

Paper B (see Appendix B) was originally published as
Wang K., Rothacher M. (2013): Ambiguity resolution for triple-frequency geometry-free and ionosphere-free combination tested with real data, Journal of Geodesy 87(6): 539-553. doi:10.1007/s00190-013-0630-7.
The final publication is available at `http://link.springer.com`.

Paper C (see Appendix C) was originally published as
Wang K., Rothacher M. (2015): GNSS triple-frequency geometry-free and ionosphere-free track-to-track ambiguities, Advances in Space Research 55(11): 2668-2677. doi:10.1016/j.asr.2015.02.028.
The final publication is available at `http://www.sciencedirect.com/science/article/pii/S0273117715001568`.

Paper D (see Appendix D) was originally published as
Wang K., Meindl M., Geiger A., Rothacher M., Scaramuzza M., Troller M., Truffer P. (2014): Assessment of Single-difference Ionospheric Residuals in a Regional Network for GBAS, in Proceedings of the 27th International Technical Meeting of The Satellite Division of the Institute of Navigation (ION GNSS+ 2014), Tampa, Florida, US, September 2014, pp. 2384-2393.

The final publication is available at `https://www.ion.org/publications/abstract.cfm?jp=p&articleID=12550`.

Two additional papers (see Appendix E) were originally published as
Fritsche M., Sośnica K., Rodríguez-Solano C.J., Steigenberger P., Wang K., Dietrich R., Dach R., Hugentobler U., Rothacher M. (2014): Homogeneous reprocessing of GPS, GLONASS and SLR observations, Journal of Geodesy 88(7): 625-642. doi:10.1007/s00190-014-0710-3.
The final publication is available at `http://link.springer.com`.

Glaser S., Fritsche M., Sośnica K., Rodríguez-Solano C.J., Wang K., Dach R., Hugentobler U., Rothacher M., Dietrich R. (2015): A consistent combination of GNSS and SLR with minimum constraints, Journal of Geodesy 89(12): 1165-1180. doi:10.1007/s00190-015-0842-0.
The final publication is available at `http://link.springer.com`.

(Glaser S., Fritsche M., Sośnica K., Rodríguez-Solano C.J., Wang K., Dach R., Hugentobler U., Rothacher M., Dietrich R. (2015): Erratum to: A consistent combination of GNSS and SLR with minimum constraints, Journal of Geodesy 89(12): 1181-1182. doi:10.1007/s00190-015-0853-x.
The final publication is available at `http://link.springer.com`.)

Contents

1 Introduction

During the last ten years, more and more countries got involved into the development of GNSS. Apart from the GPS developed by the United States (US) and the Russian Globalnaya Navigatsionnaya Sputnikovaya Sistema (GLONASS), the European Union (EU) is engaged with ESA in developing its own civilian GNSS called Galileo, and China, at the same time, is building its BDS. This does not only increase the number of available satellites and improve the global cooperation in the multi-GNSS area, but also delivers possibilities to improve the positioning accuracy and to obtain a better assessment of the positioning errors, e.g., by making use of the increasing number of the frequencies and more stable receiver and satellite clocks.

This thesis presents the results of the investigations making use of these advantages of modern GNSS. It contains three different but important areas in GNSS positioning:

1. Kinematic Precise Point Positioning (PPP) and receiver clock modeling
2. Triple-frequency ambiguity resolution
3. Assessment of differential ionospheric delays and gradients

In Chapter 2, the thesis firstly makes a general introduction of the new GNSS and data analysis, and states the theoretical foundations in the three areas mentioned above. The algorithms used for clock modeling, triple-frequency ambiguity resolution and assessment of the differential ionospheric delays, which are relevant to Papers A to D, are then explained in detail with experimental results in Chapter 3. In the end, Chapters 4 and 5 summarize the main procedures and results of Paper A to D and conclude the thesis, respectively.

In kinematic PPP, the receiver clock corrections and troposphere parameters are normally estimated together and considered to be disturbing factors due to their high correlation with the height estimates, which are less accurate than the horizontal coordinates and thus considered to be a key point of investigations. Because of the continuously improved stability and quality of the receiver clocks, the modeling instead of epoch-wise estimation of these high-quality receiver clocks could be helpful for stabilizing the adjustment and decorrelating the clocks and kinematic heights. The same should also apply for the radial component of kinematically determined GNSS orbits and the high-quality GNSS satellite clocks. In Chapter 2 (see Section 2.2), different types of receiver and satellite clocks that are available nowadays are introduced and analyzed. Chapter 3 (see Section 3.1) includes the algorithm of the pre-elimination and back-substitution scheme of epoch parameters

with clock constraints between subsequent and near-subsequent epochs, and Chapter 4 (see Section 4.1) summarizes the results of Paper A, which is about the improvement of kinematic height estimates through a stochastic modeling of high-quality receiver clocks.

Error sources like clock errors, ionospheric delays can of course be eliminated by forming different linear combinations. On the double-difference level, for example, the IF linear combination eliminates the first-order term of the ionospheric delays, and the GF linear combination, on the other hand, eliminates all the geometry-related terms like receiver coordinates, satellite orbits and clock errors and allows to investigate the ionospheric delays. However, both of them increase the noise level of the observations after generating the linear combinations. The increasing number of frequencies in new GNSS provides us more possibilities to compromise between eliminating errors and minimizing the combined noise level. The thesis mainly states the results of the investigations concerning triple-frequency GF and IF linear combinations. Chapter 2 (see Section 2.3) introduces the commonly used dual-frequency linear combinations, their purpose, advantages, disadvantages and the different types of ambiguities involved. The investigation of the triple-frequency GF and IF linear combinations and the corresponding ambiguity resolution is introduced in Chapter 3 (see Section 3.2). The main results are published in Paper B and summarized in Chapter 4 (see Section 4.2). Apart from the double-difference triple-frequency ambiguity resolution, Paper C also shows the investigations and results obtained with real data for the track-to-track ambiguities using the best two GF and IF triple-frequency linear combinations. Their main problems and benefits are summarized in Chapter 4 (see Section 4.3).

The ionospheric delay is also an error source in GNSS processing that cannot be neglected. Using the GF linear combination, all the geometry-related terms including the receiver coordinates are eliminated and only the ionospheric delays remain for investigations. Since the ionosphere is ranging from about 50 km to 1000 km above the Earth surface (Groves, 2013), the ionospheric delays on the single-difference level (between receivers) are normally considered to be significantly reduced, especially for short baselines. The assessment of the differential ionospheric delays is, however, still important for the applications with high integrity requirements, e.g., during landing and approach of the aircraft. Chapter 2 (see Section 2.4) introduces firstly the general definition of the ionospheric delay used in GNSS processing. Chapter 3 (see Section 3.3) then provides an algorithm to extract single-difference ionospheric delays from double-difference observations with resolved ambiguities and states the advantages and disadvantages of this algorithm. The results of the processing of the Swiss AGNES network from 1999 to 2013 using this algorithm are discussed and assessed in Paper D and summarized in Chapter 4 (see Section 4.4).

The thesis also mentions two papers which are relevant to the reprocessing of global network solutions combining GPS, GLONASS and Satellite Laser Ranging (SLR) observations. The results of these papers are not included in this thesis, but they provide an overview of the multi-GNSS data processing, which is highly related to the topic of this thesis. The author of this thesis was involved in the processing of the network solutions

and the analysis of the 1-day and 3-day orbit and Earth rotation parameters.

2 Theoretical fundations

2.1 New GNSS and data analysis

In the recent ten years, the GNSS consist of more family members. Apart from the GPS from the US and GLONASS from Russia, the EU and China are also developing their own satellite navigation systems. The Indian Regional Navigation Satellite System (IRNSS) and the Quasi-Zenith Satellite System (QZSS) in Japan, which have a regional coverage of the Earth, operate at the same time as regional navigation satellite systems. In this section, the basic constellation of the GNSS and new developments in recent years are introduced with the focus on GPS and the EU satellite navigation system Galileo.

As we know, the GPS is a satellite navigation system built and maintained by the US and is nowadays used for both, civilian and military purpose. The GPS satellites are distributed in 6 orbital planes with a radius of about 26580 km and are inclined by about 55° with respect to the Earth equatorial plane (Groves, 2013). As of October 14, 2015, there were 31 operational GPS satellites including 2 from the block-type IIA, 12 from the block-type IIR, 7 from the block-type IIR-M and 10 from the new block-type IIF (Navigation Center, 2015). Table 2.1 summarizes the status of the GPS constellation on October 14, 2015, with a detailed description of the Block IIF satellites (NASA, 2015; Navigation Center, 2015).

Apart from the carrier frequencies L1 (1575.42 MHz) and L2 (1227.6 MHz), the first Block IIF GPS satellite SVN62 launched in 2010 began to broadcast signals on L5 (1176.45 MHz). Dupuis et al. (2010) have shown that the rubidium clocks onboard of the Block IIF GPS satellites are improved compared to the earlier generations. In the planned phase of GPS Block III, the availability of which might be delayed to 2017 (Gruss, 2015), the new L1C signal, increased signal power and availability, better accuracy of the navigation signals and longer Space Vehicle (SV) lifetime can be expected (Gruss, 2015; Marquis and Shaw, 2011).

In recent years, EU and ESA were also engaged in developing their own GNSS called Galileo mainly for civilian usage. The Galileo satellites are planned to be sent into Medium Earth Orbit (MEO) with an orbital height of about 23222 km above the Earth's surface and an inclination of about 56° w.r.t. the Earth equatorial plane (ESA, 2014a) with the available frequency set consisting of E1 (1575.42 MHz), E6 (1278.75 MHz), E5b (1207.14 MHz), E5 (1191.795 MHz) and E5a (1176.45 MHz) (RINEX, 2013). In December 28, 2005, and April 26, 2008 (UTC), the first two experimental Galileo satellites of the Galileo In-Orbit

Table 2.1: GPS Constellation.

Block-Type	Status	Number of satellites	PRN (SVN)	Launch date
IIA	Operational	2		
IIR	Operational	12		
IIR-M	Operational	7		
IIF	Operational	10	G25 (SVN62)	May 28, 2010
			G01 (SVN63)	July 16, 2011
			G24 (SVN65)	October 4, 2012
			G27 (SVN66)	May 15, 2013
			G30 (SVN64)	February 21, 2014
			G06 (SVN67)	May 17, 2014
			G09 (SVN68)	August 2, 2014
			G03 (SVN69)	October 29, 2014
			G26 (SVN71)	March 25, 2015
			G08 (SVN72)	July 15, 2015

Validation Element (GIOVE), GIOVE-A and GIOVE-B were launched (ESA, 2005, 2008) for test and validation purposes. Different from the GPS satellites and the GIOVE-A satellite, GIOVE-B carries two highly precise Passive Hydrogen Masers (PHMs) on board as primary satellite clocks and two rubidium clocks as back-up clocks (ESA, 2008). In June and July 2012, both of the GIOVE satellites retired after the successful accomplishment of their missions (ESA, 2012a,b).

Following the GIOVE satellites, two Galileo In-Orbit Validation (IOV) satellites Proto-Flight Model (PFM) and Flight Model 2 (FM2) were launched in October 2011, and the other two IOV, FM3 and FM4, one year afterwards (ESA, 2013; Steigenberger et al., 2013). On March 12, 2013, a first position was fixed at the Navigation Laboratory at the European Space Research and Technology Centre (ESTEC) in Noordwijk, the Netherlands, using the four IOV satellites (ESA, 2013). The accuracy was between 10 m and 15 m.

On August 22, 2014, the first two Galileo Full Operational Capability (FOC) satellites were launched in French Guiana and, unfortunately, did not reach their foreseen orbits (Arianespace Service & Solutions, 2014). However, they have entered their corrected target orbits in November 2014 and March 2015 and have been recovered from the orbital injection anomaly (ESA 2014b, 2015). In March 2015 and September 2015, another four FOC satellites FM3, FM4, FM5 and FM6 were successfully launched. The details of all the launched Galileo satellites are summarized in Table 2.2 (Galileo Constellation, 2015; Gunter, 2015).

With 24 operational satellites (GLONASS constellation status, 2015), the Russian

Table 2.2: Information of the launched Galileo satellites.

Satellite	Status	PRN	Launch date
GIOVE-A	Retired	E51	December 28, 2005
GIOVE-B	Retired	E52	April 26, 2008
IOV PFM	Operational	E11	October 21, 2011
IOV FM2	Operational	E12	October 21, 2011
IOV FM3	Operational	E19	October 12, 2012
IOV FM4	Unavailable	E20	October 12, 2012
FOC FM1	Recovered		August 22, 2014
FOC FM2	Recovered		August 22, 2014
FOC FM3	Under commissioning	E26	March 27, 2015
FOC FM4	Under commissioning	E22	March 27, 2015
FOC FM5	Under commissioning	E24	September 11, 2015
FOC FM6	Under commissioning	E30	September 11, 2015

GLONASS is the only positioning system besides GPS which is fully operational and delivers global coverage. Different from the other GNSS, GLONASS broadcasts signals on different frequencies for different satellites. On the L1 and L2 band, the frequencies are defined by

$$L1 = 1602 + 0.5625 \cdot k \quad (2.1)$$

$$L2 = 1246 + 0.4375 \cdot k \quad (2.2)$$

in MHz, where k represents the channel number and varies from -7 to +6. The same channel is shared by the satellites on the opposite side of the same orbital plane (Groves, 2013). The new generation of GLONASS satellites, i.e., the GLONASS-K1 satellites, are sending an additional Code Division Multiple Access (CDMA) signal on L3OC at 1202.025 MHz (Testoyedov, 2015; Urlichich et al., 2011).

The development of the official BDS, or the second generation of the Beidou system (Beidou-2) is also progressing. The planned full constellation of BDS consists of 5 Geostationary Earth Orbit (GEO) satellites, 27 MEO satellites and 3 Inclined Geosynchronous Orbit (IGSO) satellites. Since the first launch of a Beidou-2 satellite on April 14, 2007, BDS has accomplished the first phase with 5 GEO satellites, 5 IGSO satellites and 4 MEO satellites by the end of 2012 (Liu et al., 2014) and opened the service for commercial use across the Asia-Pacific region (BBC News, 2012). It is planned that BDS will complete its full constellation with its second phase in 2020 and will thereafter provide global navigation services (Liu et al., 2014).

The increasing number of GNSS has, at the one side, generated more opportunities for global cooperation in the navigation area and stimulated fast developments in both,

technologies and applications. On the other side, higher requirements and challenges to bridge the differences and conflicts among the different systems are the consequence. With more available satellites in view and more carrier frequencies in use, a lower Dilution of Precision (DOP) and more diversity to form linear combinations can be expected. Different time systems and data structures require, however, more compatible data exchange formats and software for multi-GNSS analysis. The Receiver Independent Exchange Format (RINEX) (RINEX, 2013) is now able to merge observation data of different systems (GPS, GLONASS, GALILEO, QZSS from Japan, BDS and Satellite Based Augmentation System (SBAS) payload), different data types, frequencies and tracking channels into one observation file. The RINEX navigation file is also able to deliver mixed orbit information from different systems. In order to systematically track and analyze all the available GNSS data, the IGS has initiated the so-called Multi-GNSS Experiment (MGEX), which processes multi-GNSS data and continuously provides products like clocks and orbits (MGEX, 2014). Fritsche et al. (2014) have published a good example for the issues encountered in a combined processing of GPS and GLONASS data. The differences of the combined results and the GPS/GLONASS-only results were compared and analyzed in this paper.

2.2 Receiver and satellite clocks

Receiver and satellite clock errors are important and non-negligible error sources in GNSS positioning. The receiver clocks are usually estimated together with the receiver positions on the zero-difference level, and the satellite clocks mostly estimated within a global network. Equations 2.3 and 2.4 show the simplified zero-difference observation equations for the carrier phase observations L_1 and L_2 on frequencies f_1 and f_2:

$$L_1 = \rho + c_l \cdot \Delta t_r - c_l \cdot \Delta t^s + \Delta_{trop} - I_1 + \lambda_1 \cdot N_1, \tag{2.3}$$

$$L_2 = \rho + c_l \cdot \Delta t_r - c_l \cdot \Delta t^s + \Delta_{trop} - \frac{f_1^2}{f_2^2} \cdot I_1 + \lambda_2 \cdot N_2, \tag{2.4}$$

where ρ, Δ_{trop} and I_1 represent the geometric distance between satellite and receiver, the tropospheric delay and the ionospheric delay on L1, respectively. Δt_r and Δt^s stand for the receiver and satellite clock error. λ_1, λ_2, N_1 and N_2 represent the wavelengths and phase ambiguities on L1 and L2, respectively. c_l denotes the speed of light.

It is not difficult to see that the synchronization of receiver and satellite clocks is nothing else but fixing the differences between the receiver and satellite clock errors. In order to avoid singularities, it is necessary to select a reference clock while estimating the clock errors. CODE selects, e.g., a stable receiver clock as the reference clock on a daily basis and assumes that it can be well represented by a linear polynomial. The IGS clock products use the IGS Time Scale (IGST) instead, which is more stable than GPS Time (GPST) for short term, but still loosely steered to GPST on the longer term (Senior et al., 2003).

The GNSS receivers and satellites are connected to different types of clocks (atomic

clocks, quartz clocks, etc.). Since the clock behavior is not only dependent on the clock type, but is also influenced by the measurement environment and hardware delays (Weinbach and Schön, 2009), the evaluation of the clock stability for specific receivers or satellites is usually performed with the help of the frequency data or the phase data. Thereby, the so-called fractional frequency $y(t)$ corresponds to the time derivative of the phase clock data $x(t)$ according to Riley (2008):

$$y(t) = \frac{v(t) - v_0}{v_0} = \frac{dx}{dt}, \tag{2.5}$$

where $v(t)$ and v_0 represent the instantaneous frequency and the nominal frequency, respectively.

The phase clock data is typically described by a deterministic part and a stochastic part $\epsilon(t)$. The deterministic part usually consists of a time offset a, a frequency offset b and a frequency drift D (Allan, 1987):

$$x(t) = a + b \cdot (t - t_0) + \frac{1}{2} D \cdot (t - t_0)^2 + \epsilon(t), \tag{2.6}$$

where t_0 represents the starting time. The stochastic process consists of different kinds of noise, which can be characterized using different kinds of Allan Deviations (ADEVs). Table 2.3 summarizes the behavior of the different stochastic processes according to Riley (2008). It shows that the Modified Allan Deviation (MDEV) is able to distinguish between White Phase Noise (WPN) and Flicker Phase Noise (FPN). The different slopes of the stochastic processes can also be seen in Figure 2.1 (Riley, 2008), where the scales in the figure are only shown as an example.

In Section 2.2.1 and Section 2.2.2 different clocks types connected to GNSS receivers and satellites are introduced with their characterization and behavior.

2.2.1 Receiver clocks

In the last ten years, more and more stable oscillators have been available that are connected to GNSS receivers. Figure 2.2 shows the global distribution of H-Masers, cesium

Table 2.3: Stochastic noise and its characteristics.

Type of noise	Slope of ADEV	Slope of MDEV
White Phase Noise (WPN)	-1	-1.5
Flicker Phase Noise (FPN)	-1	-1
White Frequency Noise (WFN)	-0.5	-0.5
Flicker Frequency Noise (FFN)	0	0
Random Walk Frequency Noise (RWFN)	0.5	0.5
Frequency Drift (FD)	1	1

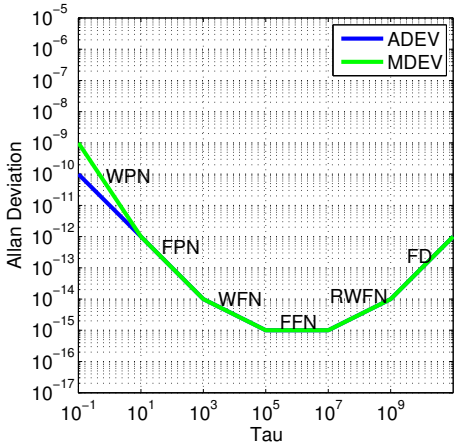

Figure 2.1: Slopes of the ADEV and MDEV.

clocks, rubidium clocks and quartz clocks connected to IGS stations on August 1, 2004, and August 1, 2014. Data were collected from the daily-updated summary file of the IGS site logs (IGS site log, 2014) in September 2014. The frequency standards that were only documented as "internal" and the former IGS stations, which have been closed down, are not contained in the figures.

Figure 2.2 shows a clear increase in the number of the high-precision Hydrogen-Masers (H-Maser) from 2004 to 2014. This increase can also be observed in Figure 2.3 showing the development of the number of the clocks available at IGS sites. Apart from the H-Masers, the number of atomic clocks (H-Masers, cesium clocks and rubidium clocks) has also increased during these ten years, especially before 2013. This indicates an even higher quality of the frequency standards available at IGS stations.

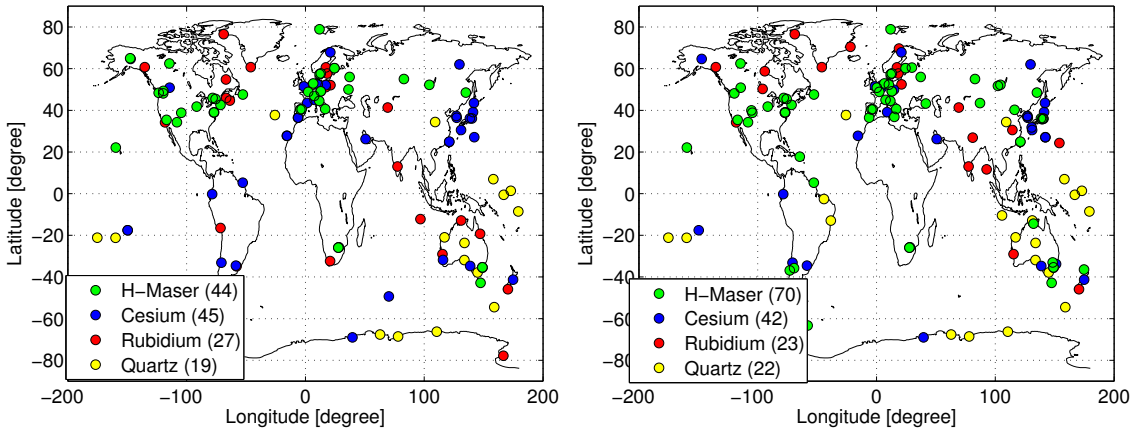

(a) August 1, 2004

(b) August 1, 2014

Figure 2.2: Global distribution of the IGS stations connected to atomic clocks and quartz clocks on (a) August 1, 2004 and (b) August 1, 2014.

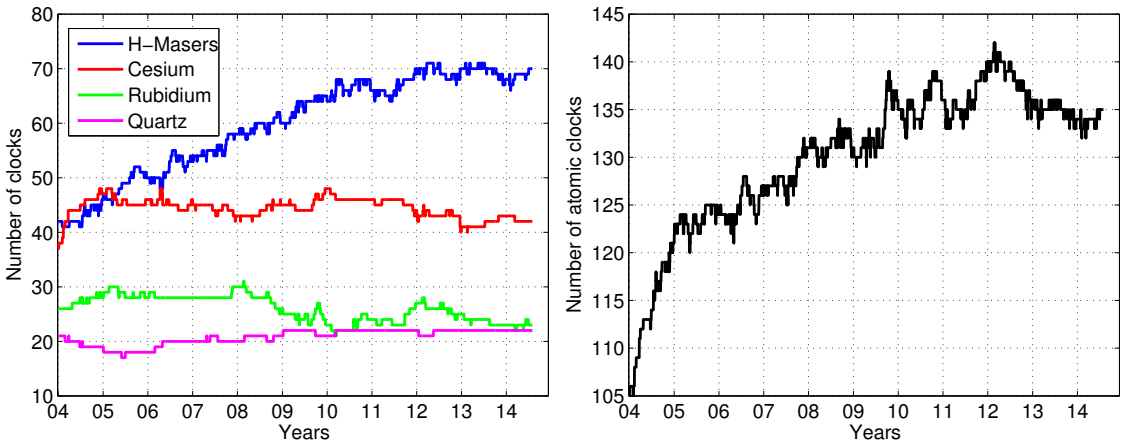

(a) All clocks (b) Atomic clocks

Figure 2.3: Number of (a) different atomic clocks and quartz clocks, and (b) all the atomic clocks from January 1, 2004, to August 1, 2014.

Figure 2.4 shows, e.g., the stochastic part of a quartz clock CAS1, a rubidium clock DUBO, a cesium clock HARB and a H-Maser ONSA after removing a linear polynomial and the MDEVs of these clocks on March 1, 2014. The standard deviations of the same clocks after removing a linear polynomial σ_{STD1} and a quadratic polynomial σ_{STD2} are listed in Table 2.4. The so-called empirical relative sigma σ_{emp} is defined with the help of the epoch-to-epoch clock changes and is a good indicator for clock constraints (see Paper A):

$$\sigma_{emp} = \sqrt{\frac{\sum_{i=1}^{n-1}(clk_{t_{i+1}} - clk_{t_i})^2}{n-1}}, \tag{2.7}$$

where clk_{t_i} indicates the clock residual after removing the deterministic part (here a linear or quadratic polynomial) at t_i, and n represents the number of the clock estimates. The phase clock data used have been extracted from the CODE final clock RINEX file from a 3-day solution with a sampling interval of 300 s for the receiver clocks (CODE products, 2014). It should be noticed that the clock estimates in the clock RINEX file are the estimated "apparent" clocks, which may absorb other errors during the adjustment due to the high correlations or insufficient parameter modeling.

After removing the deterministic model, the standard deviation of the rubidium clock DUBO and the cesium clock HARB is generally in the range of a nanosecond, while the quartz clock CAS1 behaves worse than the three atomic clocks in both, the standard deviation and the empirical relative sigma. As mentioned before, the apparent clock behavior may be influenced by a lot of factors. Clocks belonging to the same type may also behave very differently under various measurement environments. However, an obviously better behavior of the H-Masers has been observed. Figure 2.5 shows, e.g., the standard deviations of some H-Masers after removing a linear polynomial and the MDEVs of these

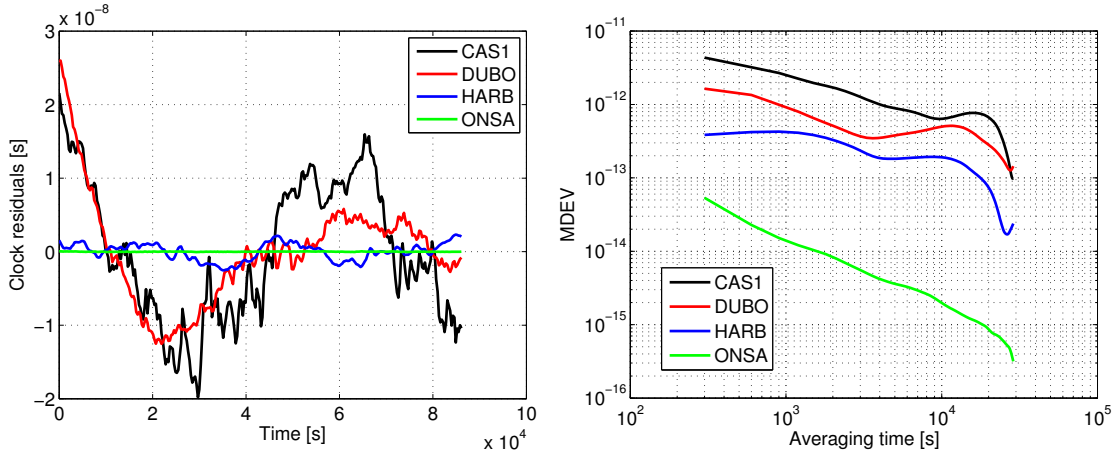

(a) Residuals (b) MDEV

Figure 2.4: (a) Clock residuals of different types of receiver clocks after removing a linear polynomial and (b) the corresponding MDEVs on March 1, 2014.

Table 2.4: Standard deviations σ_{STD} and the empirical relative sigmas σ_{emp} for different clock types after removing a linear or a quadratic polynomial on March 1, 2014.

Clock	σ_{STD1} [ns]	σ_{STD2} [ns]	σ_{emp1} [ns]	σ_{emp2} [ns]
ONSA (H-Maser)	0.0202	0.0201	0.0139	0.0139
HARB (Cesium)	1.1791	1.0616	0.2035	0.2024
DUBO (Rubidium)	7.3121	6.3894	0.6461	0.6305
CAS1 (Quartz)	9.3413	9.1981	1.5194	1.5181

H-Masers on March 1, 2014.

It is not difficult to see that the residuals of the H-Masers are generally in the range of tens of picoseconds. Their MDEVs are mostly reaching 10^{-15} after 8 hours.

2.2.2 Satellite clocks

The GPS II and IIA satellites carry two rubidium and two cesium clocks on board, while the GPS IIR and IIR-M satellites are equipped with three spaceborne rubidium clocks (Mallette et al., 2006). The new GPS IIF satellites have two rubidium and one cesium frequency standards on board (Jewell, 2014) and the planned GPS block III satellites will change the number of rubidium frequency standards again to three (Lollock, 2013). The behavior of the operational frequency standards onboard the GPS satellites of different generations are illustrated in Figure 2.6 with the MDEVs using the CODE final GPS clocks from 3-day solutions on August 1, 2014 (resampled to 300 s).

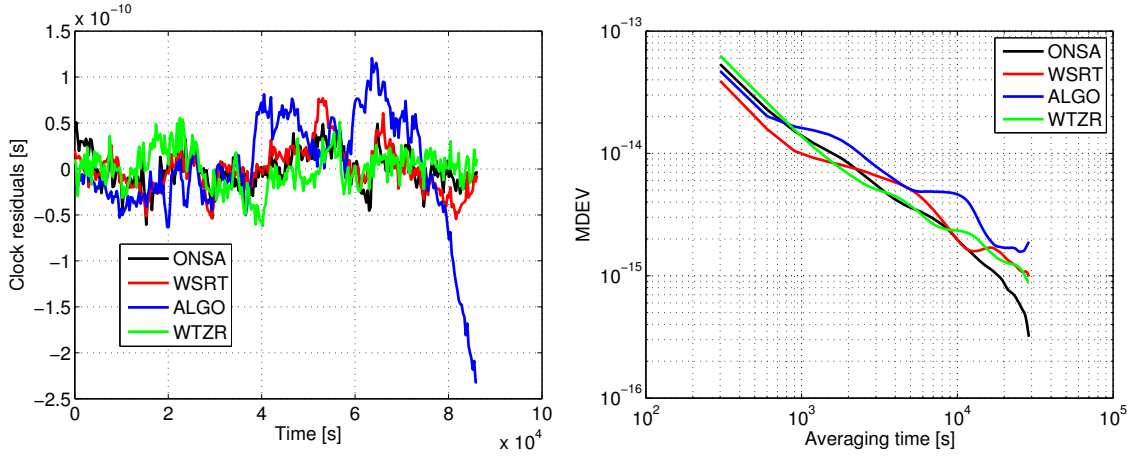

(a) Residuals (b) MDEV

Figure 2.5: (a) Clock residuals of some H-Masers after removing a linear polynomial and (b) the corresponding MDEVs on March 1, 2014.

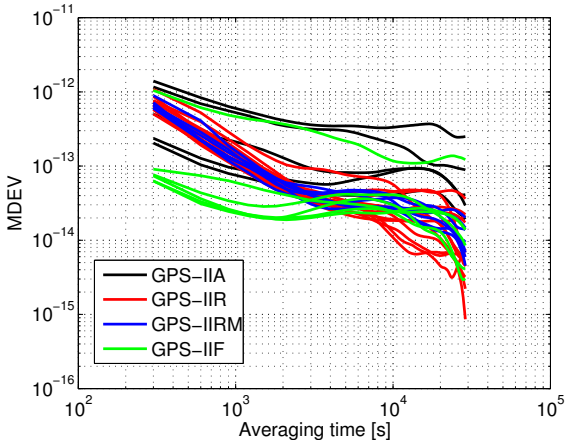

Figure 2.6: MDEVs of the GPS satellite clocks from different GPS generations on August 1, 2014.

It is not difficult to observe the general improvement from the old generation GPS IIA to the new GPS generation Block IIF. Except for the relatively bad behavior of the clock on G24 (see the highest green line), the clocks on block IIF satellites show a significantly smaller short-term noise level. However, their long-term stability is influenced by systematic effects which might be a result of the estimation of the satellite orbits. Figure 2.7 explains this with more details.

Figure 2.7 shows the MDEVs of the clock estimates and residuals of the clock estimates after removing a linear polynomial for GPS Block IIR satellite G19 and GPS Block IIF satellite G01 on August 1, 2014. We see that the MDEV of G01 is getting larger than that of G19 after an averaging time of about 2 hours and 10 minutes. This is in agreement with the high level of high-frequency noise in G19 and the large low-frequency variations

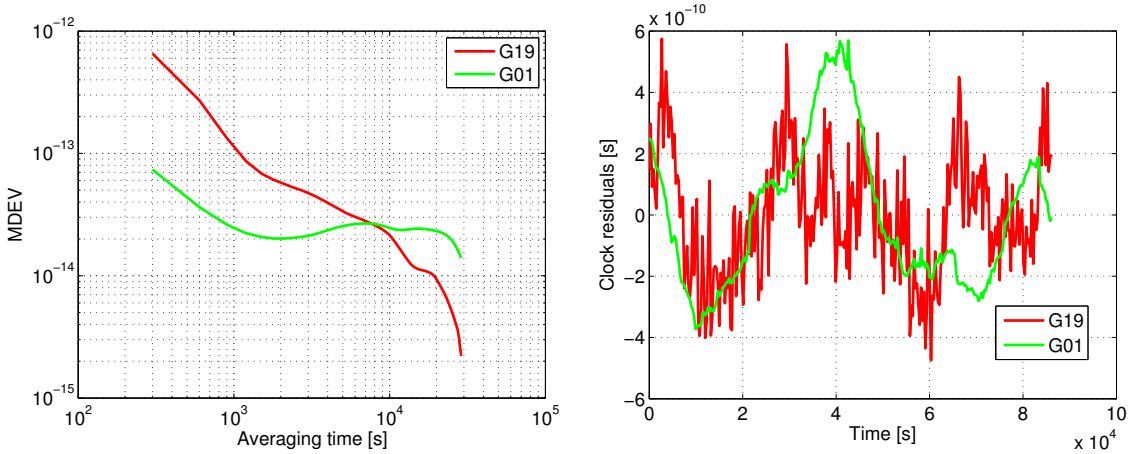

(a) MDEV (b) Residuals

Figure 2.7: (a) MDEVs of the clock estimates and (b) residuals of the clock estimates after removing a linear polynomial for GPS Block IIR satellite G19 and GPS Block IIF satellite G01 on August 1, 2014.

in G01.

Similar systematic effects can also be observed in Figure 2.8, which shows the behavior of the clock estimates of the Galileo IOV satellites E11 and E12 with H-Masers running on board after removing a linear polynomial on October 21, 2012 (Galileo Overview, 2015). The CODE MGEX clock data is used for the plots, and the plots of the MDEV starts at 3:00 GPST for E11 and at 0:30 GPST for E12, respectively, to avoid data gaps.

Looking at Figure 2.8 we see that the MDEV of both H-Masers are approaching $3 \cdot 10^{-15}$ after an averaging time of about 7 to 8 hours even with the disturbance from systematic

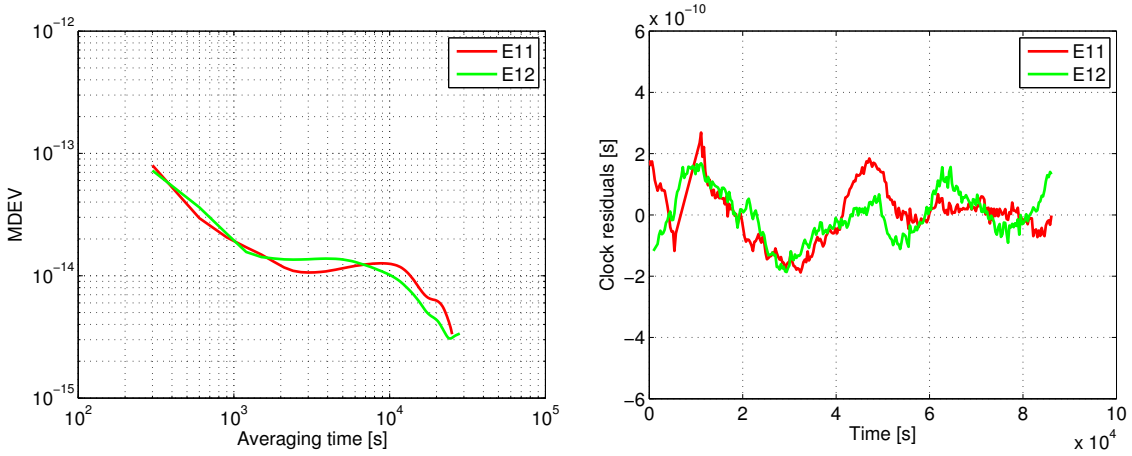

(a) MDEV (b) Residuals

Figure 2.8: (a) MDEVs of the clock estimates and (b) residuals of the clock estimates after removing a linear polynomial for Galileo IOV satellites E11 and E12 on October 21, 2012.

effects. Their long-term stability is considerably better than that of the rubidium clock on GPS Block IIF satellite G01 on August 1, 2014. The short-term stability of the H-Masers on E11 and E12 and the on-board clock on G01 at the averaging time of 300 s is similar, namely around $7 \cdot 10^{-14}$ to $8 \cdot 10^{-14}$.

2.3 Phase ambiguities and linear combinations

When resolving the phase ambiguities to integer numbers, a lot of error sources, e.g., receiver and clock errors, tropospheric delays, ionospheric delays, multipath effects, hardware delays and measurment noise, which have a significant impact on ambiguity parameters, may disturb and influence the results (Dach et al., 2007). This section focuses on the purpose, advantages and disadvantags of different linear combinations and their importance for ambiguity resolution.

2.3.1 Dual-frequency linear combinations

Equation 2.8 shows the general form of the dual-frequency linear combination of the phase measurements:

$$L_x = A \cdot L_1 + B \cdot L_2, \tag{2.8}$$

where L_x, L_1 and L_2 represent the combined phase measurement and the phase measurements on the frequencies f_1 and f_2. A and B denote the coefficients of the phase linear combination.

The mostly used linear combination in PPP applications is the so-called IF linear combination (here called L3). Based on the fact that the ionospheric delay accelerates the phase measurements and is frequency-dependent (see Equations 2.3 and 2.4), we obtain:

$$I_i = \frac{f_1^2}{f_i^2} \cdot I_1, \tag{2.9}$$

where I_i represents the ionospheric delay on frequency f_i. Appropriate factors A and B are able to eliminate the first-order term of the ionospheric delay and leave the geometry-related terms unchanged in the combined phase measurement (see Equations 2.10 and 2.11).

$$A + \frac{f_1^2}{f_2^2} \cdot B = 0 \tag{2.10}$$

$$A + B = 1. \tag{2.11}$$

The factors A and B can easily be solved for:

$$A = \frac{f_1^2}{f_1^2 - f_2^2}, \quad B = \frac{f_2^2}{f_2^2 - f_1^2}. \tag{2.12}$$

Assuming that the phase noise σ_{L1} and σ_{L2} in meters on both frequencies is the same and is equal to σ_L, the combined noise σ_{Lx} can be calculated with the coefficients A and B:

$$\begin{aligned} \sigma_{Lx} &= \sqrt{A^2 \cdot \sigma_{L1}^2 + B^2 \cdot \sigma_{L2}^2} \\ &= \sqrt{A^2 + B^2} \cdot \sigma_L. \end{aligned} \tag{2.13}$$

The combined ambiguity n_x is represented by Equation 2.14:

$$\begin{aligned} n_x &= A \cdot n_1 \cdot \lambda_1 + B \cdot n_2 \cdot \lambda_2 \\ &= -B\lambda_2(n_1 - n_2) + n_1(A\lambda_1 + B\lambda_2). \end{aligned} \tag{2.14}$$

The term $A\lambda_1 + B\lambda_2$ can be denoted by λ_3 (Dach et al., 2007).

The GF linear combination (here called L4) is, in contrast to the IF linear combination, eliminating all the geometry-related terms like the receiver and satellite clock error, the tropospheric delay and the geometric distance between the receiver and the satellite. Except for the antenna-related PCOs and PCVs, multipath effects and the measurement noise, only the ionospheric delay and the phase ambiguities are left in the observation equation. The coefficients A and B have to fulfill the following condition:

$$A + B = 0. \tag{2.15}$$

To simplify the case, A and B are defined as 1 and -1. The combined noise equals to $\sqrt{2}\sigma_L$. According to Equations 2.3 and 2.4, the ionospheric delay I_1 on L1 can easily be calculated as:

$$I_1 = \frac{L_1 - L_2}{\frac{f_1^2}{f_2^2} - 1}. \tag{2.16}$$

The dual-frequency GF and IF linear combination, the so-called Melbourne-Wübbena (MW) linear combination (Melbourne, 1985; Wübbena, 1985), removes both, the geometry-related terms and the first-order term of the ionospheric delay. Different from the GF or IF linear combination introduced above, the MW linear combination uses phase and code observations at the same time:

$$L_x = A \cdot L_1 + B \cdot L_2 + C \cdot P_1 + D \cdot P_2, \tag{2.17}$$

where P_1 and P_2 represent the code measurements on L1 and L2, respectively, and C and D stand for the factors before the code measurements. In order to fulfill the requirement of a GF and IF linear combination, the following equations are required:

$$A + B + C + D = 0 \tag{2.18}$$

$$-A - \frac{f_1^2}{f_2^2} \cdot B + C + \frac{f_1^2}{f_2^2} \cdot D = 0 \tag{2.19}$$

The resulting four parameters are:

$$A = \frac{f_1}{f_1 - f_2}, \quad B = \frac{f_2}{f_2 - f_1}, \quad C = -\frac{f_1}{f_1 + f_2}, \quad D = -\frac{f_2}{f_1 + f_2}. \tag{2.20}$$

They have been chosen in such a way that the criteria in Equations 2.18 and 2.19 are fulfilled, and the product of the wide-lane ambiguity $n_5 = n_1 - n_2$ and a large wavelength $\lambda_5 = \frac{c_l}{f_1 - f_2}$ (about 86.2 cm for GPS L1 and L2) remain in the observation equation:

$$\begin{aligned} L_x &= \frac{c_l}{f_1 - f_2} \cdot (n_1 - n_2) \\ &= \lambda_5 \cdot n_5. \end{aligned} \tag{2.21}$$

Since the code noise σ_C is dominant in the observation equation, the combined noise of the MW linear combination is highly dependent on the size of σ_C. Assuming that the phase noise σ_{L1} and σ_{L2} and the code noise σ_{C1} and σ_{C2} is the same on both frequencies and is equal to σ_L and σ_C, respectively, the combined noise can be formulated as:

$$\begin{aligned} \sigma_x &= \sqrt{A^2 \cdot \sigma_{L1}^2 + B^2 \cdot \sigma_{L2}^2} + \sqrt{C^2 \cdot \sigma_{C1}^2 + D^2 \cdot \sigma_{C2}^2} \\ &= \sqrt{A^2 + B^2} \cdot \sigma_L + \sqrt{C^2 + D^2} \cdot \sigma_C. \end{aligned} \tag{2.22}$$

With the frequencies of the different GNSS, the combined noise and the wavelength of the combined ambiguities (i.e. λ_3 and λ_5) can be calculated. The frequencies of the different GNSS (see Table 2.5) are extracted from RINEX (RINEX, 2013), and the abbreviations for different frequency pairs are listed in Table 2.6.

Assuming that the phase noise σ_L and the code noise σ_C is equal to 2 mm and 0.5 m, respectively, the combined noise of the IF phase-only linear combination and the MW linear combination for different frequency pairs are illustrated in Figure 2.9.

We see that the combined noise of the IF linear combination for GPS L1 and L2 is about 6 mm, whereas a relatively large combined noise of about 5.5 cm can be observed for Galileo E5a and E5b because of the small difference in the wavelengths between E5a and E5b. The minimal combined noise of the IF linear combination is generated by GPS L1 and L5, namely about 5.2 mm. The combined noise of the MW linear combination is relatively large because of the dominant code noise. However, it is not difficult to see that the values for the combined noise are all around 0.36 m and do not vary much with respect to different choices of the frequency pairs.

Table 2.5: Available frequencies for different GNSS.

GPS [MHz]	Galileo [MHz]	BDS [MHz]
L1=1575.42	E1=1575.42	B1=1561.098
L2=1227.6	E5a=1176.45	B2=1207.14
L5=1176.45	E5=1191.795	B3=1268.52
	E5b=1207.14	
	E6=1278.75	

Table 2.6: Abbreviations of the frequency pairs for different GNSS.

GPS	Galileo	BDS
LG12: L1/L2	LE15: E1/E5	LB12: B1/B2
LG15: L1/L5	LE16: E1/E6	LB13: B1/B3
LG25: L2/L5	LE56: E5/E6	LB23: B2/B3
	LE5ab: E5a/E5b	

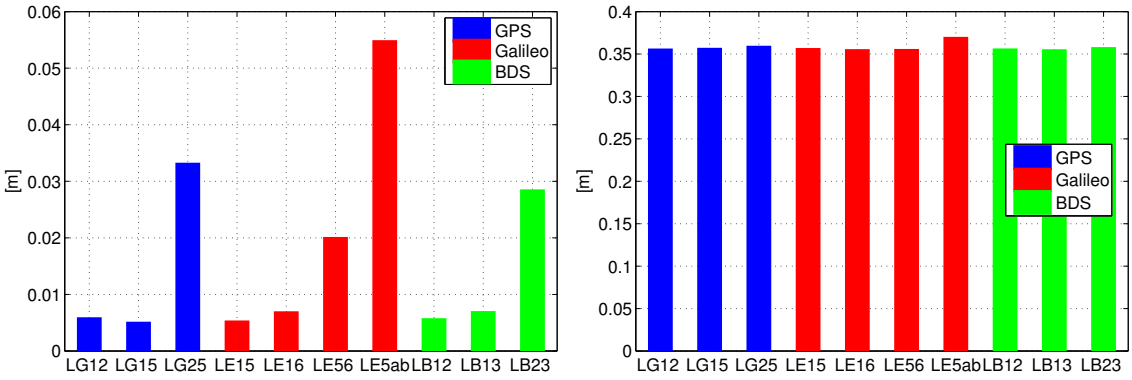

(a) IF combined noise

(b) MW combined noise

Figure 2.9: Combined noise of (a) IF phase-only and (b) MW linear combinations of different frequency pairs assuming that the phase and code noise is equal to 2 mm and 0.5 m, respectively.

Figure 2.10 shows the wavelength λ_3 and the wavelength of the wide-lane ambiguity λ_5 when selecting different frequency pairs. We see that the values of λ_3 of the IF linear combination are all around 11 to 12 cm, whereas the value of λ_5 is highly dependent on the differences between the two frequencies involved. For GPS L2 and L5 and Galileo E5a and E5b, λ_5 has reached 5.9 m and 9.8 m, respectively. This should be very helpful for ambiguity resolution.

2.3.2 Multi-frequency linear combinations

The new GNSS (GPS, Galileo and BDS) all provide signals on more than two frequencies. The new CDMA signal L3OC centered at 1202.025 MHz is also introduced for the two GLONASS-K1 satellites that are under flight tests (Testoyedov, 2015; Urlichich et al., 2011). The European Galileo system can broadcast data on even more than three frequencies. As a result, we describe linear combinations of multi-frequency signals by the following equation:

$$L_x = \sum_{i=1}^{n} \gamma_{Li} \cdot L_i + \sum_{i=1}^{n} \gamma_{Pi} \cdot P_i, \tag{2.23}$$

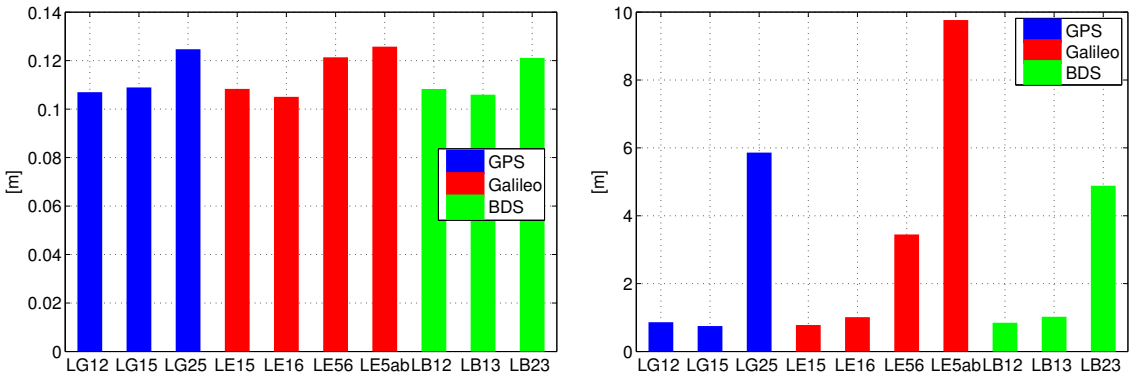

(a) λ_3 (b) λ_5

Figure 2.10: (a) λ_3 and (b) λ_5 for different frequency pairs assuming that the phase and code noise is equal to 2 mm and 0.5 m, respectively.

where L_i and P_i stand for the phase and code measurements on frequency f_i, and γ_{Li} and γ_{Pi} represent the coefficients before the phase and code measurements. If only the phase or only the code measurements are used, the corresponding coefficients γ_{Li} or γ_{Pi} are set to zero.

In order to easily resolve the phase ambiguities, it is always our goal to keep possible error sources small compared to the wavelength contained in the linear combination. If the ionospheric delays or the geometry-related terms are eliminated by forming the linear combination, or if a priori information of good quality (e.g., accurate orbits and clock corrections) is available, the goal turns into reducing the combined noise with respect to the combined wavelength, or in other words, in reducing the noise level of the linear combination expressed in cycles.

The multi-frequency GNSS data gives us more redundancy to optimize between the purpose of the linear combination and the noise level of the linear combination. However, it is also to be noticed that the number of linearly independent linear combinations required in order to resolve the ambiguities on all the frequencies increases with the number of frequencies available. In the last ten years, a large amount of studies has been performed to investigate triple-frequency (and multi-frequency) ambiguity resolution (Feng et al., 2007; Feng, 2008; Hatch, 2006; Henkel and Günther, 2012; Li et al., 2012). In this thesis, the focus is put on triple-frequency GF and IF linear combinations, which will be introduced in Section 3.2.

2.4 Ionospheric Refraction

Ionospheric refraction is one of the major error sources in zero-difference GNSS processing. The delays caused can vary from less than one meter to more than 100 meters in extreme cases (Dach et al., 2007; Gao and Liu, 2002). According to Dach et al. (2007), neglecting

the higher-order terms of the ionospheric refraction on carrier phase measurements, the ionospheric delay ΔI_i on frequency f_i can be written as:

$$\Delta I_i = \int_s (n_I - 1) ds \tag{2.24}$$

with

$$n_I = 1 - \frac{a \cdot n_e}{f_i^2}, \tag{2.25}$$

where n_I represents the ionospheric refraction coefficient, and a is a constant with the value $4.03 \cdot 10^{17} \mathrm{ms}^{-2}\mathrm{TECU}^{-1}$. TECU is called the Total Electron Content Unit (TECU) and is defined as 10^{16} electrons per square meter, and n_e denotes the electron content along the path of the signal propagation.

With Equations 2.24 and 2.25, it is not hard to see that the ionospheric refraction is dispersive. Inserting Equation 2.25 into Equation 2.24, we obtain:

$$\begin{aligned} \Delta I_i &= -\frac{a}{f_i^2} \int_s n_e ds \\ &= -\frac{a \cdot E}{f_i^2}, \end{aligned} \tag{2.26}$$

where E is the so-called Total Electron Content (TEC). For code measurements, the sign before $\frac{a \cdot E}{f_i^2}$ has to be changed to plus.

The vertical ionospheric delay is calculated with the help of a mapping function F_{map} based on the assumption that the electrons are concentrated on a single layer (Single-Layer Model). The slant and vertical TEC E and E_v then fulfill the following relationship:

$$E_v = \frac{E}{F_{map}}. \tag{2.27}$$

The vertical ionospheric refraction on frequency f_i for phase measurements can thus be described as:

$$\begin{aligned} \Delta I_i^v &= -\frac{a \cdot E_v}{f_i^2} \\ &= -\frac{a \cdot E}{f_i^2 \cdot F_{map}} \\ &= \frac{\Delta I_i}{F_{map}}. \end{aligned} \tag{2.28}$$

The state of the ionosphere is strongly influenced by the geomagnetic and solar activities (Dach et al., 2007). Figure 2.11 shows the mean global TEC values (spherical harmonics coefficient of degree 0 and order 0) extracted from the CODE global ionosphere maps between 12:00 and 14:00 UT (see Figure 4 in Paper D) from 1999 to 2013. The 11-year solar cycle can easily be seen in the figure.

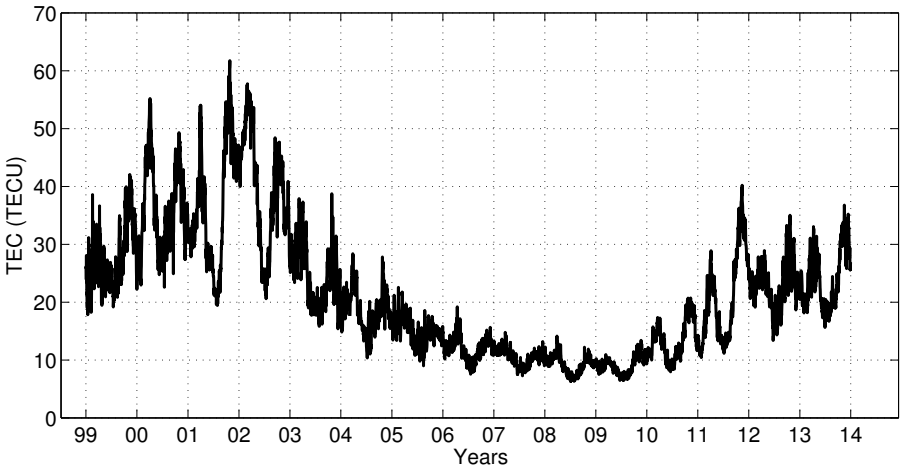

Figure 2.11: Global TEC values between 12:00 and 14:00 UT from 1999 to 2013.

For differential GNSS, the ionospheric delays are significantly reduced, especially for short baselines and under quiet ionospheric conditions. Figure 2.12 shows the slant ionospheric gradients for (a) the baseline AIGE and ARDE, which has a length of 318.3 km and is oriented in west-east direction and (b) the baseline SCHA and STA2, which has a length of 210.3 km and is oriented in north-south direction in Switzerland on June 16, 2013, with a global mean TEC value of 18.4 TECU between 12:00 and 14:00 UT. The slant ionospheric gradients are calculated based on the differential slant ionospheric delays and the baseline length with the help of the GF linear combination. The elevation cut-off angle is 10 degrees.

We see that the remaining ionospheric gradients are in the range of a few mm/km. For baselines shorter than 1 km, the remaining differential ionospheric residuals are normally

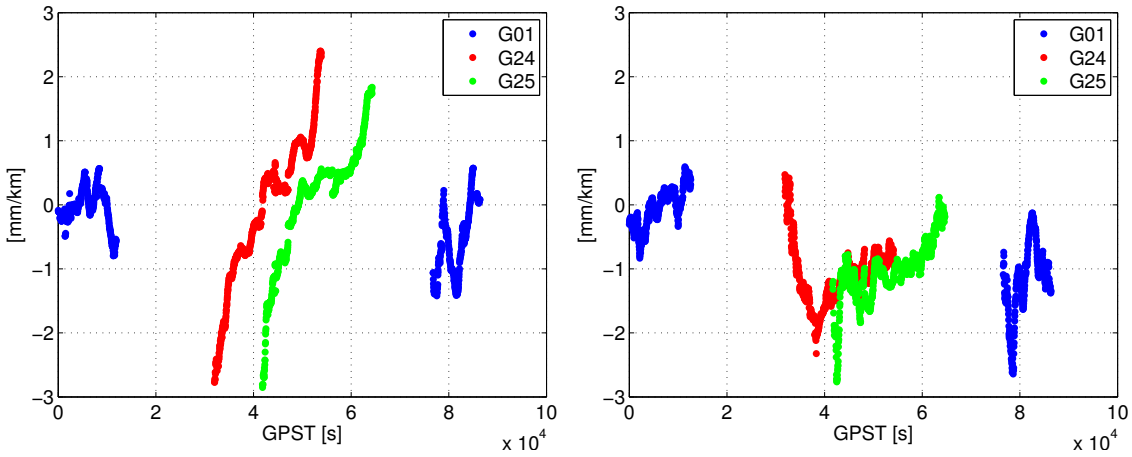

(a) AIGE-ARDE

(b) SCHA-STA2

Figure 2.12: Slant ionospheric gradients for (a) the baseline AIGE and ARDE and (b) the baseline SCHA and STA2 on June 16, 2013, in Switzerland.

considered to be in the range of the phase noise level under normal ionosphere conditions. However, the ionosphere gradients could become critical for differential GNSS under extreme ionosphere conditions. A detailed evaluation using the swisstopo's AGNES data is shown in Paper D and the algorithms used are contained in Section 3.3.

3 Advanced modeling and algorithms

3.1 Clock constraints

In traditional kinematic PPP applications, the receiver coordinates are usually estimated together with the receiver clock and troposphere parameters. The strong correlation between the height estimates of the receiver, the receiver clock estimates and the tropospheric delays (see Figure 3.1 based on (Rothacher, 2015; Rothacher and Beutler, 1998)) leads to considerably reduced stability and accuracy of these parameters. Assuming that Δh, Δt_r and $\Delta trop(0)$ represent the corrections for receiver height, the receiver clock parameter and the troposphere zenith delay parameter with all other parameters assumed to be known, the Observed-Minus-Computed (O-C) term $\tilde{l} = l - l_0$ of the observation equation can be described as (Rothacher and Beutler, 1998):

$$\tilde{l} = -\underbrace{cosz \cdot \Delta h}_{\Delta h(z)} + \underbrace{\frac{1}{cosz} \cdot \Delta trop(0)}_{\Delta trop(z)} + c_l \cdot \Delta t_r, \tag{3.1}$$

where z denotes the zenith angle of the signal, and $\Delta h(z)$ and $\Delta trop(z)$ represent the height correction and tropospheric delay in the signal direction, respectively. The partial derivatives of $\tilde{l}$ with respect to Δh, $\Delta trop(0)$ and Δt_r are thus:

$$A = \begin{pmatrix} -cosz & \frac{1}{cosz} & c_l \end{pmatrix} \tag{3.2}$$

Assuming an uniform satellite distribution, the correlation between the receiver clock corrections and the height estimates reaches values from 0.949 to 0.990 at the Equator and values from 0.967 to 0.996 at the Pole depending on the elevation cut-off angle (Dach et al., 2003).

A similar correlation as between the height component of the receiver and the receiver

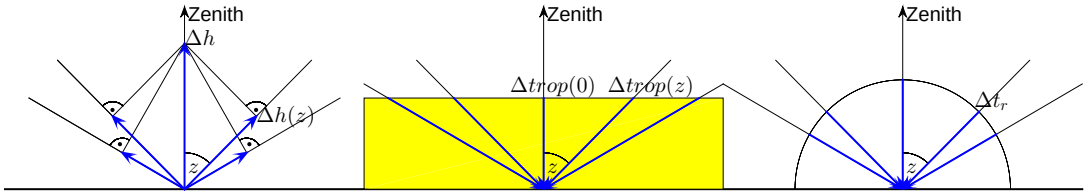

Figure 3.1: Correlation between the receiver heights and the receiver clock corrections.

clock estimates also exists between the radial component of a satellite orbit determined kinematically and the satellite clock estimates.

One method to decorrelate the receiver clock and the height estimate is to make use of appropriate clock models (see Section 2.2). Since the behavior of high-performance atomic clocks like H-Masers is usually very stable (standard deviation in tens of picosecond level w.r.t. a low-degree polynomial), these high-performance ground clocks can be described with a simple deterministic model and a stochastic model (see Section 2.2).

3.1.1 Clock modeling

To benefit from the high-performance of H-Masers at a station, a model for the clock correction Δt_r with a linear polynomial and relative constraints between the clock parameters of subsequent epochs is setup:

$$\Delta t_r = a_0 + a_1 \cdot (t_i - t_0) + r_i \tag{3.3}$$

with

$$r_i - r_{i+1} = 0, \quad P_{i,i+1} = \frac{\sigma_0^2}{\sigma_r^2}, \tag{3.4}$$

where a_0 and a_1 represent the clock offset and drift. t_i and r_i stand for the time and stochastic clock parameter at epoch i. $P_{i,i+1}$ denotes the weight for the relative clock constraint between epoch i and $i+1$ with the a priori Root Mean Square (RMS, here sigma) of the measurement σ_0 and the relative sigma σ_r for the constraint between subsequent clock parameters.

In order to avoid the singularities between the clock offset a_0, the clock drift a_1 and the stochastic clock parameter r_i, a weak absolute constraint on the stochastic clock parameters r_i is needed every epoch or every several epochs:

$$r_i = 0, \quad P_i = \frac{\sigma_0^2}{\sigma_{abs}^2}, \tag{3.5}$$

where σ_{abs} and P_i represent the absolute sigma and the weight, respectively, of the absolute constraint.

The relative sigma σ_r is an indicator for the weight of the relative clock constraint and should correspond to the stability and ADEV of the clock used. The effect of using different weights for the relative clock constraints can easily be seen by applying different relative sigmas. Figure 3.2 shows the estimated receiver clock corrections Δt_r of station ALGO on October 1, 2013, using different relative constraints. For the analysis, dual-frequency phase observations and down-weighted code observations for 24 h have been used to form the IF linear combination for kinematic PPP solutions. CODE orbits and satellite clocks were used as input information and were assumed known. The dry part of the Vienna Mapping functions (VMF1) (Boehm et al., 2006) was used as a priori troposphere model. The receiver clock parameter and the kinematic coordinates were estimated for each epoch.

The troposphere ZPD parameters and the troposphere horizontal gradients were estimated with a 2-h and 24-h interval, respectively.

In Figure 3.2, the blue line represents the estimated clock corrections without any constraint, while the red, green, black and magenta lines represent the clock corrections with stronger and stronger relative constraints. Using a relative sigma of $\sigma_r = 0.1$ mm, the clock corrections are almost constrained to the deterministic model, i.e., a straight line.

Since the receiver clock connected to the station ALGO on October 1, 2013, is a H-Maser with a standard deviation of $\sigma_{STD} = 69.7$ ps and an empirical relative sigma (see Equation 2.7) $\sigma_{emp} = 10.9$ ps as derived from the CODE RINEX clock file after removing a linear polynomial, the relative constraint with appropriate weight can stabilize the estimated kinematic height estimates. Figure 3.3a shows the standard deviation of the kinematic height estimates STD_U with respect to different relative sigmas σ_r for the H-Masers at station ALGO and WSRT on October 1, 2013. We see that the standard deviation STD_U decreases with decreasing relative sigma σ_r, i.e. with increasing weight of the relative clock constraint. However, constraining the clocks too strongly, e.g., stronger than $\sigma_r = 1.9$ mm for the H-Maser at ALGO, might also degrade the kinematic heights. The H-Maser at WSRT has been used as the reference clock (clock corrections fixed to a perfect straight line) on October 1, 2013, when estimating all the satellite clocks. As a result, the degradation does not happen for WSRT even when applying a very strong relative constraint ($\sigma_r = 0.1$ mm). It should be noted that the errors of the selected reference clock w.r.t. a linear polynomial are absorbed by the satellite clock estimates and, as a result, transfered to the other receiver clock estimates.

For receiver clocks with lower quality, e.g., the rubidium clocks at station CHUR and

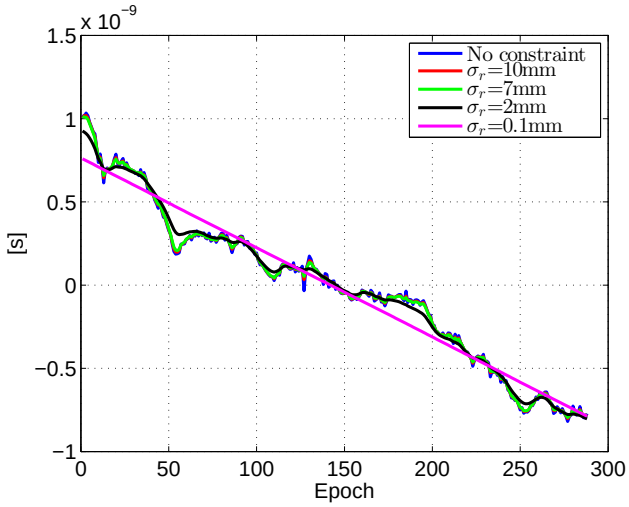

Figure 3.2: Estimated receiver clocks of station ALGO on October 1, 2013, with different relative constraints between subsequent receiver clock corrections.

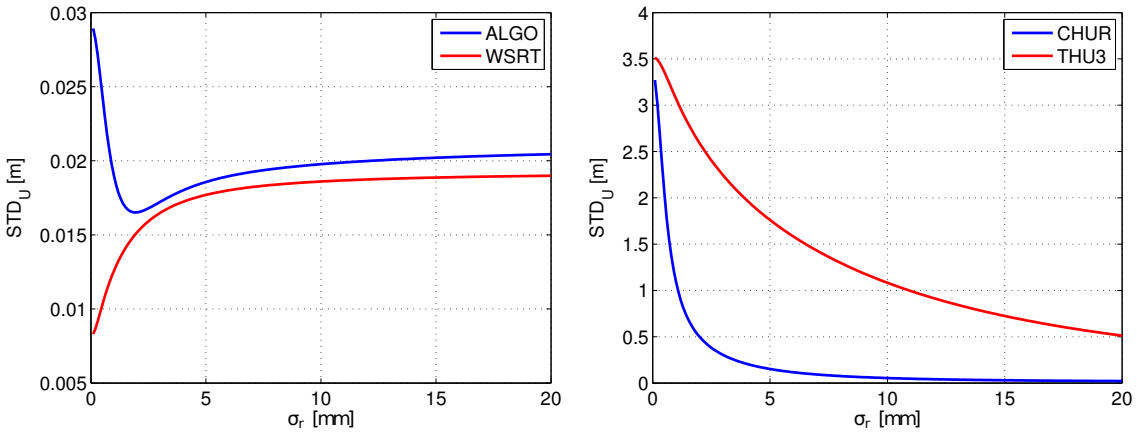

(a) H-Masers

(b) Rubidium clocks

Figure 3.3: Standard deviation of the kinematic height estimates STD_U applying different relative clock constraints for (a) the H-Masers at station WSRT and ALGO and (b) the rubidium clocks at station CHUR and THU3, on October 1, 2013.

THU3 on October 1, 2013 with a σ_{STD} of 13.2 ns and 7.7 ns and a σ_{emp} of 0.58 ns and 4.98 ns after removing a linear polynomial, respectively, constraining the clocks with the same weights (σ_r from 0.1 mm to 20 mm) may easily lead to degradations (see Figure 3.3b). This shows again that the appropriate weight of the relative constraints and the improvement of the kinematic heights are heavily depending on the clock quality. The appropriate σ_r can, e.g., be derived from the MDEV, σ_{emp} or σ_{STD} after removing a low-degree polynomial of the phase clock data.

3.1.2 Pre-elimination and back-substitution of epoch parameters with constraints between subsequent epochs

Estimating the epoch-wise receiver clock corrections and kinematic coordinates at the same time usually generates a large number of parameters, especially for observations with high sampling rates. In this section, a pre-elimination and back-substitution algorithm for the epoch-wise estimation of clock parameters on Normal Equation (NEQ) level is introduced for the kinematic PPP solutions using the IF linear combination and relative clock constraints.

Pre-elimination

Assuming that the NEQ matrix of all the non-epoch parameters, including the troposphere parameters, the float ambiguities and the coefficients of the deterministic clock model (here offset and drift), is represented by the $f \times f$ matrix N_f, and the NEQ parts of the epoch parameters are represented by N_{ii} ($i = 1, \cdots, n$ with n defined as the number of epochs) for the diagonal elements and $N_{i(i+1)}$ and $N_{(i+1)i}$ ($i = 1, \cdots, n-1$) for the subdiagonal

elements, the whole NEQ matrix N can be described by Equation 3.6 with the NEQ matrices between the non-epoch parameters and the epoch parameters denoted by N_{fi} and N_{if} $(i = 1, \cdots, n)$:

$$N = \begin{pmatrix} N_f & N_{f1} & N_{f2} & \cdots & N_{fn} \\ N_{1f} & N_{11} & N_{12} & \cdots & \mathbf{0} \\ N_{2f} & N_{21} & N_{22} & \cdots & \mathbf{0} \\ \vdots & \vdots & \vdots & \ddots & \vdots \\ N_{nf} & \mathbf{0} & \mathbf{0} & \cdots & N_{nn} \end{pmatrix}, \tag{3.6}$$

where N_{ii} is a 4×4 matrix containing the NEQ matrices of the receiver clock parameter and the kinematic coordinates in all the three directions.

The pre-elimination for the epoch parameters of the first epoch (see red elements in Equation 3.6) is performed at the moment, when the parts of the relative clock constraint $N_{1,2}^{rel}$ and the weak absolute constraints $N_{1,2}^{abs}$ are considered for the first two epochs:

$$\begin{pmatrix} N_{11}^{\star} & N_{12}^{\star} \\ N_{21}^{\star} & N_{22}^{\star} \end{pmatrix} = \begin{pmatrix} N_{11} & N_{12} \\ N_{21} & N_{22} \end{pmatrix} + N_{1,2}^{rel} + N_{1,2}^{abs}, \tag{3.7}$$

with

$$N_{1,2}^{rel} = \begin{pmatrix} 0 & 0 & 0 & 1 & 0 & 0 & 0 & -1 \end{pmatrix}^T \cdot \frac{\sigma_0^2}{\sigma_r^2} \cdot \begin{pmatrix} 0 & 0 & 0 & 1 & 0 & 0 & 0 & -1 \end{pmatrix} \tag{3.8}$$

$$N_{1,2}^{abs} = \begin{pmatrix} 0 & 0 & 0 & 1 & 0 & 0 & 0 & 0 \\ 0 & 0 & 0 & 0 & 0 & 0 & 0 & 1 \end{pmatrix}^T \cdot \begin{pmatrix} \frac{\sigma_0^2}{\sigma_{abs}^2} & 0 \\ 0 & \frac{\sigma_0^2}{\sigma_{abs}^2} \end{pmatrix} \cdot \begin{pmatrix} 0 & 0 & 0 & 1 & 0 & 0 & 0 & 0 \\ 0 & 0 & 0 & 0 & 0 & 0 & 0 & 1 \end{pmatrix}, \tag{3.9}$$

assuming that the absolute constraints are applied at each epoch. The three zero elements before 1 and -1 occupy the positions for the 3 kinematic coordinates at each epoch.

As a result, we obtain

$$N_{1,2}^{rel}([4\ 8],[4\ 8]) + N_{1,2}^{abs}([4\ 8],[4\ 8]) = \begin{pmatrix} \frac{\sigma_0^2}{\sigma_r^2} + \frac{\sigma_0^2}{\sigma_{abs}^2} & -\frac{\sigma_0^2}{\sigma_r^2} \\ -\frac{\sigma_0^2}{\sigma_r^2} & \frac{\sigma_0^2}{\sigma_r^2} + \frac{\sigma_0^2}{\sigma_{abs}^2} \end{pmatrix}, \tag{3.10}$$

where all other elements of $N_{1,2}^{rel} + N_{1,2}^{abs}$ are zero.

The pre-elimination of the first epoch is performed at the one hand for the NEQ matrix, and on the other hand for $B = A^T P \tilde{l}$, where A, P and $\tilde{l}$ represent the design matrix, the weight matrix and the O-C term in the least-squares adjustment:

$$B = \begin{pmatrix} B_f & B_1 & B_2 & \cdots & B_n \end{pmatrix}^T, \tag{3.11}$$

where B_f and B_i $(i = 1, \cdots, n)$ represent the parts for the non-epoch parameters and for the epoch parameters at epoch i $(i = 1, \cdots, n)$.

The pre-elimination of the first epoch (red elements in Equation 3.6) has an impact only on the non-epoch parameters and the second epoch (see the blue elements in Equations 3.6 and 3.11):

$$\begin{pmatrix} N_f^{pre,1} & N_{f2}^{pre} \\ N_{2f}^{pre} & N_{22}^{pre} \end{pmatrix} = \begin{pmatrix} N_f & N_{f2} \\ N_{2f} & N_{22}^{\star} \end{pmatrix} - \begin{pmatrix} N_{f1} \\ N_{21}^{\star} \end{pmatrix} \cdot (N_{11}^{\star})^{-1} \cdot \begin{pmatrix} N_{1f} & N_{12}^{\star} \end{pmatrix}, \tag{3.12}$$

$$\begin{pmatrix} B_f^{pre,1} \\ B_2^{pre} \end{pmatrix} = \begin{pmatrix} B_f \\ B_2 \end{pmatrix} - \begin{pmatrix} N_{f1} \\ N_{21}^{\star} \end{pmatrix} \cdot (N_{11}^{\star})^{-1} \cdot B_1. \tag{3.13}$$

The NEQ matrix and the B matrix after pre-elimination of the first epoch are given by:

$$N^{pre,1} = \begin{pmatrix} N_f^{pre,1} & N_{f2}^{pre} & N_{f3} & \cdots & N_{fn} \\ N_{2f}^{pre} & N_{22}^{pre} & N_{23} & \cdots & \mathbf{0} \\ N_{3f} & N_{32} & N_{33} & \cdots & \mathbf{0} \\ \vdots & \vdots & \vdots & \ddots & \vdots \\ N_{nf} & \mathbf{0} & \mathbf{0} & \cdots & N_{nn} \end{pmatrix}, \tag{3.14}$$

$$B^{pre,1} = \begin{pmatrix} B_f^{pre,1} & B_2^{pre} & B_3 & \cdots & B_n \end{pmatrix}^T. \tag{3.15}$$

In order to perform the pre-elimination of the second epoch, the relative constraint between the second and third epoch, as well as the absolute constraint of the third epoch have to be considered:

$$\begin{pmatrix} N_{22}^{\star pre} & N_{23}^{\star} \\ N_{32}^{\star} & N_{33}^{\star} \end{pmatrix} = \begin{pmatrix} N_{22}^{pre} & N_{23} \\ N_{32} & N_{33} \end{pmatrix} + N_{2,3}^{rel} + N_3^{abs}, \tag{3.16}$$

with

$$N_{2,3}^{rel}([4\ 8],[4\ 8]) + N_3^{abs}([4\ 8],[4\ 8]) = \begin{pmatrix} \frac{\sigma_0^2}{\sigma_r^2} & -\frac{\sigma_0^2}{\sigma_r^2} \\ -\frac{\sigma_0^2}{\sigma_r^2} & \frac{\sigma_0^2}{\sigma_r^2} + \frac{\sigma_0^2}{\sigma_{abs}^2} \end{pmatrix}, \tag{3.17}$$

The pre-elimination of the second epoch (red elements in Equation 3.14) of the NEQ matrix and the B matrix is similar to that of the first epoch:

$$\begin{pmatrix} N_f^{pre,2} & N_{f3}^{pre} \\ N_{3f}^{pre} & N_{33}^{pre} \end{pmatrix} = \begin{pmatrix} N_f^{pre,1} & N_{f3} \\ N_{3f} & N_{33}^{\star} \end{pmatrix} - \begin{pmatrix} N_{f2}^{pre} \\ N_{32}^{\star} \end{pmatrix} \cdot (N_{22}^{\star pre})^{-1} \cdot \begin{pmatrix} N_{2f}^{pre} & N_{23}^{\star} \end{pmatrix}, \tag{3.18}$$

$$\begin{pmatrix} B_f^{pre,2} \\ B_3^{pre} \end{pmatrix} = \begin{pmatrix} B_f^{pre,1} \\ B_3 \end{pmatrix} - \begin{pmatrix} N_{f2}^{pre} \\ N_{32}^{\star} \end{pmatrix} \cdot (N_{22}^{\star pre})^{-1} \cdot B_2^{pre}. \tag{3.19}$$

The pre-elimination is performed in this way sequentially until the $(n-1)$-th epoch is reached, when only the last epoch and the non-epoch parameters are left in the NEQ matrix and the B matrix:

$$N^{pre,n-1} = \begin{pmatrix} N_f^{pre,n-1} & N_{fn}^{pre} \\ N_{nf}^{pre} & N_{nn}^{pre} \end{pmatrix}, \quad B^{pre,n-1} = \begin{pmatrix} B_f^{pre,n-1} & B_n^{pre} \end{pmatrix}^T. \tag{3.20}$$

The pre-elimination process finishes with the elimination of the last epoch:

$$N_f^{pre,n} = N_f^{pre,n-1} - N_{fn}^{pre} \cdot (N_{nn}^{pre})^{-1} \cdot N_{nf}^{pre}, \tag{3.21}$$

$$B_f^{pre,n} = B_f^{pre,n-1} - N_{fn}^{pre} \cdot (N_{nn}^{pre})^{-1} \cdot B_n^{pre}, \tag{3.22}$$

and the final non-epoch parameters $\Delta\hat{x}_f$ can be calculated with

$$\Delta\hat{x}_f = (N_f^{pre,n})^{-1} \cdot B_f^{pre,n}. \tag{3.23}$$

Before the pre-elimination of each epoch i ($i = 1, \cdots, n-1$), the NEQ matrices of epoch i and $i+1$, as well as the NEQ matrix between the non-epoch parameters and the epoch parameters of these two epochs, described with

$$\begin{pmatrix} N_{if}^{pre} & N_{ii}^{\star pre} & N_{i(i+1)}^{\star} \\ N_{(i+1)f} & N_{(i+1)i}^{\star} & N_{(i+1)(i+1)}^{\star} \end{pmatrix}, \tag{3.24}$$

are saved for the back-substitution (no upper index pre for the first epoch). For the last epoch, only the NEQ matrices related to the last epoch

$$\begin{pmatrix} N_{nf}^{pre} & N_{nn}^{pre} \end{pmatrix} \tag{3.25}$$

are saved for the back-substitution.

Back-substitution

Before the back-substitution step, the term b (see Equation 3.27) goes through a similar pre-elimination step as B, as a preparation for the back-substitution. For the pre-elimination of the first epoch of b (see Equation 3.13), we have

$$b_2^{pre} = b_2 - N_{21}^{\star} \cdot (N_{11}^{\star})^{-1} \cdot b_1, \tag{3.26}$$

with

$$b_i = B_i - N_{if} \cdot \Delta\hat{x}_f, \quad i = 1, \cdots, n. \tag{3.27}$$

For the pre-elimination of the second epoch, b_3^{pre} is calculated with (see Equation 3.19)

$$b_3^{pre} = b_3 - N_{32}^{\star} \cdot (N_{22}^{\star pre})^{-1} \cdot b_2^{pre}. \tag{3.28}$$

The algorithm goes on like this until the $(n-1)$-th epoch is reached, when the last epoch of b remains as:

$$b_n^{pre} = b_n - N_{n(n-1)}^{\star} \cdot (N_{(n-1)(n-1)}^{\star pre})^{-1} \cdot b_{n-1}^{pre}. \tag{3.29}$$

Before the pre-elimination of the term b for each epoch i ($i = 1, \cdots, n-1$), the matrices

$$\begin{pmatrix} b_i^{pre} \\ b_{i+1} \end{pmatrix} \tag{3.30}$$

are saved for the back-substitution (no upper index *pre* for the first epoch). For the last epoch, the matrix b_n^{pre} is saved for the back-substitution.

As opposed to the pre-elimination, the back-substitution begins from the last epoch and ends with the first epoch. For the last epoch, the algorithm requires the NEQ matrix and the term b of the last epoch just before their pre-elimination (see Equations 3.20 and 3.29):

$$\Delta\hat{x}_n = (N_{nn}^{pre})^{-1} \cdot b_n^{pre}, \tag{3.31}$$

where $\Delta\hat{x}_i$ represents the estimated epoch parameters at epoch i.

Before the pre-elimination of the second but last epoch, the NEQ matrix and the term b can be described as:

$$N^{pre,n-2} = \begin{pmatrix} N_f^{pre,n-2} & N_{f(n-1)}^{pre} & N_{fn} \\ N_{(n-1)f}^{pre} & N_{(n-1)(n-1)}^{\star pre} & N_{(n-1)n}^{\star} \\ N_{nf} & N_{n(n-1)}^{\star} & N_{nn}^{\star} \end{pmatrix}, \quad b^{pre,n-2} = \begin{pmatrix} b_{n-1}^{pre} \\ b_n \end{pmatrix}. \tag{3.32}$$

The terms $N_{(n-1)(n-1)}^{\star pre}$ and b_{n-1}^{pre}, which we need for the back-substitution of the epoch $n-1$, contain, however, only the information from the first to the second but last epoch. In order to estimate the epoch parameters of epoch $n-1$, the information of epoch n should thus be gathered:

$$\begin{aligned} \begin{pmatrix} N_f^{back,n} & N_{f(n-1)}^{back,n} \\ N_{(n-1)f}^{back,n} & N_{(n-1)(n-1)}^{back,n} \end{pmatrix} &= \begin{pmatrix} N_f^{pre,n-2} & N_{f(n-1)}^{pre} \\ N_{(n-1)f}^{pre} & N_{(n-1)(n-1)}^{\star pre} \end{pmatrix} \\ &\quad - \underbrace{\begin{pmatrix} N_f^{save,n} & N_{f(n-1)}^{save,n} \\ N_{(n-1)f}^{save,n} & N_{(n-1)(n-1)}^{save,n} \end{pmatrix}}_{N^{save,n}} \end{aligned} \tag{3.33}$$

$$b_{n-1}^{back,n} = b_{n-1}^{pre} - b_{n-1}^{save,n}, \tag{3.34}$$

with (see Equation 3.24)

$$N^{save,n} = \begin{pmatrix} N_{fn} \\ N_{(n-1)n}^{\star} \end{pmatrix} \cdot (N_{nn}^{\star})^{-1} \cdot \begin{pmatrix} N_{nf} & N_{n(n-1)}^{\star} \end{pmatrix}, \tag{3.35}$$

$$b_{n-1}^{save,n} = N_{(n-1)n}^{\star} \cdot (N_{nn}^{\star})^{-1} \cdot b_n. \tag{3.36}$$

The epoch parameters of the second but last epoch are then calculated with:

$$\Delta\hat{x}_{n-1} = \left(N_{(n-1)(n-1)}^{back,n}\right)^{-1} \cdot b_{n-1}^{back,n}. \tag{3.37}$$

For epoch $n-2$, the NEQ matrix and the term b in the state as they were before pre-elimination of the $(n-2)$-th epoch are firstly corrected for contribution of the last epoch, and the relative constraint between the $(n-1)$-th and the n-th epoch at the position of

the $(n-1, n-1)$-th element has to be added to the NEQ matrix, since it is not included in $N^{save,n}_{n-1,n-1}$:

$$N^{mod,n-3} = \begin{pmatrix} N^{mod,n-3}_{f} & N^{mod}_{f(n-2)} & N^{mod}_{f(n-1)} \\ N^{mod}_{(n-2)f} & N^{mod}_{(n-2)(n-2)} & N^{mod}_{(n-2)(n-1)} \\ N^{mod}_{(n-1)f} & N^{mod}_{(n-1)(n-2)} & N^{mod}_{(n-1)(n-1)} \end{pmatrix} \tag{3.38}$$

$$= N^{pre,n-3} - \begin{pmatrix} N^{save,n}_{f} & \mathbf{0} & N^{save,n}_{f(n-1)} \\ \mathbf{0} & \mathbf{0} & \mathbf{0} \\ N^{save,n}_{(n-1)f} & \mathbf{0} & N^{save,n}_{(n-1)(n-1)} \end{pmatrix} + \begin{pmatrix} \mathbf{0} & \mathbf{0} & \mathbf{0} \\ \mathbf{0} & \mathbf{0} & \mathbf{0} \\ \mathbf{0} & \mathbf{0} & N^{rel}_{n-1} \end{pmatrix}$$

$$b^{mod,n-3} = \begin{pmatrix} b^{mod}_{n-2} \\ b^{mod}_{n-1} \end{pmatrix} = \begin{pmatrix} b^{pre}_{n-2} \\ b_{n-1} \end{pmatrix} - \begin{pmatrix} \mathbf{0} \\ b^{save,n}_{n-1} \end{pmatrix}, \tag{3.39}$$

where

$$N^{rel}_{n-1}(4,4) = \frac{\sigma_0^2}{\sigma_r^2}. \tag{3.40}$$

In this way, $N^{mod,n-3}$ and $b^{mod,n-3}$ replace $N^{pre,n-3}$ and $b^{pre,n-3}$. The elimination of the $(n-2)$-th epoch is performed for $N^{mod,n-3}$ and $b^{mod,n-3}$:

$$\begin{pmatrix} N^{back,n-1}_{f} & N^{back,n-1}_{f(n-2)} \\ N^{back,n-1}_{(n-2)f} & N^{back,n-1}_{(n-2)(n-2)} \end{pmatrix} = \begin{pmatrix} N^{mod,n-3}_{f} & N^{mod}_{f(n-2)} \\ N^{mod}_{(n-2)f} & N^{mod}_{(n-2)(n-2)} \end{pmatrix} - N^{save,n-1} \tag{3.41}$$

$$b^{back,n-1}_{n-2} = b^{mod}_{n-2} - b^{save,n-1}_{n-2}, \tag{3.42}$$

with

$$N^{save,n-1} = \begin{pmatrix} N^{mod}_{f(n-1)} \\ N^{mod}_{(n-2)(n-1)} \end{pmatrix} \cdot {N^{mod}_{(n-1)(n-1)}}^{-1} \cdot \begin{pmatrix} N^{mod}_{(n-1)f} & N^{mod}_{(n-1)(n-2)} \end{pmatrix}, \tag{3.43}$$

$$b^{save,n-1}_{n-2} = N^{mod}_{(n-2)(n-1)} \cdot \left(N^{mod}_{(n-1)(n-1)}\right)^{-1} \cdot b^{mod}_{n-1}. \tag{3.44}$$

The back-substitution goes on sequentially like this from the last epoch to the first epoch, while the NEQ matrix $N^{pre,i-1}$ and the term $b^{pre,i-1}$ before the pre-elimination of epoch i are used. The information from the $(i+2)$-th to the last epoch is sequentially saved in the matrix $N^{save,i+2}$ and the term $b^{save,i+2}_{i+1}$ as defined in Equations 3.43 and 3.44 and is then corrected with N^{rel}_{i+1} at the $(i+1)$-th epoch (see Equation 3.38). The modified matrix $N^{mod,i-1}$ and $b^{mod,i-1}$ are then ready for the elimination of the $(i+1)$-th epoch.

After that, the back-substitution of the epoch parameter at epoch i can be estimated with

$$\Delta\hat{x}_i = \left(N^{back,i+1}_{ii}\right)^{-1} \cdot b^{back,i+1}_{i}. \tag{3.45}$$

3.1.3 Pre-elimination and back-substitution of epoch parameters with constraints between near-subsequent epochs

The relative constraints can also be applied to near-subsequent epochs (e.g., among three epochs or even more). Figure 3.4 illustrates constraints between subsequent and near-

subsequent (here three) epochs:

Pre-elimination

Assuming that the relative clock constraints are considered within three epochs, the NEQ matrix N can be described similarly to Equation 3.6:

$$N = \begin{pmatrix} N_f & N_{f1} & N_{f2} & N_{f3} & \cdots & N_{fn} \\ N_{1f} & N_{11} & N_{12} & N_{13} & \cdots & \mathbf{0} \\ N_{2f} & N_{21} & N_{22} & N_{23} & \cdots & \mathbf{0} \\ N_{3f} & N_{31} & N_{32} & N_{33} & \cdots & \mathbf{0} \\ \vdots & \vdots & \vdots & \vdots & \ddots & \vdots \\ N_{nf} & \mathbf{0} & \mathbf{0} & \mathbf{0} & \cdots & N_{nn} \end{pmatrix}. \tag{3.46}$$

The relative sigma between the first and second epoch and between the second and third epoch is denoted by σ_{r1}, and the relative sigma between the first and third epoch is denoted by σ_{r2}. The absolute sigma σ_{abs} is assumed to be applied to each epoch. Then we can manipulate the epoch parameters of the first three epochs as following:

$$\begin{pmatrix} N^{\star}_{11} & N^{\star}_{12} & N^{\star}_{13} \\ N^{\star}_{21} & N^{\star}_{22} & N^{\star}_{23} \\ N^{\star}_{31} & N^{\star}_{32} & N^{\star}_{33} \end{pmatrix} = \begin{pmatrix} N_{11} & N_{12} & N_{13} \\ N_{21} & N_{22} & N_{23} \\ N_{31} & N_{32} & N_{33} \end{pmatrix} + N^{rel}_{1,2,3} + N^{abs}_{1,2,3} \tag{3.47}$$

with

$$N^{rel}_{1,2,3}([4\ 8\ 12]) + N^{abs}_{1,2,3}([4\ 8\ 12]) = \begin{pmatrix} \frac{\sigma_0^2}{\sigma_{r1}^2} + \frac{\sigma_0^2}{\sigma_{r2}^2} + \frac{\sigma_0^2}{\sigma_{abs}^2} & -\frac{\sigma_0^2}{\sigma_{r1}^2} & -\frac{\sigma_0^2}{\sigma_{r2}^2} \\ -\frac{\sigma_0^2}{\sigma_{r1}^2} & 2\frac{\sigma_0^2}{\sigma_{r1}^2} + \frac{\sigma_0^2}{\sigma_{abs}^2} & -\frac{\sigma_0^2}{\sigma_{r1}^2} \\ -\frac{\sigma_0^2}{\sigma_{r2}^2} & -\frac{\sigma_0^2}{\sigma_{r1}^2} & \frac{\sigma_0^2}{\sigma_{r1}^2} + \frac{\sigma_0^2}{\sigma_{r2}^2} + \frac{\sigma_0^2}{\sigma_{abs}^2} \end{pmatrix}. \tag{3.48}$$

The O-C term B is represented by Equation 3.49:

$$B = \begin{pmatrix} B_f & B_1 & B_2 & B_3 & \cdots & B_n \end{pmatrix}^T. \tag{3.49}$$

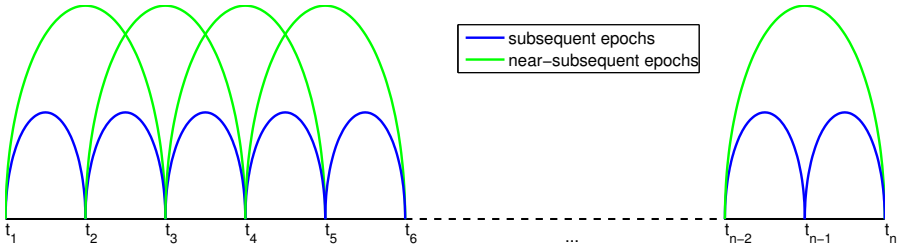

Figure 3.4: Constraints between subsequent and near-subsequent epochs.

The pre-elimination of the first epoch has an impact on the non-epoch parameters and the epoch parameters of the second and the third epoch (see the blue elements in Equations 3.46 and 3.49):

$$\begin{pmatrix} N_f^{pre,1} & N_{f2}^{pre} & N_{f3}^{pre} \\ N_{2f}^{pre} & N_{22}^{pre} & N_{23}^{pre} \\ N_{3f}^{pre} & N_{32}^{pre} & N_{33}^{pre} \end{pmatrix} = \begin{pmatrix} N_f & N_{f2} & N_{f3} \\ N_{2f} & N_{22}^{\star} & N_{23}^{\star} \\ N_{3f} & N_{32}^{\star} & N_{33}^{\star} \end{pmatrix} - \begin{pmatrix} N_{f1} \\ N_{21}^{\star} \\ N_{31}^{\star} \end{pmatrix} \cdot (N_{11}^{\star})^{-1} \cdot \begin{pmatrix} N_{1f} & N_{12}^{\star} & N_{13}^{\star} \end{pmatrix}, \tag{3.50}$$

$$\begin{pmatrix} B_f^{pre,1} \\ B_2^{pre} \\ B_3^{pre} \end{pmatrix} = \begin{pmatrix} B_f \\ B_2 \\ B_3 \end{pmatrix} - \begin{pmatrix} N_{f1} \\ N_{21}^{\star} \\ N_{31}^{\star} \end{pmatrix} \cdot (N_{11}^{\star})^{-1} \cdot B_1. \tag{3.51}$$

As a result, the NEQ matrix and the B matrix after the pre-elimination of the first epoch are given by:

$$N^{pre,1} = \begin{pmatrix} N_f^{pre,1} & N_{f2}^{pre} & N_{f3}^{pre} & N_{f4} & \cdots & N_{fn} \\ N_{2f}^{pre} & N_{22}^{pre} & N_{23}^{pre} & N_{24} & \cdots & \mathbf{0} \\ N_{3f}^{pre} & N_{32}^{pre} & N_{33}^{pre} & N_{34} & \cdots & \mathbf{0} \\ N_{4f} & N_{42} & N_{43} & N_{44} & \cdots & \mathbf{0} \\ \vdots & \vdots & \vdots & \vdots & \ddots & \vdots \\ N_{nf} & \mathbf{0} & \mathbf{0} & \mathbf{0} & \cdots & N_{nn} \end{pmatrix}, \tag{3.52}$$

$$B^{pre,1} = \begin{pmatrix} B_f^{pre,1} & B_2^{pre} & B_3^{pre} & B_4 & \cdots & B_n \end{pmatrix}^T. \tag{3.53}$$

Since the relative constraint between the second and the third epoch, and the absolute constraints on the second and third epoch have already been considered in Equation 3.48, we only need to add the relative and absolute constraints related to the fourth epoch, when pre-eliminating the second epoch:

$$\begin{pmatrix} N_{22}^{\star pre} & N_{23}^{\star pre} & N_{24}^{\star} \\ N_{32}^{\star pre} & N_{33}^{\star pre} & N_{34}^{\star} \\ N_{42}^{\star} & N_{43}^{\star} & N_{44}^{\star} \end{pmatrix} = \begin{pmatrix} N_{22}^{pre} & N_{23}^{pre} & N_{24} \\ N_{32}^{pre} & N_{33}^{pre} & N_{34} \\ N_{42} & N_{43} & N_{44} \end{pmatrix} + N_{(2,3),4}^{rel} + N_4^{abs}, \tag{3.54}$$

with

$$N_{(2,3),4}^{rel}([4\ 8\ 12]) + N_4^{abs}([4\ 8\ 12]) = \begin{pmatrix} \frac{\sigma_0^2}{\sigma_{r2}^2} & \mathbf{0} & -\frac{\sigma_0^2}{\sigma_{r2}^2} \\ \mathbf{0} & \frac{\sigma_0^2}{\sigma_{r1}^2} & -\frac{\sigma_0^2}{\sigma_{r1}^2} \\ -\frac{\sigma_0^2}{\sigma_{r2}^2} & -\frac{\sigma_0^2}{\sigma_{r1}^2} & \frac{\sigma_0^2}{\sigma_{r1}^2} + \frac{\sigma_0^2}{\sigma_{r2}^2} + \frac{\sigma_0^2}{\sigma_{abs}^2} \end{pmatrix}. \tag{3.55}$$

The pre-elimination is then performed for the second until the $(n-2)$-th epoch similarly to the first epoch. After the pre-elimination of the $(n-2)$-th epoch, only the last two

epochs are remaining:

$$N^{pre,n-2} = \begin{pmatrix} N_f^{pre,n-2} & N_{f(n-1)}^{pre} & N_{fn}^{pre} \\ N_{(n-1)f}^{pre} & N_{(n-1)(n-1)}^{pre} & N_{(n-1)n}^{pre} \\ N_{nf}^{pre} & N_{n(n-1)}^{pre} & N_{nn}^{pre} \end{pmatrix}, \tag{3.56}$$

$$B^{pre,n-2} = \begin{pmatrix} B_f^{pre,n-2} & B_{n-1}^{pre} & B_n^{pre} \end{pmatrix}^T. \tag{3.57}$$

Since the relative constraint between the last two epochs and the absolute constraint of the last two epochs have already been considered before the pre-elimination of the $(n-2)$-th epoch, the pre-elimination of the last two epochs can be performed together:

$$\begin{aligned} N^{pre,n-1} &= N_f^{pre,n-2} - \begin{pmatrix} N_{f(n-1)}^{pre} & N_{fn}^{pre} \end{pmatrix} \cdot \begin{pmatrix} N_{(n-1)(n-1)}^{pre} & N_{(n-1)n}^{pre} \\ N_{n(n-1)}^{pre} & N_{nn}^{pre} \end{pmatrix}^{-1} \\ &\quad \cdot \begin{pmatrix} N_{(n-1)f}^{pre} \\ N_{nf}^{pre}, \end{pmatrix}, \end{aligned} \tag{3.58}$$

$$\begin{aligned} B^{pre,n-1} &= B_f^{pre,n-2} - \begin{pmatrix} N_{f(n-1)}^{pre} & N_{fn}^{pre} \end{pmatrix} \cdot \begin{pmatrix} N_{(n-1)(n-1)}^{pre} & N_{(n-1)n}^{pre} \\ N_{n(n-1)}^{pre} & N_{nn}^{pre} \end{pmatrix}^{-1} \\ &\quad \cdot \begin{pmatrix} B_{n-1}^{pre} \\ B_n^{pre} \end{pmatrix}. \end{aligned} \tag{3.59}$$

The non-epoch parameters are estimated with the formula

$$\Delta\hat{x}_f = \left(N^{pre,n-1}\right)^{-1} \cdot B^{pre,n-1}. \tag{3.60}$$

Before the pre-elimination of each epoch i ($i = 1, \cdots, n-2$), the NEQ matrices of epoch i, $i+1$ and $i+2$, as well as the NEQ matrix between the non-epoch parameters and the epoch parameters of these three epochs, described with

$$\begin{pmatrix} N_{if}^{pre} & N_{ii}^{\star pre} & N_{i(i+1)}^{\star pre} & N_{i(i+2)}^{\star} \\ N_{(i+1)f}^{pre} & N_{(i+1)i}^{\star pre} & N_{(i+1)(i+1)}^{\star pre} & N_{(i+1)(i+2)}^{\star} \\ N_{(i+2)f} & N_{(i+2)i}^{\star} & N_{(i+2)(i+1)}^{\star} & N_{(i+2)(i+2)}^{\star} \end{pmatrix}, \tag{3.61}$$

are saved for the back-substitution (no upper index *pre* for the first epoch). For the seond but last epoch, only the NEQ matrices related to the last two epochs

$$\begin{pmatrix} N_{(n-1)f}^{pre} & N_{(n-1)(n-1)}^{pre} & N_{(n-1)n}^{pre} \\ N_{nf}^{pre} & N_{n(n-1)}^{pre} & N_{nn}^{pre} \end{pmatrix} \tag{3.62}$$

are saved for the back-substitution.

Back-substitution

Similar to the procedure for the back-substitution in Section 3.1.2, firstly the term b (see Equation 3.27) is pre-eliminated from the first to the $(n-2)$-th epoch. The last two epochs of b remain as:

$$\begin{pmatrix} b_{n-1}^{pre} \\ b_n^{pre} \end{pmatrix} = \begin{pmatrix} b_{n-1}^{pre} \\ b_n \end{pmatrix} - \begin{pmatrix} N_{(n-1)(n-2)}^{\star pre} \\ N_{n(n-2)}^{\star} \end{pmatrix} \cdot \left(N_{(n-2)(n-2)}^{\star pre}\right)^{-1} \cdot b_{n-2}^{pre}, \tag{3.63}$$

where b_{n-1}^{pre} and $N_{(n-1)(n-2)}^{\star pre}$ on the right-hand side of the equation are influenced by the pre-elimination of the $(n-3)$-th epoch. Before the pre-elimination of the term b for each epoch i $(i = 1, \cdots, n-2)$, the matrices

$$\begin{pmatrix} b_i^{pre} \\ b_{i+1}^{pre} \\ b_{i+2} \end{pmatrix} \tag{3.64}$$

are saved for the back-substitution (no upper index pre for the first epoch). For the second but last epoch, the matrices

$$\begin{pmatrix} b_{n-1}^{pre} \\ b_n^{pre} \end{pmatrix} \tag{3.65}$$

are saved for the back-substitution.

Different from the back-substitution for relative constraints between subsequent epochs, the back-substitution of the last two epochs can be calculated here together (see Equations 3.56 and 3.63):

$$\begin{pmatrix} \Delta\hat{x}_{n-1} \\ \Delta\hat{x}_n \end{pmatrix} = \begin{pmatrix} N_{(n-1)(n-1)}^{pre} & N_{(n-1)n}^{pre} \\ N_{n(n-1)}^{pre} & N_{nn}^{pre} \end{pmatrix}^{-1} \cdot \begin{pmatrix} b_{n-1}^{pre} \\ b_n^{pre} \end{pmatrix}. \tag{3.66}$$

Before the pre-elimination of the $(n-2)$-th epoch, the NEQ matrix and the corresponding term b can be described as:

$$N^{pre,n-3} = \begin{pmatrix} N_f^{pre,n-3} & N_{f(n-2)}^{pre} & N_{f(n-1)}^{pre} & N_{fn} \\ N_{(n-2)f}^{pre} & N_{(n-2)(n-2)}^{\star pre} & N_{(n-2)(n-1)}^{\star pre} & N_{(n-2)n}^{\star} \\ N_{(n-1)f}^{pre} & N_{(n-1)(n-2)}^{\star pre} & N_{(n-1)(n-1)}^{\star pre} & N_{(n-1)n}^{\star} \\ N_{nf} & N_{n(n-2)}^{\star} & N_{n(n-1)}^{\star} & N_{nn}^{\star} \end{pmatrix}, \tag{3.67}$$

$$b^{pre,n-3} = \begin{pmatrix} b_f^{pre,n-3} & b_{n-2}^{pre} & b_{n-1}^{pre} & b_n \end{pmatrix}^T. \tag{3.68}$$

The back-substitution of the $(n-2)$-th epoch also needs the information of the last two epochs. This is realized by the elimination of these two epochs:

$$\begin{pmatrix} N_f^{back,(n-1)n} & N_{f(n-2)}^{back,(n-1)n} \\ N_{(n-2)f}^{back,(n-1)n} & N_{(n-2)(n-2)}^{back,(n-1)n} \end{pmatrix} = \begin{pmatrix} N_f^{pre,n-3} & N_{f(n-2)}^{pre} \\ N_{(n-2)f}^{pre} & N_{(n-2)(n-2)}^{\star pre} \end{pmatrix} - N^{save,(n-1)n}, \tag{3.69}$$

$$b_{n-2}^{back,(n-1)n} = b_{n-2}^{pre} - b_{n-2}^{save,(n-1)n}, \tag{3.70}$$

with (see Equation 3.61)

$$N^{save,(n-1)n} = \begin{pmatrix} N^{pre}_{f(n-1)} & N_{fn} \\ N^{\star pre}_{(n-2)(n-1)} & N^{\star}_{(n-2)n} \end{pmatrix} \cdot \begin{pmatrix} N^{\star pre}_{(n-1)(n-1)} & N^{\star}_{(n-1)n} \\ N^{\star}_{n(n-1)} & N^{\star}_{nn} \end{pmatrix}^{-1} \cdot \begin{pmatrix} N^{pre}_{(n-1)f} & N^{\star pre}_{(n-1)(n-2)} \\ N_{nf} & N^{\star}_{n(n-2)} \end{pmatrix}, \tag{3.71}$$

$$b^{save,(n-1)n}_{n-2} = \begin{pmatrix} N^{\star pre}_{(n-2)(n-1)} & N^{\star}_{(n-2)n} \end{pmatrix} \cdot \begin{pmatrix} N^{\star pre}_{(n-1)(n-1)} & N^{\star}_{(n-1)n} \\ N^{\star}_{n(n-1)} & N^{\star}_{nn} \end{pmatrix}^{-1} \cdot \begin{pmatrix} b^{pre}_{n-1} \\ b_n \end{pmatrix}. \tag{3.72}$$

The epoch parameters of epoch $n-2$ are then calculated with:

$$\Delta\hat{x}_{n-2} = \left(N^{back,(n-1)n}_{(n-2)(n-2)}\right)^{-1} \cdot b^{back,(n-1)n}_{n-2}. \tag{3.73}$$

For the $(n-3)$-th epoch, not only the information stored in $N^{save,n}$, but also the relative constraints related to the n-th epoch, which are not included in $N^{pre,n-4}$, have to be corrected:

$$\begin{aligned} N^{mod,n-4} &= \begin{pmatrix} N^{mod,n-4}_{f} & N^{mod}_{f(n-3)} & N^{mod}_{f(n-2)} & N^{mod}_{f(n-1)} \\ N^{mod}_{(n-3)f} & N^{mod}_{(n-3)(n-3)} & N^{mod}_{(n-3)(n-2)} & N^{mod}_{(n-3)(n-1)} \\ N^{mod}_{(n-2)f} & N^{mod}_{(n-2)(n-3)} & N^{mod}_{(n-2)(n-2)} & N^{mod}_{(n-2)(n-1)} \\ N^{mod}_{(n-1)f} & N^{mod}_{(n-1)(n-3)} & N^{mod}_{(n-1)(n-2)} & N^{mod}_{(n-1)(n-1)} \end{pmatrix} \\ &= N^{pre,n-4} - \underbrace{\begin{pmatrix} N^{save,n}_{f} & \mathbf{0} & N^{save,n}_{f(n-2)} & N^{save,n}_{f(n-1)} \\ \mathbf{0} & \mathbf{0} & \mathbf{0} & \mathbf{0} \\ N^{save,n}_{(n-2)f} & \mathbf{0} & N^{save,n}_{(n-2)(n-2)} & N^{save,n}_{(n-2)(n-1)} \\ N^{save,n}_{(n-1)f} & \mathbf{0} & N^{save,n}_{(n-1)(n-2)} & N^{save,n}_{(n-1)(n-1)} \end{pmatrix}}_{N^{save,n}} \\ &\quad + \begin{pmatrix} \mathbf{0} & \mathbf{0} & \mathbf{0} & \mathbf{0} \\ \mathbf{0} & \mathbf{0} & \mathbf{0} & \mathbf{0} \\ \mathbf{0} & \mathbf{0} & N^{rel,n}_{n-2} & \mathbf{0} \\ \mathbf{0} & \mathbf{0} & \mathbf{0} & N^{rel,n}_{n-1} \end{pmatrix}, \end{aligned} \tag{3.74}$$

$$b^{mod,n-4} = \begin{pmatrix} b^{mod}_{n-3} \\ b^{mod}_{n-2} \\ b^{mod}_{n-1} \end{pmatrix} = \begin{pmatrix} b^{pre}_{n-3} \\ b^{pre}_{n-2} \\ b_{n-1} \end{pmatrix} - \underbrace{\begin{pmatrix} \mathbf{0} \\ b^{save,n}_{n-2} \\ b^{save,n}_{n-1} \end{pmatrix}}_{b^{save,n}}, \tag{3.75}$$

with

$$N^{save,n} = \begin{pmatrix} N_{fn} \\ N^{\star}_{(n-2)n} \\ N^{\star}_{(n-1)n} \end{pmatrix} \cdot (N^{\star}_{nn})^{-1} \cdot \begin{pmatrix} N_{nf} & N^{\star}_{n(n-2)} & N^{\star}_{n(n-1)} \end{pmatrix}, \tag{3.76}$$

$$b^{save,n} = \begin{pmatrix} N_{fn} \\ N^{\star}_{(n-2)n} \\ N^{\star}_{(n-1)n} \end{pmatrix} \cdot (N^{\star}_{nn})^{-1} \cdot b_n. \tag{3.77}$$

$N^{rel,n}_{n-2}([4\ 4])$ and $N^{rel,n}_{n-1}([4\ 4])$ represent the influences of the constraints between the $(n-2)$-th and the last epoch as well as between the $(n-1)$-th epoch and the last epoch on the NEQ matrix, and are equal to $\frac{\sigma_0^2}{\sigma_{r2}^2}$ and $\frac{\sigma_0^2}{\sigma_{r1}^2}$, respectively.

The pre-elimination of the $(n-2)$-th and the $(n-1)$-th epoch is performed then based on $N^{mod,n-4}$ and $b^{mod,n-4}$ (see Equations 3.74 and 3.75):

$$\begin{pmatrix} N^{back,(n-2)(n-1)}_{f} & N^{back,(n-2)(n-1)}_{f(n-3)} \\ N^{back,(n-2)(n-1)}_{(n-3)f} & N^{back,(n-2)(n-1)}_{(n-3)(n-3)} \end{pmatrix} = \begin{pmatrix} N^{mod,n-4}_{f} & N^{mod}_{f(n-3)} \\ N^{mod}_{(n-3)f} & N^{mod}_{(n-3)(n-3)} \end{pmatrix} - N^{save,(n-2)(n-1)}, \tag{3.78}$$

$$b^{back,(n-2)(n-1)}_{n-3} = b^{mod,n-3}_{n-3} - b^{save,(n-2)(n-1)}, \tag{3.79}$$

with

$$N^{save,(n-2)(n-1)} = \begin{pmatrix} N^{mod}_{f(n-2)} & N^{mod}_{f(n-1)} \\ N^{mod}_{(n-3)(n-2)} & N^{mod}_{(n-3)(n-1)} \end{pmatrix} \cdot \begin{pmatrix} N^{mod}_{(n-2)(n-2)} & N^{mod}_{(n-2)(n-1)} \\ N^{mod}_{(n-1)(n-2)} & N^{mod}_{(n-1)(n-1)} \end{pmatrix}^{-1} \cdot \begin{pmatrix} N^{mod}_{(n-2)f} & N^{mod}_{(n-2)(n-3)} \\ N^{mod}_{(n-1)f} & N^{mod}_{(n-1)(n-3)} \end{pmatrix}, \tag{3.80}$$

$$b^{save,(n-2)(n-1)} = \begin{pmatrix} N^{mod}_{(n-3)(n-2)} & N^{mod}_{(n-3)(n-1)} \end{pmatrix} \cdot \begin{pmatrix} N^{mod}_{(n-2)(n-2)} & N^{mod}_{(n-2)(n-1)} \\ N^{mod}_{(n-1)(n-2)} & N^{mod}_{(n-1)(n-1)} \end{pmatrix}^{-1} \cdot \begin{pmatrix} b^{mod}_{n-2} \\ b^{mod}_{n-1} \end{pmatrix}. \tag{3.81}$$

The epoch parameters of the $(n-3)$-th epoch is calculated similarly to Equation 3.73:

$$\Delta\hat{x}_{n-3} = \left(N^{back,(n-2)(n-1)}_{(n-3)(n-3)}\right)^{-1} \cdot b^{back,(n-2)(n-1)}_{n-3}. \tag{3.82}$$

The information of the $(n-1)$-th epoch (in $N^{mod,n-4}$ and $b^{mod,n-4}$) is then saved in $N^{save,n-1}$ and $b^{save,n-1}$ and used for correcting the $N^{mod,n-5}$ and $b^{mod,n-5}$ by back-substitution of the $(n-4)$-th epoch. However, it should be noticed that the influence of the last epoch is only partially contained in $N^{save,n-1}$ and $b^{save,n-1}$. Its influence on the $(n-2)$-th epoch should again be corrected (see $N^{save,n}_{(n-2)(n-2)}$ in Equation 3.74 and $b^{save,n}_{n-2}$

in Equation 3.75):

$$N^{mod,n-5} = N^{pre,n-5} - N^{save,n-1} - \underbrace{\begin{pmatrix} \mathbf{0} & \mathbf{0} & \mathbf{0} & \mathbf{0} \\ \mathbf{0} & \mathbf{0} & \mathbf{0} & \mathbf{0} \\ \mathbf{0} & \mathbf{0} & \mathbf{0} & \mathbf{0} \\ \mathbf{0} & \mathbf{0} & \mathbf{0} & N^{save,n}_{(n-2)(n-2)} \end{pmatrix}}_{N^{save,n}_{n-2}} + \begin{pmatrix} \mathbf{0} & \mathbf{0} & \mathbf{0} & \mathbf{0} \\ \mathbf{0} & \mathbf{0} & \mathbf{0} & \mathbf{0} \\ \mathbf{0} & \mathbf{0} & N^{rel,n-1}_{n-3} & \mathbf{0} \\ \mathbf{0} & \mathbf{0} & \mathbf{0} & N^{rel,n-1}_{n-2} + N^{rel,n}_{n-2} \end{pmatrix}, \tag{3.83}$$

$$b^{mod,n-5} = \begin{pmatrix} b^{pre}_{n-4} \\ b^{pre}_{n-3} \\ b_{n-2} \end{pmatrix} - b^{save,n-1} - \begin{pmatrix} \mathbf{0} \\ \mathbf{0} \\ b^{save,n}_{n-2} \end{pmatrix}, \tag{3.84}$$

where $N^{rel,n-1}_{n-3}([4\ 4])$ and $N^{rel,n-1}_{n-2}([4\ 4])$ represent the influences of the constraints between the $(n-3)$-th and the second but last epoch as well as between the $(n-2)$-th and the second but last epoch on the NEQ matrix, and are equal to $\frac{\sigma_0^2}{\sigma_{r2}^2}$ and $\frac{\sigma_0^2}{\sigma_{r1}^2}$, respectively. $N^{rel,n}_{n-2}([4\ 4])$ represents the influence of the constraint between the $(n-2)$-th epoch and the last epoch on the NEQ matrix, and is equal to $\frac{\sigma_0^2}{\sigma_{r2}^2}$. It should also be noticed that in Equation 3.83 the influence of the last epoch on the $(n-2)$-th epoch is neglected on the variance and covariance elements of the non-epoch parameters (see the zeros in $N^{save,n}_{n-2}$ in Equation 3.83 at the position of $N^{save,n}_{(n-2)f}$, $N^{save,n}_{f(n-2)}$ and $N^{save,n}_{f}$ in $N^{save,n}$ in Equation 3.74). The reason is that for the back-substitution of epoch i only the element $N^{back,(i+1)(i+2)}_{ii}$ is used (see Equations 3.73 and 3.82). The elements $N^{save,n}_{(n-2)f}$, $N^{save,n}_{f(n-2)}$ and $N^{save,n}_{f}$ are thus not required.

For the estimation of the epoch parameters of epoch i, the $(i+1)$-th and the $(i+2)$-th epoch of matrix $N^{mod,i-1}$ and $b^{mod,i-1}$ have been pre-eliminated considering not only the information of the $(i+3)$-th, but also the information of the $(i+4)$-th epoch. The epoch parameters are then calculated with the matrix $N^{back,(i+1)(i+2)}$ and $b^{back,(i+1)(i+2)}$ after the pre-elimination:

$$\Delta\hat{x}_i = \left(N^{back,(i+1)(i+2)}_{ii}\right)^{-1} \cdot b^{back,(i+1)(i+2)}_{i}. \tag{3.85}$$

The algorithm can also further be extended to relative constraints among m relevant epochs. For the estimation of the epoch parameters at epoch i, the $(i+1)$-th to the $(i+m-1)$-th epoch of matrix $N^{mod,i-1}$ and $b^{mod,i-1}$ are eliminated considering not only the information of the $(i+m)$-th epoch, which is saved in $N^{save,i+m}$ and $b^{save,i+m}$, but also the information from the $(i+m+1)$-th to the $(i+2m-2)$-th epoch, which are still relevant to the $N^{mod,i-1}$ and $b^{mod,i-1}$ and are cumulatively saved in $N^{save,i+m+1}$ and $b^{save,i+m+1}$. After back-substitution of the i-th epoch, $N^{save,i+m+1}$ and $b^{save,i+m+1}$ get rid

of their last epoch that will not be used for the back-substitution anymore, namely the epoch $i+2m-2$, and newly include the information of the $(i+m)$-th epoch. In this way, they turn out to be $N^{save,i+m}$ and $b^{save,i+m}$, which are useful for the back-substitution of the $(i-1)$-th epoch and always contain information of $m-2$ epochs in total (for $i \leq n-2m+2$). The epoch parameters are calculated with the matrix $N^{back,(i+1)\cdots(i+m-1)}$ and $b^{back,(i+1)\cdots(i+m-1)}$ after the elimination of the $(i+1)$-th to the $(i+m-1)$-th epoch:

$$\Delta\hat{x}_i = (N_{ii}^{back,(i+1)\cdots(i+m-1)})^{-1} \cdot b_i^{back,(i+1)\cdots(i+m-1)}. \tag{3.86}$$

Figure 3.5 shows two examples of the standard deviations of the estimated kinematic heights of station ALGO and WSRT using different relative sigmas σ_{r1} and σ_{r2} between subsequent and near-subsequent epochs on October 1, 2013. These two stations were connected to H-Masers.

Compared with the relative constraint between subsequent epochs of the same clocks (see Figure 3.3), the capability of stabilizing the kinematic heights using constraints among three epochs has increased a little bit (see Table 3.1). The relative sigmas start from 0.1 mm and end at 20 mm. It should be noted that σ_r for relative constaints between subsequent epochs has a resolution of 0.1 mm, and the resolution of σ_{r1} and σ_{r2} for relative constraints among three epochs is 0.1 mm before 3 mm, 1 mm between 3 mm and 10 mm, and 2 mm between 10 mm and 20 mm. The relative sigmas σ_{r1}, σ_{r2}, $\cdots$ could in principle be taken from the ADEV or MDEV of the phase clock biases.

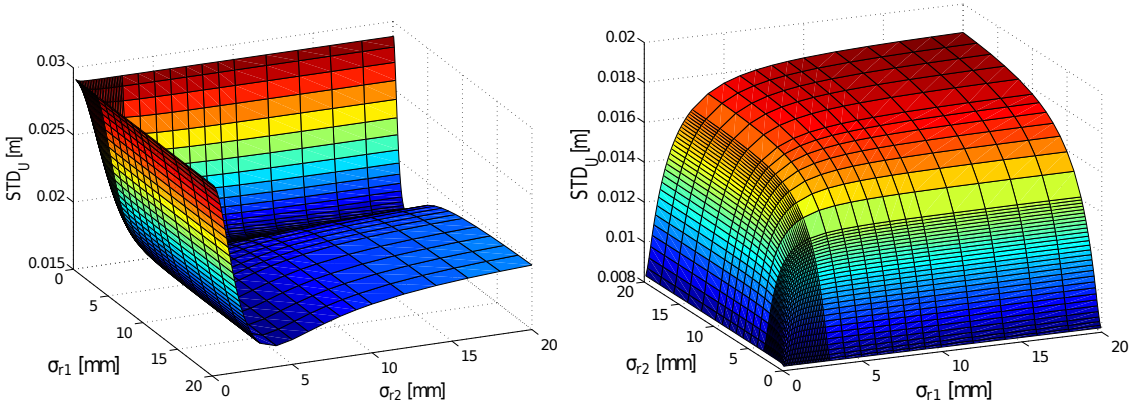

(a) ALGO (b) WSRT

Figure 3.5: Standard deviations of the kinematic height estimates STD_U by applying different relative clock constraints between subsequent and near-subsequent epochs for the H-Masers at (a) station ALGO and (b) station WSRT on October 1, 2013.

Table 3.1: Capability of stabilizing the kinematic heights by applying clock constraints between subsequent epochs and among three epochs.

Station	STD_{U2} [cm]	STD_{U3} [cm]	σ_r [mm]	σ_{r1} [mm]	σ_{r2} [mm]
ALGO	1.6513	1.6506	1.9	3.0	5.0
WSRT	0.8301	0.8191	0.1	0.1	0.1

3.2 Triple-frequency ambiguity resolution

The availability of signals on more than two frequencies has given us more possibilities and flexibility to form different types of linear combinations. This section is a summary based on Paper B and focuses on the GF and IF linear combination using both, the code and phase measurements on three frequencies.

3.2.1 The best two linear combinations

The linear combination L_x of triple-frequency code and phase measurements L_i and P_i $(i = 1, \cdots, 3)$ can generally be described by the following equation (see Section 2.3.2):

$$\begin{aligned} L_x &= \gamma_1 L_1 + \gamma_2 L_2 + \gamma_3 L_3 + \gamma_4 P_1 + \gamma_5 P_2 + \gamma_6 P_3 \\ &= \sum_{i=1}^{6} \gamma_i \cdot \Delta\rho + (\gamma_4 + \frac{f_1^2}{f_2^2}\gamma_5 + \frac{f_1^2}{f_3^2}\gamma_6 - \gamma_1 - \frac{f_1^2}{f_2^2}\gamma_2 - \frac{f_1^2}{f_3^2}\gamma_3) \cdot I_1 \\ &\quad + \underbrace{\sum_{i=1}^{3} \gamma_i \lambda_i n_i}_{\lambda_x n_x} + \epsilon, \end{aligned} \tag{3.87}$$

where γ_i $(i = 1, \cdots, 6)$ represent the coefficients in front of the phase and code measurements L_i and P_i. $\Delta\rho$ and I_1 stand for the geometry-related terms and the first-order ionospheric delay on L1, respectively. n_i and λ_i are the phase ambiguities and the wavelengths of the phase measurements on frequency f_i. ϵ represents the noise of the linear combination, i.e., the so-called combined noise. n_x and λ_x stand for the phase ambiguity and the wavelength of the linear combination L_x, respectively.

The coefficients γ_i $(i = 1, \cdots, 3)$ of the phase measurements have to fulfill the following relationship in order to guarantee the integer nature of the combined ambiguity n_x (Paper

B; Henkel and Günther, 2010):

$$\gamma_1 = \frac{a_x f_1}{f_x}, \tag{3.88}$$

$$\gamma_2 = \frac{b_x f_2}{f_x}, \tag{3.89}$$

$$\gamma_3 = \frac{c_x f_3}{f_x}, \tag{3.90}$$

where a_x, b_x and c_x are integers, and f_x represents the combined frequency. f_x is defined here as $f_x = \frac{c_l}{\lambda_x}$.

For given a_x, b_x and c_x, the coefficients γ_4 and γ_5 can be uniquely derived from γ_6 and f_x for the IF and GF linear combination, since for three unknowns (γ_i with $i = 4, 5, 6$) two conditions (IF and GF) leave still one free parameter (γ_6) in the solution:

$$\gamma_4 = \frac{m_1}{f_x} + m_2\gamma_6, \tag{3.91}$$

$$\gamma_5 = \frac{m_3}{f_x} + m_4\gamma_6, \tag{3.92}$$

where m_1 and m_3 are functions of a_x, b_x, c_x and f_i ($i = 1, \cdots, 3$), and m_2 and m_4 are purely functions of f_i ($i = 1, \cdots, 3$) (see Paper B).

Since the code noise is dominant in the combined measurement L_x, we set the goal to minimize the combined code noise in cycles. Assuming that the code noise is equal to σ_P in meters for all the three frequencies, the combined code noise can be formulated as

$$\begin{aligned} {\sigma^C_{Code}}^2 &= \frac{\sigma_P^2}{\lambda_x^2}\left(\sum_{i=4}^{6} C_i^2\gamma_i^2\right) \\ &= \frac{\sigma_P^2}{c_l^2}(f_x^2 \cdot F_1(m_2, m_4, C_4, C_5, C_6)(\gamma_6 + F_2(m_1, m_2, m_3, m_4, C_4, C_5, C_6, f_x))^2 \\ &\quad + F_3(m_1, m_2, m_3, m_4, C_4, C_5, C_6)), \end{aligned} \tag{3.93}$$

where C_i ($i = 4, \cdots, 6$) are scaling factors of the code noise on frequency f_i ($i = 1, \cdots, 3$), and $F_i(x_j)$ represents functions of the listed parameters x_j (more details in Paper B).

It is not difficult to see that the minimal code noise in cycles is equal to $\frac{\sigma_P}{c_l}\sqrt{F_3}$, when γ_6 equals $-F_2$. Assuming that the phase noise is equal to σ_L^C in cycles for all the three frequencies, the combined phase noise σ^C_{Phase} in cycles can be described by (see Paper B):

$$\sigma^C_{Phase} = \sigma^C_L \cdot \sqrt{a_x^2 + b_x^2 + c_x^2}. \tag{3.94}$$

As a result, we can see that, even if the six coefficients γ_i ($i = 1, \cdots, 6$) are all dependent on f_x, the combined phase and the minimized combined code noise in cycles are not depending on f_x, or λ_x. The relative relationship of the six coefficients and the combined noise in cycles are fixed for given integer coefficients a_x, b_x and c_x and given scaling factors C_i ($i = 4, \cdots, 6$) for the code noise under the given assumptions above.

Using the three frequencies which are currently available for BDS (B1=1561.098 MHz, B3=1268.52 MHz and B2=1207.14 MHz), the coefficients and the minimized noise on the zero-difference level for the best two linear combinations L_x and L_y are summarized in Table 3.2 under the assumption that the code noise is equal to 0.5 m and the phase noise is equal to 0.01 cycles on all the three frequencies. The corresponding combined wavelengths λ_x and λ_y are assumed to be 1 m for the calculation of the coefficients γ_i $(i = 1, \cdots, 6)$.

Figure 3.6 (Wang and Rothacher, 2015) shows the linear combinations L_x and L_y in cycles eliminating their mean values using the data of the station pair CUT2 and CUTA in Australia and the satellite pair C01 and C03 of BDS on March 21, 2014 (Raziq et al., 2012). The satellites C01, C02, C03 and C04 are geostationary satellites (see Section 2.1) and can thus be observed during the entire day. The two stations were using the same receiver type (TRIMBLE NETR9) and antenna type (TRM59800.00 SCIS). The tracking channels for both satellites on all three frequencies are Channel I. It should be noted that the phase and code measurements have gone through the pre-processing of the Bernese GNSS Software, which means that the code measurements were smoothed and show a reduced noise level.

We see that L_y and L_x follow similar patterns with different amplification factors, which could indicate that systematic effects are differently enlarged for these two linear combinations. The noise level of L_y is slightly larger than that of L_x. With the smoothed code measurements, the standard deviations of both measurements are smaller than 0.04 cycles.

Instead of just estimating the fractional parts of the combined ambiguities n_x and n_y, we are also able to compare them with the "true" ambiguities based on a modified version of the Bernese GNSS Software which is able to process the triple-frequency data of BDS. The estimated combined ambiguities n_x and n_y of the best two linear combinations L_x and L_y are compared with their "true" values obtained with the traditional algorithms of double-difference ambiguity resolution on L1 and L2, as well as with the Extra-Widelane (EWL) ambiguity $n_2 - n_3$ (Feng et al., 2007). The modification of the Bernese GNSS Software, the pre-processing of the measurements, and the resolution of the "true" ambiguities have been performed by Dr. Baoqi Sun (see Acknowledgement).

Using the data of station pair CUT2-CUTA and CUT2-CUTB and satellites C01, C02, C03 and C04 on March 21 and March 22, 2014, with a sampling interval of 30 s, the

Table 3.2: Integer coefficients a_x, b_x, c_x of the ambiguities, coefficients of the measurements γ_i and the minimized combined noise σ^C of the best two linear combinations of BDS.

a, b, c	γ_i $(i = 1, \cdots, 6)$						σ^C [cycles]
0, -1, 1	0.0000	-4.2313	4.0266	0.0041	0.0875	0.1131	0.0729
1, -3, 2	5.2073	-12.6940	8.0532	-0.5748	-0.0729	0.0812	0.2949

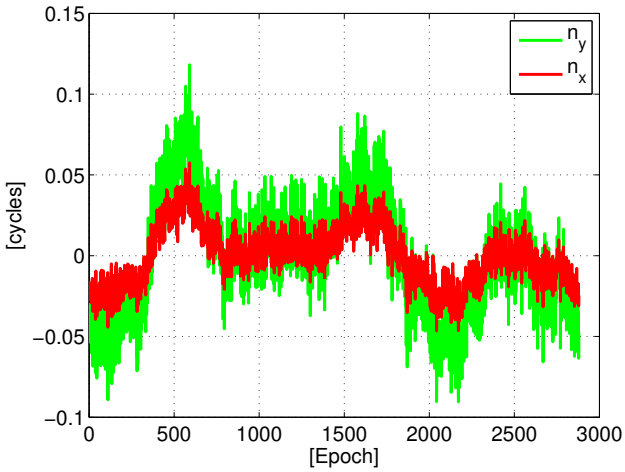

Figure 3.6: Best two linear combinations L_x and L_y (after eliminating the mean values) for the station pair CUT2-CUTA and the satellite pair C01-C03 on March 21, 2014 (Wang and Rothacher, 2015).

combined ambiguities n_x and n_y after rounding the float estimates are all equal to the "true" values. The differences between the float solutions and the integer "true" values are shown in Figure 3.7.

We see that all the differences for n_x are smaller than 0.05 cycles, about 75% of the differences for n_y are smaller than 0.12 cycles, whereas all the n_y, which show relatively

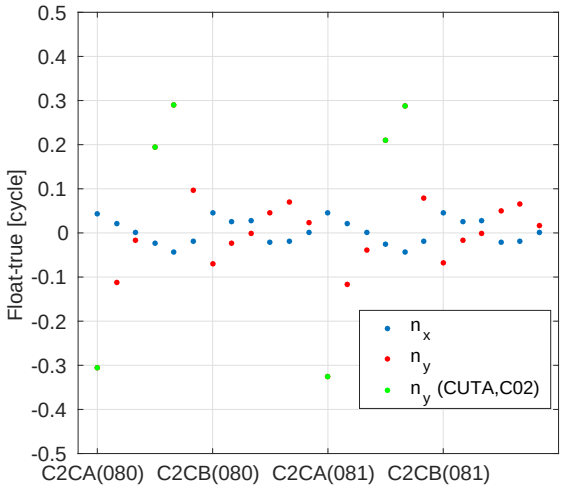

Figure 3.7: Differences between the estimated float ambiguities n_x and n_y and the "true" values obtained from the traditional and reliable dual-frequency double-difference ambiguity resolution on L1 and L2 as well as the resolved EWL ambiguities $n_2 - n_3$, using the station pairs CUT2-CUTA and CUT2-CUTB and the satellites C01, C02, C03 and C04 on March 21 and March 22, 2014.

big deviations to the true values (see green dots in Figure 3.7), are related to the station CUTA and satellite C02. Possible reason might be systematic effects like multipath for this station and satellite pair.

3.2.2 The third linear combination

In order to resolve all three ambiguities n_1, n_2, n_3 in the triple-frequency case, three linearly independent linear combinations are needed. Since it's difficult to find a third linear combination, which is linearly independent from the best two linear combinations and has, at the same time, a relatively low noise level, we have considered to use only the triple-frequency phase observations and the ambiguity-corrected phase observations using the resolved combined ambiguities n_x and n_y (Li et al., 2010). According to Equation 18 and Equation 24 in Paper B, the combined measurements of the third linear combination L_z can be formulated as:

$$\begin{aligned} L_z &= \sum_{i=1}^{3}(\gamma_{zi} + q_1\gamma_{xi} + q_2\gamma_{yi})L_i - q_1 n_x\lambda_x - q_2 n_y\lambda_y \\ &= (a_z n_1 + b_z n_2 + c_z n_3)\lambda_z \\ &= (Q_x n_x + Q_y n_y + Q_1 n_1)\lambda_z, \end{aligned} \tag{3.95}$$

where γ_{xi}, γ_{yi} and γ_{zi} represent the coefficients of the three phase measurements on frequency f_i, and a_z, b_z and c_z represent the integer coefficients of the phase ambiguities of the third linear combination. q_1 and q_2 are functions of the three integer coefficients for each of the three linear combinations L_x, L_y, L_z, the three carrier frequencies f_i $(i = 1, 2, 3)$ and the three combined frequencies f_x, f_y and f_z. Q_x, Q_y and Q_1 are functions of the integer coefficients of the three linear combinations (more details see Paper B).

From Equation 3.95 it is not difficult to obtain n_1:

$$n_1 = \frac{\sum_{i=1}^{3}(\gamma_{zi} + q_1\gamma_{xi} + q_2\gamma_{yi})L_i - q_1 n_x\lambda_x - q_2 n_y\lambda_y - (Q_x n_x + Q_y n_y)\lambda_z}{\lambda_z Q_1}. \tag{3.96}$$

After simplification, the factors before the three phase measurements can be represented by the three carrier frequencies and the speed of light:

$$\begin{aligned} n_1 = &-\frac{f_1^2(f_2+f_3)}{c_l(f_1-f_2)(f_1-f_3)}L_1 + \frac{f_2^2(f_1+f_3)}{c_l(f_1-f_2)(f_2-f_3)}L_2 \\ &-\frac{f_3^2(f_1+f_2)}{c_l(f_1-f_3)(f_2-f_3)}L_3 + \underbrace{\frac{f_2(a_y+b_y)(f_1^2-f_3^2) - f_3 b_y(f_1^2-f_2^2)}{(f_1-f_2)(f_1-f_3)(f_2-f_3)(a_x b_y - a_y b_x)}}_{coe_{nx}} n_x \\ &\underbrace{-\frac{f_2(a_x+b_x)(f_1^2-f_3^2) - f_3 b_x(f_1^2-f_2^2)}{(f_1-f_2)(f_1-f_3)(f_2-f_3)(a_x b_y - a_y b_x)}}_{coe_{ny}} n_y. \end{aligned} \tag{3.97}$$

(3.98)

Inserting the three frequencies of BDS (see Section 3.2.1) with f_1, f_2 and f_3 corresponding to B1, B3 and B2, n_1 can be expressed as

$$\begin{aligned} n_1 &= -194.3288 \cdot L_1 + 827.3872 \cdot L_2 - 633.0584 \cdot L_3 + coe_{nx} \cdot n_x \\ &\quad -coe_{ny} \cdot n_y \\ &= -37.3188 \cdot L_1^C + 195.5385 \cdot L_2^C - 157.2197 \cdot L_3^C + coe_{nx} \cdot n_x - coe_{ny} \cdot n_y, \end{aligned} \tag{3.99}$$

where L_i and L_i^C represent the phase measurements on frequency f_i in meters and in cycles, respectively.

With Equation 3.99 we can get the noise amplification factors of 1059.8 m^{-1} and 253.7 for the noise of n_1 in meters and in cycles, respectively. Assuming the noise is equal to 0.01 cycles for all the three carrier frequencies, the resulting noise for n_1 would amount to 2.537 cycles on the zero-difference level.

The formal error of n_1 decreases inversely proportional to $\sqrt{n}$, if the combined phase noise is white noise, where n represents of number of observation epochs in the corresponding validity interval of the ambiguity n_1. However, if other systematic effects or biases like multipath exist in L_i $(i = 1, 2, 3)$, n_1 will be easily influenced because of the large factors before L_1, L_2 and L_3. In this case, the biases cannot simply be reduced by increasing the number of observation epochs as in the case of white noise.

Assuming that biases δ_1, δ_2 and δ_3 (in meters) exist in the triple-frequency phase measurements, we can get a total bias δ^C (in cycles) in n_1 of

$$\delta^C = -194.3288 \cdot \delta_1 + 827.3872 \cdot \delta_2 - 633.0584 \cdot \delta_3. \tag{3.100}$$

This indicates that biases at the centimeter level in the original phase measurements can easily generate a total bias of several cycles or even more in n_1.

Figure 3.8 shows the reduced measurements, which have been used for the estimation of n_1 (see Equation 3.96), for the station pair CUT2-CUTB and the satellite pair C02-C04 on March 21, 2014. Clearly, systematic effects can be observed during the day. Phase biases are enlarged differently for each of the three frequencies and have a considerable impact on the differences Δn_1 between the estimated and the "true" values of n_1 (see Table 3.3).

From Table 3.3 we see considerable problems for the resolution of the n_1 ambiguities using the third linear combination. Only looking at the fractional parts of the estimated n_1 in Paper B, these large deviations could not be seen even if they are present. The detection and reduction of systematic effects existing in the phase measurements are crucial for fixing n_1 because of the large amplification factors in Equation 3.97 even for long tracks of geostationary satellites. However, since the amplification factors before the phase measurements L_1, L_2 and L_3 are only depending on the three frequencies themselves and the speed of light, they are kind of fixed for a specific frequency triplet under given assumptions. This indicates that the three amplification factors cannot be reduced by changing the integer coefficients or the combined frequencies f_x, f_y and f_z. In order to

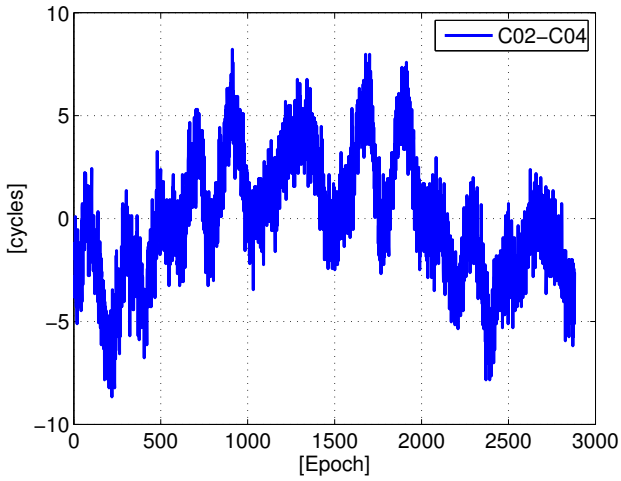

Figure 3.8: Reduced measurements for the estimation of n_1 with the station pair CUT2-CUTB and the satellite pair C02-C04 on March 21, 2014.

Table 3.3: Differences between the estimated and the "true" n_1 for the station pairs CUT2-CUTA and CUT2-CUTB on March 21 and March 22, 2014.

Station pair	Satellite pair	Δn_1 [cycles] (March 21)	Δn_1 [cycles] (March 22)
CUT2-CUTA	C01-C02	0.3322	0.2769
CUT2-CUTA	C01-C03	-0.4936	-0.4870
CUT2-CUTA	C01-C04	-0.5382	-0.4695
CUT2-CUTA	C02-C03	-0.8510	-0.7876
CUT2-CUTA	C02-C04	-0.8895	-0.7658
CUT2-CUTA	C03-C04	-0.0464	0.0161
CUT2-CUTB	C01-C02	-3.6986	-3.6594
CUT2-CUTB	C01-C03	-1.2518	-1.2580
CUT2-CUTB	C01-C04	-1.3994	-1.3287
CUT2-CUTB	C02-C03	2.4447	2.3988
CUT2-CUTB	C02-C04	2.3123	2.3446
CUT2-CUTB	C03-C04	-0.1472	-0.0698

improve the success rate of the ambiguity resolution, we should either consider reducing the systematic effects influencing the linear combination, or think of other possible methods for the third GF and IF linear combination. For baselines that are not very long, or if relatively precise information is available for, e.g., orbits, it might be more effective to use a IF and Geometry-Based (GB) phase linear combination as the third linear combination.

3.3 Ionospheric delay

As mentioned in Section 2.4, single-difference ionospheric delays and spatial gradients are normally small enough to be considered as negligible for most applications with short baselines. However, they could get critical under extreme ionosphere conditions for applications in, e.g., a GBAS network. Apart from that, ionospheric delays are also crucial for single-frequency VLBI observations in GNSS co-locations (Männel et al., 2016). Analysis and assessment of the ionospheric delays on the single-difference level are thus becoming important.

To calculate the single-difference ionospheric delays, the carrier-phase ionospheric corrections calculated using the geometry-free linear combination can firstly be leveled with the help of the code-based ionospheric corrections. The satellite and receiver inter-frequency biases are then solved and removed from the leveled ionospheric corrections to estimate high-precise TEC values (Lee et al., 2006b).

This section introduces an alternative processing strategy to estimate single-difference ionospheric delays and gradients using double-difference phase measurements with resolved ambiguities. The code measurements are only used to obtain the a priori receiver clocks. The estimated single-difference ionospheric delays are thus free from code-related biases like Differential Code Biases (DCBs) of the receivers and satellites (for the cases that signals from different tracking channels are used for the receiver pair and the satellite DCBs cannot be canceled by forming single differences) and artificial biases and jumps caused, e.g., by code smoothing.

Equation 3.101 shows the GF linear combination of phase measurements L_{4rv}^{kj} on the double-difference level:

$$L_{4rv}^{kj} = L_{1rv}^{kj} - L_{2rv}^{kj} = (\frac{f_1^2}{f_2^2} - 1) \cdot I_{1rv}^{kj} + \lambda_1 N_{1rv}^{ki} - \lambda_2 N_{2rv}^{ki} + PCV_{4rv}^{kj} + \delta_{4rv}^{kj}, \qquad (3.101)$$

where L_{1rv}^{kj} and L_{2rv}^{kj} represent the double-difference phase measurements between two receivers r, v and two satellites k, j on frequency f_1 and f_2. I_{1rv}^{kj} represents the positive ionospheric delay of code measurements on f_1, which results in a $-I_{1rv}^{kj}$ ionospheric delay on L1 phase measurements. N_{irv}^{kj} represents the double-difference ambiguity on frequency f_i. PCV_{4rv}^{kj} represents the double-difference PCVs in the GF linear combination, and δ_{4rv}^{kj} at the end of the equation stands for the non-ionospheric biases and measurement noise remaining in the GF linear combination.

After introducing the resolved double-difference ambiguities on L_1 and L_2 and the corresponding PCVs into Equation 3.101, only the term of the ionospheric delay remains in the observation equation when ignoring δ_{4rv}^{kj}. Assuming that there are n satellites observed at time $t(i)$ for the baseline rv, $n-1$ linearly independent L_4 double-difference observations can be formed. In order to estimate the single-difference ionospheric delay I_{1rv}^{k} on L1, a condition equation, e.g. a zero-mean condition over all the single-difference ionospheric de-

lays for this baseline at the corresponding epoch, is needed to avoid the singularity. In this study, we derived the ionospheric delay on L1 at the Ionosphere Pierce-Point (IPP) assuming a height of 450 km for the ionosphere single-layer from the CODE global ionosphere map (CODE products, 2014) for each station-satellite pair and each epoch, and computed the mean value of the single-difference ionospheric delays for each epoch and baseline using the map values. This mean value is then added to the estimated single-difference ionospheric delays I^k_{1rv} for a specific baseline and epoch, so that the zero-mean condition is corrected with the absolute information supplied by the CODE global ionosphere map.

The vertical single-difference ionospheric delay Iv^k_{1rv} on L1 is calculated starting from the slant single-difference ionospheric delay and using the mean mapping function:

$$Iv^k_{1rv} = \frac{I^k_{1rv}}{\frac{Fr+Fv}{2}}, \tag{3.102}$$

where Fr and Fv represent the mapping functions calculated with the elevation angles between station r and satellite k, and between station v and satellite k, respectively. Iv^k_{1rv} is, in this case, different from $Iv^k_{1r} - Iv^k_{1v}$, where the zero-difference vertical ionospheric delays Iv^k_{1r} and Iv^k_{1v} are calculated seperately with their individual mapping functions according to

$$Iv^k_{1r} = \frac{I^k_{1r}}{Fr}, \quad Iv^k_{1v} = \frac{I^k_{1v}}{Fv}. \tag{3.103}$$

Since we do not calculate the zero-difference slant ionospheric delays I^k_{1r} and I^k_{1v}, Equation 3.102 has to be corrected by the term

$$\begin{aligned} Iv_{cor} &= \frac{I^k_{1r}}{Fr} - \frac{I^k_{1v}}{Fv} - \frac{I^k_{1rv}}{\frac{Fr+Fv}{2}} \\ &= \frac{Fv - Fr}{Fr(Fr+Fv)} I^k_{1rv} + \frac{Fv - Fr}{FrFv} \underbrace{I^k_{1v}}_{\approx I^{k,model}_{1v}}, \end{aligned} \tag{3.104}$$

where the real value of I^k_{1v} is assumed to be approximately equal to the value $I^{k,model}_{1v}$ derived from the CODE global ionosphere map.

The slant and vertical ionospheric gradients can then be computed by dividing the differential slant and vertical ionospheric delays by either the IPP distance or the baseline length. It should be noted that the IPP distance for a specific baseline is always shorter than the baseline length, which indicates that the gradients calculated with the IPP distances are always larger.

3.3.1 Variation of the IPP distance

When calculating the ionospheric gradients, the IPP distance is typically used to evaluate the spatial change of the ionosphere on the single-layer. Under similar ionosphere conditions, not only the baseline length, but also the relative position of the station pair

and the satellite may affect the IPP distance, and thus affect the ionsopheric gradients significantly. In order to assess the variation of the IPP distance with the change of the relative geometry between the station pair ($Sta1$ and $Sta2$), the IPP pair ($I1$ and $I2$) as well as the satellite (Sat) (see Figure 3.9), a simplified model is generated with the assumption that the Earth is a symmetrical sphere with radius R_E, the satellite orbit is a circle with radius R_S and the IPPs are located on a single layer with radius R_I. The center of the Earth is represented by O.

In order to fix the relative geometry between one station pair and a satellite, we need the elevation angle E and the azimuth angle A_S from station 1 ($Sta1$) to the satellite (Sat) to get the position of the satellite, and the baseline length l_b and the the azimuth angle A_R from station 1 to station 2 ($Sta2$) to fix the second station. Figure 3.10 shows the relative geometry between station 1 and the satellite in the topocentric coordinate system of station 1. With the law of sines in trigonometry we can easily get:

$$\frac{\sin(90^\circ + E)}{R_S} = \frac{\sin\alpha}{R_E} = \frac{\sin(90^\circ - E - \alpha)}{l}, \tag{3.105}$$

where α represents the angle "$Sta1 - Sat - O$", and l is the distance between the satellite and station 1.

Based on Equation 3.105, α and l can be calculated according to

$$\alpha = \arcsin\frac{R_E\cos E}{R_S}, \tag{3.106}$$

$$l = \frac{\cos(E+\alpha)R_S}{\cos E}. \tag{3.107}$$

Since the IPP between station 1 and the satellite (represented by $I1$) is on the connection

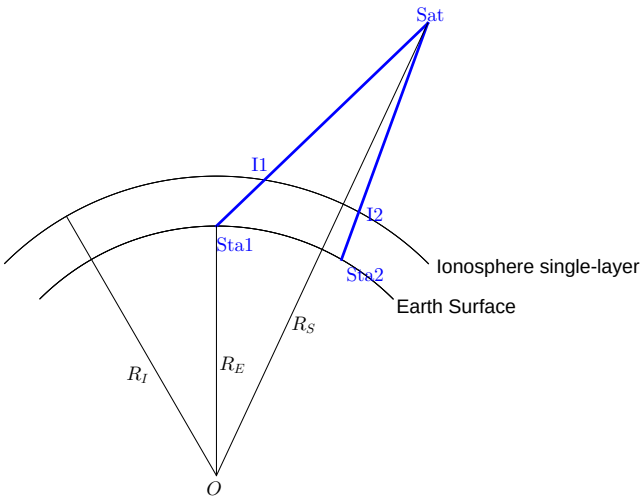

Figure 3.9: Relative geometry between the station pair, the IPP pair and the satellite (figure with changed scales).

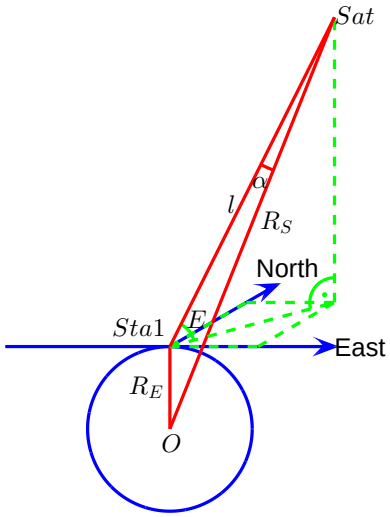

Figure 3.10: Relative geometry between station 1 and the satellite (figure with changed scales).

line "$Sta1 - Sat$", α_{I1} and l_{I1} can be similarly calculated with

$$\alpha_{I1} = \arcsin \frac{R_E \cos E}{R_I}, \tag{3.108}$$

$$l_{I1} = \frac{\cos(E + \alpha) R_I}{\cos E}. \tag{3.109}$$

The North, East and Up (NEU) coordinates of the satellite and $I1$ can thus be obtained with the formulas

$$\begin{pmatrix} N_{Sat} \\ E_{Sat} \\ U_{Sat} \end{pmatrix} = l \begin{pmatrix} \cos E \cos A_S \\ \cos E \sin A_S \\ \sin E \end{pmatrix}, \quad \begin{pmatrix} N_{I1} \\ E_{I1} \\ U_{I1} \end{pmatrix} = l_{I1} \begin{pmatrix} \cos E \cos A_S \\ \cos E \sin A_S \\ \sin E \end{pmatrix}. \tag{3.110}$$

Figure 3.11a shows the relative geometry between the station pair. The NEU coordinates of station 2 can be calculated with

$$\begin{pmatrix} N_{Sta2} \\ E_{Sta2} \\ U_{Sta2} \end{pmatrix} = R_E \begin{pmatrix} \sin\theta \cos A_R \\ \sin\theta \sin A_R \\ \cos\theta - 1 \end{pmatrix}, \tag{3.111}$$

where θ is the angle "$Sta1 - O - Sta2$" and can be calculated with

$$\theta = 2 \cdot \arcsin\left(\frac{l_b}{2R_E}\right). \tag{3.112}$$

Since the IPP between station 2 and the satellite (represented by $I2$) is on the connection line "$Sta2 - Sat$" (see Figure 3.11b), we can define the NEU coordinates of $I2$ with the variable u:

$$\begin{pmatrix} N_{I2} \\ E_{I2} \\ U_{I2} \end{pmatrix} = \begin{pmatrix} N_{Sta2} \\ E_{Sta2} \\ U_{Sta2} \end{pmatrix} + \begin{pmatrix} N_{Sat} - N_{Sta2} \\ E_{Sat} - E_{Sta2} \\ U_{Sat} - U_{Sta2} \end{pmatrix} \cdot u. \tag{3.113}$$

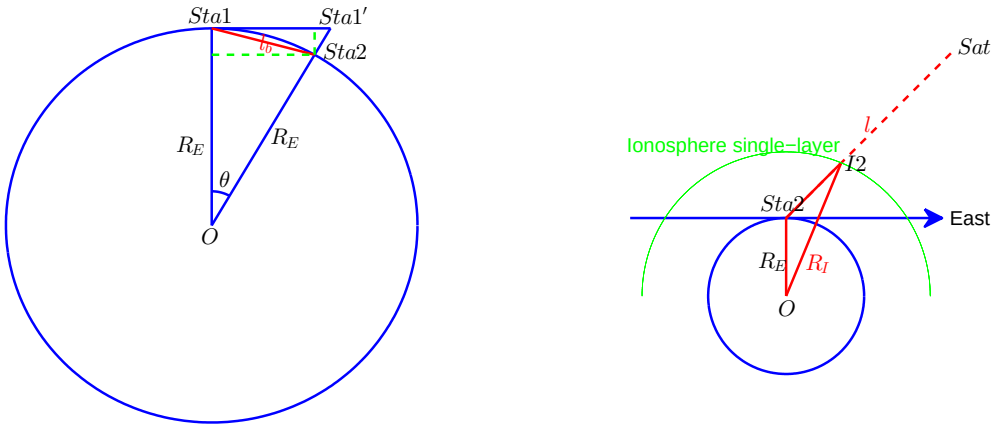

(a) Sta1-Sta2 (b) Sta2-Sat

Figure 3.11: Relative geometry between station 2 and (a) station 1, and (b) the satellite (figures with changed scales).

In order to estimate u, we use the information that the radius of the IPP layer is R_I, which is equal to the distance between O and $I2$:

$$\left| \begin{pmatrix} N_{I2} \\ E_{I2} \\ U_{I2} \end{pmatrix} - \begin{pmatrix} 0 \\ 0 \\ -R_E \end{pmatrix} \right| = R_I. \tag{3.114}$$

Inserting Equation 3.113 into Equation 3.114, we get a quadratic equation for u:

$$au^2 + bu + c = 0, \tag{3.115}$$

with

$$\begin{aligned} a &= (N_{Sat} - N_{Sta2})^2 + (E_{Sat} - E_{Sta2})^2 + (U_{Sat} - U_{Sta2})^2 > 0, && (3.116)\\ b &= 2(N_{Sta2}(N_{Sat} - N_{Sta2}) + E_{Sta2}(E_{Sat} - E_{Sta2}) && (3.117)\\ &\quad +(U_{Sta2} + R_E)(U_{Sat} - U_{Sta2})) > 0, \\ c &= N_{Sta2}^2 + E_{Sta2}^2 + (U_{Sta2} + R_E)^2 - R_I^2 = R_E^2 - R_I^2 < 0. && (3.118) \end{aligned}$$

$\frac{b}{2}$ represents the scalar product of vector "$O - Sta2$" and vector "$Sta2 - Sat$". Since the observed satellite is always above the horizontal plane of station 2, the angle between these two vectors is smaller than 90° and b is positive.

It is not difficult to see that there are two $I2$ points that fulfill this criterion, one as shown in Figure 3.11b, the other one on the extension line of "$Sat - Sta2$". In order to get the first $I2$, the variable u should be positive and can be estimated with

$$u = \frac{-b + \sqrt{b^2 - 4ac}}{2a} \tag{3.119}$$

according to the quadratic formula (Rich and Schmidt, 2004).

Figure 3.12 shows the variation of the IPP distance with the elevation angle E and the azimuth angle A_S to the satellite from station 1. The baseline length between the station pair is fixed to 300 km. The plots are generated using the simplified model introduced above with the assumptions that R_E =6371 km, $R_S = R_E$+20200 km and $R_I = R_E$+450 km. The four subfigures show the results for different azimuth angles A_R from station 1 to station 2, where the magenta point in each subfigure represents the azimuth direction of station 2 with respect to station 1. We see that the IPP distance decreases significantly at low elevations when $A_S = \pm A_R$. The range of the IPP distances varies from 4.6 km to 293.3 km.

In Figure 3.13 the azimuth angle A_S from station 1 to the satellite is fixed to 0°, and the elevation angles E are 10°, 30°, 60° and 89° in the four subfigures. The relative position between station 2 and station 1 changes in each subfigure with the baseline length from 10 km to 1000 km and the azimuth angle A_R from -180° to 180°. The magenta points represent the azimuth direction of the satellite with respect to station 1. It is not difficult to see that the IPP distance generally increases with increasing baseline length. For high elevation angles of the satellite, the change of the azimuth angle for station 2 (w.r.t. station 1) does not strongly affect the IPP distances. For low elevation angles, however, the IPP distance decreases significantly when $A_R = \pm A_S$, especially when station 2 is located in exactly the opposite azimuth direction compared to the satellite, namely when $A_R = -A_S$.

This can be further verified with Figure 3.14. The IPP distance varies with the changing baseline length and the azimuth angle from station 1 to station 2 as in Figure 3.13. The elevation angle E from station 1 to the satellite is fixed to 10°, while the azimuth angles from station 1 to the satellite are 0°, 90°, 180° and 270° in the four subfigures. We see

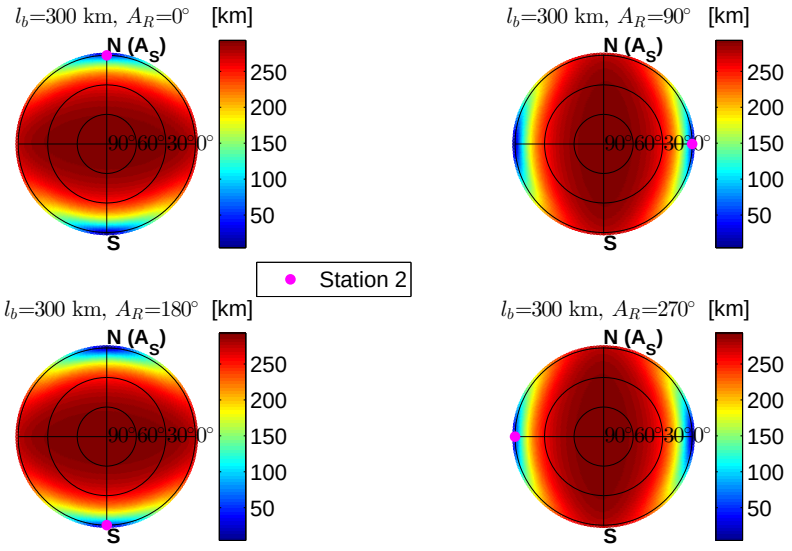

Figure 3.12: Variation of the IPP distance between $I1$ and $I2$ with respect to the elevation angle E and the azimuth angle A_S from station 1 to the satellite.

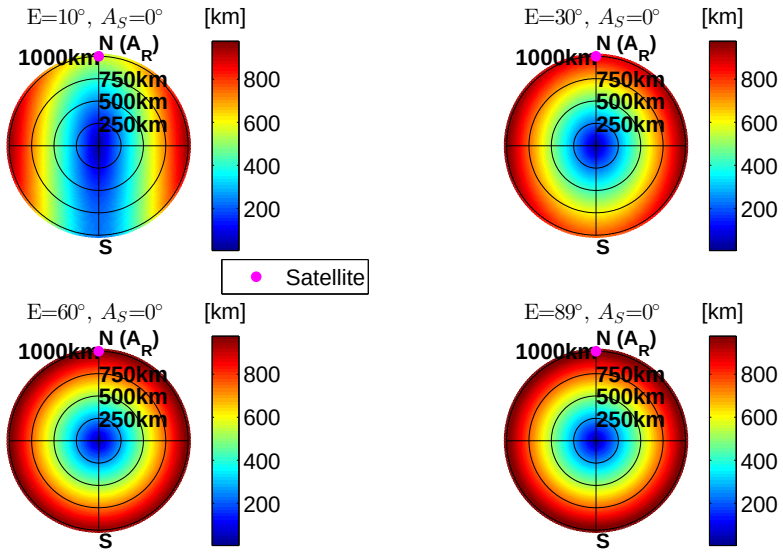

Figure 3.13: Variation of the IPP distance between $I1$ and $I2$ with respect to the baseline length l_b and the azimuth angle A_R from station 1 to station 2 at an azimuth angle of 0° from station 1 to the satellite.

that the significant decrease in the IPP distances always happens at $A_R = -A_S$, namely when the azimuth directions to station 2 and to the satellite differ by 180°.

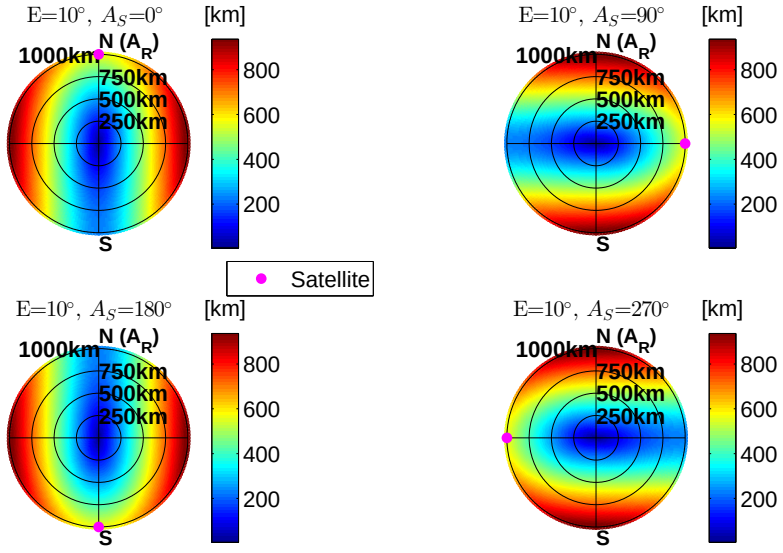

Figure 3.14: Variation of the IPP distance between $I1$ and $I2$ with respect to the baseline length l_b and the azimuth angle A_R from station 1 to station 2 at an elevation angle of 10° from station 1 to the satellite.

3.3.2 Non-ionosheric biases

The analysis of the estimated single-difference ionospheric delays and gradients is shown in Paper D in detail. Using the AGNES data from 1999 to 2013 in Switzerland, we observed a maximum differential slant and vertical ionospheric delay of 6.2 m and 2.4 m, respectively, on November 24, 2001, keeping in mind that the days with a stormy ionosphere were excluded from the vertical delays. The maximum (absolute value) slant and vertical ionospheric gradients (calculated with the IPP distance) amount to 81.2 mm/km and 33.8 mm/km, respectively, in October 2001, and over 98% of the slant and vertical gradients are within ±50 mm/km and ±20 mm/km. Calculated with the baseline length, the maximum slant gradient amounts to 42.6 mm/km on November 24, 2001.

Apart from the smoothing effect caused by using the CODE global ionosphere model and the approximated correction term in Equation 3.104, it is also worthwhile to notice that there are still non-ionospheric biases remaining in the estimated single-difference ionospheric delays. After analyzing some very short baselines (with baseline lengths shorter than 25 m) on June 16, 2013, we still observed biases remaining in the differential slant ionospheric delays at the centimeter to decimeter level. A maximal differential slant delay on this day of 12.7 cm was found for the station pair ETH2-ETHZ with a baseline length of about 13.7 m and satellite G23 (see Paper D).

Figure 3.15 (Geiger et al., 2015) shows the single-difference slant and vertical ionospheric delays for the station pair ETH2-ETHZ and satellite G23 on June 16, 2013, and the corresponding skyplot using the mean elevation and azimuth angles from the station pair to the satellite. A and B in Figure 3.15b denote the start and end points of the longer satellite arc, and the magenta point illustrates the time point, when the smallest vertical delay (see red points in Figure 3.15a) occurred. We see that the elevation-dependent variations are somewhat reduced by the mapping function when calculating the vertical delays, but the remaining patterns of both, the slant and vertical delays are still strongly elevation-dependent. Since the mean model values for this short baseline and G23 are very small (absolute value below 0.02 mm) indicating that the differential ionospheric delays of such a short baseline can almost be neglected, the patterns we see in Figure 3.15a cannot be ionospheric biases.

Figure 3.16 (Geiger et al., 2015) shows the differential slant ionospheric delays and the mean elevation angles for the station pair ETH2-ETHZ and 5 other GPS satellites. We see that elevation-dependent systematic effects can be observed in the long arcs. Multipath and remaining PCO/PCV errors might be the cause of these non-ionospheric biases.

The differential slant ionospheric delays for the station pair HOH2-HOHT with a baseline length of about 4.5 m also show a clear elevation-dependency (see Figure 3.17 from Geiger et al. (2015)). However, we see that the systematic effects of this baseline are not so obvious as those of the baseline ETH2-ETHZ. Assuming that the phase noise σ_L is equal to 0.01 cycles on L1 and L2, the noise level of the double-difference ionospheric delay on

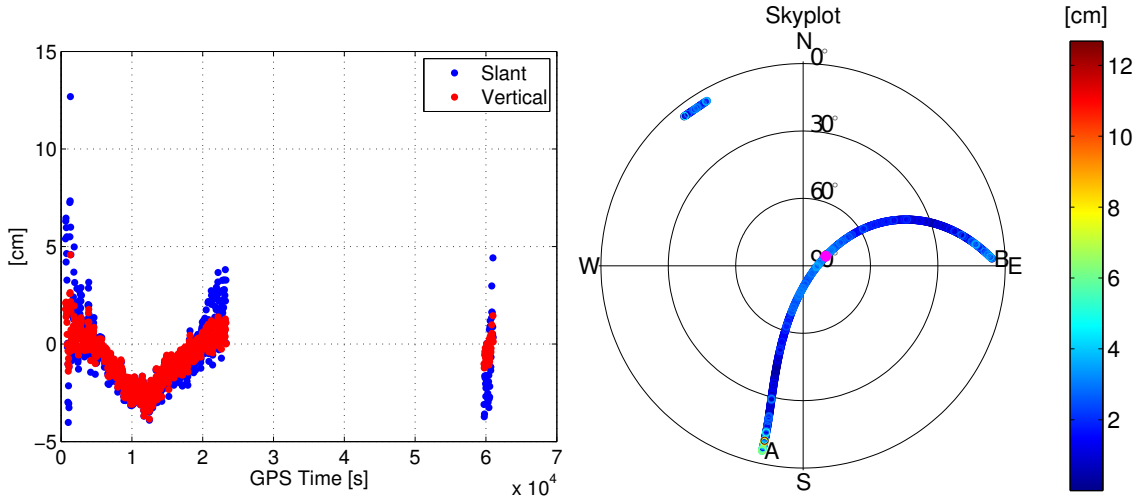

(a) Differential ionospheric delays (b) Skyplot

Figure 3.15: (a) Single-difference ionospheric delays and (b) mean elevation angles for the station pair ETH2-ETHZ and satellite G23 on June 16, 2013.

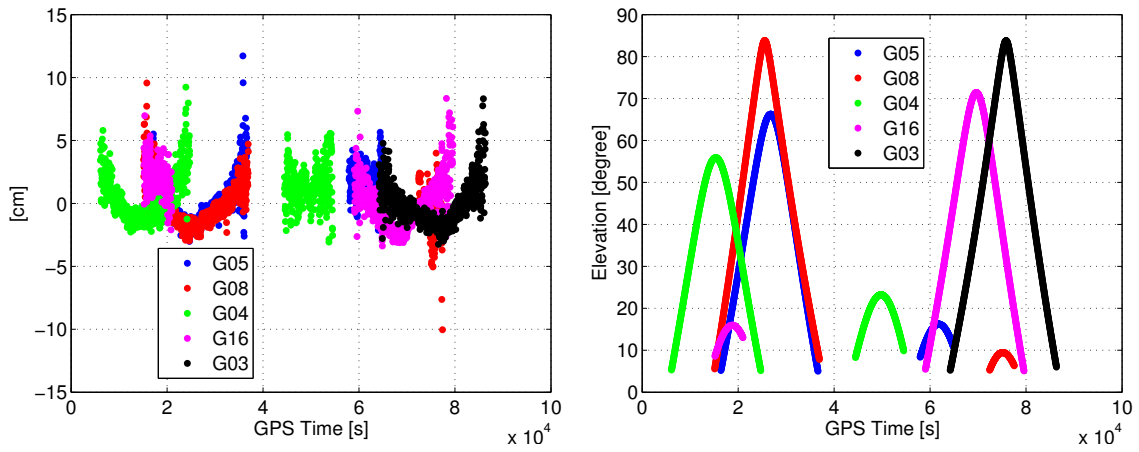

(a) Differential slant ionospheric delays (b) Elevation angle

Figure 3.16: (a) Single-difference slant ionospheric delays and (b) mean elevation angles for the station pair ETH2-ETHZ and 5 GPS satellites on June 16, 2013.

L1, σ_{I1}, which is calculated with the GF linear combination (see Equation 3.101), can be described as (Geiger et al., 2015):

$$\sigma_{I1} = \frac{2(\sqrt{(\frac{c_l}{f_1}\sigma_L)^2 + (\frac{c_l}{f_2}\sigma_L)^2}}{\frac{f_1^2}{f_2^2} - 1} = 9.6 \text{ mm} \tag{3.120}$$

The biases in Figure 3.17 are thus more likely to be explained by a superposition of noise and multipath effects.

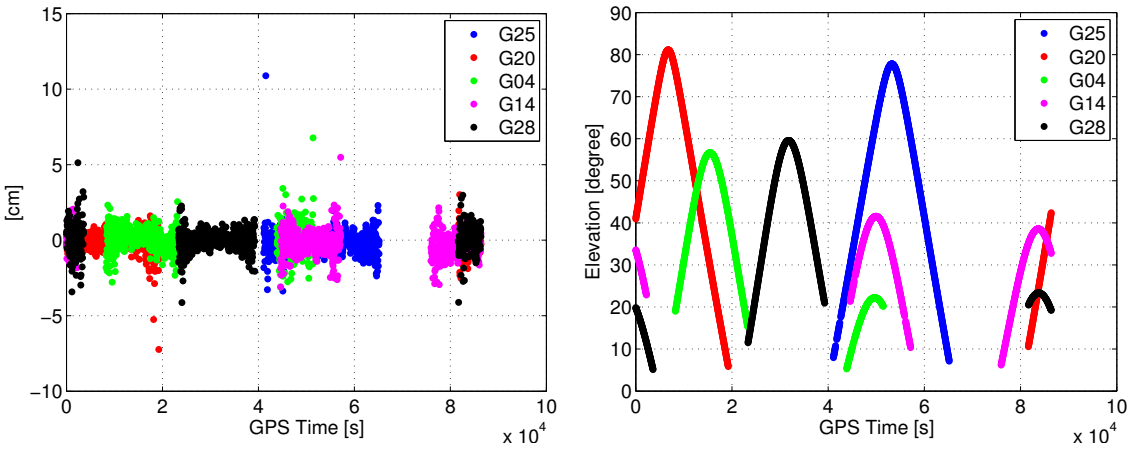

(a) Differential slant ionospheric delays

(b) Elevation angle

Figure 3.17: (a) Single-difference slant ionospheric delays and (b) mean elevation angles for the station pair HOH2-HOHT and 5 GPS satellites on June 16, 2013.

4 Summary of important results

4.1 Summary of Paper A

Paper A tries to make use of the the high stability of H-Masers that are connected to GPS receivers, and generate appropriate stochastic clock models to decooralate the receiver clock parameters and the kinematic height estimates, which are usually less accurate than the horizontal coordinates. A simple deterministic model (a linear polynomial) and relative clock constraints between subsequent (and also near-subsequent epochs) with different weights are applied to the H-Maser clock corrections with diverse stabilities. The stability of the kinematic height estimates obtained from a kinematic PPP phase solution for static receivers is taken as criterion for the improvement of the kinematic heights.

The study shows that an appropriate relative constraint for high-stability H-Masers can improve the stability of the kinematic height estimates by a factor of up to three. The best suitable relative constraint for the clocks and the corresponding improvement factor of the kinematic heights are influenced by a lot of factors such as the antenna environment, the measurement noise and the satellite geometry. However, the correlation between the clock quality and the improvement factors can also be observed. Constraining clocks with bad quality lead easily to a degradation in the kinematic height estimates. Both, experiments with real data and simulations have shown that a larger potential for improvement of the kinematic heights exists for modeling receiver clocks with better quality.

Investigations were also performed with respect to the effects of relative clock constraints on the troposphere parameters. Tests with real data have shown that an appropriate relative clock constraint for a high-stability H-Maser (z.B. $\sigma_{rel} = 2$ mm for the H-Maser at station ONSA on February 1, 2011) allows for a higher resolution of the estimated troposphere ZPD parameters (e.g. 15 minutes) and, as a result, improves the MDEV of the kinematic height estimates, while no obvious degradation of the kinematic heights is observed even when the resolution of the ZPD parameters is increased to 15 minutes. Without any clock model, in contrast, a degradation of the kinematic heights can easily be observed when estimating the ZPD parameters with a 15-minute sampling interval. As tropospheric delays may change very fast, appropriate clock constraints for high-stability receiver clocks will help to increase the resolution of the estimated troposphere parameters without degradating the kinematic heights significantly.

In order to improve the calculation efficiencies, a pre-elimination and back-substitution algorithm for epoch parameters with constraints between subsequent and near-subsequent

epochs has been developed for the least-square adjustment. This algorithm is introduced in Section 3.1 of this thesis. Investigations of the effect of relative clock constraints on other parameters in global GNSS solutions were also performed within the project "Satellite and Station Clock modelling for GNSS" funded by ESA. Paper A has only concentrated on the kinematic PPP results.

4.2 Summary of Paper B

The fast development of the GNSS in recent years has made the broadcasting signals available on more frequencies available. This gives us also more possibilities to form linear combinations with different purposes and a low noise level. Paper B concentrates on the triple-frequency GF and IF linear combinations using both, code and phase observations.

With the assumption that the code measurement noise is equal to $C_i \cdot 0.5$ m (C_i as the scaling factors of the code noise for different frequencies f_i) and that the phase noise is the same for all three frequencies (in cycles or in meters), the measurement coefficients of the linear combination with minimized code noise were formulated analytically as functions of the three carrier frequencies, the integer coefficients of the ambiguities, the scaling factors C_i and the combined frequency f_x. The minimized code noise and the relationship between the six coefficients of the linear combination are independent of the combined frequency f_x. After searching from -10 to 10 for the integer coefficients of the ambiguities, the measurement coefficients, the total combined noise (code and phase) and the theoretical success rates of the best two linear combinations were listed for different frequency triplets and scaling factors C_i.

The third GF and IF linear combination required to resolve the ambiguities on all three frequencies is a challenge, since it is difficult to find a third linear combiantion, which is linearly independent of the first two and has, at the same time, a relatively low combined noise. Therefore, we used the phase observations on the three frequencies and the ambiguity-corrected phase observations from the frist two linear combinations (Li et al. 2010). The combined noise (in cycles) was analytically formulated as a function of the carrier frequencies and the phase noise under the assumption that the phase noise on the three frequencies is the same (in cycles or in meters). For each frequency triplet, the combined noise of the third linear combination is thus not dependent of the choices of the integer coefficients anymore. However, relatively large noise amplification factors result for all the investigated frequency triplets. Biases and systematic effects, which are not considered in the model, can easily lead to huge biases in the combined measurements due to the large coefficients before the phase measurements (see Section 3.2.2).

Real data from two baselines receiving signals from the GPS Block IIF satellites and Galileo GIOVE and IOV satellites were used to test the model. Clear differences in the noise level for estimating the combined ambiguities n_x and n_y from the best two linear combinations and n_1 (resulting from the third GF and IF linear combination) can be

observed. The formal errors of the combined ambiguities n_x and n_y are mostly below the expectations, and their fractional parts are mostly within ± 0.2 cycles, while some outliers were most probably caused by the different tracking channels of the frequency triplet between two receivers. The fractional parts of the n_1 ambiguities from the third linear combination show, however, a relatively random pattern, especially for the baseline with different tracking channels.

In this thesis, the ambiguities were also estimated for geostationary BDS satellites and two very short baselines in Australia equipped with the same receiver and antenna types. The signals were observed in the same tracking channels. Compared with the "true" ambiguities obtained from the traditional dual-frequency double-difference ambiguity resolution on L1 and L2 and the resolved EWL ambiguities $n_2 - n_3$, we see that the combined ambiguities of the best two linear combinations can be resolved by rounding, while the third linear combination remains a challenge. The estimated n_1 ambiguities using the third linear combination show relatively large deviations from the "true" values, e.g., 2 to 3 cycles in some cases. These are suspected to result from the large frequency-dependent coefficients before the phase measurements, which can significantly enlarge systematic effects and biases that cannot be reduced, as in the case of white noise by increasing the number of observations.

4.3 Summary of Paper C

Paper C is an extension of the investigations introduced in Paper B. Instead of resolving the triple-frequency GF and IF ambiguities on the double-difference level, this paper tries to discuss the possibility to estimate the so-called track-to-track (different close-in-time tracks of the same receiver and the same satellite) ambiguities using the best two linear combinations for different frequency triplets. Since most of the errors, like DCBs that do not vary strongly within a certain time period (e.g. one day), are significantly reduced by forming differences between tracks for the same receiver and the same satellite, the track-to-track ambiguities are considered to be mainly influenced by the errors that lead to elevation-dependent variations in the results, like PCVs and multipath.

In the paper, tests with real data using GPS L1, L2 and L5 signals as well as Galileo E1, E5b and E5a signals are described. By comparing the fractional track-to-track ambiguities and the formal errors of these two frequency triplets, we can observe obvious differences between GPS and Galileo that are mainly caused by elevation-dependent systematic effects. In order to exclude the influences of diverse code biases, we also compared the observations differencing two phase-only IF linear combinations for each of these two frequency triplets. The elevation-dependent systematic variations are more obvious in the GPS frequency triplet. This might be caused by differences in the PCVs and PCOs for these two frequency triplets.

Although we cannot solve the track-to-track ambiguities easily on each of the three

frequencies, the combined track-to-track ambiguities of the best two triple-frequency GF and IF linear combinations are still very effective in detecting station-specific problems or problems in the observation data. Analyzing the track-to-track ambiguities using the best linear combination with Galileo E1, E5b and E5a observations, we detect that a constant offset of about 0.35-0.36 cycles in the absolute fractional parts is caused by code jumps in the raw observations of a specific type of receiver to satellite E12 in that time period. Apart from that, other station-specific problems can also be detected due to the good behaviors of the track-to-track ambiguities using the best linear combination with E1, E5b and E5a observations.

4.4 Summary of Paper D

Since the remaining ionospheric delays after forming single-differences can still be critical for a GBAS network, especially for days with extreme ionosphere conditions, the ionospheric delays and the resulting spatial gradients on the single-difference level need to be estimated and assessed for different ionosphere conditions.

Paper D introduces an algorithm to estimate single-difference ionospheric delays and gradients using double-difference phase measurements with resolved ambiguities. The estimated differential ionospheric delays are in this way free from code-related biases like DCBs and the artificial biases generated by code-smoothing. In order to extract the single-difference ionospheric delays on the double-difference level, a zero-mean condition for all the single-difference slant ionospheric delays was applied for each baseline and at each epoch. The zero-mean condition was further corrected using CODE global ionosphere maps to supply the absolute information of the ionosphere.

The differential vertical ionospheric delays were calculated using a mapping function. A correction term was calculated to reduce the deviation between the vertical delays calculated with the individual elevation angles and with the mean elevation angle. The slant and vertical ionospheric gradients were calculated by dividing the corresponding single-difference ionospheric delays by both, the baseline lengths and the IPP distances.

The estimation was performed for Switzerland using the AGNES stations from 1999 to 2013 except for several days without RINEX data. The correlations between the estimated differential slant ionospheric delays and the geomagnetic indices K_P, D_{ST}, as well as the daily mean TEC values derived from the global CODE ionosphere maps were evaluated and compared. A stronger correlation between the single-difference slant ionospheric residuals and the TEC values was observed compared to those between the differential slant ionospheric delays and the geomagnetic indices. By analyzing several very short baselines, for which the differential ionospheric delays are considered to be almost zero, we found that there are still non-ionospheric biases remaining in the estimates at the centimeter to decimeter level. Since an elevation-dependency can be observed in the non-ionospheric biases, they are suspected to be systematic effects caused by multipath or

remaining PCO/PCV errors.

The slant ionospheric gradients calculated using the baseline lengths were compared with the slant ionosphere gradient bounds of the CONUS model, which is based on the largest ionospheric gradients obtained during the analysis of the data from the U.S. Wide Area Augmentation System (WAAS) and the network of Continuously Operating Reference Stations (CORS) (Pullen et al., 2009). It should be noted that the bounds of the CONUS model also exist on the ionosphere front speed and front width that were not included in this study. In the allowed range of the CONUS model and with all possible aircraft-satellite ionosphere geometries, a vertical position error of 41 m in the worst case has occurred in the simulation and exceeds the allowed safe error limit (Pullen et al., 2009). The maximal slant gradient we observed, appeared on November 24, 2001 and amounts to 42.6 mm/km. It is below the slant ionosphere gradient bound of the CONUS model.

Based on the work of Lee et al. (2006b), the overbounding vertical gradient $\sigma_{vig}^{overbound}$ was calculated. The vertical ionospheric gradients were distributed into distance bins and normalized with the bin standard deviation and the bin mean. An inflating factor f was then calculated to bound all the non-Gaussian tails and outliers for the corresponding day and used to calculate the $\sigma_{vig}^{overbound}$ together with the bin mean and bin standard deviation. The daily maximum overbounding vertical gradients were analyzed with different bin starts. Ignoring the gradients in the first two bins (with an IPP distance shorter than 20 km), where the non-ionospheric biases still have relatively big effects and the number of IPP pairs is relatively low, about 96.9% of the $\sigma_{vig}^{overbound}$ are smaller than 4 mm/km.

In Paper D the processing of the double-difference phase measurements and the extraction of the single-difference ionospheric delays from the double-difference level using a zero-mean condition have been performed by Michael Meindl (see Acknowledgement) with the help of the Bernese GNSS Software (Version 5.2).

5 Conclusions and outlook

The fast development of the GNSS technologies in the last ten years including updates in signal structures and development of equipments has inspired a lot of new studies in the advanced modeling and the algorithms for high-precision GNSS analyses. This thesis includes investigations in a rather wide range of topics, i.e., it focuses on three important aspects of the GNSS positioning, namely receiver clocks, ambiguity resolution and ionospheric delays.

Connecting high-precision clocks with decreasing volumes, energy consumption and prices to receivers and satellite is becoming a trend in modern GNSS. With the increasing number of ground stations equipped with H-Masers and new generations of GNSS satellites, modeling the clock with meaningful deterministic and stochastic models instead of the traditional estimation of the clocks as independent epoch parameters is of great interest for many applications. This thesis includes a study of modeling the high-stability H-Maser with a simple deterministic model and relative constraints between subsequent and near-subsequent epochs, as well as the impact of such a modeling on the height estimates of kinematic PPP solutions. By changing the weights of the relative constraints, we see that the improvement of the kinematic heights differs depending on the clock quality. Although it is difficult to describe the relationship between the improvement factor, the clock quality and the relative sigmas of the clock constraints mathematically, we see that constraining the high-stability H-Masers with a relative sigma of e.g. 2 mm is generally helpful to improve the stability of the kinematic height estimates in the PPP phase solutions. In contrast, for receiver clocks with a relatively low quality, constraining the clocks may easily lead to degradations of the kinematic heights.

Apart from the kinematic heights of the receivers, station-specific and satellite-specific parameters with high temporal resolution, e.g., the radial component of the kinematic orbit solutions, may also be improved by modeling high-quality receiver or satellite clocks. With more and more ground stations and GNSS satellites equipped with H-Masers, benefit of the clock modeling for further parameters with low temporal resolution, e.g., the static receiver coordinates and the Earth rotation parameters, may also be seen in the future. In analogy to the phase measurements, modeling clocks with a lower quality should also improve the kinematic pseudorange solutions, especially under bad measurement conditions or geometries (Krawinkel and Schön, 2015; Wang et al., 2015). Compared to the high-stability H-Masers, these clocks are easier to find applications for because of their lower costs, smaller size and better mobility (Krawinkel and Schön, 2015; Wang and Rothacher, 2014).

Investigations in this area are ongoing work.

In the processing of double-difference phase measurements, ambiguity resolution is always an important part to guarantee high-precision results. The second part of this thesis introduces investigations concerning ambiguity resolution with GF and IF linear combinations using triple-frequency code and phase measurements. With the goal of minimizing the combined noise, the best two linear combinations with a relatively low combined noise level were given for different frequency triplets. The coefficients of the linear combinations and the combined noise of code and phase measurements were formulated analytically as functions of the integer coefficients of the ambiguities, the three carrier frequencies, the scaling factors of the code noise on three frequencies and the combined frequency. It was found that the relationship of the 6 coefficients for the measurements and the combined noise in cycles are independent of the combined frequency f_x under the given assumptions.

In order to find a third GF and IF linear combination, which is linearly independent of the first two linear combinations and has, at the same time, an acceptable noise level, we used only the triple-frequency phase measurements and the ambiguity-corrected phase measurements (Li et al., 2010) from the first two linear combinations. With the help of the resolved combined ambiguities n_x and n_y, the ambiguity n_1 can be estimated with a relatively large noise amplification factor in the third linear combination for each investigated frequency triplet, which is analytically formulated as functions of the three carrier frequencies. Systematic effects will also be enlarged significantly by forming the linear combination and will have a huge impact on ambiguity resolution (see Section 3.2.2).

Real data were used to test the theoretical derivations. We see acceptable fractional parts for the combined ambiguities n_x and n_y from the best two linear combinations and relatively random fractional parts n_1 from the third linear combination. Comparison of the estimated ambiguities with the "true" values from double-difference phase ambiguity resolution on L1 and L2 and the resolved EWL ambiguities $n_2 - n_3$ (see Section 3.2.1 and Section 3.2.2) using BDS satellites has further shown that the combined ambiguities n_x and n_y can successfully be resolved by rounding, while the third linear combination remains critical. Since the coefficients of the third linear combination are fixed for a certain frequency triplet based on the assumption that the phase noise on the three frequencies is the same (in cycles or in meters), the combined noise using the third linear combination that was introduced in Paper D cannot be reduced further. Alternative methods might be to reduce the systematic effects and biases before forming the linear combination or considering other algorithm to find a third GF and IF linear combination. Apart from that, phase-only IF linear combinations could be an alternative way, if the geometry part of the linear combination can be modeled with sufficient accuracy.

As an extension to the investigation of the GF and IF triple-frequency ambiguities, the triple-frequency track-to-track ambiguities are also analyzed with real data. Although unmodeled elevation-dependent errors influence the results, we still observed the benefits of this method in detecting observation problems using, e.g., the best linear combination

of the Galileo E1, E5b and E5a frequency triplet. With better knowledge of e.g. the multi-frequency PCOs and PCVs for GPS and Galileo, we may expect smaller fractional parts for the estimated track-to-track ambiguities using the best two triple-frequency linear combinations, which should deliver helpful constraint information on the observation level.

The third part of the thesis includes the investigation of the single-difference ionospheric delays and gradients for Switzerland from 1999 to 2013. Although the single-difference ionospheric delays are significantly reduced compared to the zero-difference delays, especially for short baselines, the remaining differential ionospheric delays are still of great interest for applications with high safety requirements like landing and the approach process of aircrafts, especially for ionosphere stormy days. As a result, we have analyzed the slant and vertical differential ionospheric delays and gradients using available AGNES data from 1999 to 2013 under diverse ionosphere conditions. It was found that the maximal slant ionospheric gradient (calculated with baseline length) during these 15 years in Switzerland is about 42.6 mm/km.

During the processing we have also found that there are still non-ionospheric biases remaining in the estimates. On June 16, 2013, we detected remaining biases for very short baselines (shorter than 25 m) of up to 12.7 cm. Because of the strong elevation-dependency of these biases, they are suspected to be caused by multipath or remaining PCO/PCV errors.

The algorithm using double-difference phase measurements with resolved ambiguities to extract single-difference ionospheric delays is free from the code-related biases like DCBs and brings us to a high measurement stability without artificial biases generated by code-smoothing. A fully automated processing over 15 years, which generated a huge amount of sample data and statistics, was performed with the help of the Bernese GNSS Software and Matlab. However, it should also be noticed that the absolute information of the mean slant differential ionospheric delays for each baseline per epoch relies on the global CODE ionosphere maps, which are temporally and spatially smoothed. This means that ionosphere anomalies happening during short time periods and very small areas might not be correctly considered in the epoch-wise mean values of the differential ionospheric delays. Although the ignored anomalies are reduced when dividing by the number of satellites in the corresponding epoch by generating the mean values, the influence of these unknown anomalies is still difficult to be evaluated.

In summary, a huge study potentials in all these three aspects is yet to be exploited. Further investigations using larger datasets may be performed to find the best suitable relative sigma as a function of the clock quality and the a posteriori sigma of the measurements, which reflects the measurement noise and part of the unmodelled systematic effects. Apart from that, clock constraints between near-subsequent epochs may be more deeply investigated to increase the improvement in the kinematic heights with more than one best suitable relative sigma (see Table 3.1). Furthermore, more complicated stochastic models can be considered to better model the clock noise. With the ever higher quality,

lower price and better mobility of the frequency standards connected to GNSS receivers and satellites, clocks with a higher level of stability and accuracy, e.g., optical clocks, will in future become important for many different kinds of the GNSS applications. Simplified clock models of these high-stability clocks, e.g., a linear polynomial, may then already be enough for phase-based kinematic positioning.

The triple-frequency GF and IF ambiguity resolution in this study encounters the problem of the big noise amplification factors in the third linear combination. If the GF and IF characteristic of the linear combinations are still expected to be kept, we might have to find other solutions for the third linear combination, e.g. considering more than three frequencies if available. However, phase-only IF and GB linear combinations are always a method for short baselines. Apart from that, the resolved combined ambiguity n_x and n_y may be used to constrain the relationship of the ambiguities n_1, n_2 and n_3 on the NEQ level and detect cycle slips as well as equipment problems. In the future, with the new frequency plans of different GNSS, multi-frequency linear combinations and their noise amplification factors may be dramatically changed when, e.g., C-Band signals, are sent by the GNSS satellites. In addition to that, with the increasing number of satellites sending signals with higher accuracy for the pseudorange measurements, e.g., the Galileo's E5 signal with the Alternative Binary Offset Carrier (AltBOC) modulation, code-based precise positioning will also be of great interest in the future.

The algorithm introduced in this thesis, which was used to estimate the single-difference ionospheric delays and gradients, has both advantages and disadvantages. Since the remaining non-ionospheric biases are highly elevation-dependent and are still relatively big, further studies to access these biases will certainly be addressed in the future. Apart from that, the smoothing effect of the usage of the global CODE ionosphere maps should be evaluated in more details. Extracting absolute information of the ionosphere from other sources, which can avoid the code-related biases and at the same time deliver absolute ionosphere information with higher resolution, is of high interest. Furthermore, the algorithm still awaits improvement to compromise between the elimination of low-quality data in the phase pre-processing with, e.g., data gaps or multipath at low elevation angles, and the retaining of the data with possible huge epoch-to-epoch ionospheric jumps.

Bibliography

AGNES data (2014) AGNES data, Federal Office of Topography swisstopo, AGNES, 2014. http://www.swisstopo.admin.ch/internet/swisstopo/en/home/topics/survey/permnet/agnes.html.

Allan D. W. (1987) Time and frequency (time-domain) characterization, estimation, and prediction of precision clocks and oscillators, IEEE Transactions on Ultrasonics, Ferroelectrics, and Frequency Control 34(6): 647-654. doi:10.1109/T-UFFC.1987.26997.

Allan D.W., Barnes J.A. (1981) A modified "Allan variance" with increased oscillator characterization ability, Proc. 35th Annual Freq. Control Symp.: 470-475, Philadelphia, PA, US, May 27-29, 1981. doi:10.1109/FREQ.1981.200514.

Arianespace Service & Solutions (2014) Galileo satellites experience orbital injection anomaly on Soyuz launch: Initial report, Press Release, arianespace service & solutions, Kourou, August 23, 2014. http://www.arianespace.com/news-press-release/2014/8-23-2014.asp.

BBC News (2012) China's Beidou GPS-substitute opens to public in Asia, BBC News, Technology, December 27, 2012. http://www.bbc.com/news/technology-20852150.

Bock H., Dach R., Jäggi A., Beutler G. (2009) High-rate GPS clock corrections from CODE: support of 1 Hz applications, J. Geodesy 83(11): 1083-1094. doi:10.1007/s00190-009-0326-1.

Boehm J., Werl B., Schuh H. (2006) Troposphere mapping functions for GPS and very long baseline interferometry from European Centre for Medium-Range Weather Forecasts operational analysis data, J. Geophys. Res. 111(B2): B02406. doi:10.1029/2005JB003629.

Choi B.K., Cho J.H., Lee S.J. (2011) Estimation and analysis of GPS receiver differential code biases using KGN in Korean Peninsula, Adv. Space Res. 47(9): 1590-1599. doi:10.1016/j.asr.2010.12.021.

CLKLOG (2012) A summary file of the deployment history for GPS receiver, antenna, frequency standards, and other equipment at IGS stations. ftp://igscb.jpl.nasa.gov/igscb/station/general/loghist.txt.

Cocard M., Bourgon S., Kamali O., Collins P. (2008) A systematic investigation of optimal

carrier-phase combinations for modernized triple-frequency GPS, J. Geodesy 82(9): 555-564. doi:10.1007/s00190-007-0201-x.

CODE MGEX orbit solution (2013) CODE MGEX orbit solution. `ftp://cddis.gsfc.nasa.gov/pub/gps/products/mgex/1720/`.

CODE products (2014) CODE products in 2014. `ftp://ftp.unibe.ch/aiub/CODE/`.

Dach R., Beutler G., Hugentobler U., Schaer S., Schildknecht T., Springer T., Dudle G., Prost L. (2003) Time transfer using GPS carrier phase: error propagation and results, J. Geodesy 77(1): 1-14. doi:10.1007/s00190-002-0296-z.

Dach R., Brockmann E., Schaer S., Beutler G., Meindl M., Prange L., Bock H., Jäggi A., Ostini L. (2009) GNSS processing at CODE: status report, J. Geodesy 83(3-4): 353-365. doi:10.1007/s00190-008-0281-2.

Dach R., Hugentobler U., Fridez P., Meindl M. (2007) Bernese GPS Software Version 5.0, Astronomical Institute, University of Bern.

Dow J.M., Neilan R.E., Rizos C. (2009) The International GNSS Service in a changing landscape of Global Navigation Satellite Systems, J. Geodesy 83(3-4): 191-198. doi: 10.1007/s00190-008-0300-3.

Dst Index (2014) Plot and data output of Dst and AE indices (Hourly Values), 2014. `http://wdc.kugi.kyoto-u.ac.jp/dstae/index.html`.

Dupuis R.T., Lynch T.J., Vaccaro J.R., Watts E.T. (2010) Rubidium Frequency Standard for the GPS IIF Program and Modifications for the RAFSMOD Program, in Proceedings of the 23rd International Technical Meeting of The Satellite Division of the Institute of Navigation (ION GNSS 2010), Portland, OR, US, September 21-24, 2010, pp. 781-788.

Ene A., Qiu D., Luo M., Pullen S., Enge, P. (2005) A comprehensive ionosphere storm data analysis method to support LAAS threat model development, in Proceedings of the 2005 National Technical Meeting of The Institute of Navigation, San Diego, CA, US, January 24-26, 2005, pp. 110-130.

ESA (2005) First Galileo Satellite on Orbit to Demonstrate Key Technologies, First Galileo Launch, European Space Agency, December 28, 2005. `http://www.esa.int/Our_Activities/Navigation/The_future_-_Galileo/First_Galileo_Launch/First_Galileo_satellite_on_orbit_to_demonstrate_key_technologies`.

ESA (2008) ESA's most Advanced Navigation Satellite Launched, Galileo launch – GIOVE-B, European Space Agency, April 27, 2008. `http://www.esa.int/Our_Activities/Navigation/The_future_-_Galileo/GIOVE-B_launch/ESA_s_most_advanced_navigation_satellite_launched`.

ESA (2012a) Mission Accomplished for Galileo's Pathfinder GIOVE-A, Navigation, Eu-

ropean Space Agency, July 3, 2012. http://www.esa.int/Our_Activities/Navigation/Mission_accomplished_for_Galileo_s_pathfinder_GIOVE-A.

ESA (2012b) Mission Accomplished, GIOVE-B heads into deserved retirement, Navigation, European Space Agency, July 24, 2012. http://www.esa.int/Our_Activities/Navigation/Mission_accomplished_GIOVE-B_heads_into_deserved_retirement.

ESA (2013) Galileo fixes Europe's Position in History, Navigation, European Space Agency, March 12, 2013. http://www.esa.int/Our_Activities/Navigation/Galileo_fixes_Europe_s_position_in_history.

ESA (2014a) Galileo: A constellation of 30 Navigation Satellites, Galileo Navigation, European Space Agency, June 27, 2014. http://www.esa.int/Our_Activities/Navigation/The_future_-_Galileo/Galileo_a_constellation_of_30_navigation_satellites.

ESA (2014b) Galileo satellite recovered and transmitting navigation signals, Navigation, European Space Agency, December 3, 2014. http://www.esa.int/Our_Activities/Navigation/Galileo_satellite_recovered_and_transmitting_navigation_signals.

ESA (2015) Sixth Galileo satellite reaches corrected orbit, Launching Galileo, European Space Agency, March 13, 2015. http://www.esa.int/Our_Activities/Navigation/The_future_-_Galileo/Launching_Galileo/Sixth_Galileo_satellite_reaches_corrected_orbit.

Feng Y. (2008) GNSS three carrier ambiguity resolution using ionosphere-reduced virtual signals, J. Geodesy 82(12): 847-862. doi:10.1007/s00190-008-0209-x.

Feng Y., Rizos C., Higgings M. (2007) Multiple Carrier Ambiguity Resolution and Performance Benefits for RTK and PPP Positioning Services in Regional Areas, in Proceedings of the 20th International Technical Meeting of the Satellite Division of The Institute of Navigation (ION GNSS 2007), Fort Worth, TX, US, September 25-28, 2007, pp. 668-678.

Final GNSS products (2013) Final GNSS products. ftp://cddis.gsfc.nasa.gov/pub/gps/products/1720/.

Fritsche M., Sośnica K., Rodríguez-Solano C.J., Steigenberger P., Wang K., Dietrich R., Dach R., Hugentobler U., Rothacher M. (2014): Homogeneous reprocessing of GPS, GLONASS and SLR observations, J. Geodesy 88(7): 625-642. doi:10.1007/s00190-014-0710-3.

Galileo Constellation (2015): Constellation Information, 06.10.2015, European GNSS Service Centre. http://www.gsc-europa.eu/system-status/Constellation-Information.

Galileo Overview (2015): Overview of the Satellites in the Galileo Constellation,

09.10.2015, International GNSS Service. http://igs.org/mgex/status-GAL#Characteristics.

Gao Y., Liu Z.Z. (2002): Precise Ionosphere Modeling using Regional GPS Network Data, Journal of Global Positioning Systems 1(1): 18-24. doi:10.5081/jgps.1.1.18.

Ge M., Gendt G., Dick G., Zhang F.P., Rothacher M. (2006) A new data processing strategy for huge GNSS global networks, J. Geodesy 80(4): 199-203. doi:10.1007/s00190-006-0044-x.

Geiger A., Wang K., Meindl M., Rothacher M., Scaramuzza M., Troller M., Truffer P. (2015) Non-ionosphere biases in the single-difference ionospheric residuals, European Navigation Conference 2015, Bordeaux, France, April 7-10, 2015.

Geng J., Bock Y. (2013) Triple-frequency GPS precise point positioning with rapid ambiguity resolution, J. Geodesy 87(5): 449-460. doi:10.1007/s00190-013-0619-2.

Geng J., Teferle F.N., Meng X., Dodson A.H. (2010) Kinematic precise point positioning at remote marine platforms, GPS Solut. 14(4): 343-350. doi:10.1007/s10291-009-0157-9.

GLONASS constellation status (2015) GLONASS constellation status, 14.10.2015, Federal Space Agency, Information-Analytical Centre. https://glonass-iac.ru/en/GLONASS/.

GPS.gov (2014) New Civil Signals, GPS.GOV, Official U.S. Government information about the Global Positioning System (GPS) and related topics, National Coordination Office for Space-Based Positioning, Navigation, and Timing. http://www.gps.gov/systems/gps/modernization/civilsignals/.

Groves P.D. (2013) Principles of GNSS, Inertial, and Multisensor Integrated Navigation Systems, Second Edition, GNSS Technology and Applications Series, Artech House, ISBN-13: 978-1-60807-005-3.

Gruss M. (2015) Launch of First GPS 3 Satellite Now Not Expected Until 2017, SpaceNews, February 24, 2015. http://spacenews.com/launch-of-first-gps-3-satellite-now-not-expected-until-2017/.

Gunter (2015) Spacecraft: Navigation - Europe, Gunter's Space Page. http://space.skyrocket.de/directories/sat_nav_eur.htm.

Gurtner W. (2007) RINEX: The Receiver Independent Exchange Format Version 3.00, November 28, 2007. http://epic.awi.de/29985/1/Gur2007a.pdf.

Gurtner W., Estey L. (2009) RINEX: The Receiver Independent Exchange Format Version 3.01, June 22, 2009. http://igscb.jpl.nasa.gov/igscb/data/format/rinex301.pdf.

Hatch R.R. (2006) A New Three-Frequency, Geometry-Free, Technique for Ambiguity Resolution, in Proceedings of the 19th International Technical Meeting of the Satel-

lite Division of The Institute of Navigation (ION GNSS 2006), Fort Worth, TX, US, September 26-29, 2006, pp. 309-316.

Henkel P., Günther C. (2010) Reliable Integer Ambiguity Resolution with Multi-Frequency Code Carrier Linear Combinations, Journal of Global Positioning Systems 9(2): 90-103. doi:10.5081/jgps.9.2.90.

Henkel P., Günther C. (2012) Reliable Integer Ambiguity Resolution: Multi-Frequency Code Carrier Linear Combinations and Statistical A Priori Knowledge of Attitude, Nav., J. Ins. Nav., 59(1): 61-75, Spring 2012. doi:10.1002/navi.6.

Hernández-Pajares M., Juan J.M., Sanz J., Aragon-Angel A., Ramos-Bosch P., Odijk D., de Bakker P.F., van der Marel H., Verhagen S., Fernández-Hernández I., Toledo M., Samson J. (2008) Feasibility Study of a European Wide Area Real Time Kinematic System, Proc. NAVITEC 2008, Noordwijk, the Netherlands, December 2008.

Hugentobler U. (2004) CODE high rate clocks, IGS Mail No. 4913, IGS Central Bureau Information System. `https://igscb.jpl.nasa.gov/mail/igsmail/2004/msg00136.html`.

ICAO (1996) ICAO Annex 10, International Standards and Recommended Practices, Aeronautical Telecommunications, ANNEX 10 to the Convention on International Civil Aviation, Volume I (Radio Navigation Aids), July 1996.

IGS site log (2014) Summary file of the site logs of the IGS stations, September 3, 2014. `ftp://igscb.jpl.nasa.gov/igscb/station/general/loghist.txt`.

Januszewski J. (2011) Satellite Navigation Systems, Data Messages, Data Transfer and Formats, Modern Transport Telematics: 11th Int. Conf. on Trnsp. Sys. Tel., TST 2011, Katowice-Ustroń, Poland, October 19-22, 2011, pp. 338-345. doi:10.1007/978-3-642-24660-9_39.

Jäggi A., Prange L., Hugentobler U. (2011) Impact of covariance information of kinematic positions on orbit reconstruction and gravity field recovery, Adv. Space Res. 47(9): 1472-1479. doi:10.1016/j.asr.2010.12.009.

Jewell D. (2014) Latest Words from the Acquisition Guru of the World's Gold Standard for PNT, GPS World, September 1, 2014. `http://gpsworld.com/latest-words-from-the-acquisition-guru-of-the-worlds-gold-standard-for-pnt/`.

Kim M., Lee J., Pullen S., Gillespie J. (2013) Optimized GNSS network station selection to support the development of ionospheric threat models for GBAS, in Proceedings of the 2013 International Technical Meeting of The Institute of Navigation, San Diego, CA, US, January 2013, pp. 559-570.

Klobuchar J.A. (1996) Ionosphere Effects on GPS, Global Positioning System: Theory and Applications, Vol. 1, pp. 485-515, 1996.

Kp Index (2014) Geomagnetic Kp and Ap Indices, 2014. `ftp://ftp.ngdc.noaa.gov/STP/GEOMAGNETIC_DATA/INDICES/KP_AP/`.

Krawinkel T., Schön S. (2015) Benefits of receiver clock modeling in code-based GNSS navigation, GPS Solut, published online. doi:10.1007/s10291-015-0480-2.

Lee J., Luo M., Pullen S., Park Y.S., Enge P., Brenner M. (2006a) Position-domain geometry screening to maximize LAAS availability in the presence of ionosphere anomalies, in Proceedings of the 19th International Technical Meeting of the Satellite Division of The Institute of Navigation (ION GNSS 2006), Fort Worth, TX, US, September 26-29, 2006, pp. 393-408.

Lee J., Pullen S., Datta-Barua S., Enge P. (2006b) Assessment of Nominal Ionosphere Spatial Decorrelation for LAAS, Position, Location, and Navigation Symposium, 2006 IEEE/ION, San Diego, CA, US, April 25-27, 2006, pp. 506-514. doi:10.1109/PLANS.2006.1650638.

Lee J., Seo J., Park Y.S., Pullen S., Enge P. (2011) Ionosphere threat mitigation by geometry screening in ground-based augmentation systems, Journal of Aircraft 48(4): 1422-1433, July-August 2011. doi:10.2514/1.C031309.

Li B., Feng Y., Shen Y. (2010) Three carrier ambiguity resolution: distance-independent performace demonstrated using semi-generated triple frequency GPS signals, GPS Solut. 14(2): 177-184. doi:10.1007/s10291-009-0131-6.

Li B., Shen Y., Zhang X. (2013) Three frequency GNSS navigation prospect demonstrated with semi-simulated data, Adv. Space Res. 51(7): 1175-1185. doi:10.1016/j.asr.2012.10.031.

Li J., Yang Y., Xu J., He H., Guo H. (2012) Ionosphere-Free Combinations for Triple-Frequency GNSS with Application in Rapid Ambiguity Resolution over Medium-Long Baselines, in Proceedings of China Satellite Navigation Conference (CSNC) 2012, Vol. 160, Guangzhou, China, 2012, pp. 173-187. doi:10.1007/978-3-642-29175-3_16.

Lichten S.M., Border J.S. (1987) Strategies for high-precision global positioning system orbit determination, J. Geophys. Res. 92(B12): 12751-12762. doi:10.1029/JB092iB12p12751.

Liu J., Gu D., Ju B., Yao J., Duan X., Yi D. (2014) Basic performance of BeiDou-2 navigation satellite system used in LEO satellites precise orbit determination, Chinese Journal of Aeronautics 27(5): 1251-1258. doi:10.1016/j.cja.2014.03.006.

Lollock R. (2013) Update on GPS and thoughts on its future, Stanford's 2013 PNT Challenges and Opportunities Symposium, November 2013.

Mallette L.A., Rochat P., White J. (2006) Historical Review of Atomic Frequency Standards used in Space Systems – 10 Year Update, 38th Annual Precise Time and Time Interval (PTTI) Meeting, Washington, DC, US, December 7-9, 2006.

Marquis W., Shaw M. (2011) GPS III - Bringing New Capabilities to the Global Community, InsideGNSS 6(5): 34-48, September/October 2011.

Mayer C., Belabbas B., Dunkel W. (2009) Ionospheric threat model assessment, ICAO NSP Meeting, Bretigny, France, March 17-20, 2009.

Mayer C., Jakowski N., Borries C., Pannowitsch T., Belabbas B. (2008) Extreme ionospheric conditions over Europe observed during the last solar cycle, 4th ESA Workshop on Satellite Navigation User Equipment Technologies, ESTEC, Noordwijk, the Netherlands, December 10-12, 2008.

Männel B., Rothacher M. (2016) Ionospheric corrections for single-frequency tracking of GNSS satellites by VLBI based on co-located GNSS, J. Geodesy 90(2): 189-203. doi: 10.1007/s00190-015-0865-6.

Melbourne W.G. (1985) The Case for Ranging in GPS Based Geodetic Systems, in Proceedings of the 1st International Symposium on Precise Positioning with the Global Positioning System, pp. 373-386, Rockville, MD, US, April 15-19, 1985.

MGEX (2014) Introduction of MGEX, IGS. `http://igs.org/mgex/`.

Montenbruck O., Steigenberger P., Schönemann E., Hauschild A., Hugentobler U., Dach R., Becker M. (2012) Flight Characterization of New Generation GNSS Satellite Clocks, Nav., J. Ins. Nav., 59(4): 291-302, Winter 2012. doi:10.1002/navi.22.

NASA (2015) National Space Science Data Coordinated Archive, National Aeronautics and Space Administration. `http://nssdc.gsfc.nasa.gov/`.

Navigation Center (2015) GPS Constellation Status for 14/10/2015, Navigation Center, U.S. Department of Homeland Security, United States Coast Guard. `http://www.navcen.uscg.gov/?Do=constellationstatus`.

NAVSAS Group (2012) Contact! First Acquisition and Tracking of IOV Galileo Signals, Inside GNSS 7(1): 46-55, ISSN:1559-503X, January/February 2012.

Noll C., Bock Y., Habrich H., Moore A. (2009) Development of data infrastructure to support scientific analysis for the International GNSS Service, J. Geodesy 83(3-4): 309-325. doi:10.1007/s00190-008-0245-6.

Orliac E., Dach R., Wang K., Rothacher M., Voithenleitner D., Hugentobler U., Heinze

M., Svehla D. (2012) Deterministic and Stochastic Receiver Clock Modeling in Precise Point Positioning, EGU General Assembly 2012, Vienna, Austria, April 22-27, 2012, pp. 7199.

Pullen S., Enge P. (2007) An overview of GBAS integrity monitoring with a focus on ionospheric spatial anomalies, Indian Journal of Radio & Space Physics 36(4): 249-260, August 2007.

Pullen S., Park Y.S., Enge P. (2009) Impact and mitigation of ionospheric anomalies on ground-based augmentation of GNSS, Radio Science 44(1), RS0A21. doi:10.1029/2008RS004084.

Ray J., Gurtner W. (2010) RINEX Extensions to Handle Clock Information, September 2, 2010. `http://igscb.jpl.nasa.gov/igscb/data/format/rinex_clock302.txt`.

Ray J., Senior K. (2003) IGS/BIPM pilot project: GPS carrier phase for time/frequency transfer and timescale formation, Metrologia 40(3): 270-288. doi:10.1088/0026-1394/40/3/307.

Raziq N., El-Mowafy A., Teunissen P.J.G., Nardo A., van der Marel H. (2012) Curtin and Delft Multi-GNSS M-GEX Stations: Infrastructure and Analysis Tools, IGS Workshop, Olsztyn, Poland, July 23-27, 2012.

Rich B., Schmidt P. (2004) Schaum's Outline of Elementary Algebra, Third Edition, ISBN:007141083X, McGraw-Hill, 2004.

Riley W.J. (2008) Handbook of Frequency Stability Analysis, NIST Special Publication 1065, July 2008.

RINEX (2013) RINEX, The Receiver Independent Exchange Format, Version 3.02, International GNSS Service (IGS), RINEX Working Group and Radio Technical Commission for Maritime Services Special Committee 104 (RTCM-SC104), April 3, 2013. `http://igscb.jpl.nasa.gov/igscb/data/format/rinex302.pdf`.

Rothacher M. (2001) Comparison of absolute and relative antenna phase center variations, GPS Solut. 4(4): 55-60. doi:10.1007/PL00012867.

Rothacher M. (2015) Lecture notes, Space Geodesy, Institute of Geodesy and Photogrammetry, ETH Zurich, September 2015.

Rothacher M., Beutler G. (1998) The Role of GPS in the Study of Global Change, Physics and Chemistry of the Earth 23(9-10): 1029-1040. doi:10.1016/S0079-1946(98)00143-8.

Senior K., Koppang P., Ray J. (2003) Developing an IGS time scale, IEEE Transactions on Ultrasonics, Ferroelectrics, and Frequency Control 50(6): 585-593. doi:10.1109/TUFFC.2003.1209545.

Steigenberger P., Hackel S., Hugentobler U., Montenbruck O. (2013) One year of Galileo IOV orbit and clock determination, European Geosciences Union (EGU) General Assembly, Vienna, Austria, April 7-12, 2013.

Svehla D., Schönemann E., Escobar D., Springer T. (2010) Complete Relativistic Modelling of the GIOVE-B clock parameters and its impact on POD, track-to-track ambiguity resolution and precise timing, IGS workshop, Newcastle upon Tyne, England, June 28 - July 2, 2010.

Testoyedov N. (2015) Space Navigation in Russia: History of Development, United Nations/Russian Federation Workshop on the Applications of Global Navigation Satellite Systems, Krasnoyarsk, Russia, May 18-22, 2015.

TLE (2012) Two Line Element Set for Galileo satellites. `http://www.celestrak.com/NORAD/elements/galileo.txt`.

Urlichich Y., Subbotin V., Stupak G., Dvorkin V., Povalyaev A., Karutin S., Bakitko R. (2011) GLONASS Modernization, GPS World, November 1, 2011. `http://gpsworld.com/glonass-modernization-12232/`.

USNO (2012) Block II Satellite Information, United States NAVAL Observatory (USNO). `ftp://tycho.usno.navy.mil/pub/gps/gpsb2.txt`.

Villiger A. (2014) Improvement of the Kinematic Model of Switzerland (Swiss 4D II), Dissertation, ETH Zurich, Diss ETH No. 21866, 2014.

Wang Z., Liu J., Zhang K. (2004) Multiple Carrier Ambiguity Resolution Method For Galileo, Proc. 2004 Int. Symp. GNSS/GPS, Sydney, Australia, December 6-8, 2004.

Wang K., Meindl M., Stehlin X., Gendre E., Rothacher M., Rochat P. (2015) Deterministic and stochastic modeling of low-cost clocks in pseudo-range kinematic positioning, the 26th General Assembly of the International Union of Geodesy and Geophysics, Prague, Czech Republic, June 22 - July 2, 2015.

Wang K., Rothacher M. (2011) GNSS Clock Modelling and Estimation, Swiss National Report on the Geodetic Activities in the years 2007 to 2011, Presented to the XXV General Assembly of the International Union of Geodesy and Geophysics in Melbourne, Australia, June/July 2011, pp. 30-33.

Wang K., Rothacher M. (2013) Ambiguity resolution for triple-frequency geometry-free and ionosphere-free combination tested with real data, J. Geodesy 87(6): 539-553. doi: 10.1007/s00190-013-0630-7.

Wang K., Rothacher M. (2014): Modeling of Low-Stability GPS Receiver Clocks and its Impact on Pseudo-Range Kinematic Coordinates, European Frequency and Time Forum 2014, Neuchâtel, Switzerland, June 23-26, 2014.

Wang K., Rothacher M. (2015) Triple-frequency ambiguity resolution, Swiss National Report on the Geodetic Activities in the years 2011 to 2015, Presented to the XXVI General Assembly of the International Union of Geodesy and Geophysics in Melbourne, Australia, June/July 2015, pp. 226-227.

Weber R. (2012) IGS M-GEX - The IGS Multi-GNSS Global Experiment, Wksp on GNSS Biases, Bern, Switzerland, January 18-19, 2012. `http://www.biasws2012.unibe.ch/pdf/bws12_2.3.5.pdf`.

Weinbach U., Schön S. (2009) Evaluation of the clock stability of geodetic GPS receivers connected to an external oscillator, in Proceedings of the 22nd International Technical Meeting of The Satellite Division of the Institute of Navigation (ION GNSS 2009), Savannah, GA, US, September 22-25, 2009.

Weinbach U., Schön S. (2011) GNSS receiver clock modeling when using high-precision oscillators and its impact on PPP, Adv. Space Res. 47(2): 229-238. doi:10.1016/j.asr.2010.06.031.

Wübbena G. (1985) Software Developments for Geodetic Positioning with GPS Using TI 4100 Code and Carrier Measurements, in Proceedings First International Symposium on Precise Positioning with the Global Positioning System, pp. 403-412, Rockville, MD, US, April 15-19, 1985.

Zumberge J.F., Heflin M.B., Jefferson D.C., Watkins M.M., Webb F.H. (1997) Precise point positioning for the efficient and robust analysis of GPS data from large networks, J. Geophys. Res. 102(B3): 5005-5017. doi:10.1029/96JB03860.

Abbreviations

ADEV	Allan Deviation
AGNES	Automated GNSS Network for Switzerland
AIUB	Astronomical Institute, University of Bern
AltBOC	Alternative Binary Offset Carrier
BDS	Beidou Navigation Satellite System
CDMA	Code Division Multiple Access
CET	Central European Time
CODE	Center for Orbit Determination in Europe
CONUS	Conterminous United States
CORS	Continuously Operating Reference Stations
CRB	Cramer Rao bounds
CSNC	China Satellite Navigation Conference
CSSI	Center for Space Standards and Innovation
DCB	Differential Code Bias
DFG	German Research Foundation (Deutsche Forschungsgemeinschaft)
DLR	German Aerospace Center (Deutsches Zentrum für Luft- und Raumfahrt)
DOP	Dilution of Precision
EGU	European Geosciences Union
ERP	Earth rotation parameters
ESA	European Space Agency
ESOC	European Space Operations Centre
ESTEC	European Space Research and Technology Centre
EU	European Union
EWL	Extra-Widelane
FD	Frequency Drift
FFN	Flicker Frequency Noise
FM	Flight Model
FOC	Full Operational Capability
FPN	Flicker Phase Noise
GB	Geometry-Based
GBAS	Ground Based Augmentation System
GEO	Geostationary Earth Orbit
GF	Geometry-Free
GFZ	Deutsches GeoForschungsZentrum

GIOVE	Galileo In-Orbit Validation Element
GLONASS	Globalnaya Navigatsionnaya Sputnikovaya Sistema
GNSS	Global Positioning Satellite System
GPS	Global Positioning System
GPST	GPS Time
GSOC	German Space Operations Center
H-Maser	Hydrogen-Maser
IAPG	Institute for Astronomical and Physical Geodesy
IF	Ionosphere-Free
IGS	International GNSS Service
IGSO	Inclined Geosynchronous Orbit
IGST	IGS Time Scale
IOV	In-Orbit Validation
IPP	Ionosphere Pierce-Point
IRNSS	Indian Regional Navigation Satellite System
JPL	Jet Propulsion Laboratory
MDEV	Modified Allan Deviation
MEO	Medium Earth Orbit
MGEX	Multi-GNSS Experiment
MW	Melbourne-Wübbena
NEQ	Normal Equation
NEU	North, East and Up
O-C	Observed-Minus-Computed
PCC	Phase Center Correction
PCO	Phase Center Offset
PCV	Phase Center Variation
PDF	Probability Density Function
PFM	ProtoFlight Model
PHM	Passive Hydrogen Maser
PPP	Precise Point Positioning
PTTI	Precise Time and Time Interval
PZO	Phasenzentrumsoffset
PZV	Phasenzentrumsvariation
QZSS	Quasi-Zenith Satellite System
RINEX	Receiver Independent Exchange Format
RMS	Root Mean Square
RTCM-SC	Radio Technical Commission for Maritime Services Special Committe
RWFN	Random Walk Frequency Noise
SBAS	Satellite Based Augmentation System
SLR	Satellite Laser Ranging
SNSF	Swiss National Science Foundation

SV	Space Vehicle
TEC	Total Electron Content
TECU	Total Electron Content Unit
TLE	Two Line Element Set
TUM	Technical University of Munich / Technische Universität München
US	United States
VMF1	Vienna Mapping functions 1
WAAS	Wide Area Augmentation System
WARTK	Wide Area Real Time Kinematics
WFN	White Frequency Noise
WPN	White Phase Noise
ZPD	Zenith Path Delay

Appendix: Papers

A Paper A

Paper A was originally published as

Wang K., Rothacher M. (2013): Stochastic modeling of high-stability ground clocks in GPS analysis, Journal of Geodesy 87(5): 427-437. doi:10.1007/s00190-013-0616-5.

The final publication is available at `http://link.springer.com`.

Stochastic modeling of high-stability ground clocks in GPS analysis

K. Wang[a], M. Rothacher[a]

[a]Institute of Geodesy and Photogrammetry, ETH Zurich, Robert-Gnehm-Weg 15, 8093 Zurich, Switzerland

Abstract

In current global positioning system (GPS) applications, receiver clocks are typically estimated epoch-wise in the data analyses even for clocks with high performance like Hydrogen-masers (H-maser). Applying an appropriate clock model for high-stability receiver clocks should, in view of the strong correlation between the station height and the clock parameters, significantly improve the positioning results. Recent experiments have shown that modeling the deterministic behavior of high-quality receiver clocks can improve the kinematic precise point positioning considerably. In this paper, well-behaving ground clocks are studied in detail applying constraints between subsequent and near-subsequent clock parameters. The influence of different weights for these relative clock constraints on the positioning quality, especially on the height, is investigated. For excellent clocks, an improvement of up to a factor of 3 can be obtained for the repeatability of the kinematic height estimates. This may be essential to detect small but sudden changes in the vertical component (e.g., caused by earthquakes). Troposphere zenith path delays (ZPD) are also heavily correlated with the receiver clock estimates and station heights. All these parameters are usually estimated simultaneously. We show that the use of relative clock constraints allows for a higher time resolution of the ZPD estimates (smaller than 2 h) without compromising the quality of the kinematic height estimates.

Keywords: Stochastic clock model; GPS Kinematic PPP; High-performance atomic clock; Troposphere

Introduction

In the present-day analyses of global navigation satellite system (GNSS) data, the receiver clocks and satellite clocks are typically estimated as independent parameters for each

measurement epoch in the least-squares adjustment. The resulting large number of clock parameters are strongly correlated with troposphere Zenith Path Delays (ZPD) parameters and the station height (Dach et al., 2003; Rothacher and Beutler, 1998). It can be expected that, if the quality of the high-performance receiver clocks could be fully exploited with an appropriate deterministic and stochastic model, the solutions of other parameters, especially the kinematic station height estimates, should become more stable and more accurate because of the strong correlation between the clock parameters and the station height.

The idea of a detailed stochastic modeling of receiver and satellite clocks is not really new. During the 1980s, colleagues at Jet Propulsion Laboratory (JPL) modeled clock and troposphere parameters using different stochastic processes in order to improve GNSS-relevant parameters like orbits (Lichten and Border, 1987). At that time, however, the impact of a sophisticated clock model was marginal due to the fact that the large majority of the ground-based and space-borne clocks was not sufficiently accurate and stable compared to the phase measurement noise of $1-2$ mm ($3.3-6.7$ ps) to allow for such approaches.

In the last 20 years, more and more stable atomic clocks are connected to GNSS receivers in the International GNSS Service (IGS) (Dow et al., 2009) network and used for time and frequency transfer accompanied with the stronger connections between different timing labs and the IGS stations (Ray and Senior, 2003). Such a development also takes place in space, where satellites are equipped with better and better clocks. Examples are the Hydrogen-maser (H-maser) on GIOVE-B (Galileo In-Orbit Validation Element), see Montenbruck et al. (2012), and the modified rubidium clock on GPS-IIF SVN62 (Dupuis et al., 2010). In recent years, investigations concerning clock modeling came to into focus again. Weinbach and Schön (2011) have shown that an improvement in the vertical component of kinematic Precise Point Positioning (PPP) (Zumberge et al., 1997) by up to 70 % can be expected by applying a simple deterministic clock model. They demonstrated that loose relative constraints on clock parameters may improve the vertical component in the case of pseudo-range kinematic solutions as well (Weinbach and Schön, 2009).

Because of the high quality of the H-masers available nowadays, the constraints between subsequent and near-subsequent clock epochs (the so-called relative constraints) can also be applied for phase positioning. An appropriate weighting of these relative constraints depending on the individual clock performance is very important to obtain optimal kinematic positions. Constraining the clocks too strongly (e.g. neglecting environmental influences and hardware delay variations) may lead to a degradation of the kinematic positioning results. In this study here, detailed investigations concerning the weight of the relative constraints on subsequent and near-subsequent (between every three epochs) clock parameters are performed and the benefit in kinematic positioning results using phase (and heavily down weighted code) observations is assessed.

In addition, the global positioning system (GPS) data were analyzed to study whether

the temporal resolution of troposphere parameters can be increased when constraining clocks to further improve the kinematic height estimates.

Deterministic and stochastic modeling of the receiver clock

In our approach we assume that the receiver clock can be described by a simple deterministic model (e.g., low-order polynomial) and a stochastic model:

$$clk(t_i) = a_m \cdot (t_i - t_0)^m + \cdots + a_1 \cdot (t_i - t_0) + a_0 + p(t_i),$$

$$clk(t_{i+1}) = a_m \cdot (t_{i+1} - t_0)^m + \cdots + a_1 \cdot (t_{i+1} - t_0) + a_0 + p(t_{i+1}), \tag{A.1}$$

where $clk(t_i)$ represents the receiver clock correction for measurement epoch i, a_m,..., a_1, a_0 are the coefficients of the low-degree polynomial, and $p(t_i)$ is the stochastic clock parameter for measurement epoch i.

The deviations of a clock can be divided into two categories, namely, the systematic effects such as the time offset, the frequency offset and the frequency drift, as well as the non-deterministic random errors such as white noise, flicker noise and random-walk noise (Allan, 1987). A study concerning the deterministic models of high-precision clocks and of their impact on other GPS-related parameters was done parallel to this study. The results have shown that the simplest deterministic model, namely, a linear polynomial, works the best for stabilizing the kinematic height estimates (Orliac et al., 2012). In this study, therefore, a linear polynomial is used. The clock parameters to be estimated from the GPS data are the coefficients a_1, a_0 and the stochastic clock parameters $p(t_i)$. The stochastic clock parameters $p(t_i)$ represent the deviations of the real clock from the linear polynomial given by the coefficients a_1 and a_0 in Equation A.1. The size of these deviations $p(t_i)$ depends on the clock quality. The stochastic clock parameters of subsequent epochs t_i and t_{i+1} can be constrained using a pseudo-observation with the weight $P_{i,i+1}$:

$$p(t_i) - p(t_{i+1}) = 0, \quad P_{i,i+1} = \frac{\sigma_0^2}{\sigma_{rel}^2}, \tag{A.2}$$

where σ_0 and σ_{rel} represent the a priori standard deviation of unit weight, i.e., the standard deviation of the GPS phase observations, and the standard deviation of the relative constraint between the two subsequent epochs, respectively. The weight of the relative constraints is the most important quantity in the stochastic model. In order to be consistent with the unit of σ_0, σ_{rel} is expressed in millimeter in this paper

Similar constraints can also be added for near-subsequent epochs. In general, the stochastic behavior between the ith and the $(i+n)$th epoch is then constrained according to:

$$p(t_i) - p(t_{i+n}) = 0, \quad P_{i,i+n} = \frac{\sigma_0^2}{\sigma_{rel,n}^2}, \tag{A.3}$$

where $\sigma_{rel,n}$ stands for the standard deviation of the relative constraint between near-subsequent epochs t_i and t_{i+n}. The weight $P_{i.i+n}$ can thereby be derived from, e.g., the Modified Allan Deviation (MDEV) of the clock records from the Center for Orbit Determination in Europe (CODE). The MDEV is, like the traditional Allan deviation (ADEV), a measure of the frequency stability and is able to distinguish between the white phase noise and the flicker phase noise (Allan and Barnes, 1981). $\sigma_{rel,n}$ here is the product of the MDEV value at the corresponding averaging time ($\sigma_{MDEV,n}$), the speed of light (c) and the averaging time (τ_n) itself:

$$\sigma_{rel,n} = \sigma_{MDEV,n} \cdot c \cdot \tau_n. \tag{A.4}$$

Since the drift a_1 and the offset a_0 of the linear polynomial are estimated as non-epoch parameters simultaneously with the stochastic quantities $p(t_i)$, weak absolute constraints with a small weight P_i have to be put on the stochastic parameters $p(t_i)$ to avoid the singularities between the offset, the drift and the stochastic parameters. These absolute constraints have the form

$$p(t_i) = 0, \quad P_i = \frac{\sigma_0^2}{\sigma_{abs}^2}, \tag{A.5}$$

where σ_{abs} represents the RMS of the absolute constraints.

For network solutions involving a huge number of parameters, the epoch-parameters are usually pre-eliminated for increasing the computation efficiency (Jäggi et al., 2011). Ge et al. (2006) has introduced a procedure to pre-eliminate the ambiguity parameters for both real-valued and ambiguity-fixed solutions and accelerated the computation for huge network solutions significantly. To limit the required computer resources, clock parameters are efficiently eliminated at every epoch. If relative constraints are applied, a rather complex pre-elimination and back-substitution scheme has to be used (and was implemented) for the least-squares adjustment that also works for near-subsequent epoch parameters. The stochastic clock parameters are efficiently pre-eliminated at every epoch in order to limit the computation time. Before pre-eliminating a specific epoch, the stochastic clock parameters of the subsequent and near-subsequent epochs to be constrained have to be considered. After determination of all the non-epoch parameters, a back-substitution is performed starting backwards from the last epoch. All the relevant information required for this back-substitution has to be stored step-by-step during the pre-elimination process. In this way, relative clock constraints can also be applied for relatively big regional network or even global solutions.

Identification of good H-masers

At present there are over 130 IGS stations equipped with high-performance atomic clocks. Figure A.1 shows the global distribution of these clocks on April 1st, 2012 including 68 H-masers, 43 cesium and 26 rubidium clocks (CLKLOG, 2012).

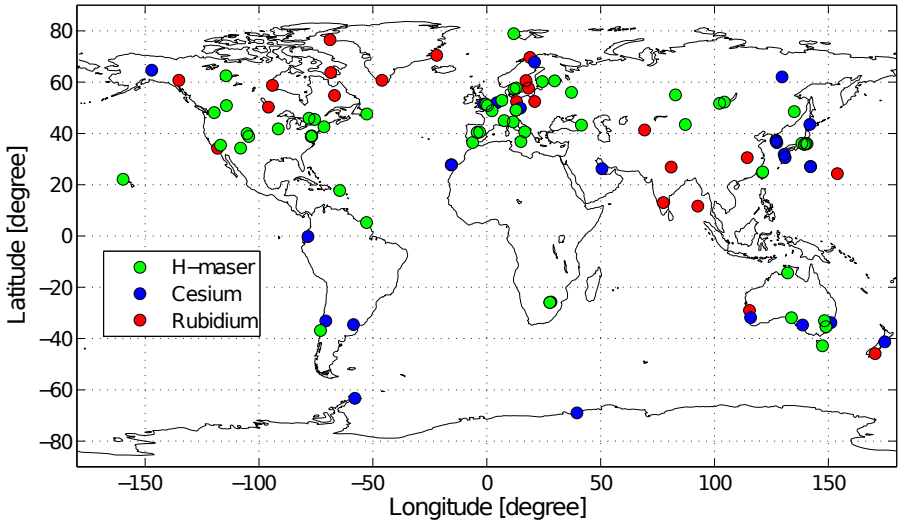

Figure A.1: Global distribution of IGS stations with high-performance atomic clocks

We can expect that the application of relative constraints on clock parameters is most beneficial for stations with very stable H-masers compared to cesium and rubidium clocks (Allan, 1987). The clock values of H-masers with jumps, equipment changes or other problems can only be estimated epoch-wise as it has been done so far. A rough characterization of these H-masers can be obtained from the analysis of the clock estimates, which are freely available in the IGS, the CODE or the European Space Agency (ESA) stored in clock RINEX files (Ray and Gurtner, 2010). In order to make sure that the clock estimates used for the clock characterization represent the actual clock behavior as precisely as possible, all clock estimates were referenced to the IGS time scale (IGST) (Wang and Rothacher, 2011; Senior et al., 2003). One way to characterize the H-masers is the empirical RMS of epoch-to-epoch differences σ_{emprel} (the so-called empirical relative sigma), that can be calculated based on the clock records in these clock RINEX files according to

$$\sigma_{emprel} = \sqrt{\frac{\sum_{i=1}^{n-1} (clk(t_{i+1}) - clk(t_i))^2}{n-1}}, \tag{A.6}$$

where n represents the number of processed epochs. It should be noticed that the detected clock jumps or problems here are mainly concerning the GPS receiver, the installation and clock adjustments rather than the H-Maser itself. For such bad behaviors, the clock values usually exceed the GPS measurement noise and allow thus the identification and exclusion of the misbehaving H-Masers.

As an example, Figure A.2 shows the daily empirical relative sigma σ_{emprel} of the H-maser located at station CEDU (CEDUNA, Ceduna, Australia) in February 2011 and, for February 15, 2011, the clock residuals after removing a linear polynomial. The values of σ_{emprel} amount to around $60-70$ ps for most of the days in February 2011, but may sometimes reach more than 150 ps. The big clock jumps on February 15, 2011 is, e.g., the

cause of the relatively big empirical relative sigma of about 200 ps.

The values σ_{emprel} are a good measure of the clock quality, especially for detecting clock jumps. In our analyses of a specific H-maser clock, the days with an empirical relative sigma σ_{emprel} bigger than 100 ps were excluded. Figure A.3 shows the mean values of σ_{emprel} for some well-behaving H-masers in February 2011, excluding the days with data gaps and the days with bad σ_{emprel} values. It can be seen that most H-masers are performing very well with a mean σ_{emprel} smaller than 30 ps (9 mm).

Estimation of kinematic station coordinates with real data

In order to assess the effect of relative clock constraints, experiments with PPP were performed using a modified version of the Bernese GPS Software (Dach et al., 2007). The kinematic (i.e. epochwise) coordinates of a static station equipped with a well-behaving H-maser were estimated together with the receiver clock parameters with a sampling rate of 300 s over a time span of 24 h. The wet part of the troposphere ZPD was estimated as a piece-wise linear function with a 2 h resolution and the wet Vienna Mapping functions 1 (VMF1) (Boehm et al., 2006). In addition, troposphere gradients were estimated with a resolution of 24 h. The satellite clocks were fixed to high-rate precise clocks from CODE (Bock et al., 2009; Dach et al., 2009; Hugentobler, 2004). Since the investigated stations are static, the standard deviations of the estimated kinematic coordinates are considered as a measure for the appropriateness of different clock constraints. Clocks with adjustments or huge jumps were excluded based on the empirical relative sigmas σ_{emprel}

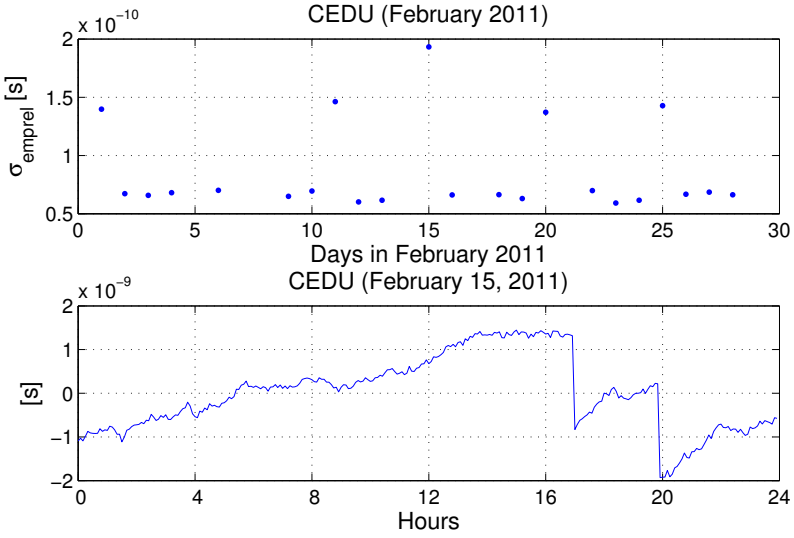

Figure A.2: Empirical relative sigma σ_{emprel} for the H-maser clock at station CEDU in February 2011 (top) and the residuals for this clock after removing a linear polynomial on February 15, 2011 (bottom).The CODE clock RINEX files were used for the plots

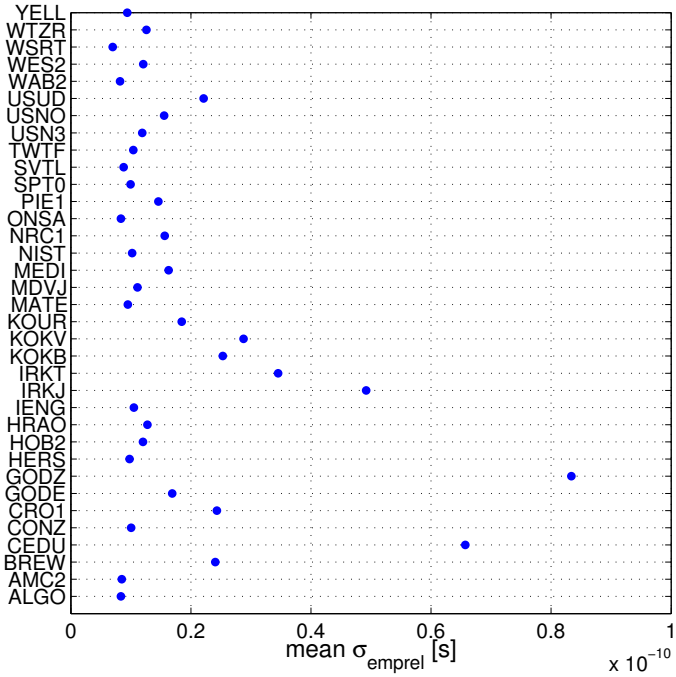

Figure A.3: Mean empirical relative sigma σ_{emprel} for some H-masers in February 2011. The IGS/CODE/ESA clock RINEX files were used for the plot

(see Equation A.6) derived from the epoch-to-epoch differences of the GPS clock estimates.

Figure A.4 shows the effect of relative constraints of different strengths on the H-maser clock estimates at station ONSA (ONSALA, Onsala, Sweden) on February 1st, 2011. The clock estimates without any constraints are shown in blue, while the red, green and magenta lines represent the clock estimates with increasing relative constraints. Finally, applying very strong constraints results in an almost straight line (black). We thus see that, as expected, increasing the relative constraints forces the clock estimates to converge towards a straight line.

Figure A.5 shows the corresponding kinematic height estimates for station ONSA on February 1st, 2011. As in Figure A.4, the blue line indicates the kinematic solution without any clock constraints, while the red, green and magenta lines represent the kinematic height estimates with increasing relative constraints. It can be observed that the kinematic height estimates of the static station ONSA are significantly improved by applying relative clock constraints, e.g., up to a factor of 2. This improvement of the height repeatability (see standard deviations σ_H in the legend of Figure A.5) is a consequence of relative constraints together with the high correlations between the clock parameters and the height estimates. This is especially important, since the height estimates from GPS are typically much less precise than the horizontal components. The black line using very strong relative constraints shows, however, a degradation of the positioning results in the vertical direction.

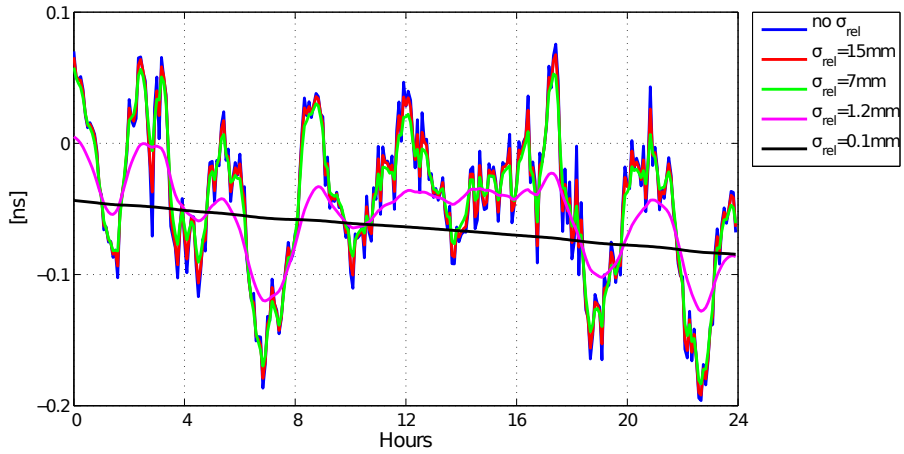

Figure A.4: Clock estimates for station ONSA using different relative constraints between subsequent clock epochs on February 1st, 2011

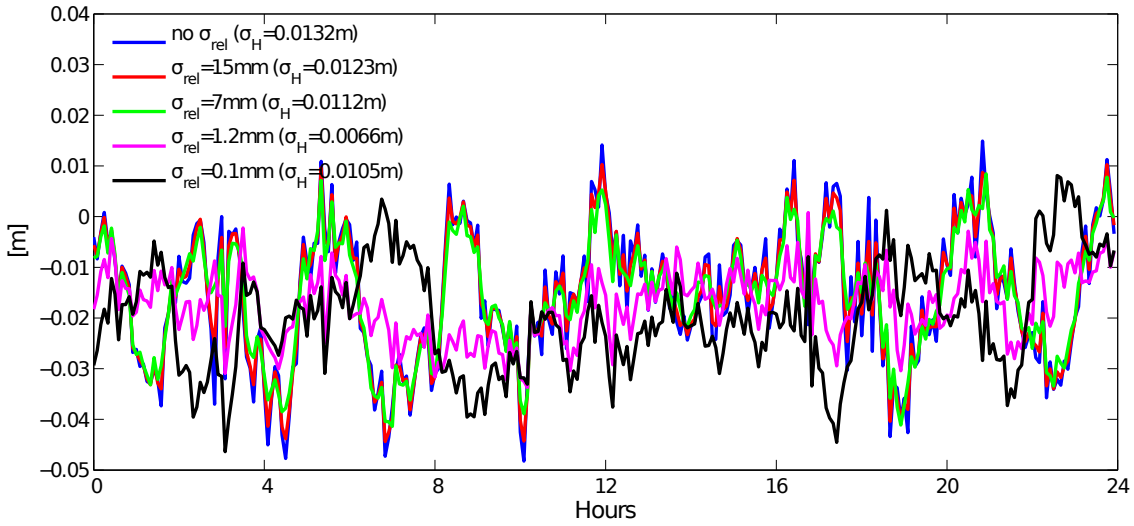

Figure A.5: Kinematic height estimates for station ONSA on February 1st, 2011 using different relative constraints between subsequent clock epochs

To study the impact of the relative constraints in more detail, a large series of kinematic solutions were produced decreasing σ_{rel} in steps of 0.1 mm from 20 mm down to 0.1 mm. Figure A.6 shows these results, i.e., the direct relationship between the weights of the relative constraints between subsequent clock parameters and the standard deviation of the kinematic coordinates for station ONSA on February 1st, 2011, in all three directions (North, East, Up). Starting with very weak constraints, the standard deviation of the kinematic height estimates (red line) decreases with increasing relative constraint (i.e., decreasing relative sigma), and shows a minimum at a relative constraint of about 1.2 mm (4 ps). With stronger relative constraints the estimated clock values cannot represent the

clock variations anymore and the results are degraded. As opposed to the height estimates, the horizontal coordinates are not improved by constraining the clock parameters. A significant degradation can be observed especially for a relative sigma smaller than 2 mm (6.7 ps). The relative sigma σ_{rel} of about 1.2 mm (4 ps), which leads to the best kinematic height estimates, degrades at the same time the horizontal coordinates and is, thus, not the optimal choice. The reason for the degradation of the kinematic horizontal coordinates with relative constraints stronger than 1.2 mm is not clear.

Figure A.7a shows the improvements in the kinematic height estimates for some well-behaving H-masers on February 1st, 2011. The solid lines represent the standard deviations of the kinematic height estimates using different relative constraints between subsequent epochs. These epoch-to-epoch relative constraints can improve the stability of kinematic height estimates reaching an optimum for a very small relative sigma σ_{rel} between 0 and 2 mm (0 and 6.7 ps). The improvement reaches a factor of about 2 to 3. However, this conclusion only holds for very stable H-masers (e.g. clock with σ_{emprel} smaller than 15 ps). For H-masers that are not that stable, the standard deviations of the kinematic height estimates grow rapidly after reaching a relative sigma σ_{rel} smaller than 2 mm (see Figure A.7b). Only very weak relative constraints may be considered for such clocks (for KOKV 8.5 mm and for IRKJ 14.2 mm).

The asterisks in Figure A.7a represent the standard deviations using not only relative constraints between subsequent epochs (called $\sigma_{rel,1}$), but also between near-subsequent epochs (every third subsequent epoch, called $\sigma_{rel,2}$). The relative sigma values $\sigma_{rel,1}$ and $\sigma_{rel,2}$ have been derived from the MDEV of the CODE clock records, and the x-coordinate of the asterisks in Figure A.7a is set to be the relative sigma $\sigma_{rel,1}$, i.e. the product of the MDEV value at 300 s derived from the clock records, the speed of light and the averaging time of 300 s. The three-epoch constraints cannot be directly compared with the optimal

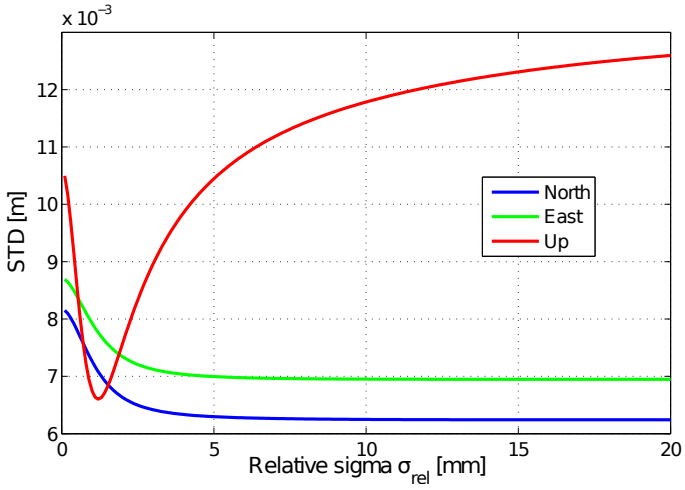

Figure A.6: Standard deviation of the kinematic coordinates for station ONSA with different relative constraints on February 1st, 2011

standard deviation of the epoch-to-epoch constraints because the CODE clock records used for MDEV comprise the measurement noise, but they also improve the stability of the kinematic height estimates significantly.

Table A.1 summarizes the improvements obtained in the kinematic height estimates for some H-maser clocks on February 1st, 2011. The clocks are sorted by their quality. The quality is based on the standard deviations σ_{STD} computed after removing a linear polynomial from the corresponding clock records (column 2). The empirical relative sigma σ_{emprel} is listed in the third column. The data from different institutes (IGS/CODE/ESA) were used to give a complete list of the evaluation for the given clocks. The corresponding agency is indicated with the first letter (see column 2). The fourth column and the fifth column document the standard deviation of the kinematic height estimates without constraints (STD_0) and with the optimal constraints (STD_{min}), which generates the most stable kinematic height estimates. The sixth column contains the standard deviation of the kinematic height estimates using relative constraints between three consecutive epochs. The seventh column lists the values σ_{rel}, which lead to the minimal standard deviation of the kinematic height estimates for the corresponding station (see Figure A.7). It should be noted that the range of σ_{rel} values tested started with a value of 0.1 mm. Even stronger relative constraints have not been studied. The improvement factor f of the kinematic height estimates (column 8) has been calculated based on

$$f = \frac{STD_0}{STD_{min}}. \tag{A.7}$$

From Table A.1 we see that for very stable H-masers the kinematic height estimates could be improved by up to a factor of 2 to 3 by applying relative constraints between 0 and 2 mm (0 and 6.7 ps). If the best relative sigma to be used is not known, an epoch-to-epoch relative constraint of 2 mm or a near-subsequent constraint derived from a MDEV

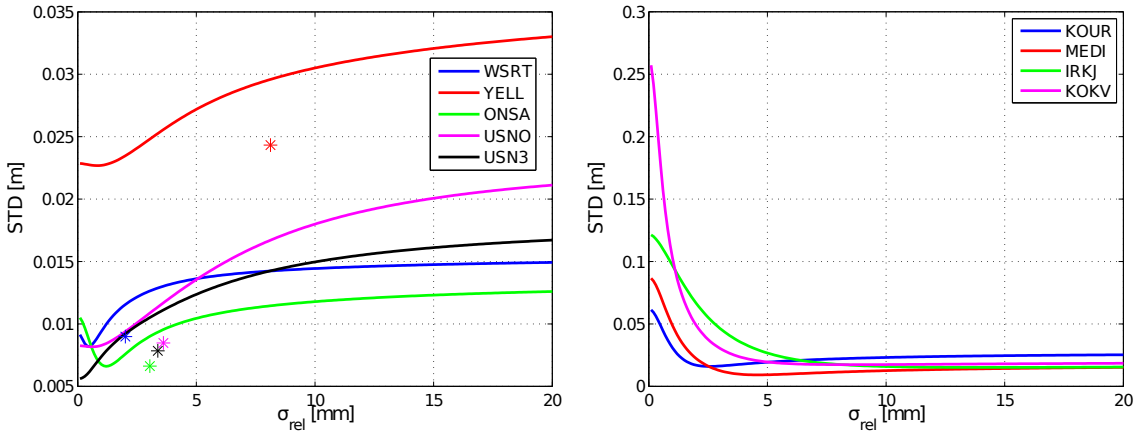

(a) stable H-masers

(b) unstable H-masers

Figure A.7: Stability improvements of kinematic height estimates for some (a) stable and (b) unstable H-masers on February 1st, 2011, using different relative constraints

Table A.1: Improvements of kinematic height estimates for some H-masers using relative constraints between subsequent and near-subsequent clock parameters on February 1, 2011

Station	Clock estimates		Kinematic height estimates				
	σ_{STD} [ps]	σ_{emprel} [ps]	STD_0 [m]	STD_{min} [m]	STD_{Covar} [m]	σ_{rel} [mm]	f
WSRT	12.9(I)	6.2	0.0153	0.0082	0.0090	0.5	1.87
ONSA	22.1(I)	10.9	0.0132	0.0066	0.0066	1.2	2.00
USNO	22.9(I)	10.6	0.0232	0.0082	0.0085	0.6	2.84
USN3	23.3(I)	10.0	0.0196	0.0056	0.0078	0.1	3.50
YELL	23.5(C)	22.0	0.0687	0.0227	0.0243	0.8	3.03
CRO1	32.8(I)	23.2	0.0356	0.0158	—	0.1	2.25
AMC2	33.7(I)	7.9	0.0192	0.0159	0.0165	2.2	1.21
HRAO	39.1(I)	12.0	0.0225	0.0114	—	0.6	1.98
HOB2	40.5(I)	15.5	0.0240	0.0098	0.0139	1.2	2.44
TWTF	44.6(I)	9.8	0.0179	0.0108	0.0109	1.2	1.66
ALGO	45.3(I)	6.5	0.0108	0.0057	0.0058	1.0	1.89
BREW	55.3(I)	23.5	0.0153	0.0094	—	1.8	1.63
KOUR	241.1(I)	20.0	0.0266	0.0159	0.0159	2.5	1.67
MEDI	342.2(I)	18.0	0.0177	0.0092	—	4.6	1.90
IRKJ	416.2(I)	55.1	0.0178	0.0152	—	14.2	1.17
KOKV	982.7(E)	33.9	0.0198	0.0173	—	8.5	1.14

The IGS/CODE/ESA clock RINEX files were used for generating the σ_{STD} and σ_{emprel}

plot may be a safe way to stabilize the kinematic solutions in the vertical direction. The improvement that can be reached depends heavily on the clock quality. Clocks with an unstable or unknown behavior are not suitable for clock modeling. Constraining such clocks may lead to much worse results. It should be mentioned that very strong and unrealistic weights for relative constraints ($\sigma_{rel} \ll 2\ mm$) may also make things worse even for very stable H-masers (see Figure A.7). The reason for this may be related to the noise level of the observations and the simultaneous estimation of other parameters (e.g., troposphere parameters). Apart from that, real clock variations may not be adequately modeled with too strong clock constraints. Looking carefully at Table A.1 we can see that the improvement factor f that can be achieved in the repeatability of the kinematic height estimates is not a simple function of the clock quality given by the deviations from a straight line (σ_{STD}) or the size of the epoch-to-epoch clock differences as defined by σ_{emprel}. Besides σ_{STD} and σ_{emprel} other factors like multipath, antenna environment seem to play a major role, too. A bad observation geometry or a limited number of the phase observations may strongly degrade the kinematic estimates in the case no clock constraint

is applied (e.g. YELL in Table A.1). The relative sigma between subsequent and near-subsequent epochs $\sigma_{rel,n}$ (see Equation A.4) derived from the CODE clock records and the optimal relative clock constraints that we obtained here (see Table A.1) do not necessarily correspond to the real clock behavior. They are also influenced by the measurement noise, the antenna environment, multipath and troposphere variations.

Let us have a look now at the optimal values for the relative constraints over a longer time period. Figure A.8a shows these optimal values for five very stable H-masers for all days in February 2011. The variations for an individual clock strongly depend on the clock behavior on the corresponding day. For most of the days in February 2011 the best σ_{rel} values are smaller than 2 mm (6.7 ps), while some outliers can also be observed. Taking the H-maser clock at station YELL (YELL CACS-GSD, Yellowknife, Canada), for example, two outliers on February 6, 2011 and February 25, 2011 can be observed in Figure A.8a, indicating an unstable clock behavior. For comparison, Figure A.8b shows σ_{emprel} (see Equation A.6) based on the CODE clock RINEX files for the H-maser at station YELL in February 2011. We see that the days with a high value of σ_{emprel} correspond to the outliers in Figure A.8a. Very strong constraints on clock parameters on these 2 days would lead to a degradation of the positioning results.

Figure A.9 shows the relationship between the clock quality (σ_{emprel} and σ_{STD}) and the improvement factor f of the kinematic height estimates with a relative clock constraint of 2 mm. The IGS/CODE/ESA clock records of the H-Masers listed in Table A.1 in February 2011 were used for the plots. We see that the number of improvement factors below 1 increases with an increasing σ_{emprel} and σ_{STD}. For the clocks with $\sigma_{emprel} < 15$ ps and $\sigma_{STD} < 50$ ps, the improvement factors are in 98% of the time above 1, thereof 49% above 1.5.

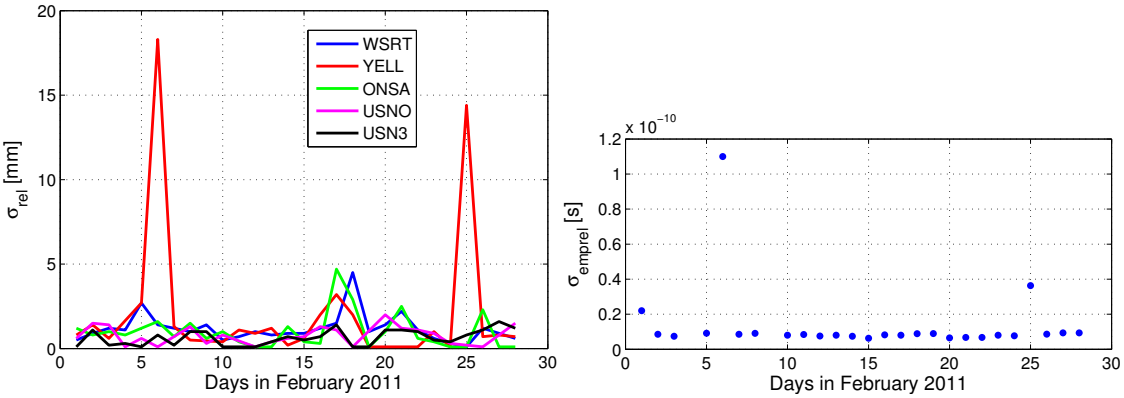

(a) optimal σ_{rel}

(b) σ_{emprel} for YELL

Figure A.8: The optimal relative sigma σ_{rel} for (a) five very stable H-masers in February 2011 and (b) the empirical relative sigma σ_{emprel} for the H-maser at station YELL during February 2011

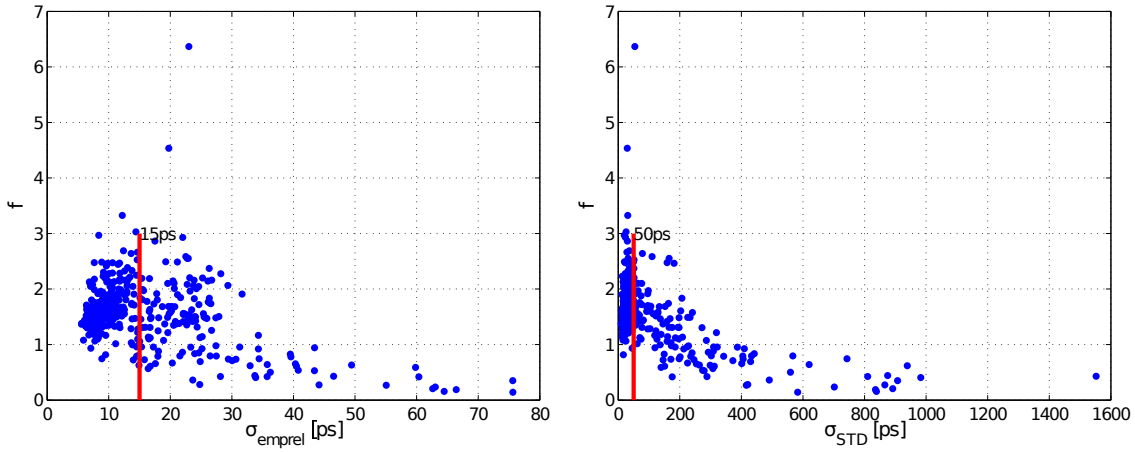

(a) f vs σ_{emprel} (b) f vs σ_{STD}

Figure A.9: Relationship between the improvement factors f with a relative clock constraint of 2 mm and (a) the empirical relative sigma σ_{emprel} and (b) the standard deviation from a linear polynomial σ_{STD} using the IGS/CODE/ESA clock records of 16 H-Masers in February 2011

In order to analyze the variations in kinematic heights over various time intervals, the MDEV of the kinematic height estimates for station ONSA on February 1st, 2011 using different stochastic clock models were computed (see Figure A.10). The black line indicates the MDEV of the kinematic height estimates obtained without any relative clock constraints. The magenta and the blue line corresponding to epoch-to-epoch relative constraints of 1.2 mm (4 ps) and the three-epoch constraints, respectively, show huge improvements in precision of the kinematic height estimates ranging from 5 min to about 3 h. It can also be seen that the quality of the kinematic height estimates is somewhat degraded for time intervals between approximately 30 min and 3 h compared to the slope of -1 for typical flicker noise (blue dashed line). Since the ZPDs were estimated with a time resolution of 2 h, this limited time resolution might be the cause of this degradation.

To verify this, different sampling intervals for the ZPD parameters were tested. The resulting MDEV of kinematic height estimates for ONSA are shown in Figure A.11 applying (a) no clock constraints or (b) relative constraints of 2 mm (6.7 ps) between subsequent clock parameters. Compared to the slope of -1 for typical flicker noise in the MDEV (see blue dashed line in Figure A.11b), obvious deviations can be observed for long time intervals. By decreasing the sampling intervals of the ZPD parameters, these deviations are considerably reduced, showing that the modeling deficiencies due to the insufficient time resolution of the troposphere parameters deteriorate the kinematic height estimates for large averaging times. The cases with a ZPD time resolution higher than 60 min are overwritten by the 60 min case. This means that no degradation of the kinematic heights takes place even if a 15 min time resolution for the ZPDs is used. the relative clock constraints thus allow for a higher temporal resolution of the troposphere parameters, which

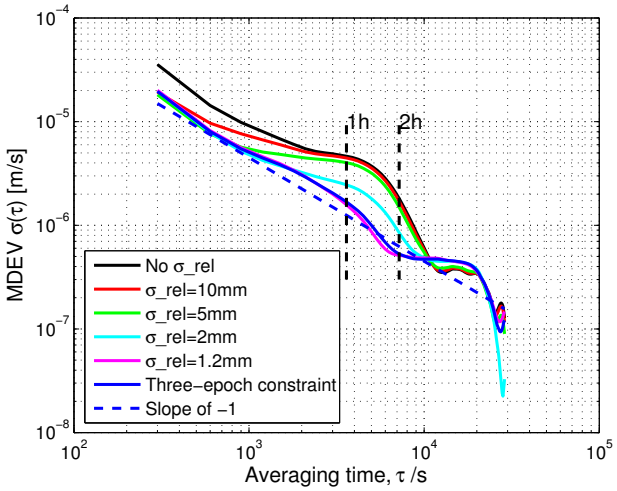

Figure A.10: MDEV of kinematic height estimates for station ONSA using different relative constraints on February 1st, 2011

may be advantageous in the case of fast changing weather conditions. In contrast, in the case without applying relative clock constraints (see Figure A.11a), the increase in the number of ZPDs eventually (15 min ZPD resolution) leads to a degradation of the kinematic height estimates at averaging intervals below about 1 h. An offset can generally be observed between Figure A.11a, b. It shows the positive effect of an appropriate relative clock constraint on the kinematic height estimates.

Experiments have also been performed with respect to even stronger relative constraints, e.g., 1.2 mm (4 ps), which corresponds to the optimal σ_{rel} for the H-maser at ONSA (see Figure A.10). However, the benefits from changing the sampling interval of ZPD parameters are not obvious any more. The improvements are very similar to the case using a constraint of 2 mm (6.7 ps) and a 60 min ZPD interval.

Estimation of kinematic station coordinates with simulated data

In order to verify the results obtained with real data, GPS code and phase observations on both frequencies were simulated with a pre-defined receiver clock behavior, a phase observation noise of 2 mm and a code observation noise of 20 cm using a modified version of Bernese GPS Software 5.0 (Dach et al., 2007). The simulated receiver clocks were generated with an offset, a drift and the deviations of the H-masers at WSRT (Westerbork Synthesis Radio Telescope, Westerbork, Netherlands), ONSA and HOB2 (Hobart AU016, Hobart, Australia) from a linear clock behavior amounting to an RMS of 14.7, 35.3 and 44.3 ps, respectively, on February 1st, 2011. After multiplication with the speed of light, the RMS of the epoch-to-epoch difference σ_{emprel} of these three real clocks amount to 1.9 mm (6.3 ps), 2.9 mm (9.7 ps) and 5.2 mm (17.3 ps), respectively.

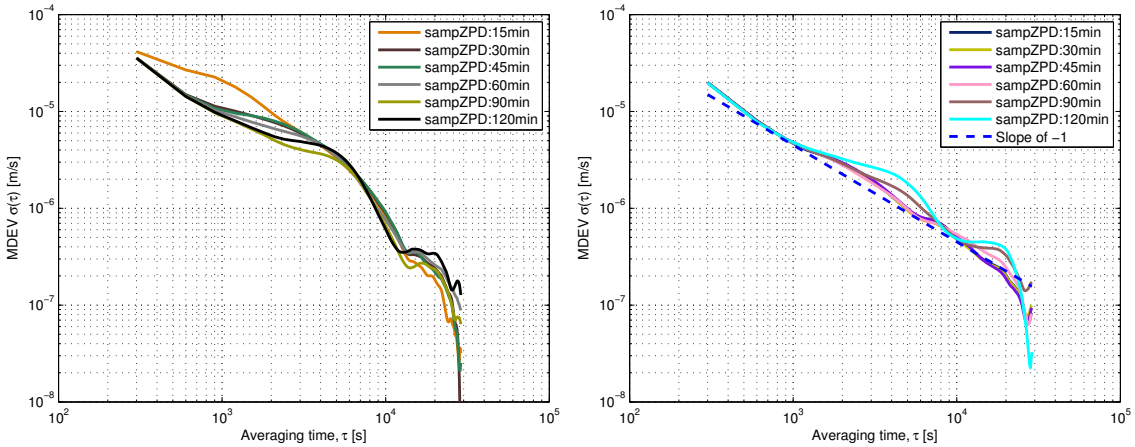

(a) without σ_{rel} (b) with σ_{rel}=2mm

Figure A.11: MDEV of kinematic height estimates for ONSA using (a) no relative constraints and (b) relative constraints of 2 mm between subsequent clock epochs on February 1st, 2011. The troposphere ZPD parameters were set up with different sampling intervals

In Figure A.12 we see the results of the simulations using different relative constraints for the receiver clocks. Different colors represent different clock qualities. We see that in this simulated case the stability of the height estimates as a function of the relative clock constraints behaves very similar to the real data case (see Figure A.7). We also see that the better the clock quality, the smaller the optimal σ_{rel}. The optimal σ_{rel} is below 2 mm (6.7 ps) for stable clocks (with σ_{simrel} = 1.9 mm (6.3 ps) and σ_{simrel} = 2.9 mm (9.7 ps)) and above 2 mm (6.7 ps) for the clock with σ_{simrel} = 5.2 mm (17.3 ps). The blue line represents the clock with a perfect behavior, i.e., without any stochastic component. For the perfect clock, the stronger the relative constraints are, the better performance we can get for the kinematic height estimates, even for very strong constraints.

Summary and conclusions

The kinematic coordinates derived from an PPP solution using phase measurements typically show an accuracy at cm-level in horizontal and at sub-decimeter level in vertical direction (Geng et al., 2010). This means that it is more difficult to detect real motions of a receiver in height than in horizontal positions. This situation can considerably be changed, if high-stability H-masers are connected to the receiver. Using a simple deterministic model (e.g., a linear polynomial) and relative constraints with an appropriate weight between subsequent epochs (e.g., 2 mm or 6.7 ps) for such a clock, the kinematic solutions can be significantly improved in the less accurate vertical direction, namely, by up to a factor of 2 to 3. The optimal weight for the relative constraints between subsequent clock epochs, which leads to the best kinematic solution, depends heavily on the quality of the clock considered. For very stable H-masers, i.e., for H-masers with a stan-

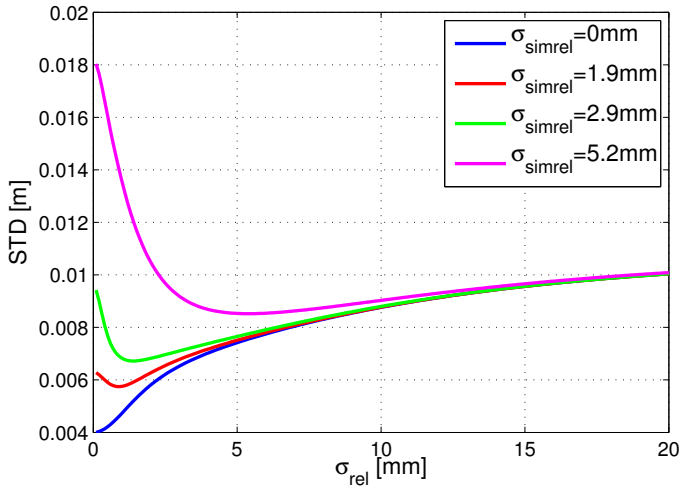

Figure A.12: Standard deviation of the kinematic height estimates derived from simulated GPS data with realistic receiver clock behavior using different relative constraints on subsequent clock parameters. The CODE clock RINEX files were used for simulation of the receiver clocks

dard deviation lower than 50 ps after removing a linear polynomial and an RMS σ_{emprel} of the epoch-to-epoch clock differences smaller than 15 ps, the optimal relative constraint typically lies between 0 and 2 mm (0 and 6.7 ps). Taking the 16 investigated H-Masers (see Table A.1) in February 2011 for example, for all the clocks that have passed the criteria that are mentioned above ($\sigma_{emprel} < 15$ ps and $\sigma_{STD} < 50$ ps), 98% of the improvement factors are above 1, 49% thereof above 1.5. It should be noticed that the σ_{emprel} derived from the GPS estimates is noisier than the real clock. It can only be considered as a measure for the clock quality, but is not directly related to the optimal relative sigma.

Relative constraints between subsequent *and* near-subsequent epochs using weights derived from the MDEV of clock records available from IGS, CODE or ESA is also a good and safe choice for stabilizing the kinematic solutions in the vertical direction. In this way, the stability of the kinematic height estimates can also be improved by up to a factor of approximately 2 to 3. Taking the 16 investigated H-Masers (see Table A.1) in February 2011 for example, for all the clocks that have passed the criteria that are mentioned above ($\sigma_{emprel} < 15$ ps and $\sigma_{STD} < 50$ ps), 99% of the improvement factors are above 1, 44% thereof above 1.5.

It is clear that the improvement in the repeatability of the kinematic heights (i.e. in changes of the kinematic heights) is roughly limited to time intervals, during which the receiver clock does not deviate by more than about 50 ps from a linear behavior.

Most benefit from the methods presented here are therefore to be expected in the quantification and detection of small height changes at cm-level over short time intervals (a few hours to one day). Prominent and important examples are certainly earthquake ground

motions and displacements, tsunami GPS buoys and land slides, provided that H-Masers or other clocks of similar performance are getting cheaper and less sensible to the environment in the future.

Because of the high correlation of the troposphere zenith delays with the station height estimates, the sampling intervals used for the ZPD estimation is always a critical issue in kinematic positioning. Experiments have shown that with an appropriate relative clock constraint increasing the sampling resolution of the ZPD parameters from 2 h to one or even half an hour clearly improves the stability of kinematic height estimates. Therefore, we may expect that clock constraints allow it to estimate troposphere parameters with a much higher temporal resolution without suffering from the high correlation between troposphere and heights, an important aspect for the determination of water vapor on ships or buoys to cover ocean areas.

It should be mentioned that no significant improvements can be obtained in the PPP solutions applying different clock models, if only one set of coordinates is estimated per day (Orliac et al., 2012). Tests have also shown that the modeling of the receiver clocks on the ground does not have a significant impact on GPS orbits and Earth rotation parameters (ERPs).

In the future, with the progress made in the field of high-performance frequency standards, more and more stable and cheap clocks will become available and the use of clock modeling will become more and more important. With the completion of the Galileo constellation in the near future, it will be possible to also make use of very stable satellite clocks. The stability of such clocks was studied by, e.g., Montenbruck et al. (2012), for the case of the GIOVE-B satellite carrying a H-Maser. Since receiver clock modeling, as mentioned above, does not have much effect on global parameters, one can conclude that making use of the very good receiver clocks improves the receiver-specific parameters (like heights and ZPDs), whereas global or satellite-specific parameters (like Earth rotation parameters and satellite orbits) show no or only very small improvements. It is to be expected in analogy, therefore, that the constraining of the high-performance satellite clocks will mainly lead to improvement in satellitespecific parameters (e.g. orbital parameters, decorrelation of orbital parameters and satellite clock corrections). Improved separation of the highly correlated satellite orbits and satellite clock parameters may help in future to better assess the deficiencies in the orbit modeling, especially in the solar radiation pressure models.

In the far future, as the clocks developed for receivers and satellites are getting more and more stable as described in this paper, the stochastic modeling of clocks over longer and longer time spans will become an integral task of high-precision GNSS analyses, leading to improvements in both, receiver- and satellite-specific parameters.

Acknowledgments

This work was funded by ESA as part of the project (Satellite and Station Clock Modeling for GNSS, Reference: AO/1-6231/09/D/SR). We would like to thank the partner institutions: Astronomical Institute, University of Bern (AIUB) and Institute for Astronomical and Physical Geodesy (IAPG), Technische Universität München (TUM), especially Etienne Orliac (AIUB) for providing the pre-processed observation data.

B Paper B

Paper B was originally published as

Wang K., Rothacher M. (2013): Ambiguity resolution for triple-frequency geometry-free and ionosphere-free combination tested with real data. Journal of Geodesy 87(6): 539-553. doi:10.1007/s00190-013-0630-7.

The final publication is available at `http://link.springer.com`.

Ambiguity resolution for triple-frequency geometry-free and ionosphere-free combination tested with real data

K. Wang[a], M. Rothacher[a]

[a]Institute of Geodesy and Photogrammetry, ETH Zurich, Robert-Gnehm-Weg 15, 8093 Zurich, Switzerland

Abstract

The recent GPS Block IIF satellites SVN62 and SVN63 and the Galileo satellites GIOVE-A, GIOVE-B, PFM and FM2 already send signals on more than two frequencies, and more GNSS satellites will provide tracking data on at least three frequencies in the near future. In this paper, a simplified general method for ambiguity resolution minimizing the noise level for the triple-frequency geometry-free (GF) and ionosphere-free (IF) linear combinations is presented, where differently scaled code noise on the three frequencies was introduced. For the third of three required linear combinations, the most demanding one in triple-frequency ambiguity resolution, we developed a general method using the ambiguity-corrected phase observations without any constraints to search for the optimal GF and IF linear combination. We analytically demonstrate that the noise level of this third linear combination only depends on the three frequencies. The investigation concerning this frequency-dependent noise factor was performed for GPS, Galileo and Compass frequency triplets. We verified the theoretical derivations with real triple-frequency GPS and Galileo data from the Multi-GNSS Experiment (M–GEX) of the International GNSS Service (IGS). The data of about 30 M–GEX stations around the world over 11 days from 29 April 2012 to 9 May 2012 were used for the test. For the third linear combinaton using Galileo E1, E5b and E5a, which is expected to have the worst performance among all the GNSS frequency triplets in our investigation, the formal errors of the estimated ambiguities are in most cases below 0.2 cycles after 400 observation epochs. If more GPS satellites sending signals on three frequencies or more stations tracking Galileo E6 signal are available in the future, an improvement by a factor of two to three can be expected.

Keywords: Triple-frequency ambiguity resolution; Geometry-free and ionosphere-free; Linear combination; GNSS

Introduction

Nowadays, different GNSS already provide or will provide their tracking data on three or even four frequencies. It is, thus, interesting to exploit the advantages of the increasing number of frequencies and search for geometry-free (GF) and ionosphere-free (IF) linear combinations with minimized noise. Hatch (2006) introduced a method for obtaining triple-frequency GF, refraction-corrected, ambiguity-resolved carrier-phase measurements. Feng et al. (2007) provided a model using the differences between geometry-based (GB), i.e. the geometry-related terms were preserved, triple-frequency code observations and GB triple-frequency phase observations to form geometry-free linear combinations, and their differences were investigated with respect to their ionospheric refractions and noise levels. Recently, Henkel and Günther (2012) introduced a more general method that uses simultaneously multi-frequency code and phase observations allowing an arbitrary scaling of the geometry, the ionospheric delay and the minimized noise level. The code noise on the three frequencies was assumed to be scaled according to the Cramer Rao bounds (CRB) (Henkel and Günther, 2012). In this paper here, we present a simplified method for GF and IF linear combinations using simultaneously triple-frequency code and phase observations with different sets of scaling factors for the code noise. For given integer coefficients of the three ambiguities, the optimized combination with the minimized combined noise can be expressed as a function of the three frequencies and the scaling factors of the code noise on the three frequencies. Different sets of scaling factors were tested with real triple-frequency Galileo data.

The GF and IF linear combination is useful especially for the case of long baselines (e.g. a global network), where the first-order term of the ionospheric delays cannot be fully eliminated, and for the case of Wide Area Real Time Kinematics (WARTK) measurements, where the geometry-related information such as the orbits, the clocks and the troposphere parameters are not available precisely enough and sometimes need to be estimated. In the case of Precise Point Positioning (PPP), the method can only be used when the satellite- and receiver-related biases are stable enough and can be estimated before the ambiguity resolution.

In order to solve the ambiguities, three linearly independent combinations are necessary. Various studies have been done in recent years to find the third GF and IF linear combination with acceptable noise. The ambiguity-corrected phase observations were used instead of the code observations to significantly reduce the noise level of the combination, and three sets of GB phase linear combinations were proposed to form a geometry-free linear combination (Li et al., 2010). Apart from that, Li et al. (2012) established a GF and IF approach for narrow-lane ambiguity resolution. In this study here, a more general method using ambiguity-corrected phase observations is used to form the third linear combination. It is analytically demonstrated that the noise level after combination is only a function of the three frequencies. This frequency-dependent factor is investigated for different GNSS.

The Galileo combination using E1, E6 and E5a has the smallest frequency-dependent factor and the best behavior among all the systems.

The theoretical derivations were verified with real data. The data were processed for 11 days in 2012 and the fractional parts and formal errors of the estimated ambiguities for all the three linear combinations were investigated.

GF and IF triple-frequency linear combinations

Ignoring hardware delays, multipath errors and higher-order terms of the ionospheric refraction, the code and phase observation equations of a specific carrier frequency on the zero-difference level can be described as follows:

$$P_i = \rho + I_1 \cdot \frac{f_1^2}{f_i^2} + \delta_{tro} + c \cdot \delta_r - c \cdot \delta^s + \epsilon_P,$$

$$L_i = \rho - I_1 \cdot \frac{f_1^2}{f_i^2} + \delta_{tro} + c \cdot \delta_r - c \cdot \delta^s + \lambda_i \cdot n_i + \epsilon_L, \tag{B.1}$$

where P_i and L_i represent the code and phase observation on frequency f_i, respectively. The symbol ρ is the distance from the satellite at the epoch of transmission to the receiver at the epoch of reception. δ_{tro}, δ_r and δ^s stand for the tropospheric delay, receiver clock correction and satellite clock correction, respectively. I_1 is the first-order term of the ionospheric refraction on carrier L_1 and c is the speed of light. ϵ_P and ϵ_L stand for the code and phase observation errors, respectively. λ_i represents the wavelength of the signal on frequency f_i and n_i represents the ambiguity on frequency f_i.

If the phase and code observations are available on three frequencies, it is possible to generate linear combinations that are both, GF and IF, i.e. they eliminate all geometry-related terms and the first-order ionospheric refraction. With the help of Equation B.1, the most general linear combination that can be formed using the code and phase observations on three carrier frequencies is given by:

$$\begin{aligned} L_x &= \gamma_1 L_1 + \gamma_2 L_2 + \gamma_3 L_3 + \gamma_4 P_1 + \gamma_5 P_2 + \gamma_6 P_3 \\ &= (\gamma_1 + \gamma_2 + \gamma_3 + \gamma_4 + \gamma_5 + \gamma_6)(\rho + \delta_{tro} + c\delta_r - c\delta^s) \\ &\quad + (\gamma_4 + \frac{f_1^2}{f_2^2}\gamma_5 + \frac{f_1^2}{f_3^2}\gamma_6 - \gamma_1 - \frac{f_1^2}{f_2^2}\gamma_2 - \frac{f_1^2}{f_3^2}\gamma_3) I_1 \\ &\quad + (\gamma_1\lambda_1 n_1 + \gamma_2\lambda_2 n_2 + \gamma_3\lambda_3 n_3) + \epsilon, \end{aligned} \tag{B.2}$$

where L_x is the combined observation. γ_i $(i = 1, \cdots, 6)$ represent the weighting coefficients of the three phase and the three code observations. ϵ stands for the observation error after combination.

The combined ambiguity n_x, which is a linear combination of the ambiguities n_1, n_2 and n_3, has to be an integer for ambiguity resolution purposes:

$$\lambda_x n_x = \gamma_1\lambda_1 n_1 + \gamma_2\lambda_2 n_2 + \gamma_3\lambda_3 n_3 = \lambda_x(a_x \cdot n_1 + b_x \cdot n_2 + c_x \cdot n_3), \tag{B.3}$$

where λ_x represents the wavelength after combination. a_x, b_x and c_x are integer coefficients of the phase combinations on three frequencies.

As a result of Equation B.3, we obtain the following relationships between the weighting coefficients γ_1, γ_2 and γ_3 and the integer coefficients a_x, b_x and c_x (Henkel and Günther, 2010):

$$\gamma_1 = \frac{a_x f_1}{f_x}, \quad \gamma_2 = \frac{b_x f_2}{f_x}, \quad \gamma_3 = \frac{c_x f_3}{f_x}. \tag{B.4}$$

Compared to the method, where a GB code combination is subtracted from a GB phase combination (Feng et al., 2007), the general combination described above has the advantage of being more general and not losing any degrees of freedom. Apart from that, the weighting coefficients γ_4, γ_5 and γ_6 of the code observations do not have to follow the same relationship as those of the phase observations (see Equation B.4).

In order to generate a GF linear combination, the factor appearing before the geometry-related terms (see Equation B.2) has to be zero. Using Equation B.4, the following equation for the weighting coefficients γ_4, γ_5 and γ_6 of the code observations can be derived:

$$\frac{a_x f_1 + b_x f_2 + c_x f_3}{f_x} + \gamma_4 + \gamma_5 + \gamma_6 = 0. \tag{B.5}$$

An IF linear combination requires the factor before I_1 (see Equation B.2) to be zero. With the help of Equation B.4, the following equation can be derived:

$$\gamma_4 + \frac{f_1^2}{f_2^2}\gamma_5 + \frac{f_1^2}{f_3^2}\gamma_6 = \frac{f_1}{f_x}(a_x + b_x\frac{f_1}{f_2} + c_x\frac{f_1}{f_3}). \tag{B.6}$$

With Equations B.5 and B.6, the code weighting coefficients γ_4 and γ_5 can be expressed as functions of γ_6:

$$\gamma_4 = \frac{m_1}{f_x} + m_2\gamma_6, \quad \gamma_5 = \frac{m_3}{f_x} + m_4\gamma_6, \tag{B.7}$$

with

$$\begin{aligned}
m_1 &= \frac{f_1((f_1^2+f_2^2)f_3 a_x + 2f_1 f_2 f_3 b_x + (f_2^2+f_3^2)f_1 c_x)}{f_3(f_2^2 - f_1^2)},\\
m_2 &= -\frac{f_1^2(f_2^2 - f_3^2)}{f_3^2(f_2^2 - f_1^2)},\\
m_3 &= \frac{f_2((f_1^2+f_2^2)f_3 b_x + 2f_1 f_2 f_3 a_x + (f_1^2+f_3^2)f_2 c_x)}{f_3(f_1^2 - f_2^2)},\\
m_4 &= -\frac{f_2^2(f_1^2 - f_3^2)}{f_3^2(f_1^2 - f_2^2)},
\end{aligned}$$

where m_1 and m_3 are functions of the three frequencies and the integer coefficients a_x, b_x and c_x with the characteristics $m_1(-a_x, -b_x, -c_x) = -m_1(a_x, b_x, c_x)$ and $m_3(-a_x, -b_x, -c_x) = -m_3(a_x, b_x, c_x)$. m_2 and m_4 are just functions of the three carrier frequencies f_1, f_2 and f_3.

Minimizing the noise level of the GF and IF triple-frequency linear combinations

Henkel and Günther (2012) has introduced a general method to minimize the noise level of the multi-frequency code carrier linear combinations. In this section, an algorithm limited to triple-frequency GF and IF linear combinations is discussed. The results of this algorithm for different frequency triplets using different scaling factors for the code noise are shown in Section "The best GF and IF triple-frequency linear combinations for different GNSS frequency triplets".

Since the code observation noise is dominant in the combined noise, the minimal code observation noise after combination is of great interest. Assuming that the code noise on the three carrier frequencies σ_{P1}, σ_{P2} and σ_{P3} can be formulated with three scaling factors C_4, C_5 and C_6 and an unscaled code observation noise σ_P in meters:

$$\sigma_{P1} = C_4\sigma_P, \quad \sigma_{P2} = C_5\sigma_P, \quad \sigma_{P3} = C_6\sigma_P, \tag{B.8}$$

the so-called code noise amplification factor N_{Code} can be formulated as follows:

$$\begin{aligned} N_{Code} &= \sqrt{C_4^2\gamma_4^2 + C_5^2\gamma_5^2 + C_6^2\gamma_6^2} = \sqrt{C_4^2(\frac{m_1}{f_x} + m_2\gamma_6)^2 + C_5^2(\frac{m_3}{f_x} + m_4\gamma_6)^2 + C_6^2\gamma_6^2} \\ &= \sqrt{(m_2^2C_4^2 + m_4^2C_5^2 + C_6^2)(\gamma_6 + \frac{m_1m_2C_4^2 + m_3m_4C_5^2}{f_x(m_2^2C_4^2 + m_4^2C_5^2 + C_6^2)})^2 + \frac{1}{f_x^2}N_{MIN}}, \end{aligned} \tag{B.9}$$

with

$$\begin{aligned} N_{MIN} &= m_1^2C_4^2 + m_3^2C_5^2 - \frac{(m_1m_2C_4^2 + m_3m_4C_5^2)^2}{m_2^2C_4^2 + m_4^2C_5^2 + C_6^2} \\ &= \frac{(m_1m_4 - m_2m_3)^2C_4^2C_5^2 + m_1^2C_4^2C_6^2 + m_3^2C_5^2C_6^2}{m_2^2C_4^2 + m_4^2C_5^2 + C_6^2} \geq 0, \end{aligned}$$

and the combined code noise σ_{Code}^C expressed in cycles of λ_x can be formulated as:

$$\begin{aligned} \sigma_{Code}^C &= N_{Code}\frac{\sigma_P}{\lambda_x} = N_{Code}\frac{\sigma_P f_x}{c} \\ &= \frac{\sigma_P}{c}\sqrt{(m_2^2C_4^2 + m_4^2C_5^2 + C_6^2)f_x^2(\gamma_6 + \frac{m_1m_2C_4^2 + m_3m_4C_5^2}{f_x(m_2^2C_4^2 + m_4^2C_5^2 + C_6^2)})^2 + N_{MIN}}. \end{aligned} \tag{B.10}$$

Equation B.10 shows that both, the code noise amplification factor N_{Code} and the combined code noise σ_{Code}^C, are the square root of a quadratic polynomial in γ_6, and are minimal, if

$$\gamma_6 = -\frac{m_1m_2C_4^2 + m_3m_4C_5^2}{(m_2^2C_4^2 + m_4^2C_5^2 + C_6^2)f_x}. \tag{B.11}$$

In this case, we have

$$\sigma_{Code}^C = \frac{\sigma_P}{c}\sqrt{N_{MIN}}, \tag{B.12}$$

where the value N_{MIN} is independent of the combined frequency f_x. Expressed in another way, the minimal σ^C_{Code} can be determined, when the integer coefficients a_x, b_x and c_x for the phase observations and the scaling factors C_4, C_5 and C_6 are given. At the same time, all six weighting coefficients γ_i $(i = 1, \cdots, 6)$ are given up to a common factor f_x (see Equations B.4, 7 and 11), that does not affect N_{MIN}.

The phase noise plays only a secondary role compared to the code noise, but it still needs to be considered. Assuming that the phase observation noise is identical in either meters or cycles for all the three frequencies, it turns out that the combined phase noise σ^C_{Phase} in cycles is also independent of the combined frequency f_x:

$$\begin{aligned} \sigma^C_{Phase} &= \frac{\sqrt{\gamma_1^2+\gamma_2^2+\gamma_3^2}\cdot\sigma_L}{\lambda_x} = \frac{\sqrt{a_x^2f_1^2+b_x^2f_2^2+c_x^2f_3^2}\cdot\sigma_L}{c}, \quad or \\ \sigma^C_{Phase} &= \frac{\sqrt{\gamma_1^2\lambda_1^2+\gamma_2^2\lambda_2^2+\gamma_3^2\lambda_3^2}\cdot\sigma^C_L}{\lambda_x} = \sigma^C_L\sqrt{a_x^2+b_x^2+c_x^2}, \end{aligned} \tag{B.13}$$

where σ_L and σ^C_L represent the phase observation noise of the three carrier frequencies in meters and in cycles, respectively.

The entire combined noise σ^C in cycles is, thus, also independent of the combined frequency f_x and can be formulated as:

$$\sigma^C = \sqrt{(\sigma^C_{Code})^2+(\sigma^C_{Phase})^2}. \tag{B.14}$$

To eliminate receiver and satellite electronic delays, typically double differences are formed for ambiguity resolution. Assuming that the linearly combined measurements have a white noise, the formal errors σ^{CD}_{Amb} (in cycles) of the ambiguity estimates on the double-difference level decrease inversely proportional to the square root of the number of observation epochs n:

$$\sigma^{CD}_{Amb} = \frac{2\sqrt{(\sigma^C)^2+(\sigma^C_{MP})^2}}{\sqrt{n}}, \tag{B.15}$$

where σ^C_{MP} represents the multipath errors in cycles for each station. In Equation B.15 it is assumed that both stations have uncorrelated code and phase noise and multipath errors. The factor of two in Equation B.15 results from forming of double-differences.

With the assumption that the observation noise has a normal (Gaussian) distribution, the probability for correct ambiguity-fixing, namely the success rate, can be calculated according to Wang et al. (2004):

$$P^D_{correct} = P(|x| < \frac{1}{2}) = P(|z| < \frac{1}{2\sigma^{CD}_{Amb}}), \tag{B.16}$$

where $P^D_{correct}$ represents the probabilities for a correct ambiguity-fixing on the double-difference level, and x and z stand for the unnormalized and normalized fractional parts of the ambiguity estimates in cycles, respectively.

The probability of correctly fixing the ambiguity is then calculated with the cumulative distribution function of the standardized normal distribution $\Phi(m)$:

$$P(|z| < m) = \Phi(m) - (1 - \Phi(m)) = 2\Phi(m) - 1, \tag{B.17}$$

with

$$\Phi(m) = \frac{1}{2}(1 + \mathrm{erf}(\frac{m}{\sqrt{2}})),$$

where erf is the error function, and m stands for $\frac{1}{2(\sigma^{CD}_{Amb})}$ in our case.

The best GF and IF triple-frequency linear combinations for different GNSS frequency triplets

To find the IF and GF triple-frequency combinations for GPS signals at L1 ($f_1 = 1575.42$ MHz), L2 ($f_2 = 1227.6$ MHz) and L5 ($f_3 = 1176.45$ MHz) with the lowest σ^C in cycles, the integer coefficients a_x, b_x and c_x were varied in the range of -10 to +10. A phase observation noise of $\sigma_L = 0.01$ cycles was assumed. For the code observation noise, two different sets of scaling factors C_4, C_5 and C_6 were tested. The first set assumes an identical noise level of $\sigma_P = 0.5$ m for all three frequencies ($C_4 = C_5 = C_6 = 1$). The best four combinations resulting in this case are listed in the top part of Table B.1. The second set uses scaling factors according to the CRB (Henkel and Günther, 2012) with $\sigma_P = 2$ m, $C_4 = C_5 = 0.2592$ and $C_6 = 0.0783$ leading to the four combinations given in the bottom part of Table B.1. The entire combined noise values σ^C and σ^C_{CRB} in cycles for these two cases are shown in the sixth column of Table B.1. The six weighting coefficients $\gamma_i (i = 1, \cdots, 6)$ are listed in the third, fourth and fifth column. The wavelength of the linear combinations was set to 1 m. The success rates on the double-difference level with 1 and 10 observation epochs for these two cases are documented in the last two columns. The combinations with opposite signs for a_x, b_x and c_x, which deliver the same σ^C and σ^C_{CRB}, are not listed in Table B.1.

The triple-frequency combinations using code and phase observations simultaneously are not only eliminating the first-order term of the ionospheric refraction and all the geometry-related terms, but they are also reducing the code noise significantly. Compared to the Melbourne-Wübbena combination for double frequencies, which leads to a noise of $\sigma^C = 0.4136$ cycles with the assumption that the code and phase noise equals 0.5 m and 0.01 cycles, respectively, we can benefit more from the triple-frequency linear combinations such as (0,-1,1) with $\sigma^C = 0.0615$ cycles and (1,-4,3) with $\sigma^C = 0.3517$ cycles. We can also see that σ^C_{CRB} for the linear combination (0,-1,1) is much smaller than σ^C, because the observation noise assumed for L5 is much smaller. However, for the other linear combinations, σ^C_{CRB} does not seem to benefit a lot from this smaller noise on L5.

Apart from GPS, the Galileo system will provide signals at E1 (1575.42 MHz), E6 (1278.75 MHz), E5b (1207.14 MHz), E5 (1191.795 Hz) and E5a (1176.45 MHz), and the

Table B.1: IF and GF triple-frequency combinations for GPS with small combined noise

a_x, b_x, c_x		$\gamma_i(i=1,\cdots,6)$			σ^C&σ^C_{CRB} [cycles]	$P^D_{correct}$ [%] n=1	n=10
$C_4 = C_5 = C_6 = 1$							
0, -1, 1	$\gamma_{1,2,3}$	0.0000	-4.0948	3.9242	0.0615	100.0	100.0
	$\gamma_{4,5,6}$	0.0021	0.0759	0.0926			
1, -4, 3	$\gamma_{1,2,3}$	5.2550	-16.3793	11.7726	0.3517	52.28	97.54
	$\gamma_{4,5,6}$	-0.6880	-0.0521	0.0917			
1, -3, 2	$\gamma_{1,2,3}$	5.2550	-12.2845	7.8484	0.3529	52.13	97.49
	$\gamma_{4,5,6}$	-0.6901	-0.1280	-0.0009			
1, -5, 4	$\gamma_{1,2,3}$	5.2550	-20.4742	15.6969	0.3612	51.12	97.14
	$\gamma_{4,5,6}$	-0.6859	0.0238	0.1844			
$C_4 = C_5 = 0.2592 \quad C_6 = 0.0783$							
0, -1, 1	$\gamma_{1,2,3}$	0.0000	-4.0948	3.9242	0.0284	100.0	100.0
	$\gamma_{4,5,6}$	0.0136	0.0132	0.1438			
1, -6, 5	$\gamma_{1,2,3}$	5.2550	-24.5690	19.6211	0.3551	51.86	97.40
	$\gamma_{4,5,6}$	-0.6493	-0.0878	0.4299			
1, -7, 6	$\gamma_{1,2,3}$	5.2550	-28.6638	23.5453	0.3560	51.75	97.36
	$\gamma_{4,5,6}$	-0.6356	-0.0746	0.5737			
1, -5, 4	$\gamma_{1,2,3}$	5.2550	-20.4742	15.6969	0.3564	51.69	97.34
	$\gamma_{4,5,6}$	-0.6629	-0.1010	0.2862			

Chinese Compass system will also transmit multi-frequency signals. The combinations for Galileo, named GalileoA (E1, E6 and E5b), GalileoB (E1, E6 and E5), GalileoC (E1, E6 and E5a) and GalileoD (E1, E5b and E5a), as well as the triple-frequency combination for Compass-III (B1 at 1575.42 MHz, B3 at 1268.52 MHz and B2 at 1191.795 MHz) (Li et al., 2012) were investigated with respect to their noise values. The phase observation noise is set to be 0.01 cycles, while the code observation noise is set to be $\sigma_P = 0.5$ m with scaling factors $C_4 = C_5 = C_6 = 1$ for the first case and $\sigma_P = 2$ m with scaling factors proportional to the CRB for the second case. The CRB for the Galileo signals are 11.14 cm for E1, 1.95 cm for E5, 7.83 cm for E5a and E5b and 11.36 cm for E6 (Henkel and Günther, 2012). For each system, the two linear combinations with the lowest combined noise are listed in Table B.2.

We see that for all investigated GNSS, the combined ambiguities can be rounded to the nearest integers with high success rates after only about 10 observation epochs. Looking at the second best linear combination, Compass-III and most of the Galileo combinations show a better performance than GPS. The σ^C_{CRB} is generally much smaller than σ^C, because the code observation noise assumed in the case of CRB is much smaller than

Table B.2: IF and GF triple-frequency linear combinations for different GNSS with small combined noise

a_x, b_x, c_x	σ^C [cycle]	$P^D_{correct}$ [%] n=1	n=10	a_x, b_x, c_x (CRB)	σ^C_{CRB} [cycle]	$P^D_{correct,CRB}$ [%] n=1	n=10
GalileoA (E1, E6 and E5b)							
0, -1, 1	0.0844	99.70	100.0	0, -1, 1	0.0323	100.0	100.0
1, -3, 2	0.3023	59.17	99.11	1, -3, 2	0.1370	93.19	100.0
GalileoB (E1, E6 and E5)							
0, -1, 1	0.1014	98.63	100.0	0, -1, 1	0.0195	100.0	100.0
1, -2, 1	0.3061	58.58	99.02	1, -5, 4	0.1279	94.94	100.0
GalileoC (E1, E6 and E5a)							
0, -1, 1	0.1182	96.56	100.0	0, -1, 1	0.0431	100.0	100.0
1, -2, 1	0.3068	58.49	99.00	1, -2, 1	0.1379	93.02	99.64
GalileoD (E1, E5b and E5a)							
0, -1, 1	0.0388	100.0	100.0	0, -1, 1	0.0181	100.0	100.0
1, -5, 4	0.3697	50.12	96.75	1, -3, 2	0.1686	86.18	100.0
Compass-III (B1, B3 and B2)							
0, -1, 1	0.0901	99.45	100.0				
1, -3, 2	0.3148	57.29	98.80				

$\sigma_P = 0.5$ m. As long as we do not know the real noise level of the triple-frequency observations, it is hard to decide which of the two selections of scaling factors is more suitable for minimizing the combined noise level of the linear combinations. Therefore, both selections were tested with real data (see Section "Verification with real data").

Resolving ambiguities on the three carrier frequencies

In order to resolve all three ambiguities n_1, n_2 and n_3, three linearly independent linear combinations are required. It is hard, however, to find a third linear combination, because all the combinations with relatively low noise are linearly dependent on the first two combinations given in Tables B.1 and B.2. For this reason, significant research has been performed in recent years to form a third linear combination with relatively low noise. In this section, the results of such an investigation are shown using a general linear combination of the phase observations on three carrier frequencies.

The resolved combined ambiguities from the first two linear combinations, n_x and n_y,

are introduced as known into the third linear combination with the ambiguity named n_z:

$$\begin{aligned} n_x &= a_x n_1 + b_x n_2 + c_x n_3, \quad n_y = a_y n_1 + b_y n_2 + c_y n_3, \\ n_z &= a_z n_1 + b_z n_2 + c_z n_3 \\ &= \frac{b_z c_y - c_z b_y}{b_x c_y - c_x b_y} n_x + \frac{b_z c_x - c_z b_x}{b_y c_x - c_y b_x} n_y + Q(a_z, b_z, c_z) n_1, \end{aligned} \tag{B.18}$$

with

$$Q(a_z, b_z, c_z) = a_z - a_x \frac{b_z c_y - c_z b_y}{b_x c_y - c_x b_y} - a_y \frac{b_z c_x - c_z b_x}{c_x b_y - b_x c_y}.$$

This means that the integer coefficients a_z, b_z and c_z of the third linear combination do not necessarily have to be integers; only a linear combination of a_z, b_z and c_z, here called $Q(a_z, b_z, c_z)$, has to be integer. Because the third linear combination is linearly independent of the first two, the integer $Q(a_z, b_z, c_z)$ is not allowed to be zero.

If the integer coefficients of the first two linear combinations have the pattern $(u, v, -(u+v))$ as listed in Tables B.1 and B.2 (see also the pattern found by Cocard et al. (2008) for the promising triple-frequency GF carrier phase linear combinations), the function $Q(a_z, b_z, c_z)$ always equals $a_z + b_z + c_z$, which means $a_z + b_z + c_z$ has to be an integer. Let us call this integer I:

$$I = a_z + b_z + c_z. \tag{B.19}$$

In order to further reduce the noise, the so-called ambiguity-corrected phase observations from the first two linear combinations can be used instead of the code observations (Li et al., 2010). The phase observations on the three carriers f_1, f_2 and f_3, and both of the ambiguity-corrected combined phase observations $\tilde{L}_x$ and $\tilde{L}_y$ are again combined linearly:

$$L_z = \gamma_{z1} L_1 + \gamma_{z2} L_2 + \gamma_{z3} L_3 + q_1 \tilde{L}_x + q_2 \tilde{L}_y, \tag{B.20}$$

with

$$\begin{aligned} \tilde{L}_x &= \gamma_{x1} L_1 + \gamma_{x2} L_2 + \gamma_{x3} L_3 - n_x \lambda_x, \quad \text{and} \\ \tilde{L}_y &= \gamma_{y1} L_1 + \gamma_{y2} L_2 + \gamma_{y3} L_3 - n_y \lambda_y, \end{aligned}$$

where γ_{xi}, γ_{yi} and γ_{zi} (i=1,2,3) represent the phase weighting coefficients for the three linear combinations, respectively. q_1 and q_2 stand for the weighting coefficients of the ambiguity-corrected phase observations from the first two linear combinations. It should be noted that the ambiguity-corrected phase observations $\tilde{L}_x$ and $\tilde{L}_y$ are neither GF nor IF.

In order to generate an IF and GF combination according to Equation B.20, the following two criteria must be fulfilled (see Equations B.4, B.5 and B.6):

$$\frac{g_z}{f_z} + q_1 \frac{g_x}{f_x} + q_2 \frac{g_y}{f_y} = 0, \tag{B.21}$$

with

$$g_i = a_i f_1 + b_i f_2 + c_i f_3, \quad i = x, y, z,$$

and

$$\frac{h_z}{f_z} + q_1 \frac{h_x}{f_x} + q_2 \frac{h_y}{f_y} = 0, \tag{B.22}$$

with

$$h_i = a_i + b_i \frac{f_1}{f_2} + c_i \frac{f_1}{f_3}, \quad i = x, y, z.$$

The parameters q_1 and q_2 can be calculated as

$$q_1 = \frac{f_x(g_y h_z - g_z h_y)}{f_z(g_x h_y - g_y h_x)}, \quad q_2 = -\frac{f_y(g_x h_z - g_z h_x)}{f_z(g_x h_y - g_y h_x)}. \tag{B.23}$$

In order to calculate the entire combined noise, Equation B.20 can then be expressed based only on the phase observations on the three frequencies:

$$\begin{aligned} L_z &= (\gamma_{z1} + q_1\gamma_{x1} + q_2\gamma_{y1})L_1 + (\gamma_{z2} + q_1\gamma_{x2} + q_2\gamma_{y2})L_2 \\ &\quad +(\gamma_{z3} + q_1\gamma_{x3} + q_2\gamma_{y3})L_3 - q_1 n_x \lambda_x - q_2 n_y \lambda_y. \end{aligned} \tag{B.24}$$

Assuming that the phase observation noise on the three carriers is identical and amounts to σ_L in meters or σ_L^C in cycles, the entire combined noise σ_z^C in cycles of λ_1 (see Equations B.18, B.19 and B.24) for the third linear combination can then be calculated as:

$$\begin{aligned} \sigma_z^C &= \frac{f_z \cdot \sigma_L \sqrt{s_a f_1^2 + s_b f_2^2 + s_c f_3^2}}{|I| \cdot c}, \quad \text{or} \\ \sigma_z^C &= \frac{f_z \cdot \sigma_L^C \sqrt{s_a + s_b + s_c}}{|I|}, \end{aligned} \tag{B.25}$$

with

$$\begin{aligned} s_a &= (\frac{a_z}{f_z} + q_1 \frac{a_x}{f_x} + q_2 \frac{a_y}{f_y})^2, \\ s_b &= (\frac{b_z}{f_z} + q_1 \frac{b_x}{f_x} + q_2 \frac{b_y}{f_y})^2, \\ s_c &= (\frac{c_z}{f_z} + q_1 \frac{c_x}{f_x} + q_2 \frac{c_y}{f_y})^2. \end{aligned}$$

Inserting Equation B.23 into B.25 we obtain the equations

$$s_a = \frac{p_a}{f_z^2}, \quad s_b = \frac{p_b}{f_z^2}, \quad s_c = \frac{p_c}{f_z^2}, \tag{B.26}$$

with

$$\begin{aligned} p_a &= (a_z + a_x \frac{g_y h_z - g_z h_y}{g_x h_y - g_y h_x} - a_y \frac{g_x h_z - g_z h_x}{g_x h_y - g_y h_x})^2, \\ p_b &= (b_z + b_x \frac{g_y h_z - g_z h_y}{g_x h_y - g_y h_x} - b_y \frac{g_x h_z - g_z h_x}{g_x h_y - g_y h_x})^2, \\ p_c &= (c_z + c_x \frac{g_y h_z - g_z h_y}{g_x h_y - g_y h_x} - c_y \frac{g_x h_z - g_z h_x}{g_x h_y - g_y h_x})^2, \end{aligned}$$

where p_a, p_b and p_c are functions of the three carrier frequencies f_1, f_2 and f_3 and the integer coefficients a_i, b_i and c_i $(i = x, y, z)$. They are independent of the three combined frequencies f_x, f_y and f_z.

Inserting Equation B.26 into B.25, we obtain:

$$\begin{aligned} \sigma_z^C &= \frac{\sigma_L \sqrt{p_a f_1^2 + p_b f_2^2 + p_c f_3^2}}{|I| \cdot c}, \quad \text{or} \\ \sigma_z^C &= \frac{\sigma_L^C \sqrt{p_a + p_b + p_c}}{|I|}. \end{aligned} \tag{B.27}$$

We see that σ_z^C (in cycles of λ_1) is independent of the combined frequencies f_x, f_y and f_z. From Equations B.18, B.19 and B.23, it is not hard to get:

$$\begin{aligned} g_i(-a_i, -b_i, -c_i) &= -g_i(a_i, b_i, c_i), \quad h_i(-a_i, -b_i, -c_i) = -h_i(a_i, b_i, c_i), \\ p_a(-a_i, -b_i, -c_i) &= p_a(a_i, b_i, c_i), \\ p_b(-a_i, -b_i, -c_i) &= p_b(a_i, b_i, c_i), \\ p_c(-a_i, -b_i, -c_i) &= p_c(a_i, b_i, c_i), \quad i = x, y, z. \end{aligned} \tag{B.28}$$

As a result, σ_z^C will not be affected, if all the signs of the integer coefficients a_i, b_i and c_i are changed simultaneously:

$$\sigma_z^C(-a_i, -b_i, -c_i) = \sigma_z^C(a_i, b_i, c_i). \tag{B.29}$$

Equation B.27 can also be formulated with the phase observation noise and a noise factor μ or μ^C:

$$\sigma_z^C = \sigma_L \cdot \mu = \sigma_L^C \cdot \mu^C, \tag{B.30}$$

with

$$\mu := \frac{\sqrt{p_a f_1^2 + p_b f_2^2 + p_c f_3^2}}{|I| \cdot c}, \quad \mu^C := \frac{\sqrt{p_a + p_b + p_c}}{|I|}.$$

If the integer coefficients (a_x, b_x, c_x) and (a_y, b_y, c_y) of the first two linear combinations follow the pattern (u, v, $-(u+v)$) as in Table B.1 and B.2, the noise factors μ and μ^C are independent of the integer coefficients a_i, b_i and c_i $(i = x, y, z)$. This conclusion agrees with the results of Li et al. (2010). We get

$$\begin{aligned} \mu &= \frac{\sqrt{f_1^4(f_2^2 - f_3^2)^2 + f_2^4(f_1^2 - f_3^2)^2 + f_3^4(f_1^2 - f_2^2)^2}}{|(f_1 - f_2)(f_1 - f_3)(f_2 - f_3)| \cdot c}, \\ \mu^C &= \frac{\sqrt{f_1^2(f_2^2 - f_3^2)^2 + f_2^2(f_1^2 - f_3^2)^2 + f_3^2(f_1^2 - f_2^2)^2}}{|(f_1 - f_2)(f_1 - f_3)(f_2 - f_3)|}. \end{aligned} \tag{B.31}$$

σ_z^C (in cycles of λ_1) was calculated for different GNSS frequency triplets with a predefined phase observation noise $\sigma_L = 5$ mm or $\sigma_L^C = 0.01$ cycles. The results are shown in Table B.3. The second and the fourth column list σ_z^C with $\sigma_L = 5$ mm and $\sigma_L^C =$

0.01 cycles, while the third and fifth column document the corresponding noise factors μ and μ^C. We see that the third linear combinations of Compass-III, GalileoA, GalileoB and GalileoC reach a lower noise factor than GPS. The noise factors μ and μ^C for GalileoC with E1, E6 and E5a are about 40% smaller than those for GPS.

The formal errors of the n_1 ambiguity estimates decrease with an increasing number of observation epochs (see Equation B.15). Figure B.1 (top) shows the formal errors σ_{Amb}^{CD} of the n_1 ambiguity estimates on the double-difference level for different GNSS frequency triplets ignoring the multipath errors because of the low weighting coefficients of the code observations (see Table B.1). The noise level of the phase observations is set to be $\sigma_L^C = 0.01$ cycles. We immediately see that the combinations GalileoA, GalileoB, GalileoC and Compass-III show an even better behavior than GPS. For GalileoC (black line) σ_{Amb}^{CD} is lower than 0.2 cycles after 213 epochs and reaches about 0.13 cycles after 500 epochs. The formal errors of the n_1 ambiguity estimates are also directly related to the success rates (see Equation B.16) of the ambiguity resolution, which are shown in Figure B.1 (bottom) with $\sigma_L = 0.01$ cycles. We conclude that under the assumptions made, the success rates for GalileoB (green line), GalileoC (black line) and Compass-III (yellow line) are above 90% after 200 epochs.

The best linear combination after resolving all three ambiguities

After resolving n_1 according to Section "Resolving ambiguities on the three carrier frequencies", the other two ambiguities n_2 and n_3 can easily be computed using the resolved combined ambiguities n_x and n_y (see Equation B.18). Making use of our knowledge of all three integers n_1, n_2 and n_3, we are now looking for the best IF and GB linear combination with minimized noise in meters.

With the help of Equation B.1, the triple-frequency phase linear combination can be

Table B.3: Combined noise and the noise factors of the third linear combination for different GNSS frequency triplets

	σ_L=5 mm		σ_L=0.01 cycles	
	σ_z^C [cycles]	μ	σ_z^C [cycles]	μ^C
GPS (L1,L2,L5)	5.0676	1013.5	2.5082	250.8
GalileoA (E1,E6,E5b)	4.5348	907.0	2.1542	215.4
GalileoB (E1,E6,E5)	3.6707	734.1	1.7431	174.3
GalileoC (E1,E6,E5a)	3.0754	615.1	1.4588	145.9
GalileoD (E1,E5b,E5a)	7.9361	1587.2	3.9813	398.1
Compass-III (B1,B3,B2)	3.9918	798.4	1.9123	191.2

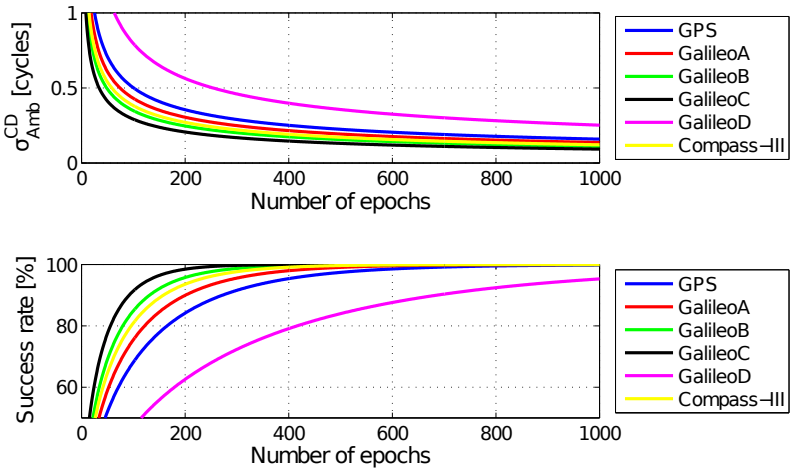

Figure B.1: Formal errors of the n_1 ambiguity estimates (top) and the success rates (bottom) as a function of the number n of observation epochs

formulated as:

$$\begin{aligned} L_P &= \gamma_1 L_1 + \gamma_2 L_2 + \gamma_3 L_3 - (\gamma_1 \lambda_1 n_1 + \gamma_2 \lambda_2 n_2 + \gamma_3 \lambda_3 n_3) \\ &= (\gamma_1 + \gamma_2 + \gamma_3)(\rho + \delta_{tro} + c\delta_r - c\delta^s) - (\gamma_1 + \frac{f_1^2}{f_2^2}\gamma_2 + \frac{f_1^2}{f_3^2}\gamma_3) I_1, \end{aligned} \tag{B.32}$$

where L_P represents the triple-frequency phase linear combination.

Li et al. (2012) have shown that the coefficients γ_1, γ_2 and γ_3 are just functions of the three frequencies. The minimal combined noise values σ_{min}^{MD} in meters for different GNSS frequency triplets on the double-difference level are listed in Table B.4 with the assumption that the phase observation noise is 0.01 cycles on each of the three frequencies. After resolving the three ambiguities, the minimized noise of the phase GB and IF linear combination is then about 1 cm for all the investigated GNSS frequency triplets.

Table B.4: Minimized combined noise of the GB and IF linear combination after solving the three ambiguities in meters on the double-difference level for different GNSS

	γ_1	γ_2	γ_3	σ_{min}^{MD} [m]
GPS (L1,L2,L5)	2.3522	-0.4964	-0.8557	0.0102
GalileoA (E1,E6,E5b)	2.5422	-0.4559	-1.0863	0.0113
GalileoB (E1,E6,E5)	2.4510	-0.3679	-1.0831	0.0109
GalileoC (E1,E6,E5a)	2.3604	-0.2875	-1.0729	0.0106
GalileoD (E1,E5b,E5a)	2.3241	-0.5591	-0.7649	0.0101
Compass-III (B1,B3,B2)	2.4521	-0.4159	-1.0362	0.0109

Verification with real data

The theoretical derivations of the GF and IF triple-frequency linear combinations were verified with real GPS and Galileo data. The two GPS–IIF satellites PRN01 (SVN63) and PRN25 (SVN62) are sending signals on the three frequencies f_1, f_2 and f_5 (USNO, 2012). Both of the GIOVE (Galileo In-Orbit Validation Element) satellites, GIOVE–A and GIOVE–B, and the two Galileo In-Orbit Validation (IOV) satellites (PFM and FM2), which were launched in October 2011, are also providing signals on more than two frequencies (NAVSAS Group, 2012). The 24-h Multi-GNSS Experiment (M–GEX) data (Weber, 2012) with a sampling rate of 30 s were collected for the period 29 April 2012 to 9 May 2012 from the IGS website `ftp://cddis.gsfc.nasa.gov/pub/gps/data/campaign/mgex/daily/rinex3/2012` (Noll et al., 2009) in the format RINEX 3.00 (Gurtner, 2007; Januszewski, 2011). About 30 M–GEX stations were available in this time period (see Figure B.2).

Fractional parts and formal errors of n_x and n_y

In order to form double-differenced triple-frequency linear combinations, at least two satellites of each system providing more than two frequencies have to be available. The two GPS–IIF satellites PRN01 and PRN25 can only be observed simultaneously from two stations during a short time interval at low elevation angles, while a relatively long overlapping time can be found for E11 (Galileo–IOV satellite PFM), E12 (Galileo–IOV satellite FM2) and E52 (GIOVE–B satellite) in the available M–GEX dataset. Because no signal on frequency E6 was recorded simultaneously for two stations with a baseline shorter than 1,000 km, the frequency combination GalileoD (E1, E5b, E5a) (see Figure B.1; Tables B.2, B.3) was used for the processing of Galileo baselines. An elevation mask of 6° was set for all satellites. The observations were weighted with the elevation angle β_E according to

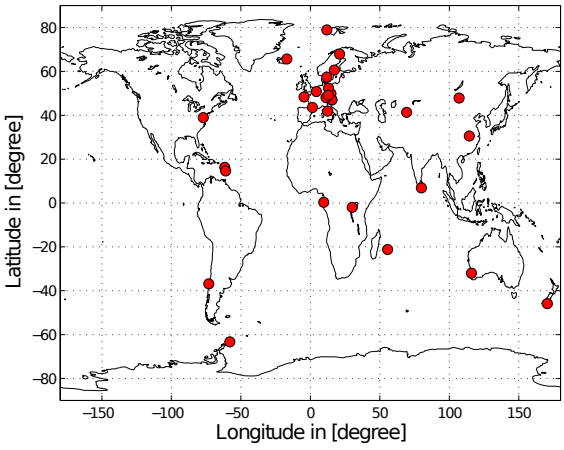

Figure B.2: Multi-GNSS experiment (M–GEX) stations on 29 April 2012

$$\begin{aligned} P_{Z_r^s} &= \sin(\beta_E)^2, \\ P_D &= \frac{1}{\frac{1}{P_{Z_1^1}} + \frac{1}{P_{Z_1^2}} + \frac{1}{P_{Z_2^1}} + \frac{1}{P_{Z_2^2}}}, \end{aligned} \tag{B.33}$$

where $P_{Z_r^s}$ and P_D represent the weight of the observations on the zero-difference and double-difference level.

Figure B.3 shows the fractional parts and the formal errors of the estimated n_x and n_y for two Galileo baselines, namely ons1 (Onsala, Sweden) – mar7 (Gavle, Sweden) with a baseline length of 470 km and brux (Brussels, Belgium) – grab (Graz, Austria) with a baseline length of 913 km (see Figure B.3a, b) as well as for two GPS baselines ons1–mar7 and kir8 (Kiruna, Sweden) – mar7 with a baseline length of 832 km (see Figure B.3c, d). Generally speaking, the estimated n_x and n_y from the first two GF and IF linear combinations mostly have an absolute fractional part below 0.2 cycles with a formal error smaller than 0.1 cycles. We see that the formal errors decrease with increasing number of observation epochs and are mostly below or around the expected values (red line and blue line; according to Equation B.15) except for some outliers generated by the Galileo baseline brux–grab. It is not hard to see that for the Galileo linear combinations, the results generated from baseline brux–grab are generally worse than the results of the baseline ons1–mar7. The reason certainly is that different tracking modes or channels for the same frequency (Gurtner, 2007) exhibit biases that do not cancel by double-differencing. In addition, since different antenna types are part of the baseline brux–grab, Phase Center Variations (PCVs) may also lead to deviations from integers. It should be noted that signals were received on the same channels for the Galileo baseline ons1–mar7 (E1X, E5bX, E5aX), but at different channels for the baseline brux–grab with E1C, E5bQ and E5aQ for station brux and E1X, E5bX, E5aX for station grab. For the GPS baselines, the results using the channels (L1C, L2W, L5X) are plotted.

Impact of receiver tracking modes on n_x and n_y

To have a closer look at the differences in the results caused by using different tracking channels, the fractional parts and the formal errors of the estimated n_x and n_y ambiguities were compared using different tracking channels for both of the GPS baselines. Only identical ambiguities (same baseline, same day and same number of observation epochs) were compared and the standard deviations of the absolute fractional parts (see column 2 and 3) and the standard deviations of the formal errors (column 4 and 5) for each tracking channel combination are listed in Table B.5. We see that the fractional n_x of the combination L1C, L2W and L5X for one station and L1C, L2X and L5X for the other station are the smallest for the case of 45 epochs, while using channels L1C, L2W and L5X for both stations seems to be the best choice for 160 epochs. Among different choices of tracking channels, we did not observe big differences for the formal errors. As expected,

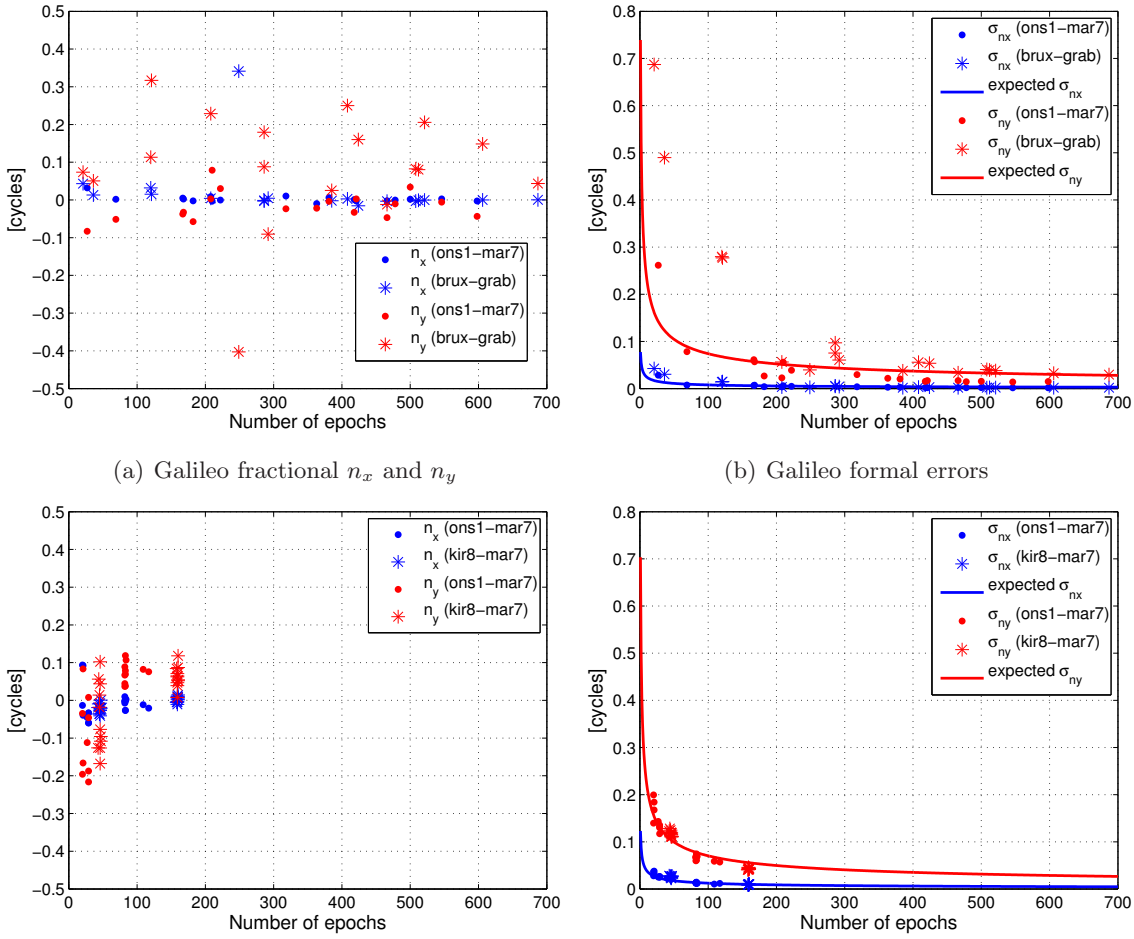

(a) Galileo fractional n_x and n_y

(b) Galileo formal errors

(c) GPS fractional n_x and n_y

(d) GPS formal errors

Figure B.3: Fractional parts (a), (c) and formal errors (b), (d) of the estimated n_x and n_y for the Galileo baselines ons1–mar7 and brux–grab and for the GPS baselines ons1–mar7 and kir8–mar7 from 30 April 2012 to 9 May 2012

the formal errors of the linear combinations with about 160 epochs are generally smaller than those with only 45 epochs. The scaling factors of the formal errors between the two cases are bigger than the expected scaling factors $\sqrt{160/45}$ because of the elevation dependency. For the case of 160 epochs, the elevation angles are generally larger than for the 45 epoch case. We also see that the real errors (column 2 and 3) are slightly smaller than the formal errors (column 4 and 5) for the case of 45 epochs and bigger than the formal errors for the case of 160 epochs. The systematic effects (such as multipath errors) play a more and more important role as the time interval considered is increasing. A more concrete investigation concerning the channel combinations will be possible, if more M–GEX data is available in the future.

Table B.5: Standard deviations of the absolute values of the fractional parts n_x and n_y and standard deviations of their formal errors for different channel combinations with different numbers of observation epoches

	Δn_x [cycles]	Δn_y [cycles]	σ_{nx} [cycles]	σ_{ny} [cycles]
Number of observation epochs: ca. 45				
L1C,L2W,L5X - L1C, L2W, L5X	0.0254	0.0932	0.0255	0.1169
L1C,L2X,L5X - L1C, L2X, L5X	0.0190	0.0902	0.0232	0.1180
L1C,L2W,L5X - L1C, L2X, L5X	0.0178	0.0974	0.0247	0.1181
L1C,L2X,L5X - L1C, L2W, L5X	0.0433	0.0866	0.0243	0.1168
Number of observation epochs: ca. 160				
L1C,L2W,L5X - L1C, L2W, L5X	0.0082	0.0782	0.0095	0.0425
L1C,L2X,L5X - L1C, L2X, L5X	0.0126	0.0606	0.0087	0.0431
L1C,L2W,L5X - L1C, L2X, L5X	0.0357	0.0541	0.0093	0.0431
L1C,L2X,L5X - L1C, L2W, L5X	0.0198	0.0847	0.0090	0.0425

Scaling factors for the code noise

As discussed in Section "GF and IF triple-frequency linear combinations", two different sets of scaling factors for the code observation noise on the three frequencies, namely the identical scaling factors $C_4 = C_5 = C_6 = 1$ and the scaling factors according to CRB, were tested with real data. Since the overlapping time interval for the observation of the two GPS satellites PRN01 and PRN25 is very short for most of the baselines, only real data of the Galileo satellites from 29 April 2012 to 9 May 2012 was used for this analysis. The differences in the formal errors using the two sets of scaling factors (CRB scaling factors minus identical scaling factors) are shown in Figure B.4. We see that in most of the cases, using identical scaling factors generates smaller formal errors for the combined ambiguity n_y of the second linear combination, especially for ambiguities n_y with short observation intervals. For the first linear combination, the case using identical scaling factors is also slightly better than using the CRB scaling factors. This gives a hint that the actual measurement noise levels of the code observations on different frequencies should be studied more carefully. In view of the better performance, the ambiguities n_x and n_y based on $C_4 = C_5 = C_6 = 1$ were thus introduced for the analysis of the third linear combination.

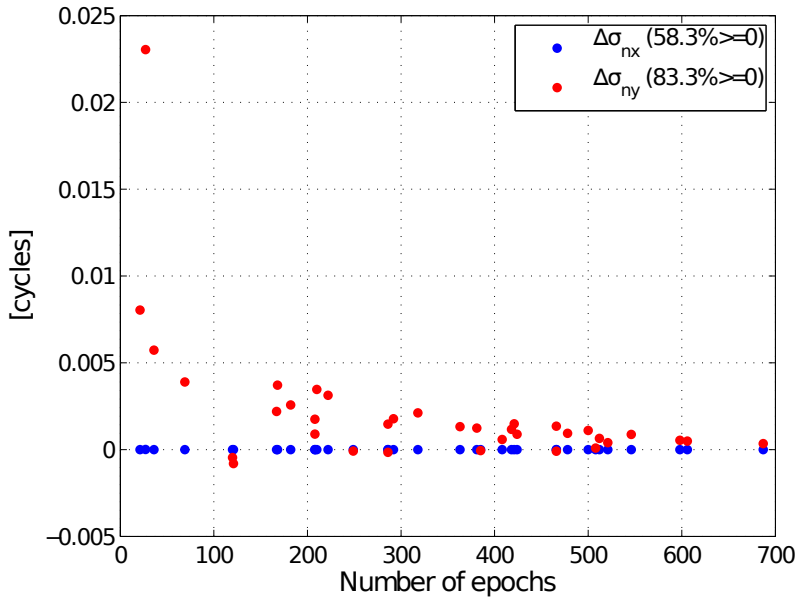

Figure B.4: Differences of the formal errors for the first two linear combinations using the CRB and identical scaling factors for Galileo baselines ons1–mar7 and brux–grab from 29 April 2012 to 9 May 2012.

The third linear combination

The linear combinations of the real observation data which were used to fix n_x, n_y and n_1 for the baseline ons1–mar7 and satellites E11 and E52 between 1:09 and 5:08 am on 29 April 2012 are shown in Figure B.5 as an example. The third linear combination L_z^{CD} was corrected by $\frac{b_z c_y - c_z b_y}{b_x c_y - c_x b_y} n_x + \frac{b_z c_x - c_z b_x}{b_y c_x - c_y b_x} n_y$ and divided by the integer I (see Equation B.18). We see that the core problem of triple-frequency ambiguity resolution is fixing the ambiguities n_1 with the third linear combination.

The triple-frequency combinations for the baselines ons1–mar7 and brux–grab on 29 April 2012 are listed in Table B.6. The frequencies on L1, L2 and L5 and on E1, E5b and E5a were available and used when forming triple-frequency linear combinations. In Table B.6, the channels which generate the lowest formal error for n_1 on 29 April 2012 were selected for each baseline. The second and fourth column document the fractional parts of the estimated combined ambiguities n_x and n_y, and the third and fifth column list their corresponding formal errors. The estimated n_1 from the third linear combination and its formal error are listed in the sixth and seventh column, and the last column lists the expected formal errors σ_{n1}^E of n_1 calculated with the theoretical derivations (see Equations B.15, B.30) based on the assumption that the phase observation noise is 0.01 cycles and independent of the elevation angle.

We see that for the third combined ambiguity, the formal error is sometimes bigger than expected and sometimes smaller. The relatively big formal error of n_1 is very likely

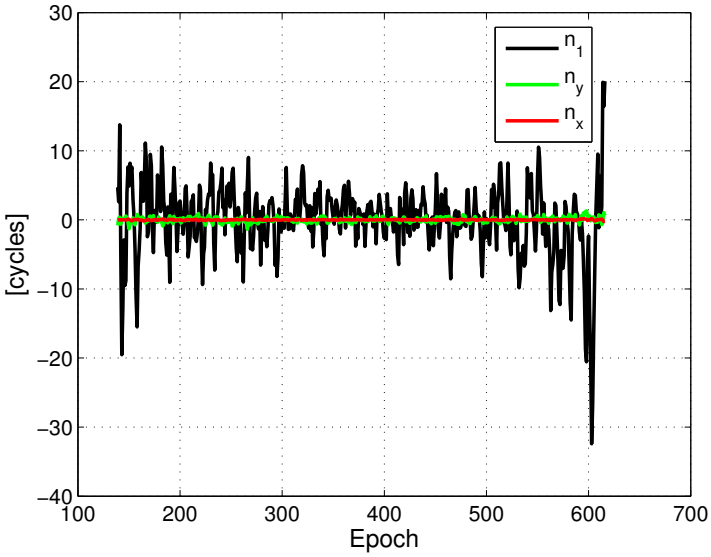

Figure B.5: The three linear combinations used for fixing n_x, n_y and n_1 for baseline ons1–mar7 and satellites E11 and E52 between 1:09 am and 5:08 am on April 29, 2012

Table B.6: The estimated ambiguities and their formal errors for three linearly independent combinations on the double-difference level using M–GEX data on 29 April 2012

Number of epochs	n_x [cycles]	σ_{nx} [cycles]	n_y [cycles]	σ_{ny} [cycles]	n_1 [cycles]	σ_{n1} [cycles]	σ^E_{n1} [cycles]
ons1–mar7 (470 km) G01, G25 (L1C, L2X, L5X – L1C, L2W, L5X)							
127	-0.0234	0.0110	0.0891	0.0588	-0.2511	0.5938	0.4451
kir8–mar7 (832 km) G01, G25 (L1C, L2X, L5X – L1C, L2W, L5X)							
159	-0.0186	0.0093	0.0790	0.0412	-0.3252	0.5109	0.3978
47	-0.0387	0.0251	-0.0745	0.1106	0.3466	1.3730	0.7317
ons1–mar7 (470 km) E11, E52 (E1X, E5bX, E5aX – E1X, E5bX, E5aX)							
478	-0.0005	0.0018	-0.0103	0.0144	0.1667	0.1864	0.3642
168	0.0026	0.0072	-0.0326	0.0568	-0.1184	0.7364	0.6143
brux–grab (913 km) E11, E12 (E1C, E5bQ, E5aQ – E1X, E5bX, E5aX)							
466	-0.0032	0.0018	-0.0123	0.0334	-0.3812	0.1594	0.3689
121	0.0153	0.0147	0.3171	0.2771	0.0640	1.3219	0.7239

caused by the real observation noise, which is bigger than expected, or the effects that are included in the observation noise such as, e.g. multipath errors. To have a closer look, Figure B.6a, b shows the third combined observation L_z^{CD} in cycles on the double-difference level divided by the factor μ^C for different pairs of stations and satellites. An

offset was subtracted for each pair and each time interval. The elevation angles for the two Galileo baselines are shown in Figure B.6c, d. We see an obvious correlation between the elevation angles, the observation noise and the formal errors of the estimated n_1.

The standard deviation σ_L^{CD} of the combined phase observations $\frac{L_z^{CD}}{\mu^C}$ in Figure B.6a, b and the mean values of the elevation-dependent weights of the double-differenced observations are given in Table B.7. The expected phase observation noise σ_L^{ECD} on the double-difference level is 0.02 cycles.

It is not hard to see that the real noise for short observation intervals is in some cases bigger than 0.02 cycles due to the low elevation angles (small weights), which results in relatively big formal errors in Table B.6.

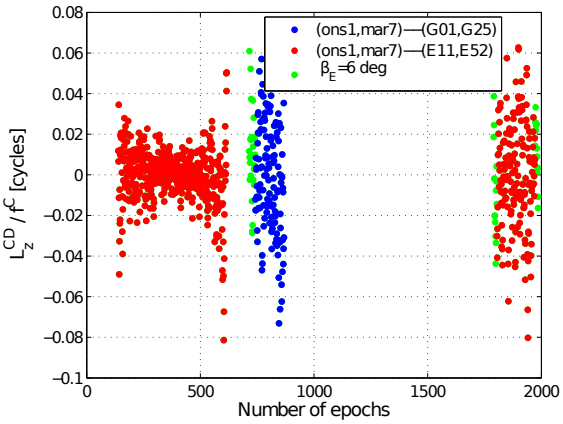

(a) $\frac{L_z^{CD}}{\mu^C}$ for ons1–mar7

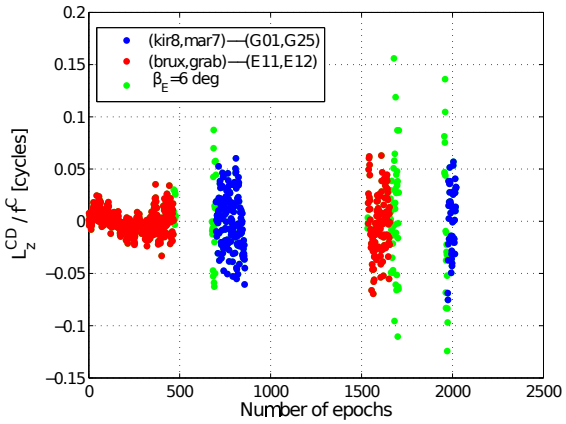

(b) $\frac{L_z^{CD}}{\mu^C}$ for kir8–mar7 and brux–grab

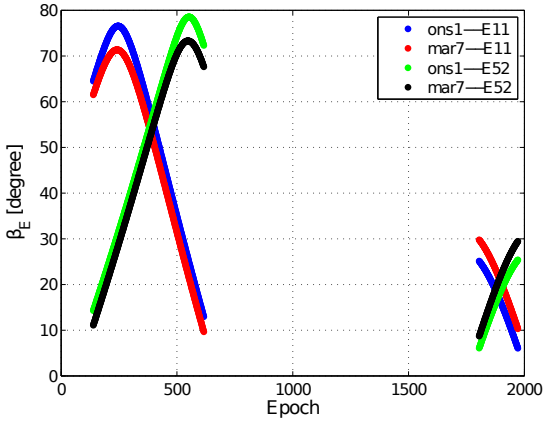

(c) Elevation of ons1–mar7

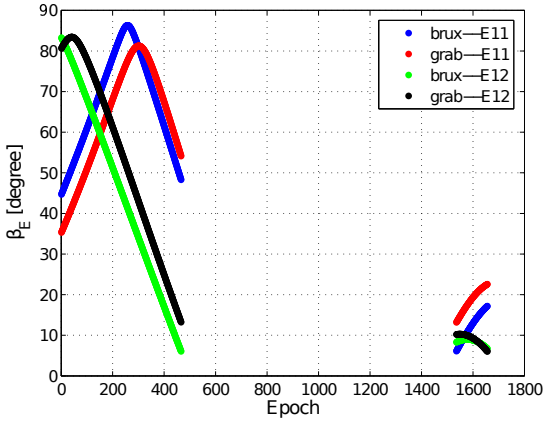

(d) Elevation of kir8–mar7 and brux–grab

Figure B.6: The third combined observation L_z^{CD} in cycles on the double-difference level divided by factor μ^C for baseline (a) ons1–mar7 and (b) kir8–mar7 and brux–grab and the corresponding elevation angles for the two Galileo baselines (c) ons1–mar7 and (d) brux–grab on 29 April 2012. The green dots represent the observations with an elevation angle lower than 6°

Table B.7: Real phase observation noise for some double-differenced observations on 29 April 2012

Baseline	Satellites	Number of epochs	σ_L^{CD} [cycles]	P_D (Equation B.33)	σ_L^{ECD} [cycles]
ons1–mar7 (470 km)	G01, G25	127	0.0269	0.0128	0.0200
	E11, E52	478	0.0133	0.1042	0.0200
		168	0.0259	0.0190	0.0200
kir8–mar7 (832 km)	G01, G25	159	0.0265	0.0197	0.0200
		47	0.0323	0.0092	0.0200
brux–grab (913 km)	E11, E12	466	0.0102	0.1393	0.0200
		121	0.0291	0.0078	0.0200

Figure B.7 shows the formal errors of the estimated n_x, n_y and n_1 for (a) the two Galileo baselines and (b) the two GPS baselines for the time period from 29 April 2012 to 9 May 2012. The red, blue and black dots represent the formal errors of the estimated n_x, n_y and n_1, respectively. The magenta lines stand for the expected formal errors of n_1 with the assumption that the phase observation noise equals 0.01 cycles on the zero-difference level. They correspond to the magenta line (Galileo) and the blue line (GPS) in Figure B.1 (top). The green line marks the boundary of 0.2 cycles for the formal errors. We see that the formal errors decrease with an increasing number of observation epochs. n_x and n_y, which are determined from the first two linear combinations, are generally much easier to be fixed than n_1 from the third linear combination. Most of the formal errors for n_1 are below or around the expected values, which suggests a phase observation noise around or lower than the assumed 0.01 cycles, except for some cases with short observation intervals and low elevation angles. The formal errors for n_1 are mostly below 0.2 cycles, if the number of observation epochs is larger than 400 epochs.

Table B.8 lists the real errors, i.e. the absolute fractional parts, and the formal errors of the estimated n_x, n_y and n_1 for the cases with more than 400 observation epochs for both of the Galileo baselines. We see that the real errors are mostly smaller than 0.01 cycles for n_x and 0.15 cycles for n_y. The real errors for the first two linear combinations are sometimes bigger than the formal errors, but do not affect the fixing of n_x and n_y. For the third linear combination, the real errors are about 67% bigger than the formal errors and are sometimes bigger than 0.3 cycles. The systematic effects, such as multipath errors, that are present in the phase-only observations, result in difficulties for the ambiguity resolution of n_1. We also see that the behavior of the baseline ons1–mar7 is much better than the baseline brux–grab for both, the second and the third linear combination. The biases caused by different tracking channels (see Section "Impact of receiver tracking modes on n_x and n_y") and, possibly, PCVs caused by different antenna types play an important role in ambiguity resolution.

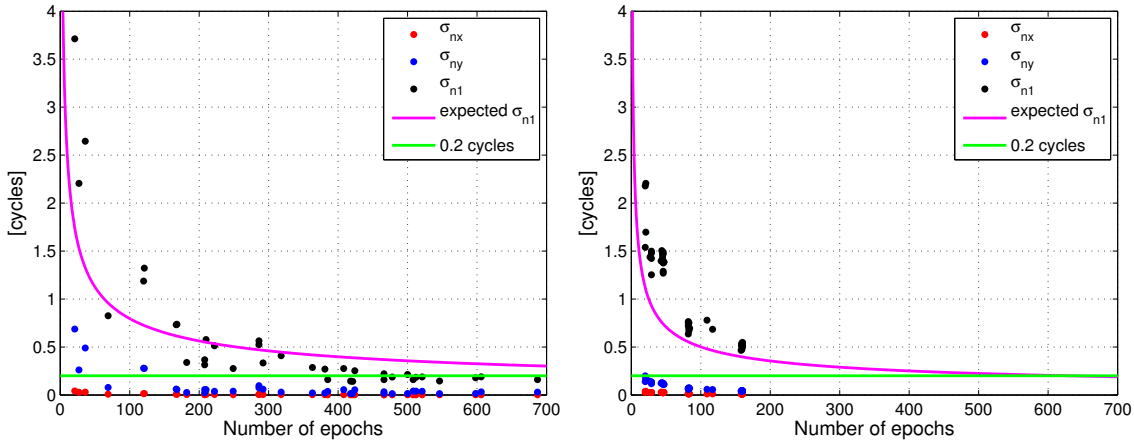

(a) Galileo baselines

(b) GPS baselines

Figure B.7: Formal errors of estimated n_x, n_y and n_1 for Galileo baselines ons1–mar7 and brux–grab and GPS baselines ons1–mar7 and kir8–mar7 from Am 29 April 2012 to 9 May 2012

Table B.8: Real and formal errors of the estimated n_x, n_y and n_1 for both of the Galileo baselines with more than 400 observation epochs

Number of epochs	$\lvert\delta n_x\rvert$ [cycles]	σ_{nx} [cycles]	$\lvert\delta n_y\rvert$ [cycles]	σ_{ny} [cycles]	$\lvert\delta n_1\rvert$ [cycles]	σ_{n1} [cycles]
ons1–mar7						
418	0.0008	0.0020	0.0327	0.0153	0.1152	0.1443
421	0.0028	0.0018	0.0026	0.0168	0.2949	0.1418
466	0.0020	0.0020	0.0469	0.0168	0.3854	0.2210
478	0.0005	0.0018	0.0103	0.0144	0.1667	0.1864
500	0.0017	0.0020	0.0342	0.0154	0.1872	0.2132
546	0.0026	0.0015	0.0058	0.0140	0.2781	0.1451
598	0.0026	0.0016	0.0436	0.0150	0.1367	0.1792
brux–grab						
408	0.0028	0.0031	0.2499	0.0558	0.3949	0.2758
424	0.0156	0.0031	0.1600	0.0537	0.3015	0.2522
466	0.0032	0.0018	0.0123	0.0334	0.3812	0.1594
508	0.0031	0.0018	0.0825	0.0404	0.3839	0.1595
512	0.0009	0.0023	0.0802	0.0393	0.1572	0.1847
521	0.0003	0.0021	0.2056	0.0381	0.4465	0.1882
606	0.0000	0.0019	0.1483	0.0326	0.3810	0.1897
687	0.0003	0.0018	0.0436	0.0295	0.2971	0.1594

However, with more and more Galileo and GPS satellites providing three frequencies in the near future, longer observation times including also higher elevation angles can be expected. It will, thus, be possible to obtain a higher success rate for fixing n_1 in the third linear combination, i.e. more n_1 ambiguities with a formal error lower than 0.2 cycles will result. To achieve better results, it will also be necessary to calibrate the PCVs as well as the differential code biases (DCBs) between channels. Furthermore, if the signals on E6 from the Galileo satellites and the signals on B1, B3 and B2 from the Compass-III satellites can be received by more stations in the future, the linear combinations of GalileoA, GalileoB, GalileoC and Compass-III (see Table B.3) will be able to generate much better results for n_1, namely better by a factor of two to three.

Summary and conclusions

In this work, we presented a simplified method for ambiguity resolution using triple-frequency GF and IF linear combinations. The code and phase observations on the three frequencies were simultaneously used to identify the two GF and IF linear combinations with the lowest noise level. It has been demonstrated that the noise level after forming the linear combinations is independent of the combined wavelength. The third linear combination with a low noise level is much more difficult to be found and poses the core problem in triple-frequency ambiguity resolution. A general method using the ambiguity-corrected phase observations without any constraints was used to search for the optimal GF and IF linear combination. We analytically demonstrated that the combined noise level is only a function of the three frequencies and not depending on the details of the linear combination. The resulting frequency-dependent factor was investigated for different GNSS frequency triplets. The Galileo combination using E1, E6 and E5a shows the best behavior among all the systems.

The theoretical derivations were verified with real data. Different scaling factors for the code noise on the three frequencies were set and tested. Using identical scaling factors has been shown to be better than using scaling factors derived from the CRB of the signals, especially for the second linear combination. The formal errors of the estimated ambiguities using E1, E5b and E5a, which is expected to show the worst performance among different GNSS triple-frequency combinations in our investigation, are mostly better than expected and below 0.2 cycles, if the observation span is longer than 400 epochs. The ambiguities with big formal errors have usually short observation times and low elevation angles. Because the number of the available triple-frequency satellites is very limited at the moment, the observation time for each ambiguity on the double-difference level is in most of the cases relatively short. With more and more triple-frequency satellites and better calibrations of PCVs and DCBs between channels in the near future, we can expect a more reliable ambiguity resolution. Furthermore, if the Galileo E6 signal of more stations will become available, an improvement factor of two to three in total can be expected.

Acknowledgments

This work was funded by ESA as part of the project (Satellite and Station Clock Modeling for GNSS, Reference: AO/1-6231/09/D/SR). We would like to thank M. Müller from the Institute of Geodesy and Photogrammetry, ETH Zürich for processing the Galileo Two Line Element Set (TLE) (TLE, 2012) and T.S. Kelso from CelesTrack for providing TLE of the four Galileo satellites (GIOVE–A, GIOVE–B, GALILEO–PFM and GALILEO–FM2) for the time interval April 29, 2012 to May 9, 2012. We also want to thank IGS for providing triple-frequency M–GEX data on its archive (`ftp://cddis.gsfc.nasa.gov/pub/gps/data/campaign/mgex/`).

C Paper C

Paper C was originally published as

Wang K., Rothacher M. (2015): GNSS triple-frequency geometry-free and ionosphere-free track-to-track ambiguities, Advances in Space Research 55(11): 2668-2677. doi:10.1016/j.asr.2015.02.028.

The final publication is available at `http://www.sciencedirect.com/science/article/pii/S0273117715001568`.

GNSS triple-frequency geometry-free and ionosphere-free track-to-track ambiguities

K. Wang[a], M. Rothacher[a]

[a]Institute of Geodesy and Photogrammetry, ETH Zurich, Robert-Gnehm-Weg 15, 8093 Zurich, Switzerland

Abstract

During the last few years, more and more GNSS satellites have become available sending signals on three or even more frequencies. Examples are the GPS Block IIF and the Galileo In-Orbit-Validation (IOV) satellites. Various investigations have been performed to make use of the increasing number of frequencies to find a compromise between eliminating different error sources and minimizing the noise level, including the investigations in the triple-frequency geometry-free (GF) and ionosphere-free (IF) linear combinations, which eliminate all the geometry-related errors and the first-order term of the ionospheric delays.

In contrast to the double-difference GF and IF ambiguity resolution, the resolution of the so-called track-to-track GF and IF ambiguities between two tracks of a satellite observed by the same station only requires one receiver and one satellite. Most of the remaining errors like receiver and satellite delays (electronics, cables, etc.) are eliminated, if they are not changing rapidly in time, and the noise level is reduced theoretically by a factor of square root of two compared to double-differences. This paper presents first results concerning track-to-track ambiguity resolution using triple-frequency GF and IF linear combinations based on data from the Multi-GNSS Experiment (MGEX) from April 29 to May 9, 2012 and from December 23 to December 29, 2012. This includes triple-frequency phase and code observations with different combinations of receiver tracking modes. The results show that it is possible to resolve the combined track-to-track ambiguities of the best two triple-frequency GF and IF linear combinations for the Galileo frequency triplet E1, E5b and E5a with more than 99.6% of the fractional ambiguities for the best linear combination being located within ±0.03 cycles and more than 98.8% of the fractional ambiguities for the second best linear combination within ±0.2 cycles, while the fractional parts of the ambiguities for the GPS frequency triplet L1, L2 and L5 are more disturbed by errors as e.g. the uncalibrated Phase Center Offsets (PCOs) and Phase Center Variations (PCVs), that have not been considered. The best two GF and IF linear combinations

between tracks are helpful to detect problems in data and receivers. Furthermore, resolving the track-to-track ambiguities is helpful to connect the single-receiver ambiguities on the normal equation level and to improve ambiguity resolution.

Keywords: GNSS; Triple-frequency ambiguity resolution; Track-to-track; Geometry-free and ionosphere-free linear combination

Introduction

With the fast development of the Global Navigation Satellite Systems (GNSS) in the last few years, many GNSS satellites transmitting signals at three or even more frequencies have become available. Examples are the GPS Block IIF satellites (GPS.gov, 2014) and the Galileo In-Orbit-Validation (IOV) satellites (RINEX, 2013). These new satellites allow the forming of triple-frequency linear combinations. During the last 10 years, significant investigations haven been performed in this area in order to cope with different levels of reduction (or elimination) of the major error sources (Hatch, 2006; Henkel and Günther, 2012; Li et al., 2010). Henkel and Günther (2012) used multi-frequency phase and code measurements to form linear combinations with different scaling of the ionospheric delays and geometry with minimized noise level. In 2013, Geng and Bock (2013) achieved rapid ambiguity resolution in triple-frequency GPS Precise Point Positioning (PPP) solutions with IF linear combination formed in the wide-lane ambiguity resolution. The availability and precision of the triple-frequency GNSS solutions are demonstrated to be improved compared with the dual-frequency navigation solutions using semi-simulated data (Li et al., 2013).

The geometry-free (GF) and ionosphere-free (IF) linear combination is especially useful in the case of long baselines (e.g. a global network), where accurate knowledge of geometry and ionospheric delays is critical, and for Wide Area Real–Time Kinematics (WARTK) measurements (Hernández-Pajares et al., 2008), if the geometry-related information such as orbits and tropospheric delays are not available precisely enough and may have to be estimated. The best two triple-frequency GF and IF linear combinations using the phase and code observations on all three frequencies with a minimized noise level were found for different frequency triplets under the assumptions of equal code noise in meters and equal phase noise in cycles for all three frequencies and verified with real data of the Multi-GNSS Experiment (MGEX) by Wang and Rothacher (2013). Since a considerable part of the remaining errors, e.g., most of the Differential Code Biases (DCBs), do not change much within short time (Choi et al., 2011), the difference of the ambiguities from two close-in-time tracks of the same satellite, the so-called track-to-track ambiguities, will mainly be affected by errors in the Phase Center Variations (PCVs) (Rothacher, 2001), multipath effects and the changes in the DCBs that change during and between tracks. The estimation of track-to-track ambiguities on the zero-difference level not only benefits from formal errors reduced by a factor of square root of two compared to those of the

double-difference ambiguities, but also allows the usage of more MGEX stations, more triple-frequency satellites and signals from more receiver tracking modes.

The estimation and resolution of track-to-track ambiguities is not a new idea. Svehla et al. (2010) has shown that the undifferenced carrier-phase track-to-track ambiguities can be fixed based on improved estimation of the clock parameters. In this paper here we will present first results concerning the resolution of undifferenced track-to-track ambiguities using the best two triple-frequency GF and IF linear combinations for GPS L1, L2 and L5 (with the integer coefficients $a_x = 0, b_x = -1, c_x = 1$ for the best linear combination and $a_y = 1, b_y = -4, c_y = 3$ for the second best linear combination) and for Galileo E1, E5b and E5a (with the integer coefficients $a_x = 0, b_x = -1, c_x = 1$ for the best linear combination and $a_y = 1, b_y = -5, c_y = 4$ for the second best linear combination) using both code and phase measurements (Wang and Rothacher, 2013) based on the MGEX data of one week in December 2012 and 11 days in April and May 2012. The fractional parts and the formal errors of the estimated track-to-track ambiguities are analyzed and their dependence on the satellite type, receiver type and receiver tracking mode is studied.

Triple-frequency GF and IF track-to-track ambiguities

For one specific satellite–receiver pair, the code and phase observations on frequency f_i can be described as follows:

$$\begin{aligned} P_i &= \rho + I_1 \cdot \frac{f_1^2}{f_i^2} + \delta_{tro} + c_l \cdot \delta_r - c_l \cdot \delta^s + \epsilon_{P_i}, \\ L_i &= \rho - I_1 \cdot \frac{f_1^2}{f_i^2} + \delta_{tro} + c_l \cdot \delta_r - c_l \cdot \delta^s + PCO_i + PCV_i + \lambda_i \cdot n_i + \epsilon_{L_i}, \end{aligned} \tag{C.1}$$

where P_i and L_i represent the code and phase observations on frequency f_i, and ρ represents the geometric distance between the satellite and the receiver, respectively. I_1 stands for the first-order term of the ionospheric delay on L_1, and δ_{tro}, δ_r and δ^s are three geometry-related terms, i.e. the tropospheric delay, the receiver clock error and the satellite clock error. The terms PCO_i and PCV_i represent the Phase Center Offset (PCO) and PCV of the corresponding antenna on frequency f_i. λ_i and n_i denote the wavelength and ambiguity of the signal on frequency f_i. The code and phase noise on frequency f_i are described by ϵ_{P_i} and ϵ_{L_i}, respectively. The speed of light is denoted by the symbol c_l. Multipath has been ignored. The differences of the hardware delays between tracks for the same station and the same satellite are considered to be significantly reduced by forming track-to-track ambiguities and are thus not listed here.

After forming the GF and IF linear combination L_x using the code and phase observations on all three frequencies, all the geometry-related terms and the first-order term of the ionospheric refraction are eliminated. What remains in the equation are only the

terms of the combined ambiguity n_x, the elevation-dependent PCOs and PCVs, and the DCBs (DCB_x) that are generated by forming the linear combination of the individual DCBs of the different frequencies and receiver tracking modes:

$$\begin{aligned} L_x &= \gamma_1 L_1 + \gamma_2 L_2 + \gamma_3 L_3 + \gamma_4 P_1 + \gamma_5 P_2 + \gamma_6 P_3 \\ &= \lambda_x n_x + (\gamma_1 PCC_1 + \gamma_2 PCC_2 + \gamma_3 PCC_3) + DCB_x + \epsilon_x, \end{aligned} \tag{C.2}$$

with

$$\begin{aligned} PCC_i &= PCO_i + PCV_i, \quad i = 1, 2, 3 \\ n_x &= a_x \cdot n_1 + b_x \cdot n_2 + c_x \cdot n_3, \end{aligned}$$

where PCC_i represents the Phase Center Correction (PCC) on frequency f_i. The weighting coefficients of the observations γ_i $(i = 1, ..., 6)$ are functions of the three integer multipliers a_x, b_x and c_x of the ambiguities (γ_1, γ_2 and γ_3 see Equation C.8, γ_4, γ_5 and γ_6 see Wang and Rothacher, 2013), the three frequencies and the frequency f_x of the linear combination achieving the minimized combined noise σ^C of the linear combination, ignoring the PCC_i and DCB_x and assuming that the phase noise in cycles and the code noise in meters is the same for the three frequencies, respectively (Wang and Rothacher, 2013). ϵ_x stands for the combined observation error.

The minimized combined observation noise σ^C on the zero-difference level can be calculated for different frequency-triplets, each of them defined by a specific set of a_x, b_x and c_x that were varied from -10 to 10 each in Wang and Rothacher (2013). Ignoring the errors that still remain, e.g. PCC_i and multipath, the formal error of the track-to-track ambiguity σ^{tt} can be described as:

$$\sigma^{tt} = \frac{\sqrt{2} \cdot \sigma^C}{\sqrt{n}}, \tag{C.3}$$

where n represents the number of observation epochs and the observation noise is assumed to be uncorrelated Gaussian noise.

The theoretical formal errors of the track-to-track ambiguities for one observation epoch using the best two triple-frequency GF and IF linear combinations (L_x and L_y) for different frequency triplets with the GPS signals on L1 (1575.42 MHz), L2 (1227.6 MHz) and L5 (1176.45 MHz) and the Galileo signals on E1 (1575.42 MHz), E6 (1278.75 MHz), E5b (1207.14 MHz), E5 (1191.795 Hz) and E5a (1176.45 MHz) are shown in Table C.1 and Figure C.1. The phase and code noise is assumed to be 0.01 cycles and 0.5 m, respectively. For comparison, the corresponding formal errors of the Melbourne-Wübbena linear combinations using L1 and L2 or E1 and E6 are also listed in Table C.1 and displayed in Figure C.1. The integer coefficients a_x, b_x, c_x and a_y, b_y, c_y for the best and the second best linear combination, and the formal errors of the corresponding track-to-track ambiguities for one epoch ($\sigma^{tt}_{x,1}$ and $\sigma^{tt}_{y,1}$) and 100 epochs ($\sigma^{tt}_{x,100}$ and $\sigma^{tt}_{y,100}$) are listed in Table C.1 (integer coefficients also see Wang and Rothacher, 2013).

Table C.1: Formal errors of the track-to-track ambiguities using the best two triple-frequency GF and IF linear combinations for different frequency triplets as well as the Melbourne-Wübbena linear combinations using L1 and L2 or E1 and E6.

	a_x, b_x, c_x	$\sigma^{tt}_{x,1}$ [cycles]	$\sigma^{tt}_{x,100}$ [cycles]	a_y, b_y, c_y	$\sigma^{tt}_{y,1}$ [cycles]	$\sigma^{tt}_{y,100}$ [cycles]
GPS (L1,L2,L5)	0, -1, 1	0.0870	0.0087	1, -4, 3	0.4974	0.0497
GalileoA (E1,E6,E5b)	0, -1, 1	0.1193	0.0119	1, -3, 2	0.4275	0.0428
GalileoB (E1,E6,E5)	0, -1, 1	0.1434	0.0143	1, -2, 1	0.4330	0.0433
GalileoC (E1,E6,E5a)	0, -1, 1	0.1671	0.0167	1, -2, 1	0.4339	0.0434
GalileoD (E1,E5b,E5a)	0, -1, 1	0.0548	0.0055	1, -5, 4	0.5228	0.0523
MW (L1,L2)		0.5849	0.0585			
MW (E1,E6)		0.4979	0.0498			

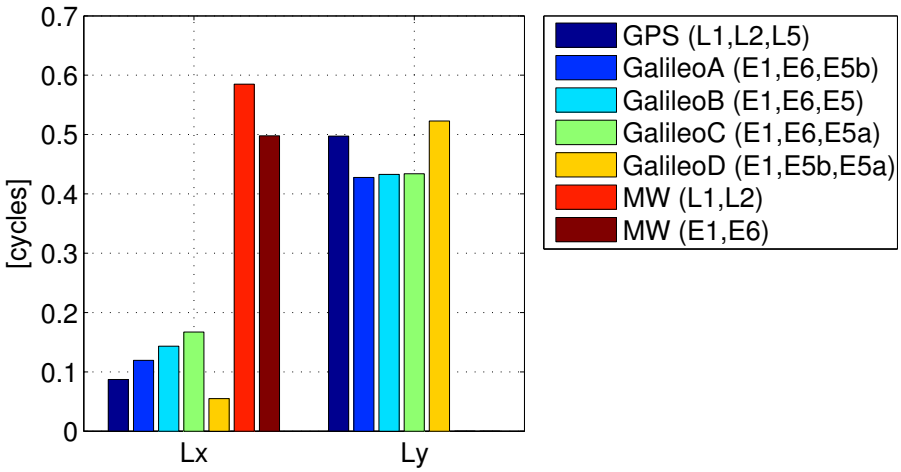

Figure C.1: Formal errors of the track-to-track ambiguities for one epoch using the best two triple-frequency GF and IF linear combinations for different frequency triplets and the Melbourne-Wübbena linear combinations using L1 and L2 or E1 and E6.

We see that the ambiguities of the best linear combinations of all the investigated frequency triplets have much smaller formal errors than those of the traditional dual-frequency Melbourne-Wübbena linear combinations using L1 and L2 or E1 and E6 (see Figure C.1 and Table C.1). The smallest formal track-to-track ambiguity error for the best linear combination L_x is generated by the frequency triplet E1, E5b and E5a. Accumulating for 100 epochs, the formal errors of all frequency triplets are reduced to below 0.02 cycles for the best linear combination L_x and to below 0.06 cycles for the second best linear combination L_y.

Tests with real data

In order to verify the theoretical derivations, the real MGEX data from December 23, 2012 to December 29, 2012 collected from the IGS website (Noll et al., 2009) was used to generate the undifferenced triple-frequency GF and IF linear combinations and to estimate the track-to-track ambiguities. During the selected week, about 45 MGEX stations (see Figure C.2) with signals from the GPS Block IIF satellites PRN25 (SVN62), PRN01 (SVN63), PRN24 (SVN65) and the Galileo IOV satellites E11 (PFM), E12 (FM2), E19 (FM3) and E20 (FM4) were available for the tests.

Since the number of triple-frequency tracks containing the E6 signal during the test interval was still very low, the tests were only performed for the GPS frequency triplet L1, L2, L5 and the Galileo frequency triplet E1, E5b and E5a. RINEX observation files with version 3.00 (or above) allow for receiving observations of the same carrier with different receiver tracking modes (Gurtner and Estey, 2009). In our tests, the tracking modes listed in Table C.2 were available for the triple-frequency linear combinations.

In order to get rid of the observations with large noise originating from, e.g., multipath effects on the zero-difference level, a relatively high elevation mask of 15 degrees was set for forming the linear combinations and the least-square adjustment. The GPS and Galileo orbits generated by the Center for Orbit Determination in Europe (CODE) with a sampling interval of 15 min (Final GNSS products, 2013; CODE MGEX orbit solution, 2013; Noll et al., 2009) were resampled to 30 s with the help of the Bernese GPS Software (Dach et al., 2007) in order to correspond with the sampling interval of the observations.

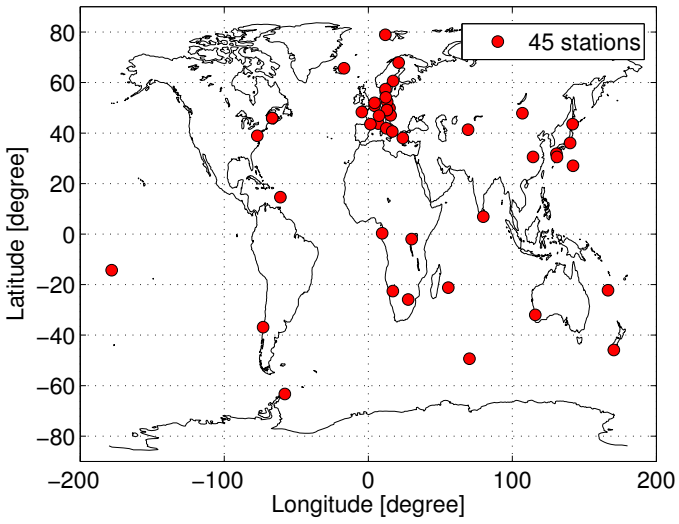

Figure C.2: The MGEX stations on December 23, 2012.

Table C.2: Receiver tracking modes for the GPS frequency triplet L1, L2, L5 and the Galileo frequency triplet E1, E5b and E5a (see Gurtner and Estey, 2009).

	Receiver tracking modes
L1,L2,L5	CDX, CLQ, CXX, CWQ, CWX, WXX, WWX
E1,E5b,E5a	CQQ, XXX

Fractional parts and formal errors of the track-to-track ambiguities

After generating the best and the second best triplefrequency GF and IF linear combination for both frequency triplets (for GPS and Galileo) mentioned above, the ambiguities on the zero-difference level were estimated using a least-square adjustment, and the track-to-track ambiguities n^{tt} were calculated by forming the difference of two ambiguities n^{t1} and n^{t2} belonging to the same receiver, the same satellite, but to two different tracks on the considered day.

$$n^{tt} = n^{t1} - n^{t2} \tag{C.4}$$

The formal error of the track-to-track ambiguity σ^{tt} was calculated with the formal errors of the uncorrelated ambiguities on both tracks σ^{t1} and σ^{t2}.

$$\sigma^{tt} = \sqrt{(\sigma^{t1})^2 + (\sigma^{t2})^2} \tag{C.5}$$

Tracks shorter than 50 observation epochs (25 min) were eliminated. Data separated by gaps longer than 10 epochs (5 min) were considered to be discontinuous (i.e. as separate tracks). In addition, some tracks were eliminated because of incorrect cycle slip detection or unexplained jumps of a fraction of a cycle. Stations with a lot of these problems were also eliminated.

Figure C.3 shows the fractional parts and the formal errors of the estimated track-to-track ambiguities using the best and the second best linear combination for the corresponding GPS and Galileo frequency triplets. The x-axis represents the combined track length l defined by:

$$l = \frac{2}{\frac{1}{l_1} + \frac{1}{l_2}}, \tag{C.6}$$

where l_1 and l_2 stand for the length of the two tracks. Assuming that the formal error of each track σ^{ti} decreases with $\sqrt{l_i}\,(i = 1, 2)$, according to error propagation the combined track length l is then equal to $\frac{1}{\frac{1}{l_1}+\frac{1}{l_2}}$. The factor 2 is set in order to generate a track length l that is equal to l_1 (or l_2), if l_1 equals l_2. In this way l is more sensitive to the shorter track.

From Figure C.3 we can see that for the frequency triplet E1, E5b and E5a, all the fractional n_x^{tt} from the best linear combination L_x are within ± 0.03 cycles except one outlier for satellite E20, and most (98.8%) of the fractional n_y^{tt} from the second best linear

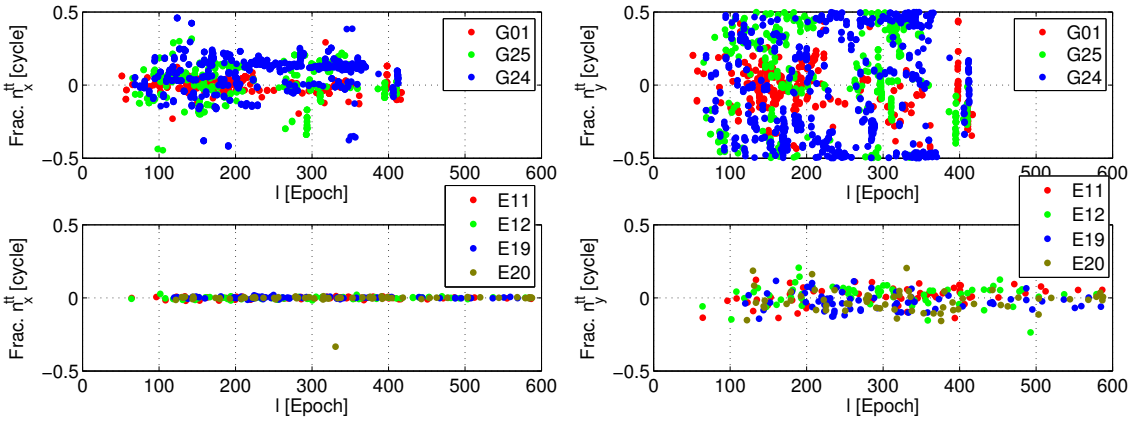

(a) Fractional n_x^{tt} (b) Fractional n_y^{tt}

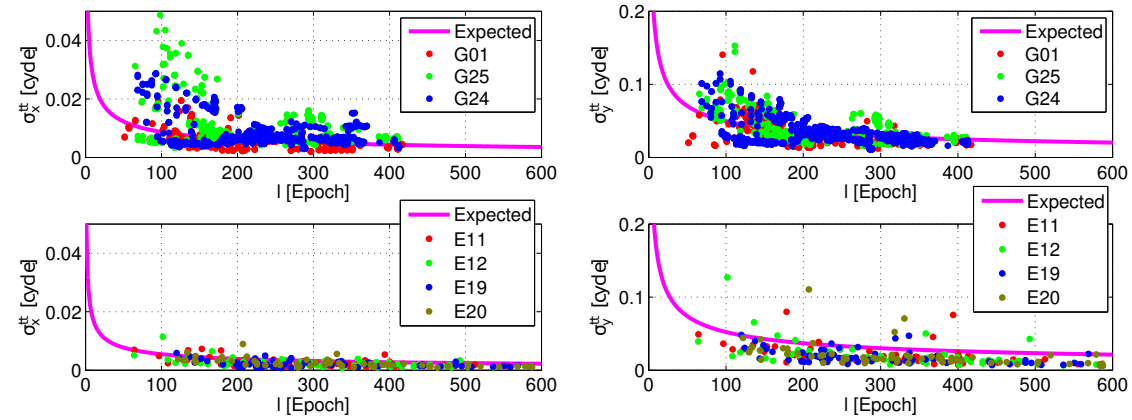

(c) σ_x^{tt} (d) σ_y^{tt}

Figure C.3: Fractional parts (a), (b) and formal errors (c), (d) of the estimated track-to-track ambiguities using the best and the second best linear combinations for the GPS frequency triplet L1, L2, L5 and the Galileo frequency triplet E1, E5b and E5a as a function of the combined track length.

combination L_y are within ± 0.2 cycles. The corresponding formal errors σ_x^{tt} and σ_y^{tt} are mostly lower than the expectations (see the magenta lines and Table C.1), which means smaller than 0.01 and 0.06 cycles, respectively, after 100 epochs. Compared with E1, E5b and E5a, the GPS frequency triplet L1, L2 and L5 shows a relatively big scatter in both, the fractional parts and the formal errors of the estimated track-to-track ambiguities. The n_y^{tt} ambiguities using L1, L2 and L5 cannot easily be resolved because their fractional parts are more or less randomly distributed. Furthermore, the fractional parts and the formal errors are not found to depend on the receiver tracking mode.

When estimating the track-to-track ambiguities, errors that are frequency- or elevation-dependent still remain in the linear combinations. Figure C.4 shows, e.g., the best linear combination L_x in cycles for station USN4 on December 23, 2012, using L1C, L2L and L5Q from the GPS satellite G24 and for station MYVA on December 23, 2012, using L1C,

L2W and L5X from the GPS satellite G25. The elevation angles for the corresponding periods are shown in the lower part of the figure. We see very obvious elevation-dependent variations and an increase of the noise at low elevations in the linear combination. The variation in the time interval from the 2357th to the 2880th epoch in Figure C.4a and from the 7th to the 599th epoch in Figure C.4b may be generated by PCOs and PCVs. The influence of the PCOs and PCVs on the undifferenced observation δ_L in cycles can be formulated as follows (see Equation C.2):

$$\begin{aligned} \delta_L &= (\gamma_1 \cdot PCC_1 + \gamma_2 \cdot PCC_2 + \gamma_3 \cdot PCC_3)/\lambda_x \\ &= \frac{a_x \cdot f_1}{c_l} PCC_1 + \frac{b_x \cdot f_2}{c_l} PCC_2 + \frac{c_x \cdot f_3}{c_l} PCC_3, \end{aligned} \tag{C.7}$$

where (see Henkel and Günther, 2012; Wang and Rothacher, 2013)

$$\gamma_1 = \frac{a_x \cdot f_1}{f_x}, \quad \gamma_2 = \frac{b_x \cdot f_2}{f_x}, \quad \gamma_3 = \frac{c_x \cdot f_3}{f_x}. \tag{C.8}$$

For the best two linear combinations of the frequency triplet L1, L2 and L5 we get, based on Table C.1:

$$\begin{aligned} \delta_{Lx} &= -4.0948\ PCC_2 + 3.9242\ PCC_3, \\ \delta_{Ly} &= 5.2550\ PCC_1 - 16.3793\ PCC_2 + 11.7726\ PCC_3, \end{aligned} \tag{C.9}$$

where δ_{Lx} and δ_{Ly} represent the influence of the $PCC_i\,(i = 1, 2, 3)$ on the combined observations L_x and L_y in cycles. Similarly, for the frequency triplet E1, E5b and E5a we get

$$\begin{aligned} \delta_{Lx} &= -4.0266\ PCC_2 + 3.9242\ PCC_3, \\ \delta_{Ly} &= 5.2550\ PCC_1 - 20.1329\ PCC_2 + 15.6969\ PCC_3. \end{aligned} \tag{C.10}$$

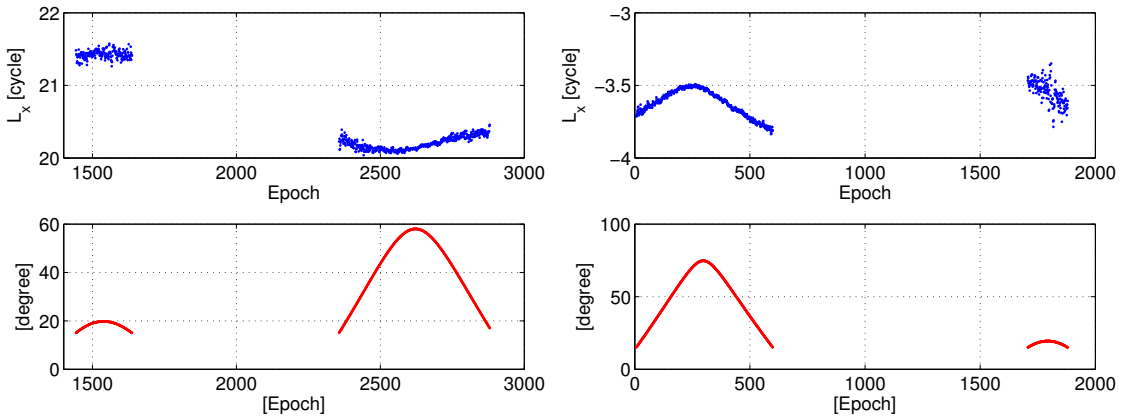

(a) USN4 (b) MYVA

Figure C.4: The best triple-frequency GF and IF linear combination in cycles for (a) station USN4 on December 23, 2012, using signals on L1C, L2L and L5Q from the GPS satellite G24 and (b) station MYVA on December 23, 2012, using signals on L1C, L2W and L5X from the GPS satellite G25 and their elevation angles.

In order to get rid of the disturbances generated by the code-related biases and test only the behavior of the PCOs and PCVs on the triple-frequency level, we formed the phase-only GF and IF linear combination as the difference of two IF linear combinations for the frequency triplet L1, L2 and L5:

$$\begin{aligned} L_{IFIF} &= \frac{f_1^2 L_1 - f_2^2 L_2}{f_1^2 - f_2^2} - \frac{f_1^2 L_1 - f_3^2 L_5}{f_1^2 - f_3^2}, \\ \delta_{L_{IFIF}} &= \left(\frac{f_1^2}{f_1^2 - f_2^2} - \frac{f_1^2}{f_1^2 - f_3^2}\right) PCC_1 - \frac{f_2^2}{f_1^2 - f_2^2}\, PCC_2 + \frac{f_3^2}{f_1^2 - f_3^2}\, PCC_3 \\ &= 0.2851\ PCC_1 - 1.5457\ PCC_2 + 1.2606\ PCC_3, \end{aligned} \tag{C.11}$$

where L_{IFIF} represents the difference of the two IF linear combinations in meters, and $\delta_{L_{IFIF}}$ stands for the influence of the PCCs on L_{IFIF} in meters. L_{IFIF} for the longer tracks of the two data sets used in Figure C.4 are plotted in Figure C.5. We see that the elevation-dependency exists also in the phase-only GF and IF linear combinations with a range of about 10 cm.

Figure C.6 shows two relatively long tracks for the same stations on the same day as plotted in Figure C.5. The frequency triplet E1, E5b and E5a for the Galileo satellites E11 and E20 is used instead. We see that the elevation-dependency is almost uniquely seen in the noise level, but there are no obvious systematic variations visible in the L_{IFIF} observations.

This shows that PCOs and PCVs, which are different for the frequency triplet L1, L2, L5 and E1, E5b and E5a, may well be responsible for the different behavior of the fractional ambiguities we see for GPS and Galileo, and demonstrates that PCOs and PCVs have to be known and should be taken into account in the processing.

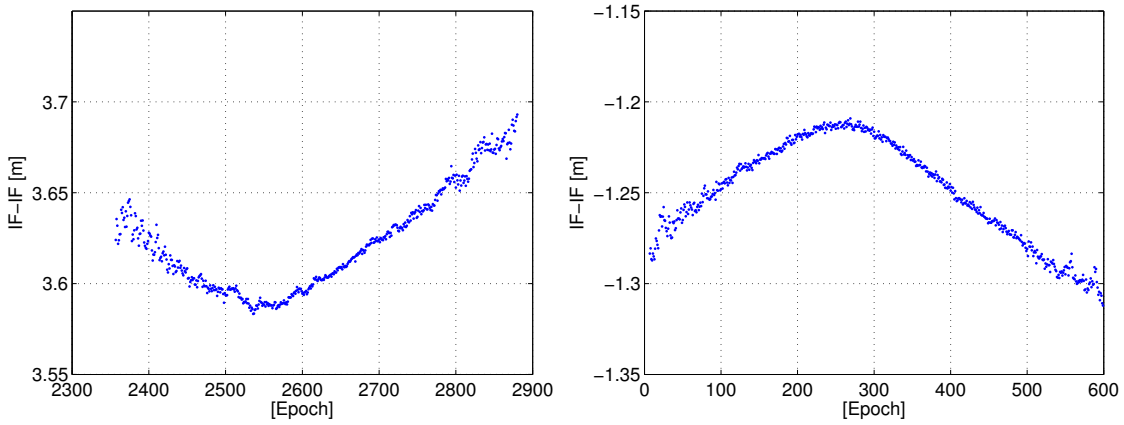

(a) USN4 (b) MYVA

Figure C.5: The phase-only GF and IF linear combinations in meters for (a) station USN4 on December 23, 2012, using signals on L1C, L2L and L5Q from the GPS satellite G24 and (b) station MYVA on December 23, 2012, using signals on L1C, L2W and L5X from the GPS satellite G25.

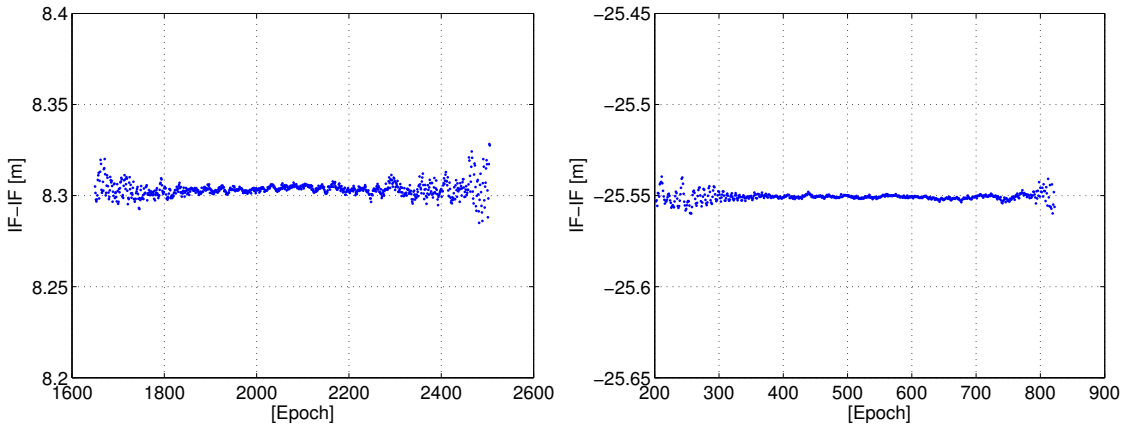

(a) USN4 (b) MYVA

Figure C.6: The phase-only GF and IF linear combinations in meters for (a) station USN4 on December 23, 2012, using signals on E1C, E5bQ and E5aQ from the Galileo satellite E20 and (b) station MYVA on December 23, 2012, using signals on E1X, E5bX and E5aX from the Galileo satellite E11.

Detection of problems

Since the triple-frequency GF and IF linear combinations already eliminate all the geometry-related errors and the first-order term of the ionospheric delay, they are well-suited to detect systematic errors due to antenna- or receiver-specific problems and inconsistencies. Figure C.7 shows the formal errors σ_y^{tt} using the second best linear combination for the frequency triplet L1, L2, L5 and E1, E5b and E5a categorized by the stations with different colors and symbols. The magenta lines represent the expected formal errors of the second best linear combination for the two frequency triplets. We can see that the same station represented by the purple stars in Figure C.7 (top), and (bottom) delivers large formal errors for both frequency triplets.

Figure C.8 shows another example. The MGEX data from April 29, 2012, to May 9, 2012, was used for the processing, and the fractional parts of the track-to-track ambiguities n_x^{tt} using the best linear combination for the frequency triplet E1, E5b and E5a are categorized by the satellite and the receiver type (abbreviated by Ri). We can see a relatively constant offset of about $\pm 0.35 - 0.36$ cycles, which is generated by the receiver type R4 and the Galileo IOV satellite E12 (except for two outliers). The stations with station-specific problems (see Figure C.11) were not included in this figure.

The reason of this offset is found to be caused by unusual code jumps of about 33554431 m generated by the R4 receivers for E12 in the test time interval. Figure C.9a shows the code jumps on E1, E5b and E5a for the satellite E12 and station GRAC, which is equipped with a R4 receiver, on May 1, 2012. The E1 and E5b code measurements are visually overwritten by the E5a measurements. No phase jump could be detected at the same epochs. Figure C.9b shows the code jumps on E1, E5b and E5a for the outliers of about

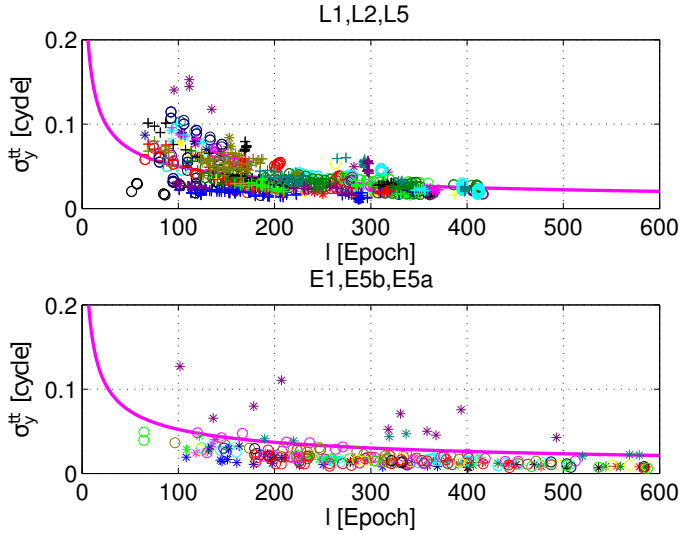

Figure C.7: Formal errors of the estimated track-to-track ambiguities using the second best linear combination for the GPS frequency triplet L1, L2, L5 and the Galileo frequency triplet E1, E5b and E5a categorized by the stations.

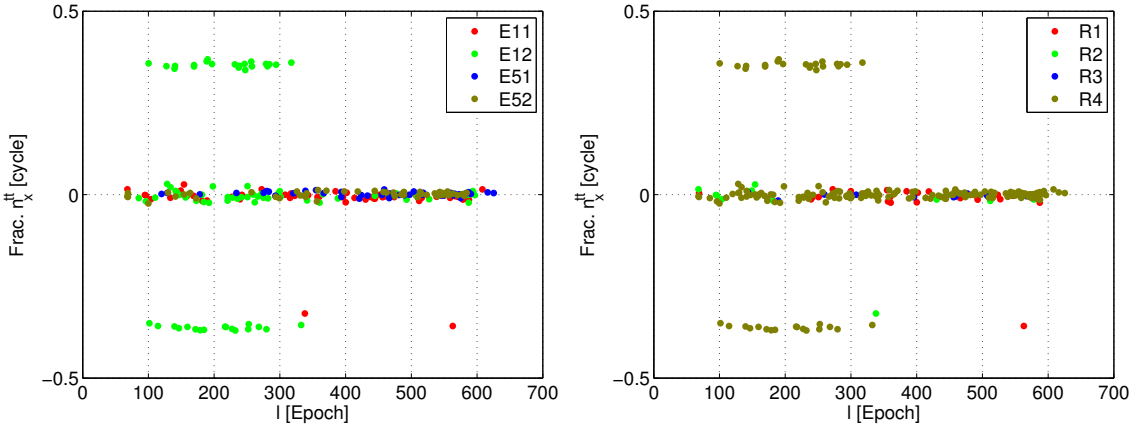

(a) Satellite

(b) Receiver type

Figure C.8: Fractional part n_x^{tt} of the estimated track-to-track ambiguities using the best linear combination for the Galileo frequency triplet E1, E5b and E5a categorized by (a) the satellite and (b) the receiver type. The MGEX data from April 29, 2012, to May 9, 2012, was processed for the plots.

$\pm 0.35 - 0.36$ cycles (see Figure C.8) which were related to the R4 receivers and to E12. The code jump between two subsequent epochs can be calculated with

$$\delta P_f(t_{i,i+1}) = |(P_f(t_{i+1}) - P_f(t_i)) - (L_f(t_{i+1}) - L_f(t_i))|, \tag{C.12}$$

where $\delta P_f(t_{i,i+1})$ represents the absolute code jump on frequency f between the i-th and the (i+1)-th epoch, and $P_f(t_i)$ and $L_f(t_i)$ stand for the code and phase measurements,

respectively, on frequency f at epoch t_i in meters. An offset of 33554431 m was subtracted for all the three frequencies in Figure C.9b. The relationship between this offset and the offset of $\pm 0.35 - 0.36$ cycles in the fractional n^{tt} using the best linear combination for the frequency triplet E1, E5b and E5a can be explained by Equations C.13 and C.14

$$\Delta_{E1,E5b,E5a} = \frac{(\gamma_4 + \gamma_5 + \gamma_6) \cdot 33554431\ m}{1\ m}, \tag{C.13}$$

$$\Delta_{offset} = |\Delta_{E1,E5b,E5a} - [\Delta_{E1,E5b,E5a}]| = 0.357\ cycles \tag{C.14}$$

where γ_4, γ_5 and γ_6 represent the coefficients of the code observations on frequency E1, E5b and E5a using the best linear combination and amount to 0.0004, 0.0479 and 0.0540, respectively, with the assumption that the code and phase noise are equal to 0.5 m and 0.01 cycles, respectively, on all three frequencies and the combined wavelength is set to be 1 m (Wang and Rothacher, 2013). $\Delta_{E1,E5b,E5a}$ and $[\Delta_{E1,E5b,E5a}]$ represent the resulting deviation of the track-to-track ambiguity in cycles and its nearest integer. Δ_{offset} indicates the absolute offset of the fractional track-to-track ambiguity.

Some other problems may also be detected by estimating the track-to-track ambiguities using the triple-frequency GF and IF linear combinations. One outlier in Figure C.8 of about -0.36 cycles (see the red point in Figure C.8b) is, e.g., caused by the code differences between E1 and E5a/E5b for station GRAB and satellite E11 on May 6, 2012 (see Figure C.10), where the E5b code observations are visually overwritten by the E5a code observations. Station-specific problems for, e.g., MYVA and OHIX can also easily be detected by the large scatter of the fractional n_x^{tt} using the best linear combination of the frequency triplet E1, E5b and E5a (see Figure C.11).

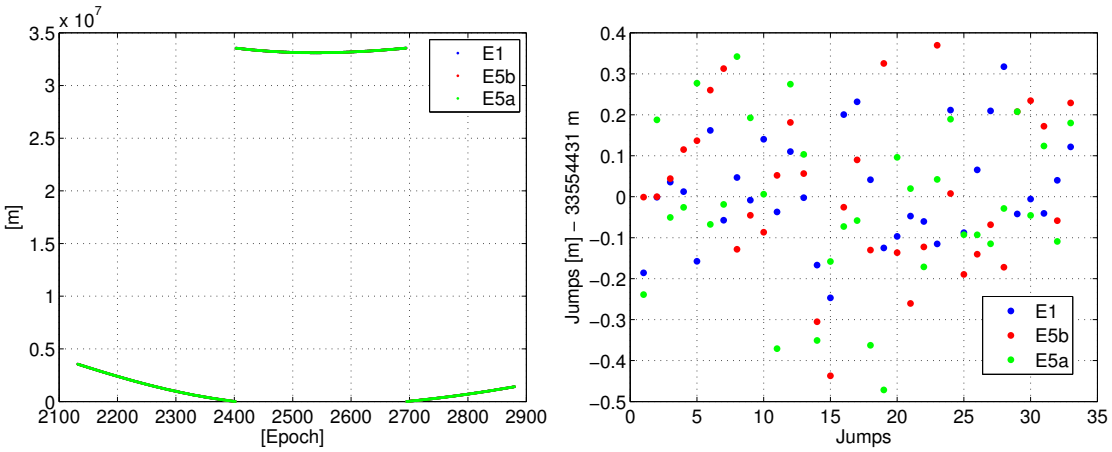

(a) Code jump

(b) Offset

Figure C.9: Code jumps of the signals on E1, E5b and E5a for (a) station GRAC and satellite E12 on May 1st, 2012 and (b) all the outliers of about $\pm 0.35 - 0.36$ cycles generated by the R4 receivers and E12.

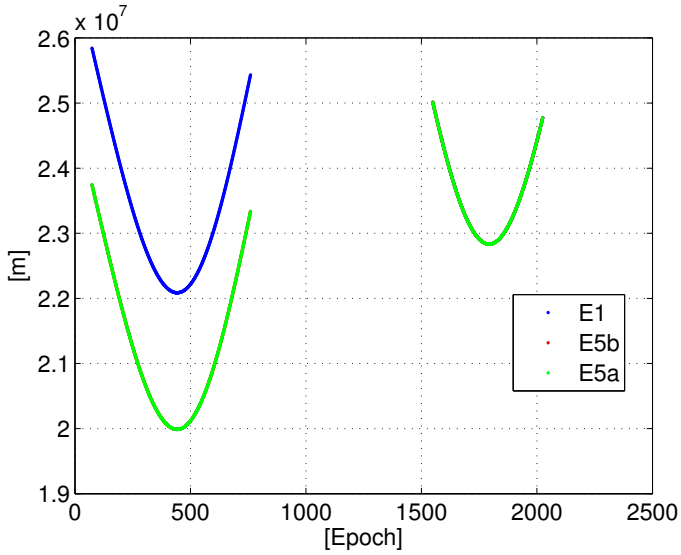

Figure C.10: Code differences between E1 and E5b/E5a for station GRAB and satellite E11 on May 6, 2012. The E5b code observations (red points) are visually overwritten by the E5a code observations (green points).

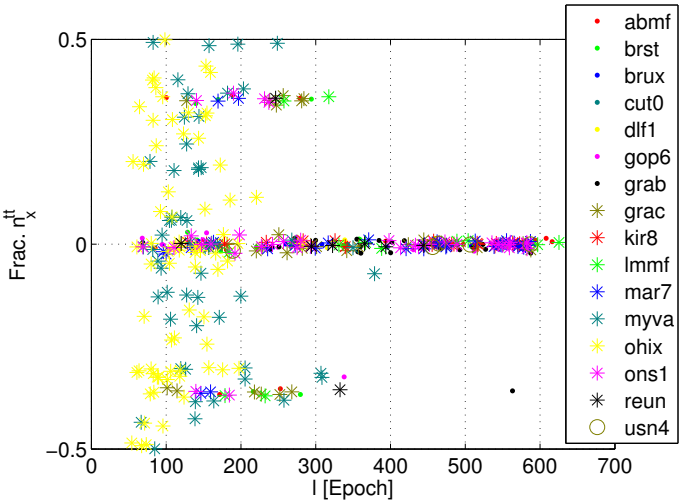

Figure C.11: Station-specific problems detected in the fractional n_x^{tt} ambiguities using the best linear combination for the frequency triplet E1, E5b and E5a.

Summary and conclusions

Using the triple-frequency GF and IF linear combination to estimate the track-to-track ambiguities does not only eliminate all the geometry-related errors and the first-order term of the ionospheric delay, but also receiver- and satellite-specific biases that do not change in time. Compared with the dual-frequency Melbourne-Wübbena linear combination using, e.g., L1 and L2 or E1 and E6, or the double-differenced ambiguities using the same triple-

frequency linear combination, the track-to-track ambiguities benefit from a lower noise level. According to our investigations for the test interval from December 23, 2012, to December 29, 2012, it is possible to resolve the combined track-to-track ambiguities n_x^{tt} and n_y^{tt} using the best two linear combinations for the Galileo frequency triplet E1, E5b and E5a with more than 99.6% of the fractional n_x^{tt} being located within ± 0.03 cycles and more than 98.8% of the n_y^{tt} within ± 0.2 cycles. Most of the formal errors (99.6% for σ_x^{tt} and 97.6% for σ_y^{tt}) are lower than 0.01 and 0.06 cycles, for n_x^{tt} and n_y^{tt}, respectively, after 100 epochs.

The track-to-track ambiguities for the GPS frequency triplet L1, L2 and L5 have, however, a much bigger scatter. This may be explained by the PCOs and PCVs between different frequencies, which have not been considered in the data processing. A better calibration of the PCOs and PCVs for all three frequencies is thus required for resolving the GPS track-to-track GF and IF ambiguities.

Resolving the combined track-to-track ambiguities n_x^{tt} and n_y^{tt} gives us important information about the zero-difference ambiguities between tracks, and may contribute to the general triple-frequency ambiguity resolution by constraining the resolved track-to-track ambiguities (e.g., on the normal equation level). The estimated track-to-track ambiguities can also be used for the detection of problems in the data, since they are already free of most of the error sources in GNSS data processing. Furthermore, the best two linear combinations L_x and L_y can be used for cycle slip detection in all the three carrier frequencies on the zero-difference level, provided that the measurement at the three frequencies do not jump at the same time by the same number of cycles.

In this paper we focused on the best two GF and IF linear combinations. It is difficult, however, to find a third GF and IF linear combination with a relatively low combined noise, which is linearly independent of the best two linear combinations of the frequency triplet. The track-to-track ambiguities can thus not be resolved on each carrier using only the best two GF and IF linear combinations. The best two GF and IF linear combinations might be combined, however, with another linear combination, e.g., an IF linear combination using only the phase measurements to complete the set of three independent linear combinations for the three original ambiguities and to resolve the track-to-track ambiguities and connect the tracks directly for each carrier. Studies on this topic are yet to be performed.

Acknowledgments

This work was funded by European Space Agency (ESA) as part of the project (Satellite and Station Clock Modeling for GNSS, Reference: AO/16231/09/D/SR). We would like to thank IGS for providing triple-frequency MGEX data on its archive (<ftp://cddis.gsfc.nasa.gov/pub/gps/data/campaign/mgex/>) and Werner Enderle and Drazen Svehla for their support as technical officers of the project.

D Paper D

Paper D was originally published as

Wang K., Meindl M., Geiger A., Rothacher M., Scaramuzza M., Troller M., Truffer P. (2014): Assessment of Single-difference Ionospheric Residuals in a Regional Network for GBAS, in Proceedings of the 27th International Technical Meeting of The Satellite Division of the Institute of Navigation (ION GNSS+ 2014), Tampa, Florida, US, September 2014, pp. 2384-2393.

The final publication is available at `https://www.ion.org/publications/abstract.cfm?jp=p\&articleID=12550`.

Assessment of Single-difference Ionospheric Residuals in a Regional Network for GBAS

K. Wang[a], M. Meindl[a], A. Geiger[a], M. Rothacher[a], M. Scaramuzza[b], M. Troller[b], P. Truffer[b]

[a]Institute of Geodesy and Photogrammetry, ETH Zurich
[b]Skyguide – Swiss Air Navigation Services Ltd.

Abstract

During approach and landing of airplanes, the Ground Based Augmentation System (GBAS) is used to augment the Global Positioning System (GPS) positioning by delivering differential corrections. The ionospheric delays are typically considered to be removed by generating differential observations if the baseline between the GBAS station and airplane is relatively short. However, the situation may change in case of strong or stormy ionospheric activities. The remaining differential ionospheric residuals that are not eliminated might cause large slant pseudorange errors and degrade the positioning results significantly, especially in the vertical direction.

In this work the Global Positioning System (GPS) data of the swisstopos Automated GNSS Network for Switzerland (AGNES) were processed over 15 years from 1999 to 2013. We used the double-difference phase observations with reliably resolved ambiguities to establish the station-pair single-difference ionosphere residuals in the slant and vertical direction. An epoch-wise zero-mean condition over all satellites and per baseline was applied to avoid singularities and the estimated single-difference slant ionospheric residual was corrected with the 2-hour global ionosphere maps provided by the Center of Orbit Determination in Europe (CODE). The spatial gradients were calculated using the Ionosphere Pierce-Point (IPP) distances or the baseline length depending on the concrete case. It was found that the absolute maximum slant ionosphere gradients calculated from the slant differential ionospheric residuals and the baseline length during these 15 years are below the slant ionosphere gradient bound of the Conterminous United States (CONUS) ionospheric anomaly threat model.

At last, the so-called overbounding vertical ionosphere gradients $\sigma_{vig}^{overbound}$, which confine all the non-Gaussian tails on a daily basis, were calculated for all days from 1999 to

2013 except the days with very stormy ionosphere activities. Ignoring the gradients with an IPP distance shorter than 20 km, over 96% of the $\sigma_{vig}^{overbound}$ values are smaller than 4 mm/km.

Introduction

The ionospheric delays are always considered to be an important influence factor for the GNSS positioning error on the zero-difference level. Depending on the activity of the ionosphere and the location of the investigated area, the ionospheric delays for a single-frequency receiver usually vary from several meters to more than 100 meters (Gao and Liu, 2002). For differential GNSS positioning between the GBAS stations and the airborne user during the approach and landing phase of the airplanes, the ionosphere effects are mostly considered to be sufficiently low. However, in certain cases the remaining part of the differential ionospheric delays could reach a high value, e.g. 412 mm/km in northern Ohio in the U.S. on November 20, 2003 (Pullen et al., 2009), and thus generate huge position errors in the vertical direction.

In practice, an overbounding vertical ionosphere gradient $\sigma_{vig}^{overbound}$ is broadcast in the Type 2 message from the ground system to the airplane to describe the one-sigma ionosphere overbounding value for the nominal conditions (Lee et al., 2006b). Under stormy ionosphere conditions, however, the ionosphere gradients can only be calculated in the slant direction because of the breakdown of the thin-shell model (Pullen et al., 2009). Various studies have been performed in the last ten years to assess the impact of huge anomalous ionosphere gradients on positioning results, to establish and validate the threat model, to adapt the geometry screening functionality of the GBAS station and to compromise between the safety and the availability (Ene et al., 2005; Kim, 2013; Lee et al., 2006a, 2011; Mayer et al., 2008, 2009; Pullen and Enge, 2007). In this work here, the slant and vertical differential ionospheric residuals were estimated and analyzed on the single-difference level using the stable AGNES network from 1999 to 2013 (AGNES data, 2014; Villiger, 2014). The range of the possible non-ionospheric biases remaining in the residuals are analyzed using several very short baselines. The correlations between the slant ionospheric residuals and different indices, including the geomagnetic index K_P and D_{ST} and the mean global Total Electron Content (TEC) value between 12:00 and 14:00 UT derived from the CODE global ionosphere maps, are studied and discussed. Afterwards, the $\sigma_{vig}^{overbound}$ are calculated for different distance bins and for all days except the very stormy days. The maximum slant gradients are also calculated for all days, analyzed and compared with the CONUS threat model.

Data Selection

The processing was based on the GPS observations of the AGNES network from January 1, 1999, to December 31, 2013. The AGNES stations are relatively uniformly distributed within Switzerland (see Figure D.1). The number of stations available has increased from 6 at the beginning of 1999 to about 40 in 2013 as shown in Figure D.2. This has led to a significant increase in the number of possible baselines from about 15 to 780.

Figure D.3 shows the histogram of the baseline lengths within the AGNES network on June 16, 2013. We see that most of the station pairs are separated by 30 km to 190 km. It should be mentioned that 11 very short baselines, i.e. with a length smaller than 25 m, are available on this day. These baselines are important for estimating the non-ionospheric biases that remain in the single-difference ionosphere residuals.

Storm Classes

The geomagnetic indices K_P and D_{ST} are good indicators for the Earth magnetic perturbation and are useful for defining the ionosphere storm classes (Lee et al., 2006b). In this work, we only use them to distinguish between the stormy ionosphere days and all days that are under quiet, moderate and active ionosphere conditions, which are defined as "nominal" in this paper. We assume that the ionosphere condition is considered as stormy, if the daily peak K_P index (Kp Index, 2014) is not smaller than 9 or if the daily minimal D_{ST} index (Dst Index, 2014) is lower than -350 nT. Using this criterion, 6 days listed in Table D.1 between 2000 and 2004 turned out to be stormy.

Figure D.4 shows the daily peak K_P index, daily minimal D_{ST} index and the global mean TEC values (the degree 0 and order 0 coefficient) between 12:00 and 14:00 UT given

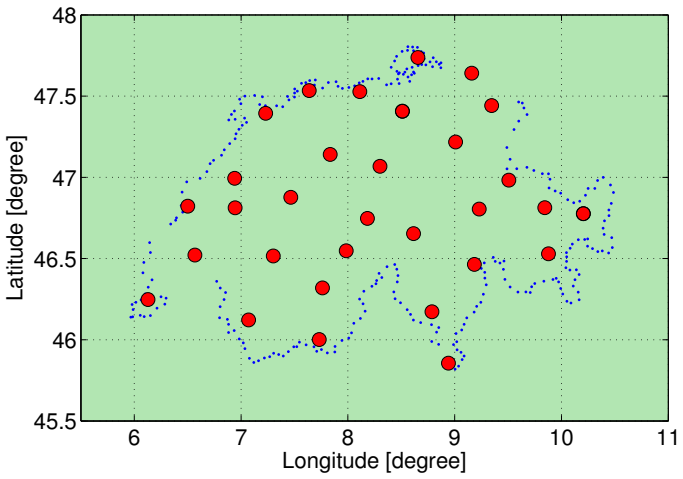

Figure D.1: The AGNES network on June 16, 2013.

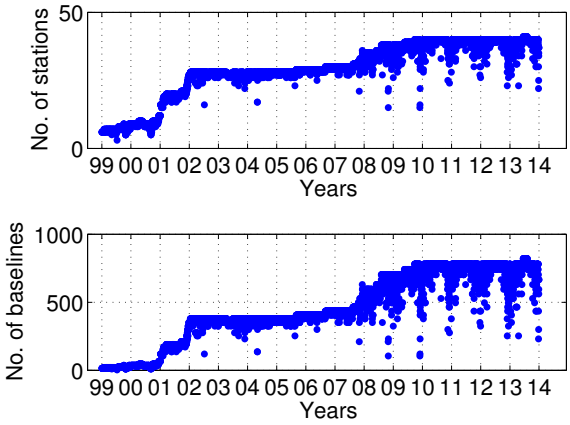

Figure D.2: Number of the available AGNES stations and baselines from 1999 to 2013.

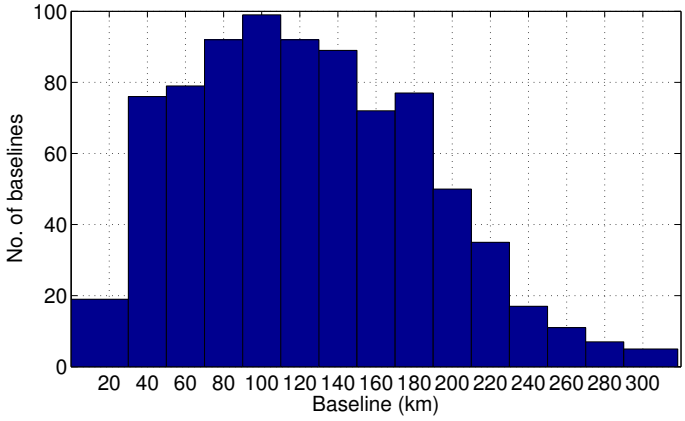

Figure D.3: Histogram of the baseline lengths within the AGNES network on June 16, 2013.

in the 2-hour CODE global ionosphere maps (CODE products, 2014). We see that the absolute values of the K_P and D_{ST} indices are generally larger before 2005 and after 2011. However, the 11-year solar cycle with the peaks in 2000 and 2011 in the last 15 years (Lee et al., 2006b; Klobuchar, 1996) is more obvious in the global mean TEC values.

A detailed study of the correlation between these indices and the slant differential ionospheric residuals is given in Section "Correlation with the Indices" below.

Processing Strategy

In the processing we used the GPS double-difference phase observations on both, L1 (1575.42 MHz) and L2 (1227.6 MHz). The ionospheric delays were extracted on the single-difference level. The double-difference observation equations for phase measurements on

Table D.1: Geomagnetic indices of the stormy ionosphere days from 1999 to 2013.

Datum	Peak K_P	Minimal D_{ST} [nT]
Jul. 15, 2000	9	-289
Mar. 31, 2001	8.7	-387
Oct. 29, 2003	9	-350
Oct. 30, 2003	9	-383
Nov 20, 2003	8.7	-422
Nov 8, 2004	8.7	-374

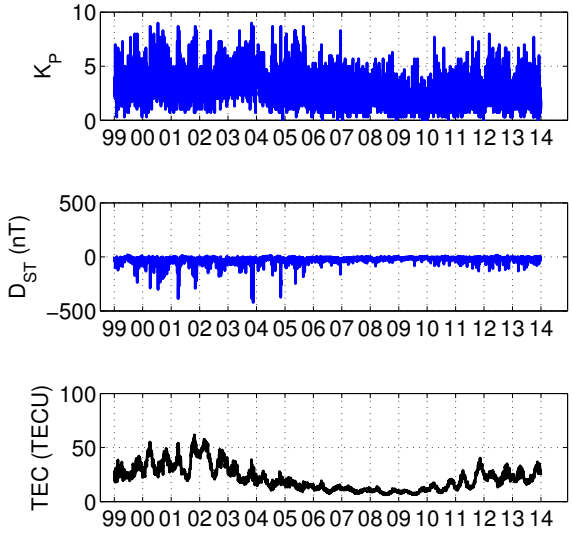

Figure D.4: The daily maximum K_P index, the daily minimum D_{ST} index and the global mean TEC values from 1999 to 2013.

L1 and L2 can be written as

$$L_1 = \rho + \Delta trop - I_{ab}^{ij} + \lambda_1 \cdot N_1 \tag{D.1}$$

$$L_2 = \rho + \Delta trop - I_{ab}^{ij} \cdot \frac{f_1^2}{f_2^2} + \lambda_2 \cdot N_2 \tag{D.2}$$

where L_i (i =1,2) represents the phase measurements on frequency f_i (i =1,2), and ρ and $\Delta trop$ indicate the geometric distances and the tropospheric delays on the double-difference level, respectively. I_{ab}^{ij} stands for the double-difference ionospheric delay between receivers a and b and satellites i and j on L_1. λ_i and N_i (i =1,2) represent the wavelength and the double-difference ambiguity on frequency f_i (i =1,2), respectively.

Slant Differential Ionospheric Delay and its Gradient

With the help of the Bernese GPS Software (Dach et al., 2007), the phase ambiguities N_1 and N_2 were reliably resolved and the double-difference ionospheric delay I_{ab}^{ij} on L_1 could be accurately estimated using the geometry-free linear combination. In order to extract the ionospheric delays on single-difference level, a zero-mean condition was applied for each epoch and all the single-difference ionospheric delays I_{ab}^{i} $(i = 1, \cdots, n)$ for each station pair a and b to avoid singularities:

$$\sum\nolimits_{i=1}^{n} I_{ab}^{i} = 0 \tag{D.3}$$

The single-difference ionospheric residual is then again corrected with a mean model value I_{ab}^{model} derived from the 2-hour CODE global ionosphere map for each baseline per epoch:

$$I_{ab}^{i\_model} = I_{a}^{i\_model} - I_{b}^{i\_model} \tag{D.4}$$

$$I_{ab}^{model} = \frac{\sum_{i=1}^{n} I_{ab}^{i\_model}}{n} \tag{D.5}$$

where n represents the number of GPS satellites available for the station pair a and b at the corresponding epoch. The single-difference slant ionospheric delay I_{ab}^{i} at epoch t calculated with Equation D.1 to D.3 is then corrected by adding the mean model value I_{ab}^{model} at the same epoch and written as

$$I_{ab} = I_{ab}^{i} + I_{ab}^{model}. \tag{D.6}$$

The estimated slant differential ionospheric delay is thus free from code-related biases such as the differential code biases (DCB) and has the same noise level as the phase measurements, namely millimeter level. However, it should be noted that the model values derived from the CODE global ionosphere maps are temporally and spatially smoothed.

With the slant differential ionospheric delays, two sets of slant ionosphere gradients are calculated. One set with the baseline length l, and the other set with the IPP distance l_{IPP}:

$$g_{ab\_l} = \frac{I_{ab}}{l} \tag{D.7}$$

$$g_{ab\_IPP} = \frac{I_{ab}}{l_{IPP}} \tag{D.8}$$

Vertical Differential Ionospheric Delay and its Gradient

The slant differential ionospheric delays are mapped into the vertical direction based on the thin-shell model. The mapping function F used in the processing is derived from ICAO (1996):

$$F = (1 - (\frac{R \cdot \cos\epsilon}{R + h})^{2})^{-\frac{1}{2}} \tag{D.9}$$

where R =6378136.3 m and h =350 km denote the radius of the Earth and the height of the ionosphere thin-shell model, respectively. ϵ stands for the elevation angle from station to satellite.

Since the differential ionospheric delays are extracted from the double-differences, the vertical delays Iv_{ab} can only be calculated on the single-difference level as shown in Equation D.10:

$$Iv_{ab} = \frac{I_{ab}}{F_{ab}} \tag{D.10}$$

with

$$F_{ab} = \frac{F_a + F_b}{2}, \tag{D.11}$$

where F_a, F_b and F_{ab} represent the mapping functions for station a, station b and the station-pair mean mapping function, respectively.

The vertical delays Iv_{ab} calculated in this way are different from the vertical delays extracted at the zero-difference level Iv_{ab_zd}

$$Iv_{ab\_zd} = \frac{I_a}{F_a} - \frac{I_b}{F_b}. \tag{D.12}$$

The difference Iv_b is given by

$$\begin{aligned} \Delta I &= Iv_{ab\_zd} - Iv_{ab} \\ &= \frac{I_b + I_{ab}}{F_a} - \frac{I_b}{F_b} - \frac{2 \cdot I_{ab}}{F_a + F_b} \\ &= \frac{F_b - F_a}{F_a \cdot F_b} \cdot I_b + \frac{F_b - F_a}{F_a \cdot (F_a + F_b)} \cdot I_{ab} \end{aligned} \tag{D.13}$$

with I_b approximately equals to the ionosphere model values from station b to satellite i derived from the global CODE ionosphere map at the corresponding epoch.

The vertical differential ionospheric delays are then corrected with ΔI and described as Iv_{ab}^{map}:

$$Iv_{ab}^{map} = Iv_{ab} + \Delta I \tag{D.14}$$

Afterwards, the vertical ionosphere gradients are calculated with the IPP distances l_{IPP}:

$$gv_{ab\_IPP}^{map} = \frac{Iv_{ab}^{map}}{l_{IPP}} \tag{D.15}$$

Analysis of the Ionospheric Residuals

Figure D.5 shows the daily maximum (absolute value) differential ionospheric delays in the slant and vertical direction. The vertical delays of the stormy ionosphere days (see Table D.1) have been excluded. We see that the slant and vertical ionospheric residuals on the single-difference level reach 6.2 m and 2.4 m on November 24, 2001. The 11-year solar cycle is also visible in the plot.

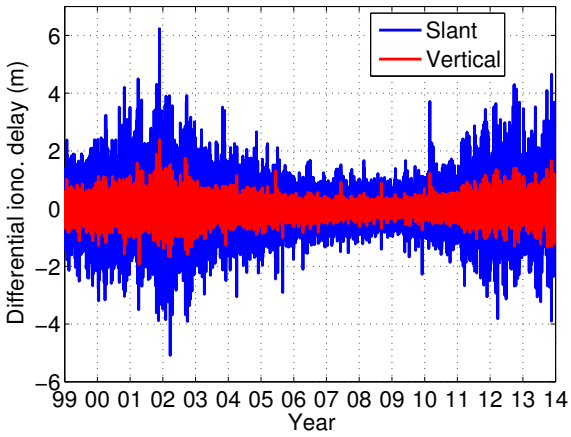

Figure D.5: Daily maximum differential ionospheric delays in the slant and vertical direction using the AGNES stations from 1999 to 2013.

Looking into the details of, e.g., the vertical delays, we can see that most of the daily maximum vertical differential delays appear between 10:00 and 14:00 in Central European Time (CET) (see Figure D.6), and concentrate mostly in the south direction (about 49% between 150° and 210° in the station-pair mean azimuth to the satellite) with low elevation angles (about 67% below 30° in the station-pair mean elevation) (see Figure D.7). This indicates possible non-ionospheric errors like multipath that still remain in the residuals. The hole in the north direction in Figure D.7 is due by the GPS satellite constellation as seen from Switzerland.

As mentioned before, the zero-mean condition applied for each baseline per epoch for the slant differential ionospheric delays is corrected for by adding the mean model values from the global CODE ionosphere maps. Figure D.8 shows the daily maximum (in absolute

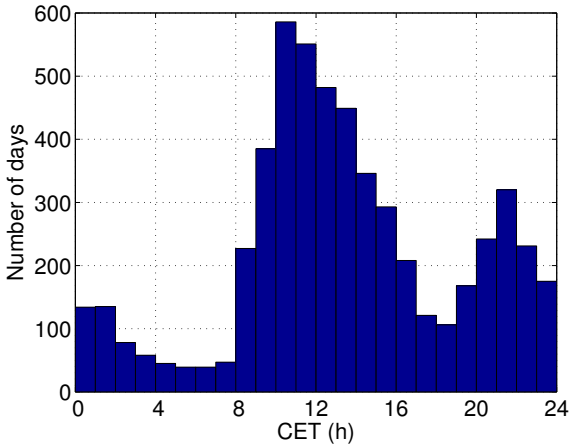

Figure D.6: Histogram of the daily maximum vertical differential ionospheric residuals with respect to Central European Time (CET) from 1999 to 2013.

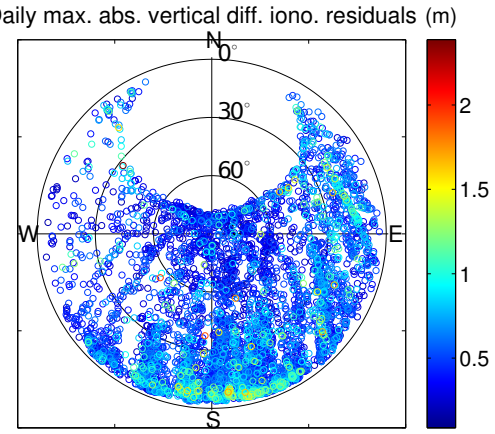

Figure D.7: Skyplot of the daily absolute maximum vertical differential ionospheric residuals in meters from 1999 to 2013.

values) and the daily mean of these model corrections. We see that the daily maxima are in the decimeter to meter range, while the mean values are mostly at centimeter level. The trend of the maximum corrections also corresponds more or less to the activity of the ionosphere. The maximal model correction amounts to about 2.35 m on November 24, 2001, while the corrections between 2006 and 2010 are in general smaller. These corrections have a large influence on the results and can not be neglected.

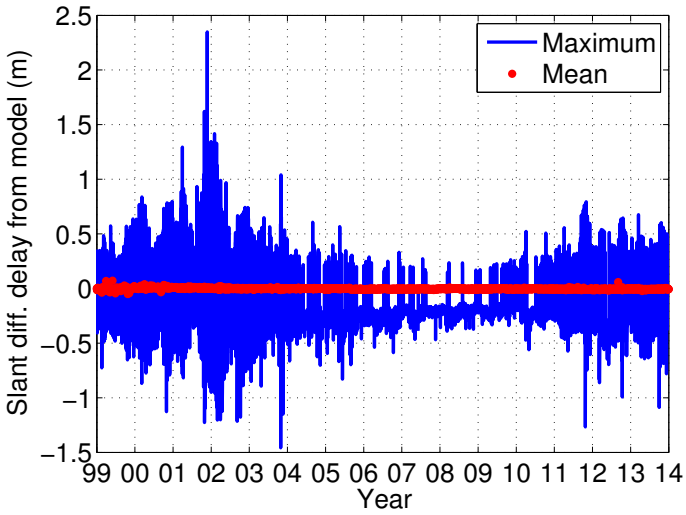

Figure D.8: The daily maximum and daily mean values of the baseline-wise epoch mean slant differential ionospheric delays derived from the CODE global model from 1999 to 2013.

Remaining Non-ionospheric Biases

In the AGNES network there are several very short baselines, i.e. shorter than 25 m. They are not used for calculating the gradients, but are very useful to investigate the remaining non-ionospheric biases, since the differential ionospheric residuals for such short baselines should almost be zero.

The day June 16, 2013 with very weak ionosphere activity ($K_P = 0.7$, $D_{ST} = -1$ nT) was selected for the analysis of these very short baselines. Figure D.9 shows the slant differential residuals (top), the mean (red dots, bottom) and the standard deviation (blue lines, bottom) of the residuals for 11 very short baselines on June 16, 2013. We see that the standard deviations of the slant residuals are in the millimeter to centimeter range. The maximal observed value is 12.7 cm and is generated by the station pair ETH2 and ETHZ with a baseline length of about 13.7 m.

Figure D.10 shows the skyplot of the slant differential ionosphere delays for the station pair ETH2 and ETHZ on June 16, 2013. The slant delays increase with decreasing elevation angles, while the azimuth-dependency is not very obvious. Further analysis also shows that the biases are not strongly related to CET (see Figure D.11).

This analysis shows that the non-ionospheric biases remaining in the estimated slant differential ionospheric delays are generally at cm-level and are elevation-dependent. Multipath is one of the possible error sources.

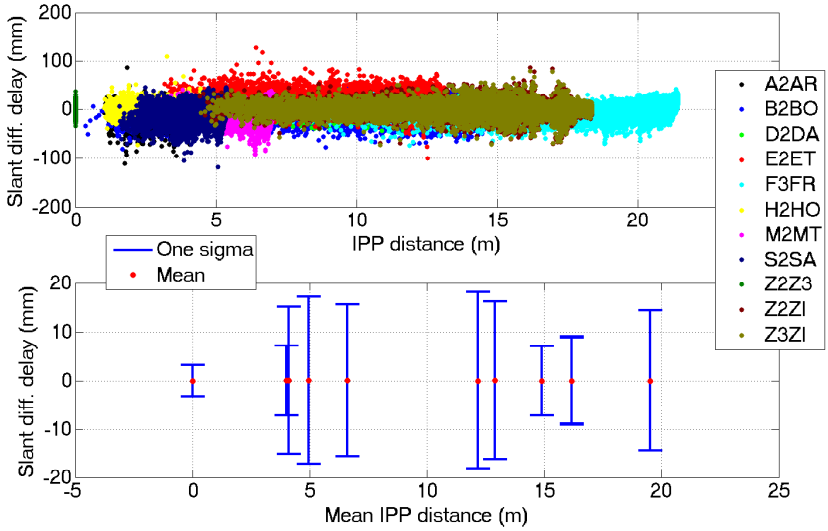

Figure D.9: Slant differential ionosphere residuals for very short baselines on June 16, 2013.

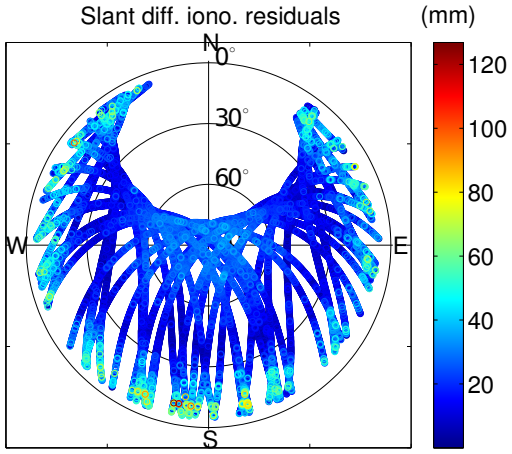

Figure D.10: Skyplot of the differential slant ionosphere residuals for station pair ETH2 and ETHZ on June 16, 2013.

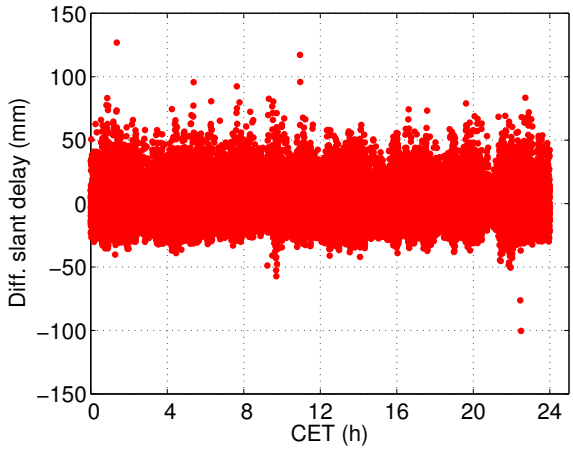

Figure D.11: Slant differential ionosphere delays for station pair ETH2 and ETHZ with respect to CET on June 16, 2013.

Correlation with the Indices

Figure D.12 shows the relationship between the absolute daily maximum (in absolute values) slant differential ionospheric delays and the geomagnetic indices K_P, D_{ST}, as well as the mean TEC values between 12:00 and 14:00 UT derived from the CODE global ionosphere maps (CODE products, 2014). We see that the absolute daily maximum delays increase proportionally to the absolute values of all three indices.

In order to compare the correlation between the slant delays and these three indices, the indices and the slant delays are modified, so that the auto-correlations of their absolute

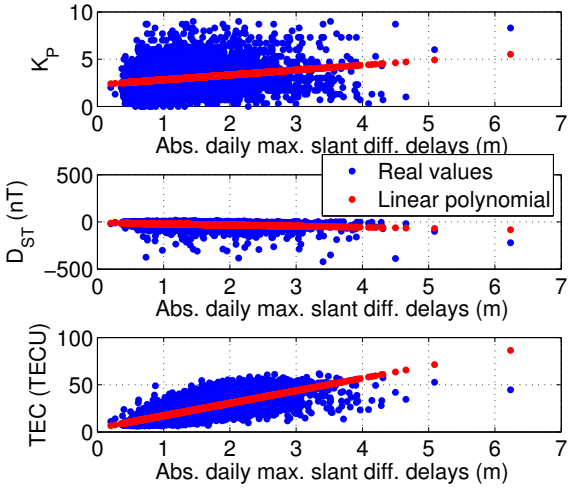

Figure D.12: Correlation between the absolute daily maximum slant differential ionospheric delays and different indices.

values at zero lag are equal to 1:

$$I_S^{mod} = \frac{|DI_S|}{\sqrt{xcorr(|I_S|,0)}} \tag{D.16}$$

$$K_P^{mod} = \frac{|DK_P|}{\sqrt{xcorr(|K_P|,0)}} \tag{D.17}$$

$$D_{ST}^{mod} = \frac{|DD_{ST}|}{\sqrt{xcorr(|D_{ST}|,0)}} \tag{D.18}$$

$$TEC^{mod} = \frac{|DTEC|}{\sqrt{xcorr(|TEC|,0)}}, \tag{D.19}$$

where DI_S, DK_P, DD_{ST} and $DTEC$ represent the daily maximum (in absolute values) slant differential ionospheric delay, the daily peak K_P index, the daily lowest D_{ST} index and the mean TEC value. I_S^{mod}, K_P^{mod}, D_{ST}^{mod} and TEC^{mod} stand for the modified slant delays and the modified indices. $xcorr(x,0)$ represents the auto-correlation of time series x at zero lag. The auto-correlations of I_S^{mod}, K_P^{mod}, D_{ST}^{mod} and TEC^{mod} are thus one.

Figure D.13 illustrates the cross correlations of the modified slant delays I_S^{mod} and the modified indices. We see that a positive correlation exists between the modified slant differential delays and all the three indices, while the correlation between TEC^{mod} and I_S^{mod} is the highest. The two local maxima at circa 4000 days (see the green line) could correspond to the 11-year solar cycle.

Analysis of the Ionosphere Gradients

The ionosphere gradients were calculated based on the slant and vertical differential ionospheric delays. Figure D.14 shows the daily maximum (in absolute values) slant and

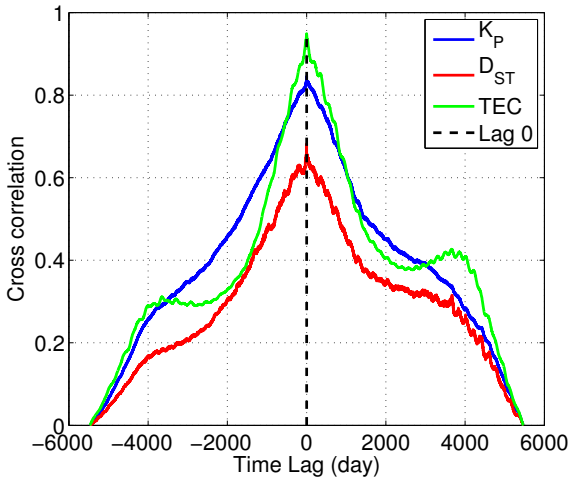

Figure D.13: Comparison of the cross correlations between the modified slant differential delays and the modified indices using the data from 1999 to 2013.

vertical ionosphere gradients g_{ab_IPP} and $gv^{map}_{ab\_IPP}$ from 1999 to 2013 for IPP pairs not shorter than 5 km. The stormy ionosphere days were excluded from the vertical gradients (red lines). We see that the range of the slant gradients is within ±50 mm/km in about 98.9% of the time, while the vertical gradients are in about 98.7% of the time within ±20 mm/km. The maximum absolute value reaches 81.2 mm/km for the slant gradients on October 20, 2001, and 33.8 mm/km for the vertical gradients on October 24, 2001, respectively. Both gradient time series decrease gradually after 2003 and increase again after 2011.

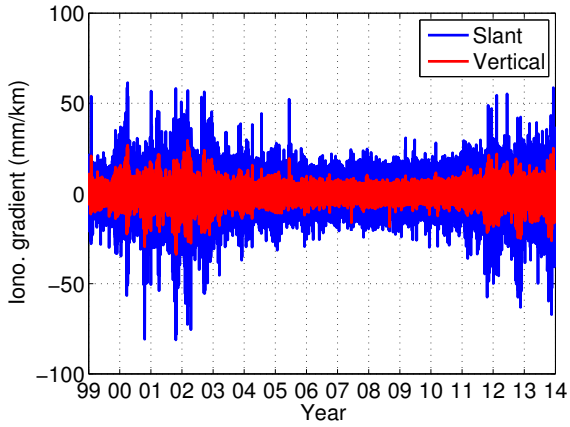

Figure D.14: Daily maximum slant and vertical ionosphere gradients from 1999 to 2013.

Overbounding Vertical Ionosphere Gradients

The so-called overbounding vertical ionosphere gradient $\sigma_{vig}^{overbound}$ is calculated based on the work of Lee et al. (2006b). The vertical ionosphere gradients were distributed into different distance bins according to their IPP distances and normalized in each bin with the mean gradient μ_{bin} of the bin and the standard deviation σ_{bin} of the bin. The bin distance is defined as 10 km in this study.

Afterwards, the zero-mean one-sigma Gaussian Probability Density Function (PDF) (see magenta line in Figure D.15) is inflated until all the non-Gaussian tails (outside ±3 mm/km) of the actual normalized gradients (see blue dots in Figure D.15) are bounded (see the green line in Figure D.15). Figure D.15 shows the inflated PDF for an quiet ionosphere day, namely July 20, 2006. The inflating factor f on this day is 2.09.

With the inflating factor f, the bin mean μ_{bin} and the bin standard deviation σ_{bin} of the vertical gradients, the overbounding vertical ionosphere gradient $\sigma_{vig}^{overbound}$ was calculated according to Lee et al. (2006b) in each bin:

$$\sigma_{vig}^{overbound} = |\mu_{bin}| + f \cdot \sigma_{bin} \tag{D.20}$$

Figure D.16 shows the $\sigma_{vig}^{overbound}$ (top) and the number of the IPP pairs (bottom) in each distance bin. In the first bin only IPP pairs longer than 5 km are considered. We see that the $\sigma_{vig}^{overbound}$ are mostly below 1 mm/km and increase rapidly when the distance bin gets smaller than 20 km. This might partially be caused by the low number of IPP pairs in the first two bins (1232 and 45968). However, we can see that the number of IPP pairs decreases also to below $5 \cdot 10^4$ when the distance bin is longer than 250 km. Another reason for the rapid increase might be the non-ionospheric biases remaining in the ionospheric residuals. Residual biases at centimeter level can cause gradient biases of several mm/km with an IPP distance of 10 km.

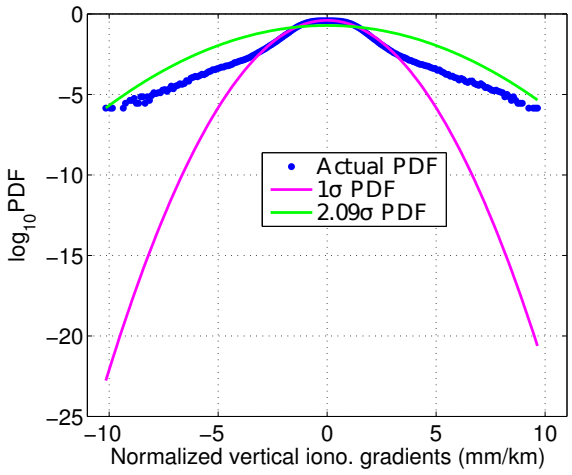

Figure D.15: Inflated PDF of the normalized vertical ionosphere gradients on July 20, 2006.

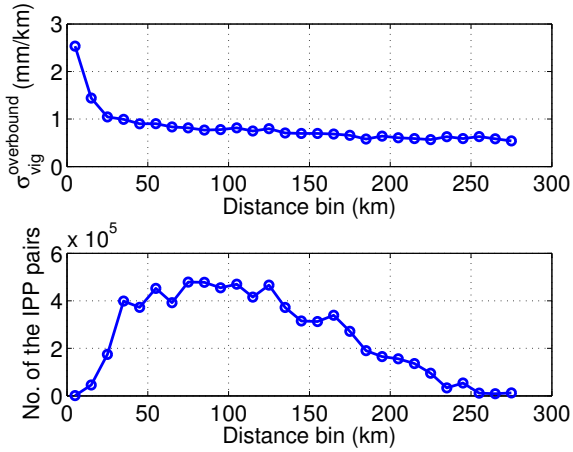

Figure D.16: $\sigma_{vig}^{overbound}$ and the number of IPP pairs in each 10-km distance bin on July 20, 2006.

The daily maximum $\sigma_{vig}^{overbound}$ over these 15 years are plotted in Figure D.17. The four subfigures indicate the daily maximum $\sigma_{vig}^{overbound}$ with different bin starts. For example, the first figure (top left in Figure D.17) shows the daily maximum $\sigma_{vig}^{overbound}$ starting from the first bin, the bin start is 5 km since all IPP pairs not longer than 5 km are excluded, and the second figure (top right in Figure D.17) shows the daily maximum $\sigma_{vig}^{overbound}$ starting from the second bin, namely 10 km. The black dots represent the days with a relatively strong ionospheric activity ($K_P \geq$7 or D_{ST} <-200 nT). The stormy ionosphere days were excluded from the vertical gradients. It should be noticed that the daily inflating factor f used in all four subfigures are the same, namely the one calculated with all the normalized vertical gradients per day. The daily inflating factors from 1999 to 2013 are plotted in Figure D.18.

It is not difficult to see that most of the daily maximum $\sigma_{vig}^{overbound}$ are generated in the first and the second distance bin because of the remaining non-ionospheric biases. The

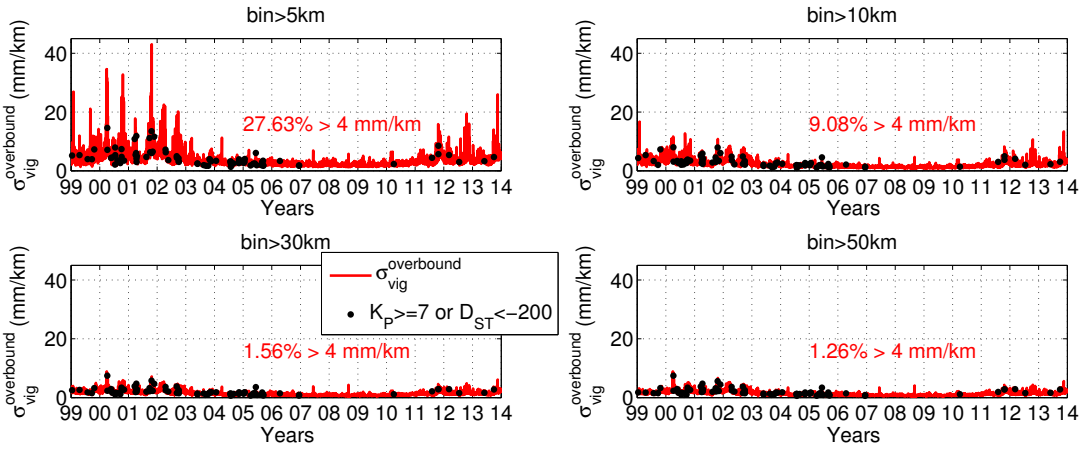

Figure D.17: Daily maximum $\sigma_{vig}^{overbound}$ with different bin starts from 1999 to 2013.

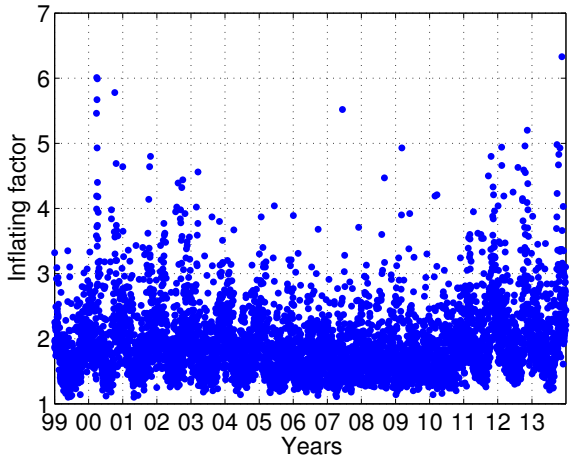

Figure D.18: Inflating factor f from 1999 to 2013.

huge $\sigma_{vig}^{overbound}$ in these two bins are mainly generated by the large bin mean μ_{bin} and the bin standard deviation σ_{bin} (see Figure D.19). The inflating factor f, however, does not vary much with the ionosphere activity (see Figure D.18). However, it is interesting to see that the inflating factor f shows a yearly pattern and is always getting larger in winter. In the years with strong ionosphere activity, this periodical behavior of f is even more pronounced.

Figure D.20 shows the mean number of IPP pairs per day used for the estimation of the $\sigma_{vig}^{overbound}$ for each distance bin from 1999 to 2013. The IPP pairs shorter than 5 km were excluded from the first bin. The number increases gradually during these 15 years and most of the IPP pairs concentrate at distances between 50 km and 150 km. In the years 1999, 2000 and 2001, the mean number of IPP pairs per day between 5 km and 10 km

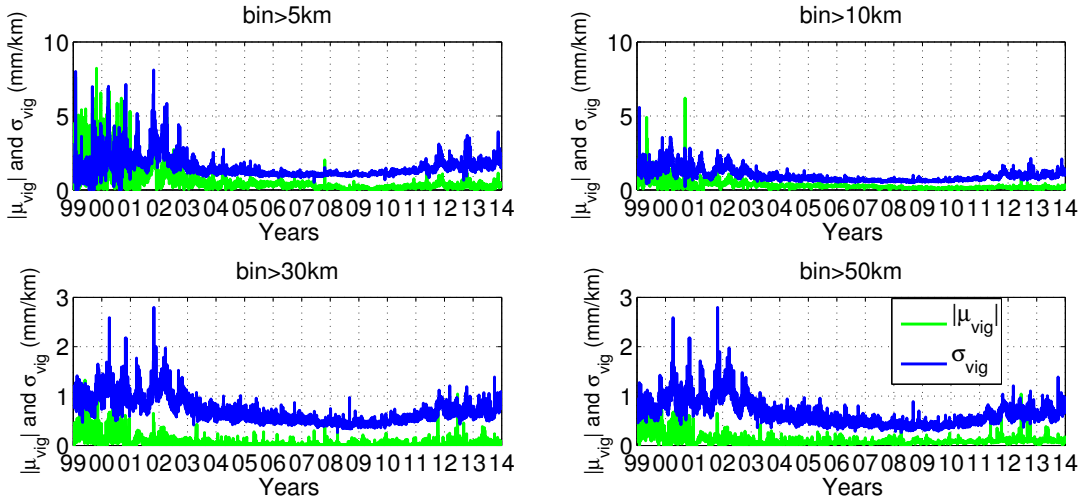

Figure D.19: $|\mu_{bin}|$ and σ_{bin} for daily maximum $\sigma_{vig}^{overbound}$ from 1999 to 2013.

(first bin) is even below 500. Considering the relatively large non-ionospheric biases and the low observation number in the first two bins, we suggest not to take into account the $\sigma_{vig}^{overbound}$ in these two bins. Ignoring the values in these two bins, about 96.9% of the daily maximum $\sigma_{vig}^{overbound}$ over these 15 years are below or equal to 4 mm/km, the suggested value in Lee et al. (2006b). The maximum $\sigma_{vig}^{overbound}$ of 11.74 mm/km appears on April 3, 2000, ignoring the first two bins.

Comparison with the CONUS Threat Model

The slant ionosphere gradients were calculated not only for the stormy ionosphere days, but for all days under diverse ionospheric conditions considering all the IPP pairs not shorter than 5 km. In order to comply with the slant gradients used for the CONUS model (Ene et al., 2005), the set of slant gradients calculated with the baseline length was used and the resulting daily maximum absolute values are plotted as blue dots in Figure D.21. The red dots represent the days with stormy ionospheric activity and the magenta line illustrates the slant ionosphere gradient bound of the CONUS ionospheric anomaly threat model (Pullen et al., 2009).

We see that the daily maximum absolute slant gradients are far below the slant ionosphere gradient bound of the CONUS model, the largest slant gradient of 42.6 mm/km occurring on November 24, 2001, for the station pair ETHZ and SCHA with a baseline length of 38.3 km. The maximum slant gradient appeared in the late afternoon (between 17:00 and 18:00) of CET (see Figure D.22) at a low elevation angle of about 7.5 degrees (see Figure D.23).

With the assumptions that the actual separation of the GBAS reference point and the airplane at a 200 ft decision height d is 6 km, that the time constant of the single-frequency carrier-smoothing filter t amounts to 100 s and the velocity of the aircraft in the landing process $v_{a/c}$ is 0.07 km/s (Pullen et al., 2009), the maximum differential pseudorange error

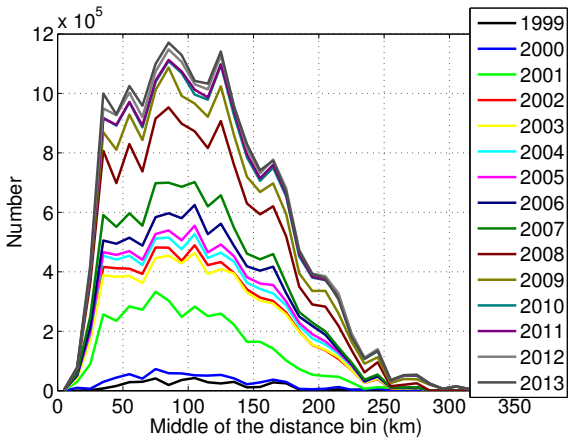

Figure D.20: Mean number of IPP pairs per day for each distance bin from 1999 to 2013.

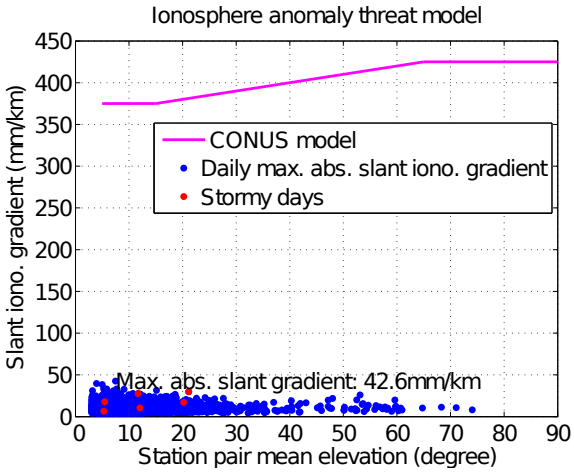

Figure D.21: Comparison of the daily maximum absolute slant ionosphere gradients with the CONUS ionospheric anomaly threat model.

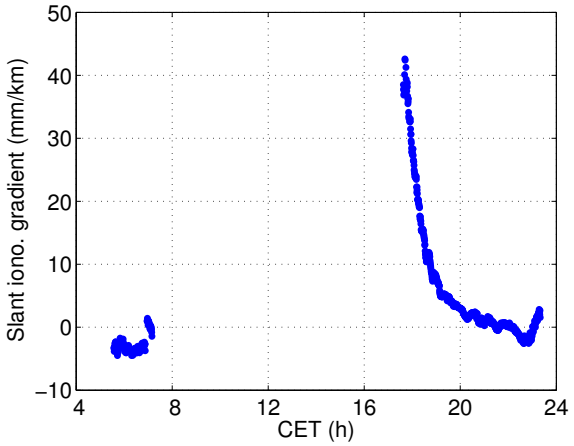

Figure D.22: Slant ionosphere gradient for the station pair ETHZ and SCHA occuring on November 24, 2001.

p_{err} generated by the maximum absolute slant ionosphere gradient g_S amounts to

$$\begin{aligned} p_{err} &= g_S \cdot (d + 2 \cdot t \cdot v_{a/c}) \\ &= 42.6 \, \frac{mm}{km} \cdot 20 \; km \\ &= 0.852 \; m \end{aligned} \tag{D.21}$$

according to Pullen et al. (2009).

It should be noted that the CONUS ionospheric anomaly threat model also considers the ionosphere front speed and front width. These parts of the threat model have not been considered in this study.

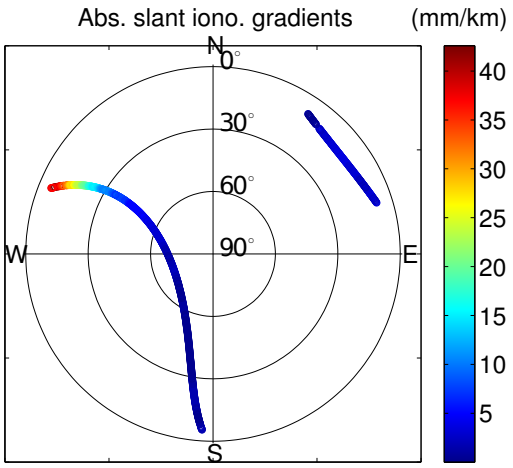

Figure D.23: Skyplot of the slant ionosphere gradients for the station pair ETHZ and SCHA on November 24, 2001.

Conclusion

In order to assess the ionospheric errors remaining in the differential GPS observations between the GBAS reference stations and the airborne user in Switzerland, the single-difference ionospheric delays and the ionosphere gradients were estimated based on the GPS data from the AGNES stations over 15 years. The results derived from double-difference phase observations with resolved ambiguities are free from code-related biases like DCBs. Nevertheless, the global CODE ionosphere model values used to correct for the epoch-wise zero-mean condition per baseline might cause temporal and spatial smoothing effects on the results.

Using the modified slant ionospheric residuals, the modified geomagnetic indices K_P, D_{ST}, and the modified mean TEC values between 12:00 and 14:00 UT derived from the CODE global ionosphere maps, we observed positive correlations between the slant residuals and all three indices. The correlation of the differential slant ionospheric residuals with the TEC values is stronger than with the other two geomagnetic indices.

The daily maximum (absolute values) differential ionospheric residuals are mostly (99.82%) within ±4 m in the slant direction and ±2 m (99.98%) in the vertical direction. The daily maximum vertical differential residuals are mostly concentrated around local noon in Switzerland. Through the analysis of the slant differential ionospheric residuals for some very short baselines, we know that non-ionospheric biases on the centimeter level still remain in the residuals. This may affect the estimated ionosphere gradients for short IPP distances significantly.

The absolute daily maximum slant and vertical ionosphere gradients calculated with the IPP distances are in 98.85% of the time within 50 mm/km and in 98.68% of the time within 20 mm/km. The $\sigma_{vig}^{overbound}$ increases for the bins with short bin distance because

of the remaining non-ionospheric biases and the low observation numbers. Ignoring bins shorter than 20 km, about 96.9% of the daily maximum $\sigma_{vig}^{overbound}$ in Switzerland during the 15 years in Switzerland are below 4 mm/km.

The slant ionosphere gradients calculated with the baseline length are estimated for all days under different ionospheric conditions and compared with the slant ionosphere gradient boundary of the CONUS ionospheric anomaly threat model. The biggest value of the absolute daily maximum slant gradient is 42.6 mm/km which lies well below the CONUS slant ionosphere gradient boundary.

Acknowledgements

This work has been financed by Flughafen Zrich AG as part of the Skyguide (Swiss Air Navigation Services Ltd.) project “Impact of Ionospheric Activities onto GNSS Signal during Approach and Landing” within the frame of the Swiss-wide program to implement new technologies (CHIPS). We would also like to thank swisstopo for providing the AGNES data for the processing.

E Additional Papers

The papers that I have contributed during my dissertation, but were not included in this thesis, are listed here.

Fritsche M., Sośnica K., Rodríguez-Solano C.J., Steigenberger P., Wang K., Dietrich R., Dach R., Hugentobler U., Rothacher M. (2014): Homogeneous reprocessing of GPS, GLONASS and SLR observations, Journal of Geodesy 88(7): 625-642. doi:10.1007/s00190-014-0710-3.

The final publication is available at `http://link.springer.com`.

Glaser S., Fritsche M., Sośnica K., Rodríguez-Solano C.J., Wang K., Dach R., Hugentobler U., Rothacher M., Dietrich R. (2015): A consistent combination of GNSS and SLR with minimum constraints, Journal of Geodesy 89(12): 1165-1180. doi:10.1007/s00190-015-0842-0.

The final publication is available at `http://link.springer.com`.

(Glaser S., Fritsche M., Sośnica K., Rodríguez-Solano C.J., Wang K., Dach R., Hugentobler U., Rothacher M., Dietrich R. (2015): Erratum to: A consistent combination of GNSS and SLR with minimum constraints, Journal of Geodesy 89(12): 1181-1182. doi:10.1007/s00190-015-0853-x.

The final publication is available at `http://link.springer.com`.)